The copyright of this thesis vests in the author. No quotation from it or information derived from it is to be published without full acknowledgement of the source. The thesis is to be used for private study or non-commercial research purposes only.

Published by the University of Cape Town (UCT) in terms of the non-exclusive license granted to UCT by the author.

University of Cape Town

DEVELOPMENT OF A PLASMA SOURCE ION IMPLANTATION FACILITY FOR THE MODIFICATION OF MATERIALS' SURFACES.

University of Cape Town

By

Kevin Alan Meyer

Submitted in fulfilment
of the requirements for the degree of
Doctor of Philosophy

Department of Physics,
Faculty of Science,
University of Cape Town,
2001

Preface

The experimental work described in this thesis was carried out at the National Accelerator Centre, Faure, under the supervision of Doctor Victor M. Prozesky and under the co-supervision of Professor Craig M. Comrie, Department of Physics, University of Cape Town and Professor Michael J. Alport, School of Pure and Applied Physics, University of Natal, Durban, from April 1996 to November 1999.

These studies represent original work by the author and have not been submitted in any form to another University. Where use was made of the work of others it has been duly acknowledged in the text.

University of Cape Town

Acknowledgements

I would like to take this opportunity to thank everyone who offered advice and assistance during the research period, especially the following:
My supervisors (Craig Comrie, Vic Prozesky and Mike Alport), the staff and researchers of the Materials Research Group, Mira Topic of UCT's Materials Engineering, the materials modification group at the Forschungszentrum Rossendorf, the Van de Graaff accelerator group at the AEC/NECSA.

Special thanks to Lawrence Ashworth of the Materials Research Group Workshop, Karl Springhorn and the rest of the Electronic Workshop staff. I would also like to take this opportunity to thank all my fellow postgraduate students for many valuable discussions. There are probably many others to whom I am indebted, to them I offer my gratitude.

I am also grateful for funding received from the Foundation of Research Development/National Research Foundation.

To my parents, without whom none of this would have been possible.

University of Cape Town

Dedication

To MLBO. For putting up with me through the difficult times and sharing the good times.

University of Cape Town

Abstract

In Plasma Source Ion Implantation high energy [10–50 keV] plasma ions are implanted into materials to modify surface properties, achieving surface hardening, increased wear and corrosion resistance. Plasma Source Ion Implantation is also used for doping semiconductors and could form an essential step in the manufacture of multilayered wafers.

This thesis describes the development and construction of the plasma implantation facility at the Materials Research Group of the National Accelerator Centre; in particular, the development of the Plasma Assisted Materials Modification Laboratory, the analytical tools available at the Materials Research Group and surrounding universities, basic research into the implantation of steels, the x-rays emitted as a side-effect of plasma source ion implantation and the development of an analytical technique of interest to silicon wafer-cutting technologies.

A chemistry laboratory at National Accelerator Centre was converted into a plasma processing laboratory. A plasma chamber was modified to accommodate the high voltage feedthrough from the high voltage pulsed power supply. A control system (hardware and software) was developed to allow remote control and monitoring of the plasma processing facility.

A modular and upgradable high voltage pulsed power supply (RUP-4a) was constructed and has a maximum implant energy of 30 kV, peak current of 11 A and a mean current of 30 mA. Pulse length can be varied from less than 1 μs, to greater than 100 μs.

The "NetLab" software suite are computer programs that present a Graphical User Interface which allows the user to control some implantation parameters via a dedicated data capture computer which communicates with the equipment. The user interface software uses TCP/IP networking protocols allowing remote access to this laboratory.

During plasma source ion implantation, x-rays are generated, predominantly by the bremsstrahlung processes. It was decided to investigate the nature of the x-rays, since this phenomenon is a safety hazard and a correlation between the x-ray flux and the target surface condition was suspected.

Traditionally plasma source ion implantation has been used to harden metals and some basic research was performed for three industrial applications. Recently, it has been used in the silicon industry for large scale wafer doping and as a first step in constructing new generation wafers. An attempt was made at implanting hydrogen into silicon to investigate wafer cleaving techniques, and an in-situ analytical technique was developed to examine the behaviour of the implanted hydrogen as a function of temperature.

University of Cape Town

Contents

Preface i

Acknowledgements iii

Dedication v

Abstract vii

List of Symbols xvii

List of Abbreviations xix

1 Introduction 1

1.1 The National Accelerator Centre . . . 1

1.1.1 Research at the National Accelerator Centre . . . 1

1.1.2 Research at the Materials Research Group . . . 1

1.2 Development of the PSII facility at the National Accelerator Centre . . . 2

1.3 Thesis structure . . . 2

1.3.1 The plasma processing facility . . . 3

1.3.2 Analytical tools . . . 4

1.3.3 Fundamental Research and Applications . . . 5

2 Surface modification 7

2.1 Surface Hardening . . . 7

2.2 Surface coating techniques . . . 7

2.3 Surface modification techniques . . . 8

2.3.1 Thermal techniques . . . 8

2.3.2 Modification by addition . . . 9

2.3.3 Gas nitriding . . . 9

2.4 Implantation Methods . . . 9

2.4.1 Surface modification versus coating techniques . . . 9

2.4.2 Ion beam implantation . . . 10

University of Cape Town

2.4.3 Plasma Source Ion Implantation Concept 11
2.5 Ion implantation processes 12
2.5.1 Determining ion implantation flux 12
2.5.2 Retained dose 13
2.5.3 Ion induced sputtering 13
2.5.4 Ion induced electron emission 14
2.6 Summary 14

3 Introduction to Plasmas **17**
3.1 Plasma Formation - DC discharge 17
3.1.1 Ionization cross-section and mean-free-path 17
3.1.2 Primary electron current limitations 19
3.1.2.1 Space charge limited emission 19
3.1.2.2 Temperature limited emission 19
3.1.2.3 Temperature versus Space charge limitations 19
3.2 Probe Theory 20
3.2.1 Plasma analysis with the Langmuir Probe 20
3.3 Plasma sheaths 23
3.3.1 Target packing density 24
3.4 Summary 24

4 Construction of the PSII laboratory **25**
4.1 Chemistry laboratory to PSII laboratory 25
4.2 Cabling 26
4.3 PSII plasma chamber 27
4.3.1 Rear flange 27
4.3.2 Other flanges 28
4.3.3 Filaments 28
4.3.4 Chamber cooling 29
4.3.5 Probes 30
4.4 Stepper motor controllers 31
4.5 Chamber wiring for plasma generation and ancillary circuits 34
4.5.1 Discharge current control circuit 34
4.5.2 Flow rate delay switch 36
4.6 Remote control and monitoring of laboratory 36
4.7 Summary 37

5 High-voltage power-supply **39**
5.1 Overview 39

University of Cape Town

5.1.1 Design philosophy 39
5.2 Circuit description 40
5.2.1 Description of circuit Components 40
5.2.2 RUP-4a Principle of operation 41
5.2.3 Operation of tetrode 41
5.2.4 Electrical operation 42
5.3 Implant Operation 43
5.3.1 Principle of operation 43
5.3.2 Inputs and controls 43
5.4 Physical description 43
5.4.1 X-ray shielding 44
5.4.2 Tetrode cooling 45
5.4.3 Voltage and current measurements 45
5.5 Safety 45
5.5.1 Interlocks 45
5.6 Upgrade options 46
5.6.1 Increasing implantation voltage 46
5.6.2 Increasing implantation current 46
5.7 Operational precautions 46
5.7.1 Arc detection 46
5.7.2 Operational limits 46
5.7.3 Turning off the tetrode filaments 47
5.8 Summary 48

6 The "NetLab" Software **49**
6.1 Introduction 49
6.1.1 User manual 49
6.1.2 Inter-program communication 49
6.1.3 Design philosophy 50
6.1.4 Software purpose 50
6.2 Software components 51
6.2.1 The TCP/IP library 51
6.2.2 The TDS-220 library 51
6.2.3 The "NetLab" kernel 52
6.3 User interface 52
6.3.1 The Experiment Application window 52
6.3.2 Implantation control window 53
6.3.3 The TDS-220 Oscilloscope window 53

University of Cape Town

6.4 Possible extensions . . . 54
6.5 Summary . . . 55

7 Analytical Techniques 57
7.1 Nuclear techniques . . . 57
7.1.1 General theory . . . 57
7.1.1.1 Stopping power . . . 58
7.1.1.2 Cross-section . . . 59
7.1.1.3 Kinematic Factor . . . 60
7.1.1.4 Straggling . . . 61
7.1.1.5 Yield . . . 62
7.1.2 Analysing spectra . . . 62
7.1.3 Elastic Recoil Detection Analysis . . . 63
7.1.4 Rutherford Backscattering Spectrometry . . . 64
7.1.4.1 Channelling . . . 65
7.1.5 Nuclear Reaction Analysis . . . 67
7.2 Nuclear analytical apparatus . . . 69
7.2.1 The nuclear microprobe chamber at the Materials Research Group . . . 69
7.2.2 The RBS chamber at the Materials Research Group . . . 70
7.3 X-ray diffraction . . . 72
7.3.1 Introduction . . . 72
7.3.2 Scattering from planes in a solid - X-ray diffraction . . . 73
7.3.3 Applications of XRD . . . 74
7.3.4 Metallurgical applications . . . 74
7.3.5 XRD Equipment at the Materials Research Group . . . 75
7.3.6 Microhardness measurements . . . 77
7.3.7 Dynamic depth hardness measurements . . . 78
7.3.8 Microhardness Equipment . . . 79
7.3.9 Auger electron spectroscopy - AES . . . 79
7.3.10 Other techniques . . . 81
7.4 Summary . . . 81

8 X-ray analysis 83
8.1 Introduction . . . 83
8.2 Electron sources . . . 84
8.2.1 Displaced plasma electrons . . . 84
8.2.2 Ion induced electron emission . . . 84
8.2.3 Measuring the secondary electron flux . . . 86
8.2.3.1 Retarding field energy analyser . . . 86

University of Cape Town

8.2.3.2 Scintillator . . . 87
8.2.3.3 By comparison with models of the implanted ion flux . . . 87
8.3 X-ray production . . . 88
8.3.1 Bremsstrahlung background continuum . . . 88
8.3.2 Characteristic x-rays . . . 88
8.3.3 Attenuation . . . 89
8.3.4 Simulation . . . 89
8.4 Experiment and measurements . . . 90
8.4.1 Hardware . . . 90
8.4.2 Time resolved measurements . . . 92
8.4.3 Comparison with predicted x-ray emission . . . 94
8.5 Safety . . . 96
8.6 Summary . . . 96
8.6.1 Further work . . . 97

9 Metal applications **99**
9.1 Background of PSII . . . 99
9.1.1 PSII research at the National Accelerator Centre . . . 99
9.1.2 Preparation of metallic samples . . . 100
9.2 Steel sliding seal . . . 100
9.2.1 Methods of hardening . . . 100
9.2.2 Implantation procedure . . . 101
9.2.3 Testing . . . 101
9.2.4 Results . . . 102
9.2.5 Conclusions . . . 102
9.3 Diesel fuel pump components . . . 103
9.3.1 Composition . . . 103
9.3.2 Sample preparation . . . 103
9.3.3 Implantation procedure . . . 103
9.3.4 Results . . . 104
9.3.5 Discussion . . . 105
9.3.6 Conclusions . . . 106
9.4 Sand sampling probe . . . 106
9.4.1 Probe description . . . 106
9.4.2 Hardening procedures . . . 107
9.4.3 Results . . . 107
9.4.4 Conclusions . . . 109
9.5 Summary . . . 109

University of Cape Town

10 Silicon applications 111
10.1 Introduction and background 111
10.1.1 Wafer doping and related techniques 111
10.1.2 Silicon cleaving applications 111
10.2 Research at this facility 113
10.2.1 Implantation of hydrogen into silicon 113
10.2.2 In-situ analysis of hydrogen implanted silicon 114
10.3 Silicon sample preparation 114
10.4 Hydrogen PSII of silicon 114
10.4.1 ERDA analysis and Results 115
10.4.2 Conclusions 116
10.5 In-situ ERDA during annealing 116
10.5.1 Apparatus 117
10.5.2 XSYS data processing 119
10.5.3 Measurements 120
10.5.4 Results 124
10.5.5 Other features - RBS spectra of sample E09 127
10.5.6 Conclusions 128
10.6 Summary 129

11 Conclusions 131
11.1 The implantation facility 131
11.2 X-ray emission research 132
11.3 Metal applications 132
11.4 Silicon applications 132
11.5 Future projects 132

Appendices 134

A PSII sheath theory 135
A.1 Time scales 135
A.2 Dimensionless co-ordinates 136
A.3 The initial plasma sheath 136
A.4 Sheath Evolution 138
A.5 Extensions to the basic theory 139
A.5.1 Sheath conformality to target shape 140
A.5.2 Additional considerations: pulse rise-time, displacement current, collisions, etc. . . . 140
A.5.3 One dimensional special cases 140
A.5.4 Two-dimensional simulations 140

University of Cape Town

A.5.5 Plasma filling-in 140

B Ion - surface physics 141
B.1 Ion induced sputtering 141
B.2 Sputtering of single element targets 142
B.2.1 Deposited energy 142
B.2.2 Sputtering yield 143
B.3 Semi-empirical formula for sputtering of single element targets 143
B.3.1 Calculations 145
B.3.2 Sputtering at glancing angles 146
B.3.3 Ion implantation and the steady state condition 146
B.4 Sputtering of alloys and compounds 147
B.4.1 Preferential sputtering 148
B.4.2 Composition changes 148
B.4.3 Composition depth profiles 148
B.5 High dose ion implantation 149
B.6 Factors that influence concentration in high-dose ion implantation 150
B.7 Sputtering from spikes 150

C Computers and electronic hardware 153
C.1 Facility Configuration 153
C.2 Interfaces 154
C.2.1 The GPIB interface 154
C.2.2 The PC parallel printer port 155
C.2.3 Joystick port 156
C.3 Data acquisition 157
C.3.1 Data acquisition hardware 157
C.3.2 Data and voltage sources 158
C.4 Voltage sources 158
C.4.1 The CompuGen CG-840 arbitrary waveform generator card 158
C.5 Data sources 159
C.5.1 The GageScope CS-220 oscilloscope card 159
C.5.2 The Tektronix TDS-220 digital oscilloscope 160
C.6 Bi-directional devices - The Keithley 6517 and 617 electrometers 161

D "NetLab" User Manual 163

E Datasheets 177

Bibliography 197

University of Cape Town

List of Symbols

I_{sat}^{+}	Ion saturation current
I_{sat}^{-}	Electron saturation current
I_D	Discharge current (A)
V_f	Filament potential (V)
m_i	Ion mass (kg)
m_e	Electron mass (kg)
n_i	Ion density (kg)
n_e	Electron density (cm^{-3})
n_n	Neutral gas density (cm^{-3})
n_0	Plasma density (cm^{-3})
n_s	Plasma sheath edge density (cm^{-3})
N_∞	Plasma background density (cm^{-3})
τ_{pi}	Ion plasma period (s)
τ_{pe}	Electron plasma period (s)
τ_{pulse}	Pulse width (s)
ω_{pi}	Ion plasma frequency (radians.s^{-1})
ω_{pe}	Electron plasma frequency (radians.s^{-1})
f_{pi}	Ion plasma frequency (Hz)
f_{pe}	Electron plasma frequency (Hz)
λ_m	Mean free path for collisions (m)
λ_D	Debye length (m)
ϕ	Potential (V)
ϕ_f	Floating potential (V)
ϕ_p	Plasma Potential (V)
ϕ_{probe}	Probe potential (V)
ϕ_{target}	Target potential (V)
ϕ_s	Plasma sheath edge potential (V)
V_{ap}	Potential applied to probe(V)
T_e	Electron temperature (eV)

University of Cape Town

T_i	Ion temperature (eV)
ϵ_0	Permittivity of free space ($C^2.N^{-1}.m^{-2}$)
q_e	Charge of an electron (1.602×10^{-19}Q)
S_0	Planar ion matrix sheath thickness (cm)
r_0	Spherical ion matrix sheath thickness (cm)
ν_d	Drift velocity
ν_e	Electron thermal velocity
ν_i	Ion thermal velocity
erf	Error function
C_s	Ion acoustic speed ($cm.s^{-1}$)
A_p	probe area (m^2)
λ_{ion}	Ion implantation depth

University of Cape Town

List of Abbreviations

AES	Auger Electron Spectrometry
AFM	Atomic Force Microscopy
CVD	Chemical Vapour Deposition
DLC	Diamond-like Carbon
GDOS	Glow-discharge Optical Spectroscopy
GUI	Graphical User Interface
IBAD	Ion Beam Assisted Deposition
NRA	Nuclear Reaction Analysis
PBII	Plasma Based Ion Implantation
PIII	Plasma Immersion Ion Implantation
PIXE	Particle Induced X-ray Emission
PSII	Plasma Source Ion Implantation
PTFE	Polytetrafluoroethene
PVD	Physical Vapour Deposition
RBS	Rutherford Backscattering Spectrometry
RGA	Residual Gas Analyser
SEM	Scanning Electron Microscopy
STIM	Scanning Transmission Ion Microscopy
XRD	X-ray Diffraction
XRF	X-ray Fluorescence

University of Cape Town

Chapter 1

Introduction

1.1 The National Accelerator Centre

The National Accelerator Centre is a multidisciplinary research facility situated about 30 kilometres from Cape Town. One of four national facilities, it is funded by the National Research Foundation, which is, in turn, a science council of the Department of Arts, Culture, Science and Technology. The National Accelerator Centre is, therefore, a South African facility, paid for, and responsible to the people of South Africa.

University of Cape Town

1.1.1 Research at the National Accelerator Centre

Research at the National Accelerator Centre is centred around two accelerators, a 200 MeV cyclotron, and a 6 MV Van de Graaff electrostatic accelerator. The cyclotron is used for fundamental nuclear research, radioisotope production and beam therapy applications. Research applications include the development of new and purer radioisotopes for radiopharmaceuticals and research into the development and efficacy of proton and neutron beam therapy for the treatment of cancers and related growths. The 6 MV Van de Graaff accelerator is housed in the buildings of the Materials Research Group and used mainly as an analytical tool in materials research.

1.1.2 Research at the Materials Research Group

The Materials Research Group consists of two main research divisions, the Solid State division, and the Ion Beam Analysis division.

The Solid State division

Research in the Solid State division has been concentrated in two main areas of interest; preparation and electronic characterisation of thin film superconductors, and research into metal-silicide reactions and chemistry. With the recent acquisition of two Bruker x-ray diffraction (XRD) machines, research is also being performed in XRD applications. The construction of the Plasma Source Ion Implantation (PSII) facility therefore extends the research areas of the Solid State division.

The Ion Beam Analysis division

The IBA division is concerned primarily with the applications of ion beams to materials analysis. With active projects incorporating analysis of minerals (for geological applications), botanical samples (*inter alia* for environmental applications) and biological samples (for medical applications), this multidisciplinary facility defies easy classification.

1.2 Development of the PSII facility at the National Accelerator Centre

The PSII facility was constructed at the Materials Research Group to broaden the scope of research of the group. In this sense, the PSII facility can be considered as a stand-alone construction, existing independently of the rest of the group (as could the XRD facility, for example). However materials research is best performed in a tight sample manufacturing and analysis environment, whereby the processed materials are thoroughly analysed immediately after manufacture. In this manner, it is easier to gain a deeper understanding of the physical processes involved. Thus it is apparent that the PSII facility must be used and understood in the context of the larger analytical capabilities of the Materials Research Group. It is with this philosophy in mind that this project was undertaken: to describe not only the construction of the PSII facility, but also how the analytical capabilities of the Materials Research Group can be harnessed for maximum benefit to PSII-related research.

University of Cape Town

1.3 Thesis structure

An overview of the structure of the thesis can be seen in figure 1.1, which shows the three main components-

- *The plasma processing facility* - which encompasses the plasma chamber (discussed in chapter 2), the RUP-4a high voltage pulsed power supply (chapter 5) and the custom written software (chapter 6) to facilitate remote user-control of the implantation process. The data acquisition and processing hardware is described in appendix C.
- *The analytical tools* - encompasses the analytical techniques (chapter 7) used to examine the materials processed by plasma methods.
- *Fundamental Research and Applications* - encompasses a detailed examination of x-ray radiation produced during ion implantation (chapter 8), an examination of PSII hardened metals used in industrial processes (chapter 9) and the implantation and analysis of hydrogen implanted silicon used in the manufacture of high-tech silicon wafers (chapter 10). The x-ray radiation analysis was done to facilitate an assessment of the surface conditions of the implanted material and the health implications for laboratory workers.

Plasma processing	**Analytical tools**
Plasma chamber	Nuclear techniques
RUP-4a power supply	X-ray techniques
Data acquisition and processing	Microhardness techniques
Custom software	

Fundamental Research and Applications
X-ray measurements
Steel hardening experiments
Silicon implantation and analysis

Figure 1.1: Overview of the thesis structure, showing the three main components - Plasma processing, Analytical tools, and Fundamental research and applications.

1.3.1 The plasma processing facility

The Plasma chamber

The PSII facility uses an approximately $1m^3$ aluminium alloy plasma chamber, which is on loan from the Plasma Physics Research Institute of the School of Pure and Applied Physics, University of Natal, Durban. Ohmically heated tantalum filaments are used to provide the primary ionising electrons used for plasma formation. Features of the chamber include multiple, independently controlled Langmuir probes (for plasma analysis and diagnostics), multiple viewports and flanges (including one flange that has been modified to accept an RF antenna for future RF plasma generation capabilities) and a large plasma volume.

The RUP-4a high voltage pulsed power supply

This pulsed power supply was designed by Dr. J. Brutscher to use a tetrode thermionic valve for switching the high voltage and was constructed at the Forschungszentrum Rossendorf (Rossendorf Research Centre) within the scope of this project. The Rossendorfer Universal Pulsgenerator, model 4a (RUP-4a, the economy version), is a self-contained variable voltage (up to -30 kV) pulsed (width from < 1 μs up to 1 ms, repeat rate up to 3 kHz under special circumstances) power supply (maximum recommended switching power of 600 W). The maximum implantation current of 8 A and duty-cycle ($< 4\%$) complete the operational parameters. The output voltage and pulse timing can be remotely programmed using a 0–10 V analogue voltage to select the output voltage and a TTL logic input to operate the tetrode switch.

University of Cape Town

Data acquisition and processing

Two computers using interface cards combined with an optional digital oscilloscope and electrometer are used to record parameters of interest during the plasma implantation process. One computer is kept in the PSII laboratory, and is used as a data capture and control computer. It uses a digital oscilloscope and several interface cards to (1) measure the chamber pressure, implantation current and implantation voltage, (2) control the implantation voltage and timing parameters and (3) control the stepper motors. The second computer implements the user interface and communicates with the data capture computer via the internet using the TCP/IP network protocol. This was done to allow remote control and monitoring of the implantation experiments. A necessary requirement since implantation at voltages higher than -25 kV produce high levels of x-ray radiation in the plasma processing laboratory.

Custom written software

As described above, two computers are used in the PSII laboratory; a data capture computer and a user-interface computer. Thus two independent software packages were written: one to interact with the user (the "NetLab" user interface), the other to interact with the hardware (the "NetLab" kernel). The user interface was written in IDL[1] (Interactive Data Language) and allows the user to view and set implantation parameters from a single easy to use graphical program interface. The data capture software ("NetLab" kernel) was written in 'C' and runs under Linux. This software is not designed to be used by a human. Instead, it is an interface to the hardware, accepting commands from the user-interface, communicating with the connected devices and returning responses to the user interface for processing and display.

University of Cape Town

1.3.2 Analytical tools

Since analysis of experimental data is fundamental to all physics research (other than theoretical- and metaphysics), the analysis of materials implanted with the PSII facility is a fundamental aspect of the PSII research program.

During the construction of this facility several techniques appropriate for the analysis of PSII implantation were identified and used. While many other techniques also exist, the described techniques are available at the National Accelerator Centre or at nearby universities and are sufficient for most purposes.

These analytical techniques can be classified into three broad categories: nuclear analytical methods, non-nuclear x-ray methods and surface microhardness methods.

Nuclear analytical techniques

The main nuclear analytical techniques available at the Materials Research Group are Proton Induced X-ray Emission (PIXE), Nuclear Reaction Analysis (NRA), Rutherford Backscattering Spectrometry (RBS) and Elastic Recoil Detection Analysis (ERDA). Except for PIXE, all these techniques can be used to establish quantitative elemental depth and dose information. Since PIXE only gives concentration

[1]Research Systems Incorporated, 4990 Pearl East Circle, Boulder, Colorado 80301-9959, USA. URL: http//www.rsinc.com/

information of elements with mass greater than sodium and no depth information, it has not been of particular interest to PSII research and will not be discussed any further. All the other techniques each have specialised advantages and disadvantages, and are chosen according to the information desired: NRA is effective at determining depth and concentration profiles of those elements which have suitable nuclear reaction cross-sections (like nitrogen, carbon and oxygen). ERDA is a very simple technique that is efficient at establishing hydrogen and helium depth and dose distributions. RBS is another simple technique that is effective at determining dose and depth information of heavier elements. It can also be used in conjunction with ERDA for normalisation purposes, or alone to simply investigate damage to crystal lattices (with RBS channelling techniques). In results presented in this thesis, RBS analysis was used most often to normalise spectrum yields of ERDA measurements of samples undergoing in-situ heating to observe the effect of temperature on hydrogen profiles in an ion-cut application.

X-ray methods

X-ray analytical techniques can be used to establish surface composition (Auger Electron Spectroscopy - AES) and near-surface crystalline structure and parameters (using x-ray diffraction techniques). There are two XRD machines at the National Accelerator Centre, and since XRD analytical methods can be used for PSII materials analysis, they are appropriate to the development of the PSII facility and will be discussed.

Microhardness measurement techniques

Since some of the PSII applications involve improving surface hardness, these measurements provide a qualitative indication of the effectiveness of the PSII procedure. While there are no microhardness indenters at the National Accelerator Centre, facilities exist at the Materials Engineering Department of the University of Cape Town, and the Mechanical Engineering Department of the University of Stellenbosch, two local universities.

University of Cape Town

1.3.3 Fundamental Research and Applications

During the course of developing this facility, two projects of a fundamental research nature were investigated, namely, the measurement of time and energy resolved bremsstrahlung x-ray measurements, and in-situ ERDA measurements of hydrogen depth profiles as a function of substrate temperature. In addition to these projects, three steel hardening investigations were performed and one investigation into the PSII of hydrogen into silicon (for ion-cut applications).

Chapter 8: X-ray measurements

X-rays are generated during any plasma implantation process by the bremsstrahlung stopping of electrons which are repelled from the target. In particular, electrons repelled from the target are accelerated to the high target potential. When these electrons are stopped by the chamber walls, they radiate x-rays . Standard nuclear spectroscopy equipment was used to measure the time and energy resolved nature of the bremsstrahlung x-ray radiation.

Chapter 9: Steel hardening applications

Three different steel types used in industrial applications were implanted with nitrogen to determine their PSII induced hardness properties In the final application, a probe used to sample a sand transport line, was implanted and the processed samples were returned to the plant for field testing.

Chapter 10: Hydrogen implantation of silicon

Following the results of M. Bruel [Bru96b] using PSII-implanted hydrogen to cleave silicon wafers, it was decided to implant hydrogen into silicon with this facility to gauge the ability of this facility to perform research into ion-cut techniques and to study the implanted hydrogen behaviour in Si at high temperatures.

Chapter 10: In-situ ERDA of hydrogen implanted silicon

Silicon wafers that were implanted with hydrogen using direct accelerator ion-beam implantation were used to develop the capacity to perform in-situ ERDA measurements. This experimental technique was developed for the Materials Research Group and used to observe depth and concentration profiles of hydrogen in silicon as a function of the sample temperature.

University of Cape Town

Chapter 2

Surface modification

Surface modification is the process whereby the surface properties of a material are modified independently of the bulk properties. The modification may be done to improve surface wear rates or improve corrosion resistance. In nearly all cases, the surface modification step is the final step in the manufacture process and is usually a technologically advanced process. This chapter outlines the various forms of surface modification and introduces the PSII concept. It concludes with some special considerations pertinent to the PSII process of ion implantation.

University of Cape Town

2.1 Surface Hardening

Once certain compositions and phases were identified as having desirable physical properties, people began developing techniques and processes to favour the formation of these phases and alloys. However, not all of these properties are mutually inclusive; extremely hard materials tend to be brittle (with a low tolerance for impact stresses, while resilient materials tend to be very soft) and steels with excellent corrosion resistance tend to have lower hardness. Thus it became desirable to create materials with regions or layers with different tribological properties. The development of these techniques made it possible, for example, to manufacture drill bits with bulk strength and resilience, but with hard surfaces to provide better cutting edges and wear resistance. Surface hardening can be achieved by using one of two main processes; either by the addition of a hard surface coating, or by modifying the existing surface and converting it into a different alloy.

2.2 Surface coating techniques

There are many surface coating techniques available today. Ranging from nickel and zinc coatings for iron and steel, such as hot-dip galvanising and electroplating to improve corrosion resistance, while electrodeless deposition of nickel, phosphorous or boron provides wear and corrosion resistance. Coatings can be deposited by vapour deposition processes, such as chemical vapour deposition (CVD) or physical vapour deposition (PVD).

The disadvantage with coating technology lies with the fact that the surface dimensions of the target are increased by the thickness of the coating, along with the associated risks of bonding failure.

Chemical Vapour Deposition

In CVD, a gas containing volatile components of the elements to be deposited are introduced into a reaction chamber. By controlling the conditions within the reaction chamber, the appropriate chemical reaction deposits the coating onto the surface of the substrate. Aluminium and gallium arsenide films can be produced by metalorganic CVD (MOCVD) methods which use organo-metallic compound vapours which are stable at room temperature, but react at elevated temperatures. Plasma aided CVD is a low pressure CVD technique which achieves the appropriate coating at a lower substrate temperature by using a plasma to increase the energy of the reactants.

Physical Vapour Deposition

PVD is performed under a partial vacuum (10^{-3}–10^{-4} torr) and at least one of the deposited species is atomised from a solid in the processing chamber. Electron beam PVD uses an electron beam to heat the solid to be vaporised. By using a cooled target holder, techniques like this and laser ablation deposition (and pulsed laser deposition - PLD) have no practical upper limit to which the solid surface can be heated. These processes can be used to create hardened layers by using such diverse materials as ceramics, titanium nitride (TiN), tungsten carbide (WC), diamond-like-carbon (DLC), etc.

University of Cape Town

2.3 Surface modification techniques

Unlike the surface coating techniques described above which create a new layer on the existing surface, surface modification techniques specifically only modify the existing surface. These surface modification techniques can be extremely simple, for example, thermal techniques, or complex, for example, metal-arc ion implantation or ion beam assisted deposition (IBAD).

2.3.1 Thermal techniques

Thermal techniques rely on creating a more beneficial phase [Ask88a] than the existing phase of the bulk material. Steels which are heated to above their upper critical temperature and left to form austenites, can be hardened with rapid quenching. The sudden cooling prevents the breakdown of the austenite and a martensitic phase is formed. This martensite has a body centred tetragonal lattice in which all of the dissolved carbon is held in interstitial positions, and is the hardest of the steel phases. By the application of intense local heating, using oxyacetylene torches, lasers or induction heating (and subsequent cooling), the steel surface can be brought into the austenitic range without affecting the core. With subsequent quenching the surface will become martensitic. Induction hardening uses high current through a coil to induce heating in the surface of the metal target and is usually applied only to small components, such as axles and camshafts, while flame hardening can be applied to sections of larger objects, such as turbine engine blades and machine tool beds.

2.3.2 Modification by addition

Post manufacture surface modification techniques also use the addition of elements to transform the material surface into a different compound with more appropriate properties. Common elements added are carbon, nitrogen and boron. Initially these elements were introduced into the surface of the steel to be hardened by packing the steel into an air-tight container with an appropriate carrier medium, such as petroleum coke for carbon, ammonia for nitrogen and potassium fluoborate for boron. After appropriate heating the elements diffuse into the surface to form the appropriate carbide, nitride or boride over a particular case depth. Later on, ion implantation techniques were developed to implant these elements directly, with a much greater efficiency.

2.3.3 Gas nitriding

Gas nitriding is one of many methods of introducing nitrogen into the surface of the material to be hardened, usually by the formation of nitrides. The target material is heated in a nitrogen gas environment and thermal diffusion carries the nitrogen into the target surface.

University of Cape Town

2.4 Implantation Methods

These methods implant the desired element species directly into the surface of the material to be modified, and for ballistic methods the surface condition is not important, e.g. implantation can occur through an oxide layer. The two dominant methods involve either ion implantation or gas/plasma immersion techniques.

2.4.1 Surface modification versus coating techniques

Process	Advantages	Disadvantages
Coating	• Complex coatings possible • Conducting and insulating targets can be processed	• Layer delamination • Complex target manipulation hardware required • Extremely surface dependent
Implantation	• No delamination • Low temperature • Relatively cheap	• High energy implant • X-ray health hazard • Pulsed power supply (PSII only) • Target manipulation hardware (beamline only)

Table 2.1: Advantages and disadvantages of surface coating *versus* implantation

A summary of surface modification and surface coating techniques are listed in table 2.1. In detail, the primary advantage of ion implantation over surface coating techniques is that implanted materials do not suffer from possible delamination, which coatings are prone to. However, implantation techniques require that the modified surface can be created with implantation; hence titanium nitride surfaces can only be created by implanting nitrogen into titanium, presently, one can not easily implant TiN, for example.

2.4.2 Ion beam implantation

Ion beam implantation uses some method of ionising the species to be implanted, for example, glow discharge or RF plasma techniques. Electric fields are then used to extract the ions from the ion source and to accelerate the ions to the desired energy to achieve implantation to the required depth. Ion beam techniques allow fine control of ion mass and energy to provide very precise control of target compound and phase formation. However, since ion beam techniques are line-of-sight, they require special masks to prevent implantation of areas where implantation is not desired, and complex manipulation hardware to bring all areas to be implanted into the beam line. These precautions are necessary to prevent excessive damage to the target surface due to non-normal ion implantation vectors (§B.3.2). Ion beam techniques do tend, however, to have a greater range of available ion species over other implantation methods.

The addition of target manipulation and beam-rastering hardware adds complexity and expense to the process, limiting the size of the target that can be processed. Temperature build-up in the processed region further complicates the process if distortion due to local thermal expansion and overheating is to be avoided. The additional problem of retained dose and surface degradation due to sputtering [Con88b] (figure 2.1) when the ions strike the target surface at oblique angles requires the construction of target-specific tailored masks (figure 2.2). However, the sputtering of this mask can contaminate the target.

University of Cape Town

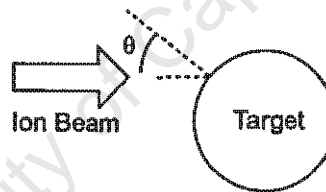

Figure 2.1: The maximum retained dose (D) for ion implantation depends strongly on the angle of incidence of the ion, $D \sim \cos^{\frac{8}{3}} \theta$

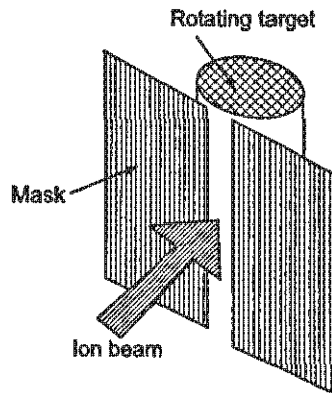

Figure 2.2: Conventional line-of-sight beamline ion implantation requires masking of convex targets to minimise sputtering.

A variation of the ion beam technique is IBAD, where the target is first coated with a thin film, and then implanted with an ion beam. The implanted ions collide with the deposited layer, knocking them

deeper into the target, to assist in improving the coating-target bond.

2.4.3 Plasma Source Ion Implantation Concept

PSII is an ion-implantation technique developed and patented by J.R. Conrad *et al* [Con87a]. It is cost effective, since by its very nature no beam rastering or target masking hardware is required. Since PSII is plasma based, special emphasis is placed on plasma-based ion sources. For metallurgical reasons, nitrogen is the most common ion source. Also referred to as Plasma Immersion Ion Implantation (PIII or PI^3), it is the process whereby the target to be processed is immersed in a plasma consisting of the ions to be implanted. By pulse-biasing the target to high negative voltages (10–150 kV [Mat94a, Rea94a]), the plasma ions in the vicinity of the target are accelerated into the target. Since the ions are accelerated across the sheath (§3.3) which forms around the target, the entire target surface is processed simultaneously. Also, since the ions are accelerated along the electric field lines, they tend to strike the target surface with approximately normal incidence (figure 2.3), thus minimising the problem of retained dose and eliminating the requirement of a mask. Preliminary investigations into dose uniformity on multiple targets in a test of batch mode processing yielded promising results [Con88c]. Very much a young science, PSII has been the focus of four international workshops since 1993 (Michigan [1993], Sydney [1995], Dresden [1996], Dearborn [1998]).

University of Cape Town

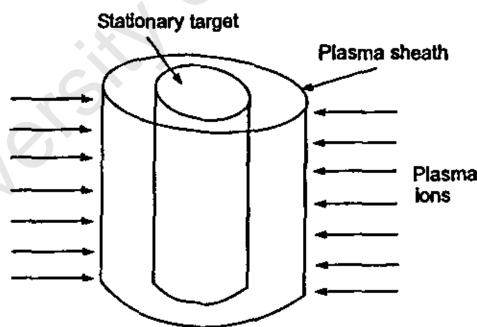

Figure 2.3: In PSII implantation, the ions are accelerated from the sheath edge, to strike the entire target surface with nearly normal incidence thus reducing the sputtering and retained dose problem.

To summarise the advantages of PSII over traditional ion-beam techniques (figure 2.4):

- Elimination of beam rastering and target manipulation hardware,
- Elimination of target masking and reduction of surface sputtering and retained dose problems,
- The ion source hardware and controls are at near-ground potential,
- Greater production throughput, especially for large and/or diverse targets,
- The smaller, less expensive, easier to operate PSII hardware allow for "in-house" operation, versus the "outside service facility" operation mode prevalent in the ion-beam industry.

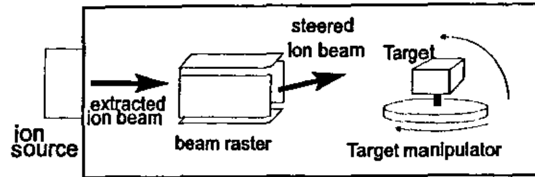

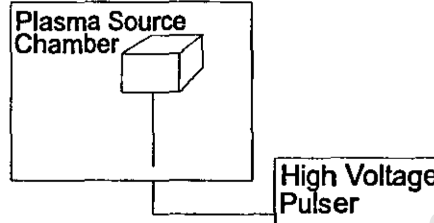

Figure 2.4: A comparison of the hardware requirements of conventional beamline ion implantation *versus* PSII. Ion beam implanters require, at minimum, target manipulation and beam rastering hardware, while PSII implanters require a plasma chamber and pulsed power supply.

University of Cape Town

2.5 Ion implantation processes

In an ideal implantation process, where the desired dose (D) of the implanted species is known, it would simply be a matter of establishing the implantation current (I_{implant}), the implantation surface area ($A_{\text{target surface}}$) and the charge state ($Q$) of the implantation ion species to determine the implantation time according to the following relation:

$$t = \frac{D \cdot Q}{I_{\text{implant}} \cdot A_{\text{target surface}}} \cdot \frac{Z}{M} \tag{2-1}$$

where $\frac{M}{Z}$ is the number of ions implanted per molecule.

In reality, the situation is more complex than this because of a combination of different processes such as sputtering (which removes already implanted ions), secondary electron emission (which affects the implantation current I_{implant}) and retained dose (the probability of an ion remaining in the target).

These processes will be discussed individually, below.

2.5.1 Determining ion implantation flux

The actual implanted ion flux can be measured directly by use of a specially manufactured target. Mändl *et al* [Man97c] constructed a target with an orifice in the surface, and fit a faraday cup within the target. During implantation they were able to measure the implantation ion flux directly.

However, aside from specifically contrived examples such as this, the ion dose can only be determined approximately either by calculation and elimination of other current contributions (§8.2) or by post implantation analysis of retained dose (chapter 7).

2.5.2 Retained dose

The term 'retained dose' describes that portion of the implanted ions which remain in the sample. In ion implantation, the dominant process which affects the retained dose is the angle of incidence. The angle of incidence accounts for both the probability of an ion penetrating into the sample, and for the ion to remove one or more target ions (sputtering). Measurements have shown that the retained dose depends on the angle θ from the surface normal with which an incoming ion strikes the target surface, and can be approximated [Con89a] by

$$R \propto \cos^{\frac{8}{3}}(\theta) \tag{2-2}$$

The retained dose is also affected by the solubility of the implanted ion species in the target material. If the implanted ion concentration exceeds the saturation levels, it will tend to leave the target through a process of diffusion. Although, by their ballistic nature, ion implantation techniques can locally exceed the saturation of the implanted ion species, but this will be an unstable situation.

2.5.3 Ion induced sputtering

Depending on implanted ion species, target composition, target geometry and implantation energy, there is a probability that an implanted ion will knock off some target atoms from the target. The number of atoms knocked off per incident implanted ion is called the sputtering yield (Y).

The theory of ion induced sputtering is described in greater detail in appendix B but the significant results will be reproduced here.

Steady state condition and high dose ion implantation

The steady state condition determines the maximum implantable dose. Since the surface is being eroded by sputtering during implantation, it is apparent that, at high doses, sufficient material can be sputtered to expose the original implanted ions. Assuming no diffusion from the bulk, the steady state condition is [Nas96a]

$$N_A/N_B = r(Y-1)^{-1} \tag{2-3}$$

where N_A and N_B are the surface concentrations per unit volume of the projectiles and target respectively, Y is the sputtering yield, and r is the preferred sputtering factor and accounts for differences in surface binding energies, etc, $r > 1$ implies that A is preferentially sputtered over B.

Preferential sputtering and compositional changes

In materials consisting of multiple atomic species, there may be different sputtering rates for the different species. For high dose implantation the effects of preferential sputtering can greatly affect the surface composition. Due to the complexity of predicting the sputtering of multiple-species alloys, this is an effect which must be considered, but is best observed experimentally.

University of Cape Town

Calculations

Using the semi-empirical formula of Matsuname *et al* [Mat84a] and Yamamura & Itoh [Yam89a], the sputtering yield of the two simple cases relevant to this project, that of 30 keV H into Si and N into Fe can be calculated to be 0.02 and 1.25 respectively (table B.2).

2.5.4 Ion induced electron emission

Not only are ions sputtered from the target by the high energy implanted ions, but electrons are also ejected. These electrons contribute to both the measured implantation current, and the outbound electron flux repelled from the target. The repelled electrons can generate x-rays when they strike the chamber walls by bremsstrahlung and they contribute to the implantation current (equation 6-1). Since the desired implantation dose determines the implantation time, which is often calculated using the mean implantation current, the secondary electron emission co-efficient needs to be known. The theory of ion induced electron emission is described briefly in §8.2.2.

University of Cape Town

Secondary electron emission co-efficient, γ

The emission of a secondary electron is determined by a complex process of energy-loss collisions: the implanted ion collides with target ions and knocks off one or more electrons. These electrons are scattered back toward the surface but are impeded by further collisions within the target (possibly knocking off additional electrons). Only those electrons ejected close to the surface (a distance determined by the mean free path of collisions) have enough energy to be ejected.

Factors influencing γ

Molecular effects: At higher energies (>100 keV) the greater mass of implanted molecular ions over single ions result in a greater energy loss (due to the Z^2 dependence of stopping powers) and hence greater probability of ejecting an electron during collisions. There is also the increased probability of ejecting an electron from the implanted molecule.

Surface layers: The presence of a surface oxide and other adsorbed gasses has been shown to affect the emission of electrons [Fer82a].

Determining γ

Due to the complexity of predicting γ for industrial targets (which typically have a complex shape and composition), the ion implantation current is often separated from the total implantation current by comparing predicted doses with measured doses in a series of controlled experiments, on a per-target basis usually by a combination of modelling and experimental measurements, or by measuring the secondary electron flux directly (§8.2).

ion beam implantation and PSII.

Ion induced sputtering is a factor affecting ion implantation techniques. Sputtering rates and steady state conditions which impose upper limits to the implantable dose must therefore be carefully considered.

Ion induced electron emission results in an additional electron flux from the target. This electron flux affects calculations of implanted current based on measurements of implantation current, and also contribute to the electron flux responsible for bremsstrahlung x-ray emission.

University of Cape Town

University of Cape Town

Chapter 3

Introduction to Plasmas

3.1 Plasma Formation - DC discharge

The plasmas produced by this facility are produced by electron bombardment of a neutral gas at low pressures. Primary electrons emitted from ohmically heated filaments and accelerated by an externally provided DC discharge collide with neutral gas atoms with enough energy to remove at least the first valence electron. These valence electrons are scattered with less energy than the incident primary electron, and are called secondary electrons. Most electrons in the plasma are secondary electrons. The ionization cross-section is a function of primary electron energy, and peaks at about 75 eV for the gases used in this facility (H_2, for Si wafer cleaving, and N_2, for metals hardening). The ionisation cross section of hydrogen is shown in figure 3.1, and the probability of ionisation of nitrogen is shown in figure 3.2. These figures are reproduced from Brown [Bro76a].

University of Cape Town

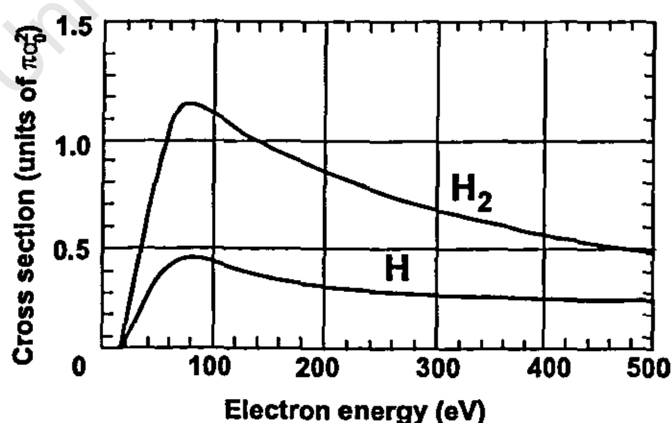

Figure 3.1: The ionization cross-section of H and H_2, by electron collision, as a function of electron energy Reproduced from Brown [Bro76a]

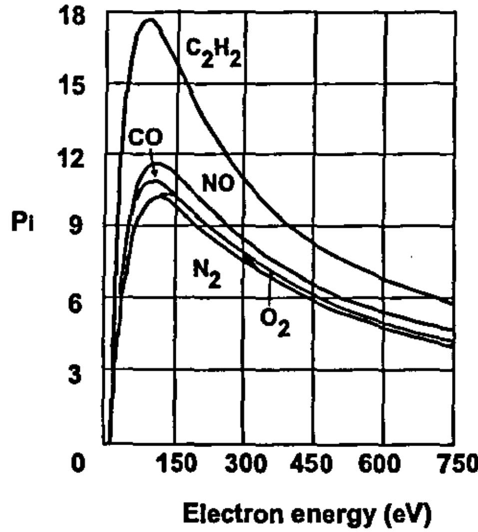

Figure 3.2: The probability of ionisation of N_2, O_2, CO, NO and C_2H_2, by electron collision, as a function of electron energy. Reproduced from Brown [Bro76a]

3.1.1 Ionization cross-section and mean-free-path

The mean distance between collisions or mean-free-path (λ_m), is defined by Chen [Che84a] in terms of momentum loss in collisions between electrons and neutral atoms. The mean-free-path is an important length in plasma physics as it helps define the regime in which a plasma (or plasma process) is considered collisionless, and hence simplifies the theories used to predict the process behaviour.

The probability of momentum loss can be expressed in terms of the equivalent cross-section σ that the atoms would have if they were perfect absorbers of electron momentum. An ionisation event occurs when the momentum transferred from the incident primary electron gives the neutral gas atom enough energy to be excited into at least its first excited state, releasing a secondary plasma electron.

Considering electrons incident upon a slab of area A and thickness dx containing n_n neutral atoms per unit volume, where each atom is an opaque sphere of cross-sectional area σ, the number of atoms in the slab is

$$n_n A\ dx.$$

The fraction of the slab blocked by atoms is

$$n_n A\ dx\ \sigma / A = n_n \sigma\ dx.$$

If a flux Γ of electrons is incident on the slab, the flux emerging on the other side is

$$\Gamma' = \Gamma(1 - n_n \sigma\ dx).$$

Thus the change of Γ with distance is

$$d\Gamma / dx = -n_n \sigma \Gamma$$

or

$$\Gamma = \Gamma_0 e^{-n_n \sigma x} \equiv \Gamma_0 e^{-\frac{x}{\lambda_m}}.$$

University of Cape Town

$$\lambda_m = \frac{1}{n_n \sigma} \tag{3-1}$$

3.1.2 Primary electron current limitations

In general the primary electron current, and hence primary electron flux, is limited by two factors, space charge, and cathode temperature.

3.1.2.1 Space charge limited emission

Intially, only a small current can flow between the cathode and anode in the low pressure neutral-atom gas. This is due to the space charge from electrons which accumulate near the cathode and repel newly emitted electrons. The space charge limited current is given by the Child-Langmuir law [Lan23a]:

$$J = \frac{4}{9}\epsilon_0 \left(\frac{2e}{m_e}\right)^{\frac{1}{2}} \frac{U^{\frac{3}{2}}}{d^2} = 2.333 \times 10^{-6} \frac{V_d^{\frac{3}{2}}}{d^2} A.\mathrm{cm}^{-2} \tag{3-2}$$

where V_d is the discharge bias in Volts, d the distance between the anode and cathode in cm, and J is expressed in units of A.cm^{-2}, which for these experiments, where $V_d = 60$ V, $d \simeq 5$ cm, is about 40μA.cm^{-2}.

3.1.2.2 Temperature limited emission

In plasma discharge devices, the initially small space charge limited current processes rapidly allow a sheath to form around the cathode which reduces d to a few Debye lengths. The total emission current is, however, limited by the filament temperature. The temperature limited emission current is given by the Richardson law:

$$J = BT^2 e^{-\frac{W}{kT}} A.\mathrm{cm}^{-2} \tag{3-3}$$

where W and T are the work function and temperature of the filament metal, and $B = 4\pi m_e k^2/h^2 = 120$A.cm$^{-2}.K^{-2}$. Since the plasmas produced in this facility use tantalum filaments, with a work function $W = 4.25$eV.K^{-1}, $J \approx 9$mA.cm^{-2}.

3.1.2.3 Temperature versus Space charge limitations

Comparisons of temperature and space charge limiting processes show that in the presence of a plasma, $J_{\mathrm{spacecharge}} \ll J_{\mathrm{temperature}}$ so the discharge current, which is just the emission current, is a sensitive function of the filament temperature and surface area.

Since plasma density is proportional to discharge current, it was decided to install an automatic feedback circuit to monitor the discharge current and control the filament temperature. The circuit, which is described in §4.5.1, controls filament temperature by regulating the filament current, and thus maintains a constant discharge current independent of fluctuations in filament temperature, as the bombarding ions sputter away the filament.

University of Cape Town

3.2 Probe Theory

In 1924, I. Langmuir pioneered the use of electric probes in plasma diagnostics. While simple to implement, the theory governing probe responses is very complicated. The Langmuir probe itself is merely a conducting surface, usually planar-circular, cylindrical or spherical in shape, which is immersed into the plasma, typically in one of two basic probe configurations, a double probe or a single probe. In the double probe configuration, the current is measured as a function of the applied potential difference between the two probes. In the single probe configuration, the current is measured as a function of the potential difference between the probe and the chamber walls, which are usually held at ground potential (figure 3.3).

By analysing the current drawn by the probe as a function of the applied potential, one can determine the state of some of the plasma parameters, for example, the electron temperature (T_e) and density (n_e), the floating potential (ϕ_f) and the plasma potential (ϕ_p). Potentials used in plasma calculations are all performed with respect to the plasma potential.

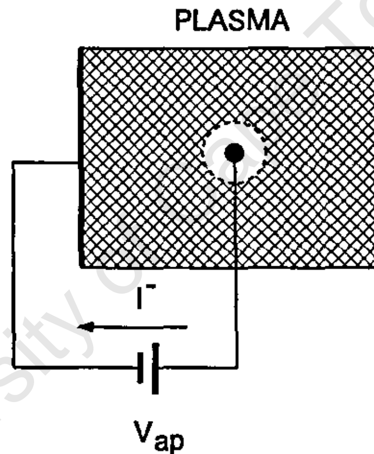

University of Cape Town

Figure 3.3: A typical Langmuir single-probe circuit, to measure the electron current, (I^-). By reversing the polarity of the applied potential, the ion current can be measured.

3.2.1 Plasma analysis with the Langmuir Probe

There are many theories describing the interpretation of the Langmuir current-voltage characteristic trace to extract the plasma parameters. Differences in assumptions about the ion and electron velocity distributions, average velocities, external magnetic fields, probe surface condition, and other parameters can all be taken into account to improve analysis, see Chu *et al* [Chu75a] for examples.

The electron temperature, T_e, and density, n_e, determine the magnitude of the plasma sheath which forms around the targets during implantation, and are used to calculate the expected implanted ion dose. However, since the retained dose is always less than the implanted dose due to several mechanisms (§B), dose and implantation time calculations based on plasma density and implantation current are inherently inaccurate. For this reason a rigourous analysis of probe measurements are not required and only a simplified theory will be described.

The following discussion will be limited to the analysis of a discharge plasma with a single probe based on the following assumptions:

- The applied potential $V_{ap} = \phi_{\text{probe}}$,
- Ion and electron densities are equal (quasi-neutrality),
- Ion and electron mean free paths are much larger than the probe radius,
- Electron temperature (T_e) is much larger than ion temperature (T_i),
- The probe radius is much larger than the Debye length (λ_D),
- The ions and electrons have Maxwellian velocity distributions,
- The ions and electrons traverse the probe sheath without collisions.

This theory can be used by software to extract the plasma parameters.

A typical Langmuir characteristic current *versus* voltage trace is shown in figure 3.4. If the applied

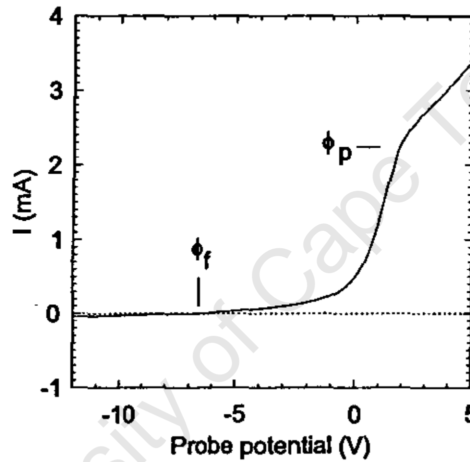

Figure 3.4: A typical Langmuir characteristic trace showing the floating (ϕ_f) and plasma (ϕ_p) potentials.

University of Cape Town

potential is much more negative than the floating potential, ϕ_f, only a small portion of the electron energy distribution (the very high energy electrons) is measured by the probe, and the current measured is almost entirely an ion current. If the ion currents are small, the thickness of the sheath around the probe is given by the Debye radius

$$\lambda_D = \sqrt{\frac{kT_e}{4\pi n_0 q_e^2}} \tag{3-4}$$

where T_e is the electron temperature and n_0 the plasma density. For larger currents the sheath thickness is determined by the Child-Langmuir Law for space-charge limited currents, equation 3-2, rewritten:

$$x = \frac{2}{3}\left(A_p\epsilon_0\left(\frac{2e}{m_e}\right)^{\frac{1}{2}}\frac{V_p^{\frac{3}{2}}}{I}\right)^{\frac{1}{2}} \tag{3-5}$$

where I is the measured probe current, A_p the surface area of the probe, and $V_p = V_{ap} - \phi_p$ is the potential difference between the plasma and the probe.

For the plasmas typical of this facility where the ion temperature (T_i) is much smaller than the electron temperature (T_e), the ions are accelerated toward the probe by the probe pre-sheath potential.

The Bohm Sheath Criterion requires ions to enter the sheath with a velocity greater than C_s, the ion acoustic velocity:

$$C_s = \sqrt{\frac{kT_e}{m_i}} \tag{3-6}$$

Thus the ion current measured by a probe at potentials much more negative than the plasma potential is given by

$$I = n_s q_e A_s \nu_d = n_s q_e A_s \sqrt{\frac{kT_e}{m_i}} \tag{3-7}$$

where n_s is the plasma density at the sheath edge, A_s the effective surface area of the sheath, and ν_d the ion velocity limited by the Bohm sheath criterion. By defining the sheath edge to be the region where the ion velocity exactly equals the ion acoustic velocity, requires a sheath potential $\phi_s \approx \frac{kT_e}{2q_e}$. If the electrons have a Maxwellian velocity distribution, n_s is given by:

$$n_s = n_0 e^{\frac{q_e \phi_s}{kT_e}} = n_0 e^{-\frac{1}{2}} \tag{3-8}$$

It is convenient to approximate $e^{-\frac{1}{2}}$ with $\frac{1}{2}$ to get an ion saturation current of

$$I^+_{sat} = \frac{1}{2} n_0 q_e A_s \sqrt{\frac{kT_e}{m_i}} \tag{3-9}$$

As the probe potential is increased, the electrons will be collected, first the fast energetic electrons, then the slower ones.

It is in this potential regime, where the electrons are first collected, that evidence of the ionizing primary electrons can be seen. From Hershkowitz [Her79a], at low pressures ($< 10^{-5}$mbar), the primary electron contribution is visible as a straight line on the I-V Langmuir trace. At higher pressures, the characteristic loses its straight-line shape, but primary electron contributions can still be inferred from the floating potential. When primary electrons are present, the floating potential (ϕ_{f0}) is found to be more negative than its true value, found by balancing plasma ion currents with only plasma secondary electrons: $\phi_{f0} = \phi_p - 5.4T_e$.

The measured current will steadily decrease as the negative electron contribution increases with respect to the positive ion current. The potential at which they exactly balance, and no current is measured, is called the floating potential, ϕ_f. This is the potential acquired by an isolated body in a plasma, and is given by

$$\phi_f = \frac{kT_e}{2q_e} \cdot \ln\left(\frac{m_i}{m_e} \cdot \frac{T_e}{T_i}\right). \tag{3-10}$$

Magnitude analysis reveals that the floating potential is primarily determined by the electron temperature. At applied potentials above the floating potential, the current becomes negative and strongly dependant on the applied potential. Since only those electrons with energies greater than the probe potential are collected, the shape of this region is determined by the electron velocity distribution. For a Maxwellian velocity distribution

$$dN_e(\nu \rightarrow \nu + d\nu) = 4\pi N \left(\frac{m}{2\pi kT_e}\right)^{\frac{3}{2}} \cdot e^{-\frac{m_e \nu^2}{2kT_e}} \cdot \nu^2 d\nu \tag{3-11}$$

University of Cape Town

the current at a retarding potential of V will be $I(V) = e^{-\frac{m_e v^2}{2kT_e}} \cdot I^-_{sat}$. Where I^-_{sat} is given by Chu [Chu75a] as

$$I^-_{sat} = A_p n_0 q_e \sqrt{\frac{kT_e}{2\pi m_e}} j_e \tag{3-12}$$

where $j_e = e^{\frac{q_e \phi}{kT_e}}$.

Further increases in the applied potential above a potential ϕ_p, result in a break in the trend of the characteristic and the current once again becomes relatively independent of the applied potential and determined by the Child-Langmuir Law. The potential ϕ_p at which this occurs is called the plasma potential.

Electron temperature is determined easily by plotting the probe characteristics on a semilogarithmic scale, whence equation 3-12 is expressed as

$$\ln I^-_{sat} = -\frac{eV}{kT_e} + \ln\left(A_p n_0 q_e \sqrt{\frac{kT_e}{2\pi m_e}} e^{\frac{q_e \phi}{kT_e}}\right).$$

Thus the gradient in this region is equal to $-\frac{q_e}{kT}$. Ion and electron densities can be determined from equation 3-9.

3.3 Plasma sheaths

Plasma sheaths are regions of disturbed ion and electron density. Since the electrons are very much lighter and move faster than the ions, any conductor placed in a plasma creates a localised electron "sink". The net negative potential difference that is created by this electron depletion results in an electric field which counters the further loss of electrons. This electric field only penetrates a very short distance into the plasma, called the Debye Length (λ_D), given by equation 3-4. This region of space where the electric potential exists is called the plasma sheath.

If a high negative voltage is placed on the conductor, the plasma reacts with the electrons being pushed away from the conductor, and the ions attracted toward it. The plasma is thus depleted of all charged species very close to the conductor, and the plasma sheath extends to a distance r_s much larger than the Debye length, as given for planar and spherical approximations by equations 3-13 and 3-14, and are derived in appendix A:

Planar:

$$r_s = (2\epsilon_0 \phi_0 / n_0 q_e)^{\frac{1}{2}} \text{ or } r_s(\text{cm}) = 1050[\phi_0(\text{volts})/n_0(\text{cm}^{-3})]^{\frac{1}{2}} \tag{3-13}$$

Spherical:

$$r_s \simeq (3\epsilon_0 \phi_0 r_0 / n_0 q_e)^{\frac{1}{3}} \text{ or } r_s(\text{cm}) \simeq 118\left(\frac{\phi_0(\text{volts}) r_0(\text{cm})}{n_0(\text{cm}^{-3})}\right)^{\frac{1}{3}} \tag{3-14}$$

Equations 3-13 and 3-14 approximate the initial sheath thickness, when the pulse is applied. The sheath then expands to uncover more plasma ions, which are implanted. As is described in appendix A, the sheath evolution can be determined by numerically integrating the following equations:

University of Cape Town

Planar:

$$\frac{ds}{dt} = \frac{4\epsilon_0}{9n}\sqrt{\frac{2}{q_e M}}\frac{V^{\frac{3}{2}}}{S^2} \quad (3\text{-}15)$$

Spherical:

$$\frac{dr}{dt} = \frac{4\epsilon_0}{9n}\sqrt{\frac{2}{q_e M}}\frac{V^{\frac{3}{2}}}{r^2\alpha^2} \quad (3\text{-}16)$$

If the target potential is maintained for long enough, the sheath will eventually expand to the thickness prescribed by the steady-state Child-Langmuir law, equation 3-5. However, in most PSII applications the pulse length is kept sufficiently short and this never happens.

3.3.1 Target packing density

Since the ions which are implanted into the target originate from the plasma sheath (either in the sheath, or from the sheath edge), it is important that sheaths from neighbouring targets do not collide. Should this happen, the plasma ions will be depleted from that region, resulting in an corresponding reduced implantation dose in the target. If only a single target is being implanted, it is sufficient to verify that the sheath does not reach the chamber walls (or other conducting obstructions). This can be done by calculation and verified with probe measurements of ion or electron saturation currents.

3.4 Summary

The plasmas produced in this facility are produced by electron bombardment of a neutral gas at low pressures. The gases used include hydrogen and nitrogen. The formation of a plasma is dependant on the ionisation cross-section of the gas and filament temperature and area.

Langmuir probes are used in the analysis of plasmas. By analysing the current drawn by the probe as a function of the applied potential, the plasma parameters (electron temperature, plasma density, floating potential and plasma potential) can be determined.

When a conductor, for example a Langmuir probe or a metal sample, is placed in a plasma, a sheath is formed around the conductor. A plasma sheath is a region of disturbed ion and electron density. Sheath dimensions affect, for example, dose uniformity in targets that are packed too close together. Plasma density and electron temperature are required to determine sheath thickness.

University of Cape Town

Chapter 4

Construction of the PSII laboratory

This chapter describes the construction of a functional plasma source ion implantation laboratory at the National Accelerator Centre. It covers the design aspects of the PSII laboratory. Subsequent chapters describe the construction of the high voltage power supply and development of the "NetLab" software used to control the PSII process.

University of Cape Town

4.1 Chemistry laboratory to PSII laboratory

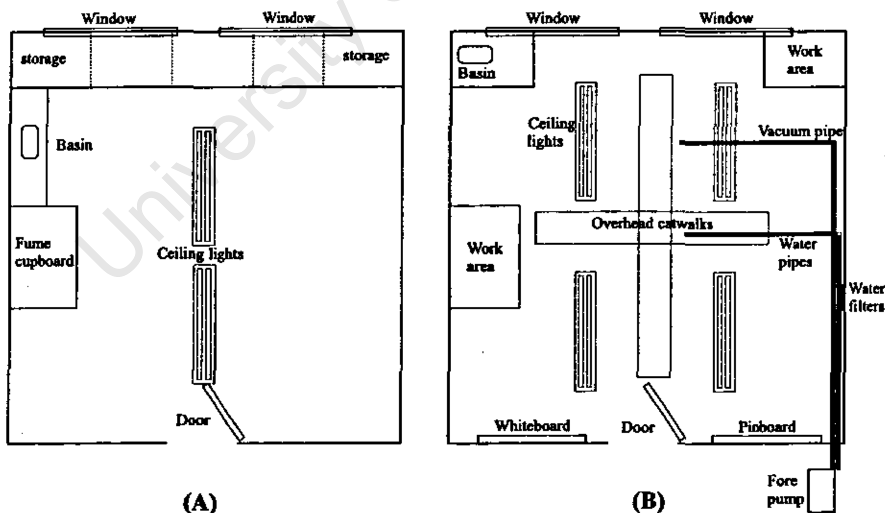

Figure 4.1: Plan view of (A) the original layout of the laboratory, and (B) the modified laboratory. The available floor space was increased, additional lighting, catwalks and a recirculated water circuit was installed.

At the beginning of this project the proposed plasma source ion implantation laboratory had to be converted from a chemistry laboratory to a form more suitable for the proposed new use. As can be seen from figure 4.1, the fume cupboard was converted into a flat work area, the basin was moved to

a more convenient location and the work areas cut back into two smaller areas. In addition to these modifications, the overhead catwalks, additional lighting, shelving, pinboard and whiteboard were added. The recirculated water circuit of the Van de Graaff accelerator was extended to include the plasma laboratory (§4.3.4).

4.2 Cabling

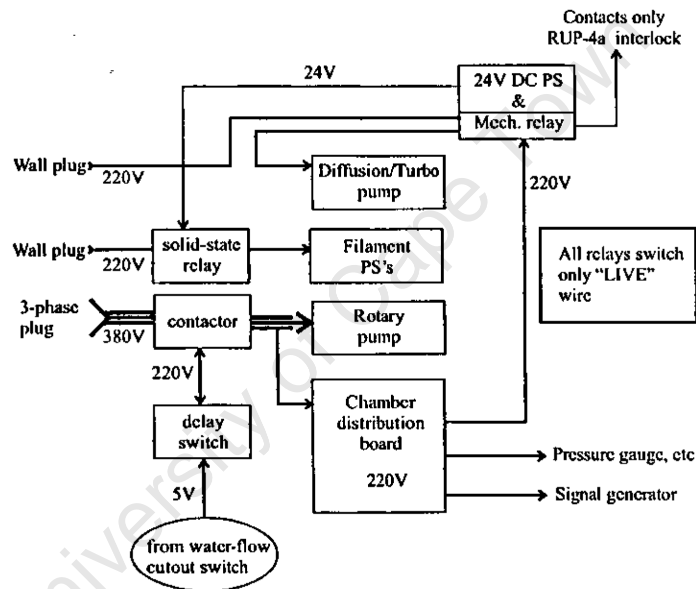

Figure 4.2: Figure showing electricity distribution in the laboratory. There is a 380 V three phase AC circuit, multiple 220 V single phase AC circuits, and a 24 V DC circuit. The 24 V DC is used to operate the RUP-4a safety interlock and a solid state relay.

The plasma laboratory is very cable-intensive. Since underfloor cabling was not a viable option (solid concrete floor, and it was not desirable to have a step leading into the lab), it was decided to fit overhead catwalks. It was also decided to re-wire portions of the laboratory to implement two 3-phase electrical outlets. These 3-phase supplies are used by the rotary fore-pump and the air-conditioning unit. Additionally, since the vacuum pump requires a minimum flow-rate of cooling water, it was considered imperative to that a flow-rate sensor be fitted and used to automatically switch off parts of the laboratory in the event of water flow loss. Since the plasma generation power supplies, the vacuum pumps, the high voltage pulsed power supply and the computers are all high power devices, it was decided to distribute the load of these devices over all of the remaining single-phase electrical outlets (figure 4.2).

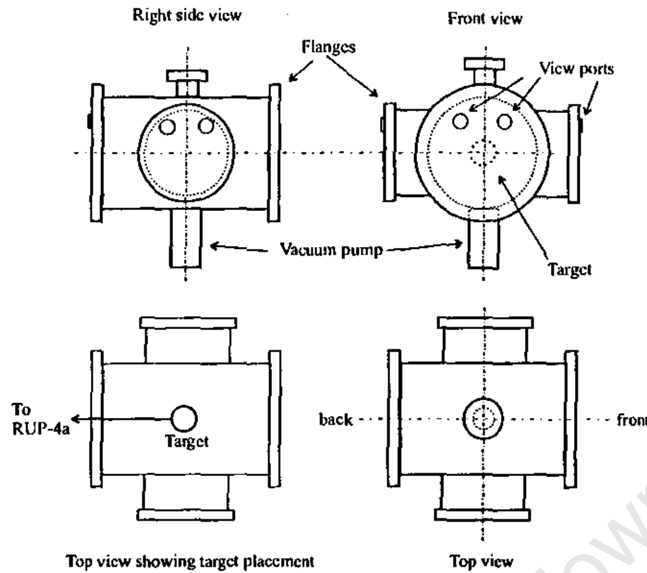

Figure 4.3: Schematics of the PSII chamber. The plasma chamber is a union of two intersecting cylinders. The chamber has several view-ports and numerous electrical feedthroughs.

University of Cape Town

4.3 PSII plasma chamber

The plasma chamber is on loan from the Plasma Physics Research Institute of the School of Pure and Applied Physics, University of Natal, Durban. It is an aluminium alloy chamber in the form of the union of two cylinders (figure 4.3). The main cylinder has a radius of radius 0.33m and is 1.04m in length. The smaller cylinder of the union houses the filament assemblies. Each side protrudes from the plasma chamber by 0.23m with a ≈0.24m inner radius. It was originally designed for use as a triple-plasma device, but is presently being operated with a single plasma region.

To optimise access to all the flanges and to maximise access to the "front" flange, the chamber was placed longitudinally in the centre of the laboratory, with the long axis of the chamber parallel to the long axis of the available floor space.

4.3.1 Rear flange

Since the rear flange was originally configured to house another plasma source, a new rear flange was manufactured at the National Accelerator Centre in order to accommodate the high voltage feedthrough from the high voltage pulsed power supply (chapter 5).

This high-voltage electrode enters the rear flange of the chamber via a large polytetrafluoroethene (PTFE) electrical feedthrough (figure 4.4). The high voltage connects to the target holder with steel wire.

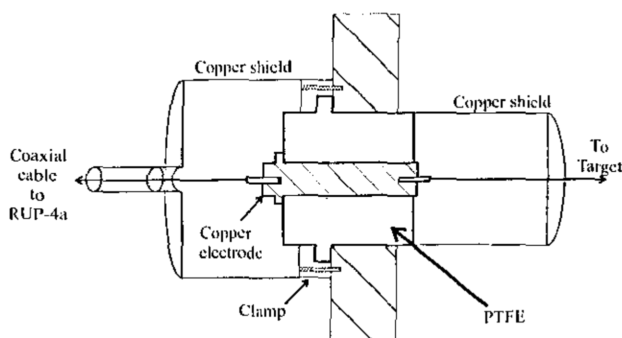

Figure 4.4: Figure showing the PTFE insulator fitted to the rear flange of the PSII chamber. The copper shield fitted on the outside is connected to the screen of the HV co-axial cable from the RUP-4a power supply, and is used to prevent electromagnetic interference. The copper electrode has been constructed to accept 4 mm banana plugs for connecting the target to the high voltage power supply.

University of Cape Town

4.3.2 Other flanges

The front flange contains the probe hardware, which includes 6 stepper motors for 2 motorised probes and a third manually operated probe.

The top flange has been modified to accept the high-voltage feedthroughs required for the 13.65 MHz RF-antenna for when the chamber is operated in the RF-plasma source configuration.

The diffusion vacuum pump is fitted to the bottom flange. The two side flanges have numerous smaller electrical feedthroughs and each has two smaller view ports. The side view ports are manufactured out of armour glass, while the front view ports consist of machined Perspex to allow for greater x-ray transparency. This is especially useful for the x-ray energy experiments, since the lower energy cut-off with the Perspex window is approximately 5 keV as opposed to greater than 30 keV for the armoured glass.

4.3.3 Filaments

Thin tantalum wire (0.10 mm diameter) was used as filaments, which were wound onto the 6 mm diameter stainless steel electrodes, 15 cm apart. By winding five filaments per side, the current demand did not exceed the 40 A maximum current deliverable by the filament power supplies, while still lasting long enough to require replacing after about 40 hours of continuous use. The filaments tended to break as a result of movements in the filament structure resulting from thermal expansion (the tantalum wire became very brittle after being heated and susceptible to mechanical shock). The filament structure is shown in figure 4.5. The grounded backing plate is used to reduce space-charge limit effects, thus improving plasma formation.

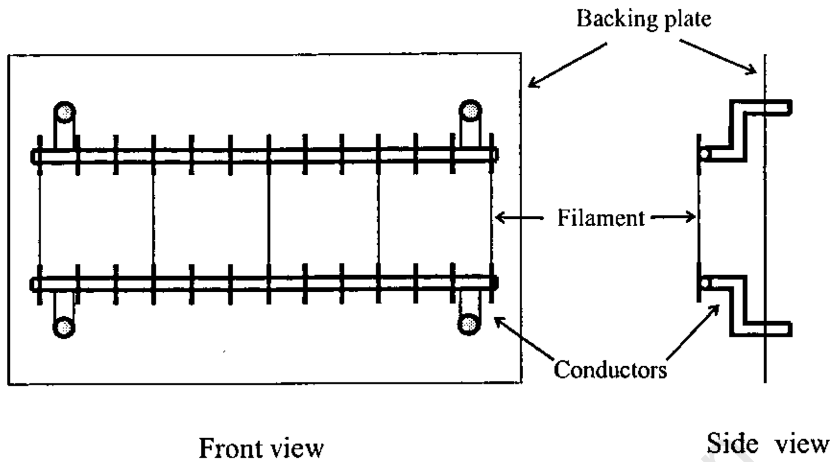

University of Cape Town

Figure 4.5: Diagram showing the filament structure. The filament electrodes are 6 mm steel rods with multiple pegs for winding the filaments around. The electrodes are 15 cm apart, with a grounded backing plate.

4.3.4 Chamber cooling

Steel conductors are used to deliver electricity to the filaments and since both the heat of the filaments and resistive heating due to the 20 A filament current can cause conductor temperatures to increase high enough to compromise the vacuum seal integrity. The vacuum pumps (both the original oil diffusion pump and the present turbomolecular pump) also require cooling. Thus a water cooling circuit needed to be constructed.

In the interests of environmental conservation it was decided to include the plasma laboratory in the Van de Graaff accelerator recirculated water system. This required extending one pipe from the nearby electrical characterisation laboratory, to bring in a water source, and laying down a return pipe to return the water to the recirculated system.

A water flow rate sensor was attached to the pump water exhaust, to ensure a minimum water flow rate through the vacuum pump.

Two filters, an initial 60 μm coarse sieve and a 1 μm fine filter were added to remove physical impurities in an attempt to minimise potential sources of blockage and build-up in the $\approx$4mm diameter chamber cooling waterways.

Cooling is provided by passing water through a network of 6 mm copper pipes attached to the chamber flanges. In addition, to protect the vacuum seal O-rings around the filament electrodes, special water-cooled copper collars are used to provide cooling. The collars are mounted around the electrodes and fitted up against the PTFE plug which houses the O-rings. A sectional view is given in figure 4.6.

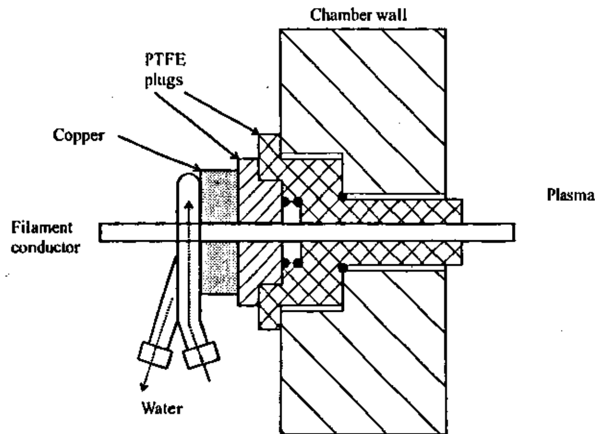

Figure 4.6: Cross-sectional side view of the filament electrodes showing the placement of the copper cooling collar and vacuum seal O-rings. Cooling is provided by water circulated through the attached copper pipe.

University of Cape Town

4.3.5 Probes

The front flange of the plasma chamber has two stepper motor controlled probes and one manually adjusted probe fitted to it, fitted along a vertical line through the centre of the flange. Similar probe hardware was used to examine two-dimensional plasma sheath behaviour [Mey96a]. To facilitate similar work in the future, hardware and software was assembled to operate one of these probes.

Probe geometry

As shown in figure 4.7, there are two probe designs used in the PSII chamber. The probe mounted

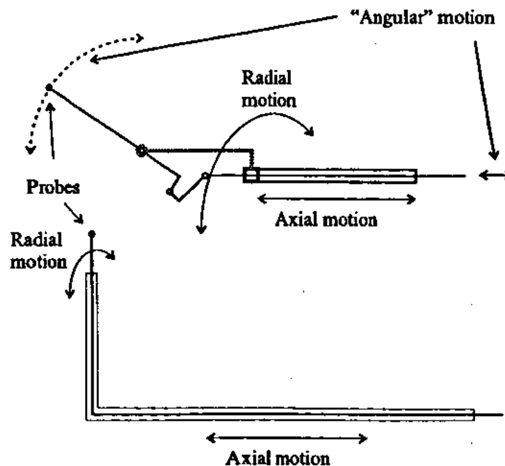

Figure 4.7: Diagram showing the layout and operation of the two Langmuir probes. The lower probe is a fixed "L"-shaped arm, which restricts the position of the probe to the surface of a cylinder. The upper probe has pivots which allow it to be positioned anywhere within the volume of a cylinder defined by the maximum reach of the probe.

lowest on the flange is constructed in the traditional "reclined - L" geometry, with the longer arm of the "L" mounted along the horizontal plane, and the probe mounted at the end of the shorter arm. Thus the probe can be driven along the axial plane of the chamber by the axial stepper motor (which drives a worm-gear onto which the probe arm is mounted). A second stepper motor rotates the arm perpendicular to the axial plane, thus allowing the probe itself to scribe an arc. This second stepper motor is called the radial stepper motor. Together, these two stepper motors can be used to position the probe anywhere on the two-dimensional "plane" in the cylindrical co-ordinates determined by z and θ for a fixed r, the length of the short arm of the probe.

The second probe, mounted along the centre-line of the main chamber, is more complex with another degree of freedom. In this probe, the elbow of the "L" is not fixed at 90° but can be swivelled from $-15°$ to $+100°$, as is demonstrated in greater detail in figure 4.8. By using three stepper motors it would be

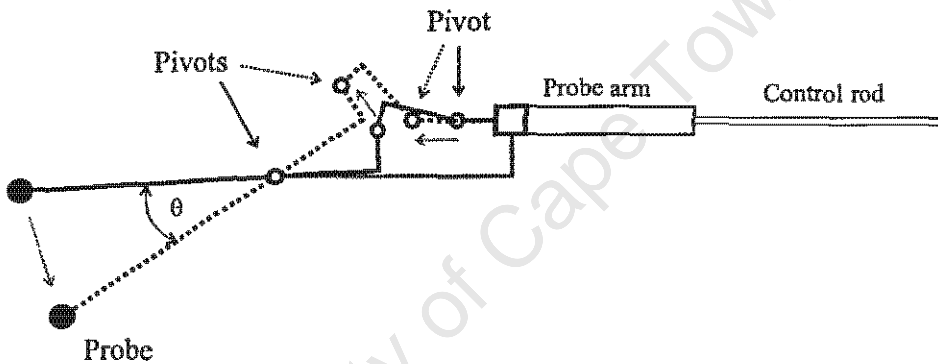

Figure 4.8: Schematic showing probe operation in greater detail. As the control rod is pushed into the probe arm, the two pivots allow the probe to sweep through a varying angle (θ). The probe can be positioned anywhere within the volume of a cylinder defined by the maximum reach of the probe by moving the arm axially and sweeping the probe.

University of Cape Town

possible to scan this probe within a continuous three-dimensional volume. This probe could thus perform 3-dimensional sheath evolution measurements around PSII targets.

4.4 Stepper motor controllers

Since the plasma chamber is equipped with two independently controllable probes, with two and three stepper motors respectively, it was decided to construct two stepper-motor controller and driver circuits. These circuits are split into two stages: a TTL controller circuit and a power driver circuit.

The controller circuits are based on the L297 (Appendix E) stepper motor controller integrated circuit which uses TTL signals, provided by the data capture computer's printer port, to provide *motor select (ENABLE)*, *direction select (CW/CCW)* and *step (CLOCK)* signals (figure 4.9) and generate the appropriate pulses to operate the eight power transistors of the driver circuit. Pulse timing is determined by the setting of an external variable resistor connected to the joystick port of the computer (appendix C.2.3).

The stepper motors each have two sets of coils which must be energised in sequence and with alternating polarity in order to move through a single step, and require 200 steps per revolution. The power driver circuit uses four power transistors in a push-pull configuration and a 12 V DC power-supply to operate the motors, as shown in figure 4.10. By energising opposite pairs of transistors, B_1 & B_4 or B_2 & B_3,

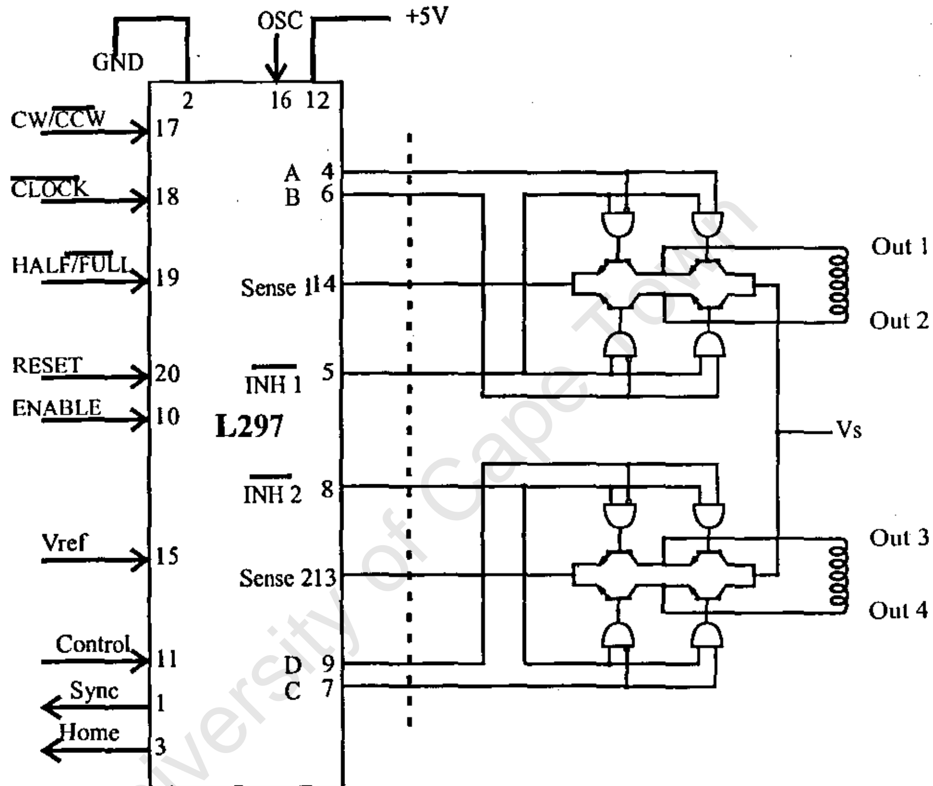

Figure 4.9: Schematic diagram showing the connections between the L297 stepper motor controller and the high current driver circuit.

the voltage drive current could be switched through the stepper motor coil in both directions. See the datasheets in appendix E for a detailed description of the operation and function of the stepper motors. The plasma chamber is also fitted with micro-switch end-stops to limit the extent of the stepper motor travel. These switches have been incorporated into the controller logic to implement the end-stop at a hardware level. The circuits are shown in figure 4.12. Thus if the forward end-stop has been triggered, the TTL logic circuits prevent any further forward-step requests from being decoded by the L297. The end-stop state can be sensed by the controlling PC, and is used by the controlling software to return the number of un-executed steps.

While these probes were not fully utilised in this thesis the stepper motor control circuitry was built to allow control of two of the probes for future work. Their presence makes this facility truly unique

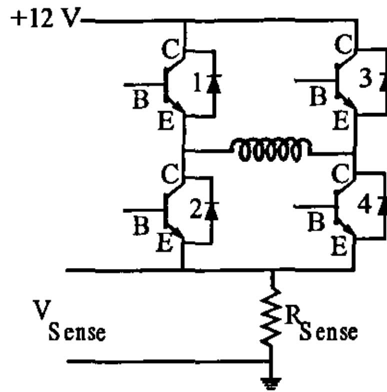

Figure 4.10: Circuit diagram of one half of the stepper motor driver circuit. V_{Sense} is used by the L297 controller to reduce the drive current.

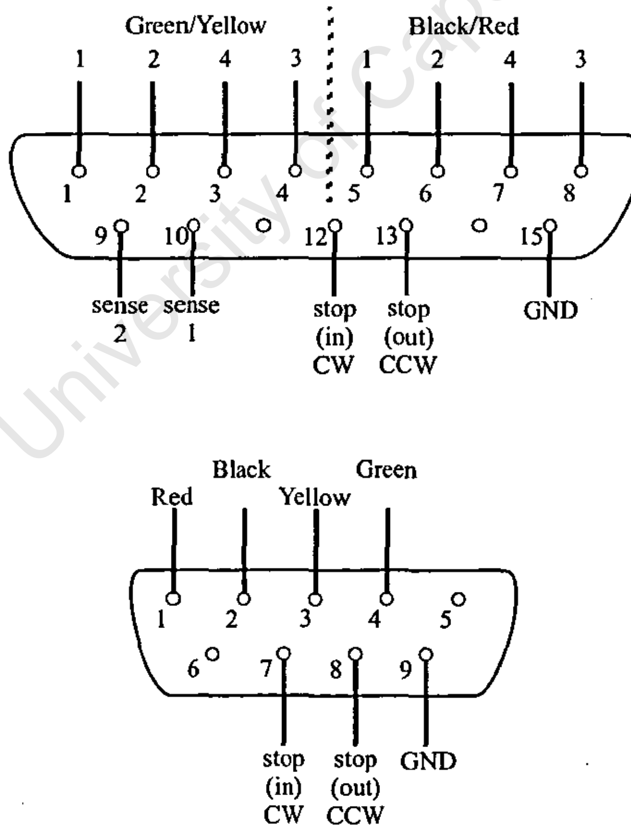

Figure 4.11: Wiring of the stepper motor cables. The 15-pin plug connects the TTL logic circuit to the high current stepper driver circuit, the 9-pin plug connects the high current driver to the stepper motor.

University of Cape Town

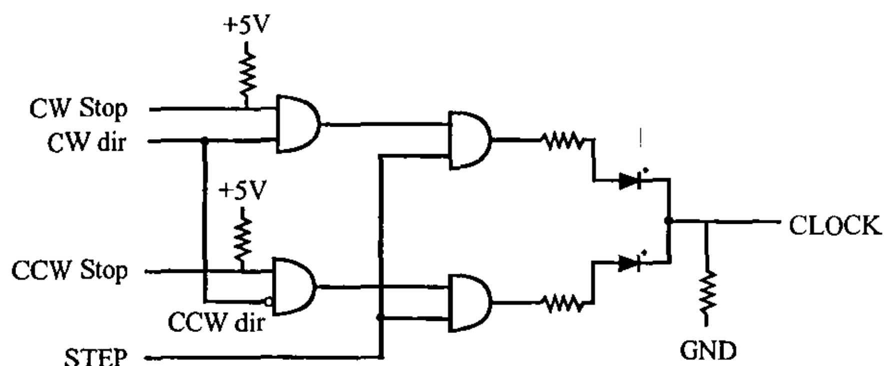

Figure 4.12: Circuit diagram showing the hardware logic that prevents the stepper motor from being operated past the end-stop.

University of Cape Town

in the world, as no other PSII facility has probes as complex as these, which are able to scan in three dimensions.

4.5 Chamber wiring for plasma generation and ancillary circuits

The plasma generation electronics consists primarily of two DC power-supplies which provide the filament and discharge currents. The filament supply is a 10 to 22 V, 40 A maximum supply, consisting of a 12 V fixed voltage supply in series with a 0 to 10 V variable supply. This unit is used to provide the current for ohmic heating of the filaments (§4.3.3). A discharge bias of 60 V is applied between the filaments and the chamber, and is used to accelerate thermionically emitted electrons from the filaments into the plasma volume. These are the primary ionising electrons used for plasma creation. The chamber wiring schematic diagram is shown in figure 4.13. To minimise resistive heating and losses, 25mm^2 welding cable was used to carry the filament current, shown in bold in figure 4.13. Two wires of a conventional 15 A, 3 core electrical cable was used to carry the discharge current, which under normal operating conditions never exceeded 2 A.

4.5.1 Discharge current control circuit

Since the plasma density is directly determined by the discharge current, it is desirable to include some form of automatic control to maintain a constant current. Thus a constant current control circuit was built based on the same circuit used at the Plasma Physics Research Institute. This circuit functions by comparing the discharge current with a preset value and adjusts the filament current accordingly. Since the discharge current is predominantly temperature-limited (§3.1.2.3), an increased filament current increases the filament temperature, and hence the discharge current. Thus as the filament is eroded away by ion bombardment and surface vaporisation, reducing the effective emitting surface area, the temperature is increased to maintain a constant discharge current. The circuit schematic is shown in figure 4.14.

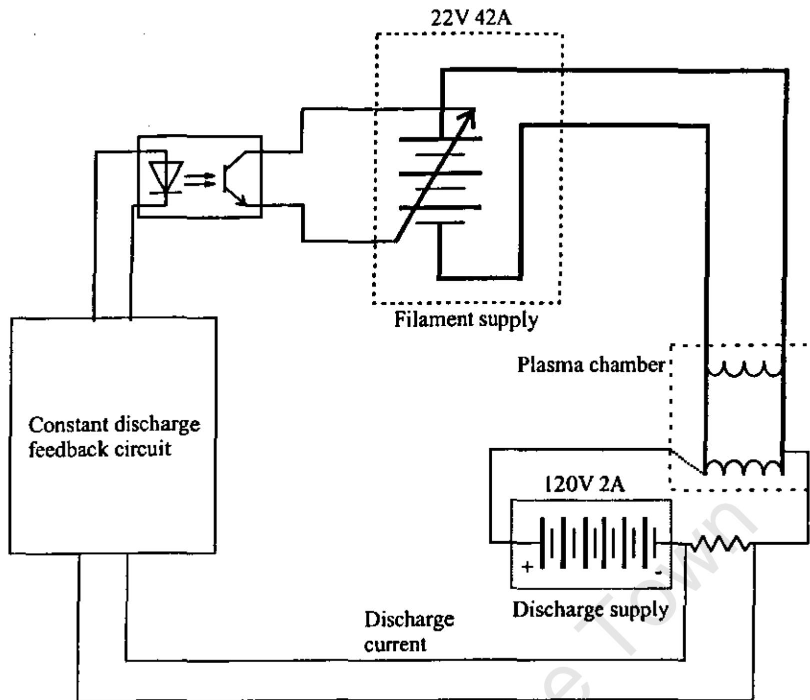

Figure 4.13: Schematic diagram showing the plasma generation wiring for the filament and discharge currents.

University of Cape Town

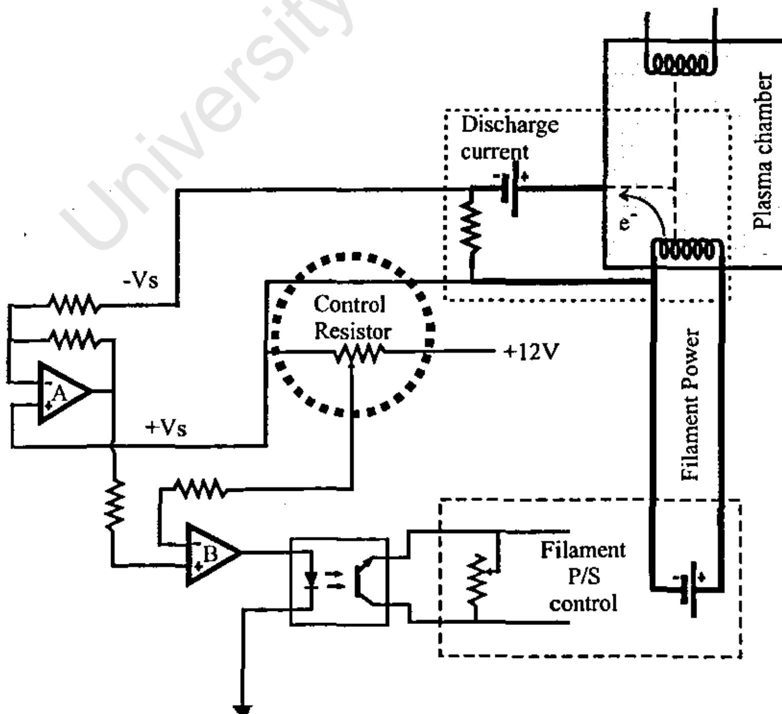

Figure 4.14: Schematic diagram of the constant current control circuit

4.5.2 Flow rate delay switch

A water flow-rate sensor was fitted to monitor the water flow leaving the vacuum pump. However it soon became apparent that transient fluctuations in the water pressure could cause the circuit to trip in non-fatal situations. Thus it was decided to fit a delay circuit (figure 4.15). This circuit used the

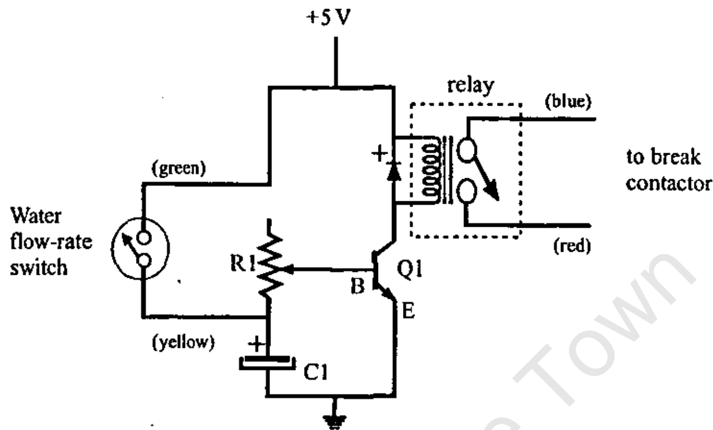

Figure 4.15: Circuit diagram of the flow-rate switch delay circuit.

flow-rate sensor to maintain the charge in a capacitor, which was in turn used to energise a transistor controlled relay. Thus when the flow-rate sensor goes open circuit, as in when the water flow drops below the minimum flow rate, the capacitor provides the necessary base current to maintain the fail-safe relay, however it will be discharged by a decay resistor. If the water-flow returns and the flow-rate sensor goes closed circuit, the capacitor will be recharged, and continue to hold the fail-safe relay. However, if the water flow does not return, after about 15 seconds the capacitor charge will drop below a threshold value required to maintain the transistor base current, and the fail-safe contactor will be switched off. This contactor is used to energise the vacuum pumps, the high voltage stage of the implant pulsed power-supply, and the plasma generation power-supplies. Thus in the event of water flow failure, these devices, which require the vacuum and hence the correct operation of the vacuum pumps, will all be turned off.

The contactor is also a "fail-safe" device, which has to be manually turned on upon the resumption of water-flow.

University of Cape Town

4.6 Remote control and monitoring of laboratory

Due to the high x-ray levels present in the laboratory when the implantation voltage exceeds 25 kV, a remote control system was developed to enable operation of the facility from an office situated next to the plasma processing laboratory. This control system relies heavily on the data processing software and hardware described in chapter 6 and appendix C respectively.

4.7 Summary

A chemistry laboratory at the National Accelerator Centre was modified to suit the new purposes of the plasma processing laboratory, with the addition of overhead catwalks, electrical outlets and recirculated water piping. The chamber, on loan from the School of Pure and Applied Physics, University of Natal, Durban, was modified to accommodate the high voltage feedthrough from the high voltage pulsed power supply. A water cooling circuit was also installed to cool the vacuum pumps and the steel conductors delivering electricity to the filaments.

Cabling required to support plasma production and monitoring were installed and electronic circuits were then developed and constructed to enhance the functionality of the laboratory. In particular, circuitry was added to maintain a constant discharge current (and hence plasma density), switch off parts of the facility in the event of loss of cooling water and allow control of the stepper motors. A control system (hardware and software) was developed to allow remote control and monitoring of the plasma processing facility.

University of Cape Town

University of Cape Town

Chapter 5

High-voltage power-supply

University of Cape Town

In the simplest case, a PSII facility consists of only two critical components, a plasma chamber and the negative high voltage pulsed power supply. The plasma chamber is described in some detail in §4.3. The design and construction of the high voltage pulsed power supply will be described in detail in this chapter.

It was designed by Dr Jörg Brutscher[1] of the Forschungszentrum Rossendorf based on an earlier design [Bru96a] and was built in a collaborative effort during a two month visit to the Forschungszentrum Rossendorf (between February and April 1997). It was delivered to the facility in June 1997, and commissioned by Dr Brutscher in a collaborative project at the National Accelerator Centre in July 1997.

5.1 Overview

5.1.1 Design philosophy

The high-voltage pulsed power supply, designated RUP-4a (Rossendorfer Universal Pulsgenerator - economy version), was designed for maximum variability, simple construction and ease of maintenance. Designed as an implantation power supply for small to medium plasma ion implantation applications, this device was constructed in a collaborative exercise at the Forschungszentrum Rossendorf. The unit is controlled either through an internal pulse generator and voltage control, or via an external pulse generator and 0 to 10 V voltage source. In this manner pulses of arbitrary voltage, width and frequency can be generated. It is even possible to implant with pulse bursts or other arbitrary pulse trains.

The maximum pulse parameters are determined by

- the maximum power the switching tube can dissipate,
- the implant current limiting resistor and,
- the maximum voltage from the charging module.

The maximum power limitation places upper limits on the duty cycle and implantation frequency for any given chosen implantation voltage. These limits are given in table 5.1 on page 47.

[1] Now with GBS Elektronik, Rossendorf, email:gbs@tz-rotech.de

5.2 Circuit description

The RUP-4a uses a highly modular design that can be separated into 4 basic parts, as shown in figure 5.1:

- a variable high voltage positive DC supply,
- a high voltage storage capacitor,
- a high voltage switching circuit, and
- switching circuit control logic.

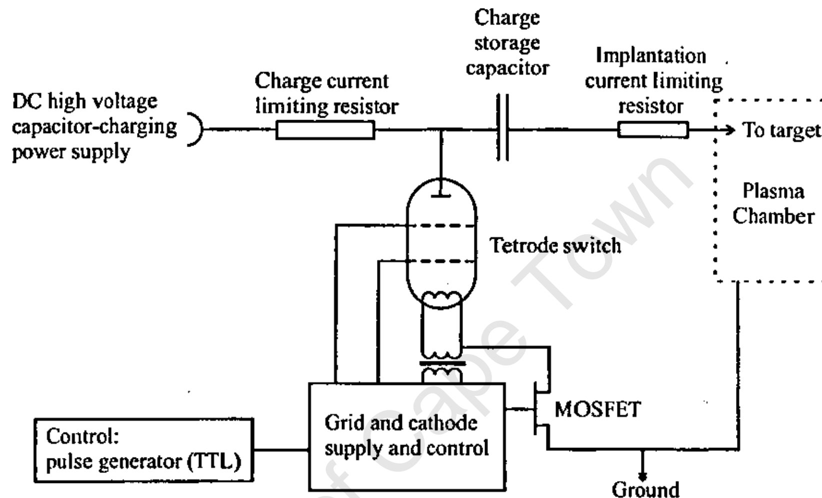

Figure 5.1: Schematic diagram showing the operation of the RUP-4a high voltage pulse generator.

University of Cape Town

5.2.1 Description of circuit Components

High voltage DC, variable potential, capacitor charging supply

In this design the high-voltage variable charging supply can be of any design able to satisfy the operational criteria of stable voltage and current delivery. This power supply is used to charge the storage capacitor in figure 5.1. The implantation potential is determined by this power supply. The present design uses a 30 kV, 88 mA (maximum) supply, (Kaiser systems, model number 1101065-22).

High-voltage storage capacitor

The high-voltage storage capacitor is charged by the charging supply mentioned above. This capacitor stores the charge for the high-voltage pulses to the work-piece. The two high-voltage resistors perform current limiting, the first one limits the charging current to the storage capacitor, the second limits the pulse current between the capacitor and the work-piece. The present design uses a 50 kV, 40 nF storage capacitor, an 8.2 kΩ, 100 W charge limiting resistor, and a 75 Ω, 200 W pulse current limiting resistor.

High voltage switching circuit

The high-voltage switching circuit is based around an EIMAC 8960 tetrode thermionic valve. This device is capable of switching 50 kV DC with a peak cathode current of 18 A and a 1200 W peak anode power dissipation. In the present configuration the peak current is limited to 11 A and it is recommended that at 30 kV, the mean current not exceed 20 mA (600W). This tetrode thermionic valve is used in conjunction with a MOSFET to complete the ground circuit used to switch the high voltage. By switching the positive plate of the capacitor to and from ground, it is possible to produce the negative high voltages required for implantation at the work-piece electrode.

Switching circuit control logic

The switching control logic determines the pulse timing parameters. This is the only portion of the pulse generator which operates at 5 V TTL levels. The timing parameters can either be determined by two 10-turn variable resistors on the top front panel, or by external sources. The two variable resistors determine the pulse width and frequency of the internal pulse generator and can vary these two parameters within a broad range. The ranges are selected via DIP switches on the timing logic circuit board, to generate pulse widths between 1 and 100 μs, at frequencies between a few Hz up to 1 kHz.

University of Cape Town

5.2.2 RUP-4a Principle of operation

The RUP-4a pulsed power supply operation can be separated into two distinct modes; the charging mode and the discharging mode. In the charging mode, the capacitor charging module charges up the storage capacitor and the tetrode switch is non-conducting. In this mode the positive pole of the capacitor connects via a charging resistor to the charging module and the negative pole of the capacitor is exposed to the plasma via the work piece holder. In the presence of a plasma, the circuit is completed by the plasma. Without the plasma, the voltage divider circuit provides a high-resistance path to ground.

In the discharge mode, the charging module is inhibited, and the tetrode is used to switch the high voltage of the discharge capacitor. The cathode of the tetrode switch is brought to ground potential via a MOSFET. In this mode the positive pole of the storage capacitor is brought to ground potential by the tetrode and MOSFET and hence the workpiece in the plasma, which is connected to the negative pole of the capacitor via a current limiting resistor, is raised to a high negative voltage.

5.2.3 Operation of tetrode

The EIMAC 8960 tetrode belongs to a class of electronic components called thermionic valves. It is a multielectrode (figure 5.2) evacuated electron tube, containing a thermionic cathode as the electron source. The voltage at the anode plate can be modulated by voltages applied to the screen and control grids. In the triode configuration, a control grid is placed between the anode and cathode. Voltages applied to the control grid affect the anode current, and it is thus possible to switch high voltages and currents. The tetrode has an additional grid, called the screen grid, between the control grid and the anode. This extra grid is used to reduce the control grid/anode capacitance, which allows AC transmission. The screen grid

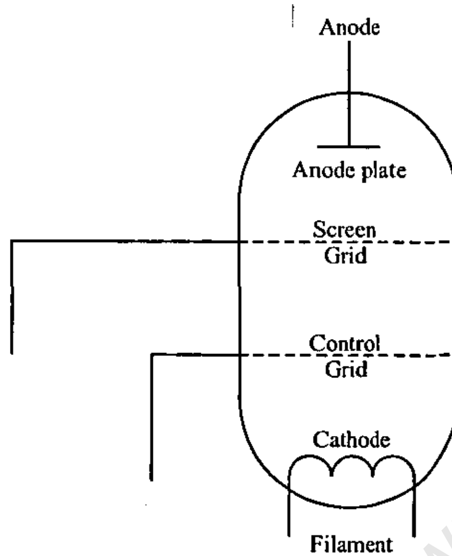

Figure 5.2: Schematic diagram showing the internal structure of a tetrode thermionic valve.

University of Cape Town

is usually held at a fixed positive potential.

5.2.4 Electrical operation

The electrical operation of the RUP-4a is as follows:

- in standby mode, only the cooling fan for the tetrode is in operation.
- the tube filaments are turned on when the second stage of the power-supply is energised via the "filament power" front panel switch.
- the third stage, enabled via the "high voltage/grid supply" front panel switch, energises the high-voltage capacitor charging supply module and energises the tetrode switch grids. If the internal pulse generator is enabled, activation of this third stage also starts the generation of implantation pulses according to the settings of the internal pulse generator and implant voltage variable resistors. For this reason it is always advised to ensure that the internal voltage select and implantation frequency and width resistors are minimised before activating the third stage.

Pulse switching

Activation of the third stage enables the capacitor charging module. This unit charges the storage capacitor via a charge-limiting resistor. In the present configuration, which uses a 8.2 kΩ resistor and a 40 nF capacitor, it takes about 2 ms to charge the capacitor to 99.9% of the charging potential. With no pulse trigger the tetrode switch is non-conducting and the grids are energised in preparation for a trigger. Upon triggering, a MOSFET circuit creates a conducting path between the tetrode cathode and the plasma chamber, thus completing the ground leg of the capacitor-discharge circuit.

5.3 Implant Operation

5.3.1 Principle of operation

Two RC networks are used to supply power to the tetrode grids. This is done to damp any oscillations which might occur in the switching circuit and to provide timed current limiting. Within the first few μs of applying the high voltage pulse to the workpiece, both networks are still fully charged and allow the tetrode to carry maximum current (12 A). Between 4 and 20 μs later, the grid supplies are degraded such that the tube can only carry the long-time current maximum of 60% of the peak current. This implementation improves tube life by reducing anode currents later in the pulse. This method of operation does not adversely affect normal operation since in normal operation the peak current occurs within the first few μs due to the capacitive nature of the power supply circuit, inductive loading of the plasma, displacement current, and sheath formation. During the sheath expansion phase when the implantation voltage has stabilised, the implantation current is much lower.

5.3.2 Inputs and controls

The RUP-4a has three primary parameters: implantation voltage (0 to 30 kV), pulse frequency (up to 1 kHz) and pulse width (1 μs to 1 ms, depending on load). These three parameters can be controlled by either the internal pulse generator circuit and voltage control potentiometer, or via external circuits. There are two BNC inputs and selector switches on the top front panel to enable external control of both the pulse timing (frequency and width) and the implantation potential. The present configuration uses the arbitrary waveform generator (CompuGen 840) to generate both these inputs in conjunction with a pulse generator. The CompuGen 840 provides the pulse frequency and implantation potential, and the pulse generator determines the pulse width. This allows almost complete computer control of the implantation parameters. With the "NetLab" software developed for this facility (chapter 6), this functionality allows almost complete remote control and monitoring of the implantation process and supports integration with the RAISE[2] project.

5.4 Physical description

The RUP-4a was assembled in a 1.6-metre tall cabinet. The internal structure of the cabinet can be separated into four distinct compartments, as shown in figure 5.3.

- At the bottom, the switching control electronics and mains power transformer. The bottom front panel houses the main power switch, the push-button switches to enable and disable the tube grid and filament power supplies and the analogue meters used to monitor the filament current, screen grid voltage and control grid voltage. The bottom rear panel houses the connectors for mains input, the interlock and the grounding lug.
- the middle bottom compartment houses the EIMAC 8960 tetrode thermionic valve. Due to x-ray radiation given off due to bremsstrahlung emission from the anode plate, this compartment is

[2]Remote Access to and Interaction with Scientific Equipment: url:http://raise.nac.ac.za/

University of Cape Town

entirely lead shielded (§5.4.1).

- the middle top compartment houses the current limiting resistors and the storage capacitor. This compartment also houses the current & voltage monitoring circuits, with appropriate BNC connectors on the front panel, and the antenna used for arc detection. The high-voltage co-axial cable emerges from the side panel of this compartment.
- the top compartment houses the DC HV capacitor charging module, the internal pulse generator circuits and the arc detection circuit. The front panel contains the variable resistors for the pulse timing and voltage control, switches and connectors to select external control, and the analogue meter displaying the currently output implantation potential.

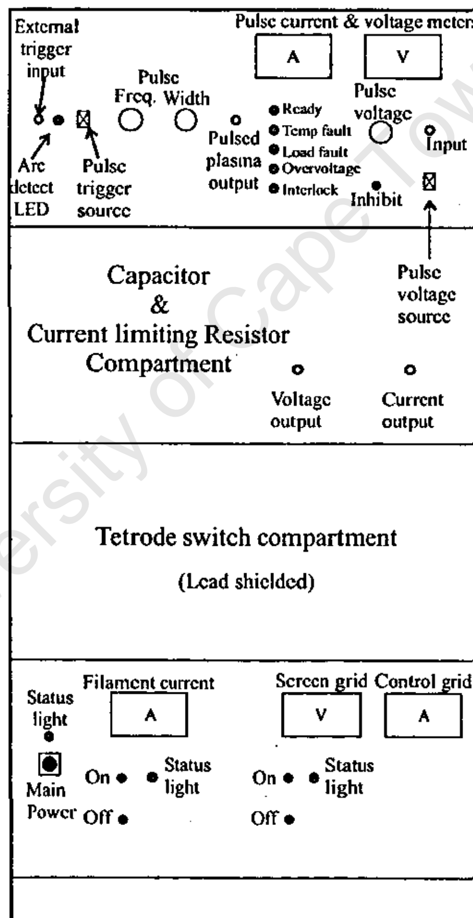

Figure 5.3: Layout of the RUP-4a power supply cabinet.

5.4.1 X-ray shielding

Since the electrons emitted from the cathode are stopped at the anode plate during the pulse, and since the pulse voltage can exceed 10 kV, high levels of bremsstrahlung (electron induced x-ray radiation) can be emitted from the tetrode. For this reason the entire tube compartment has been lined with overlapping

3mm-thick sheets of lead. The device has been tested under maximum permissible load conditions and verified to emit x-ray radiation with less than 0.7μSv/hr.

5.4.2 Tetrode cooling

All thermionic valves have a heated filament which provides the electron source, or cathode. In addition to the heat generated by these filaments, heat is also generated by energetic electron collisions in the grids and at the anode plate during pulse switching. To prolong tube life expectancy, the tube is fitted with an air-cooled cooling assembly. Tube cooling is achieved in the RUP-4a by forcing air through an EIMAC SK-510 air system socket and an EIMAC SK-506 air-system chimney. The 8960 tetrode valve is plugged into the socket, which is fitted with contacts to provide electrical contact to the tetrode. The chimney is placed over both the tetrode and the socket, being held in place by springs on the socket. An axial fan is fitted to the underside of the tube compartment and is used to force air through the air cooling assembly.

University of Cape Town

5.4.3 Voltage and current measurements

Measurement of the pulse voltage is performed using the built-in voltage divider. This voltage divider is a capacitive compensated resistance divider calibrated to operate at a ratio of 1:5000.

Measurement of the output current is performed using either the analogue meter (for mean current) or the Rogowski coil (for instantaneous current). The output current Rogowski coil is a 23-turn coil with a 2.3 Ω shunt resistor. This circuit is only reliable for measuring AC current, with a 10% decay for a 230 μs square-wave pulse. The accuracy of the circuit improves for shorter pulses.

The implantation voltage and current can be monitored by using the appropriate connection on the power-supply front panel. There are two BNC connectors which produce a 1:5000 and 1:10 representative signal of the voltage and implant current respectively. By connecting an oscilloscope to these outputs the implantation voltage and current can be monitored in real-time. When it is necessary to monitor the average current remotely, such as when the implantation voltage exceeds 25 kV, a closed-circuit video camera can be used to monitor the mean current meter.

5.5 Safety

The high voltages generated within this device and the x-ray emission generated both in the switching tube and the plasma chamber walls make this a potentially lethal device. Extreme care must be taken to prevent accidental electrocution or over-exposure to x-rays. An interlock has been fitted for additional safety.

5.5.1 Interlocks

An interlock connected to the vacuum pump power circuit prevents the RUP-4a from being operated without the vacuum pumps being operated. This will prevent the device from being operated while the

chamber is open. However, it is still essential to properly ground the target electrode with the appropriate grounding rod before touching it, to discharge the storage capacitor.

Since there are no interlock switches connected to the RUP-4a compartment panels, it is crucial that the device be properly switched off and disconnected from the mains power before any of the compartment panels are removed.

5.6 Upgrade options

The RUP-4a was constructed in such a way as to be easily upgraded. The device can easily be upgraded to increase the maximum implant potential, while the modifications necessary to increase the maximum implantation current are more involved.

5.6.1 Increasing implantation voltage

The present maximum implantation potential of 30 kV can be easily be upgraded to a maximum of 50 kV by changing the capacitor charging module in the top compartment. If this is done, then the front panel voltage meter will have to be adjusted to accommodate the new full-scale range. The 50 kV limit is imposed by the EIMAC 8960 tetrode switch.

University of Cape Town

5.6.2 Increasing implantation current

The maximum current switching ability can be doubled by the addition of a second 8960 tetrode without disturbing the first one. In order to effect this change, certain power supplies and hardware will have to be duplicated (tetrode cooling assemblies, filament transformer, filament current display, etc) the grid supply boards would have to be extended and the current limiting capacitor would have to be doubled in the first stage of the voltage multipliers. Since it is also recommended to switch the tubes on separately, additional relays and switches will have to be added.

5.7 Operational precautions

5.7.1 Arc detection

The RUP-4a uses an arc detection circuit to automatically detect electric arcs in the plasma and inhibit the pulse generation circuit when such an event occurs. The arc detection circuit uses an antenna in the capacitor storage compartment of the cabinet and a high-pass circuit to detect the high frequency electromagnetic pulse generated by an electric arc. During an electric arc breakdown the high frequency currents produce an RF signal that is detected by the arc-detection circuit which disables the pulse generation circuitry.

5.7.2 Operational limits

The control circuitry operates the tetrode switch to switch the capacitor into and out of the plasma high voltage circuit. In this way the target can be pulsed with voltages up to 30 kV at a frequency of up to

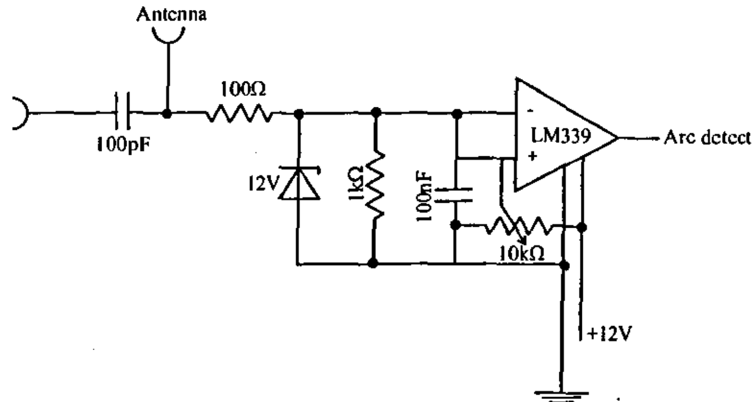

Figure 5.4: Arc-detection circuit of the RUP-4a power supply

Implantation voltage (kV)	maximum Power (W)	maximum pulse current (A)	maximum duty cycle (%)	maximum avg. current (mA)
30	600	11	0.17%	20
20	600	11	0.25%	30
10	800	10	0.7%	80
5	1000	9	2%	200
2	1000	8	6%	500
1	1000	4	20%	1,000

Table 5.1: High voltage power supply maximum implant parameters. This table shows the operating limits of the implantation power supply.

University of Cape Town

1 kHz. The maximum pulse duration is determined by the mean current. To protect the tetrode switch, it is recommended to remain within the tube switching power limits. At 30 kV a limit of 600W translates to a mean current of 20 mA, while at 1 kV, the 1kW switchable power results in a mean current 'limitation' of 1 A. The mean current in turn determines the peak current. The table of recommended maxima is given in table 5.1. The instantaneous current is limited by a load resistor and the plasma load itself. Typical instantaneous peak currents are of the order of 11 A, with an average instantaneous current of about 1 A.

Table 5.1 determines that, for example, a 30 kV implant with a pulse frequency of 1 kHz, is limited to a pulse width of about 1.7 μs, and that the mean current should not exceed 20 mA. There are no hard-wired checks to prevent the tube power capabilities from being exceeded, so it is up to the operator to ensure that this does not happen.

5.7.3 Turning off the tetrode filaments

To maximise tube life the tetrode filaments should not be turned off if the power-supply is going to be used within 8 hours of the end of an experiment. Most of the damage to the tube filaments occurs during the power on and off cycles, due to thermal shock to the system.

5.8 Summary

The RUP-4a high voltage pulsed power supply has been constructed with a modular philosophy and is thus upgradable. The present construction allows for a maximum implant energy of 30 kV, peak current of 11 A and a mean current of 30 mA. Pulse length can be varied from less than 1 μs, to greater than 100 μs.

University of Cape Town

Chapter 6

The "NetLab" Software

The "NetLab" software was written to facilitate better control of the plasma implantation procedure. The package enables complete control of the entire implantation procedure, except for changing chamber samples. Present hardware limitations restrict control of such parameters as pressure, plasma gas selection, and discharge current, however, these parameters can be monitored.

6.1 Introduction

The "NetLab" software package describes a suite of programs written to facilitate operation of the PSII facility. With the aid of this software package, the users and operator of the facility can both

- monitor the more important facility parameters, such as chamber pressure, implantation voltage & current, and
- control the RUP-4a power supply.

In addition to presenting acquired information from any of the connected devices, the software can also perform complex calculations and present data with the powerful graphical abilities of IDL.

6.1.1 User manual

A comprehensive manual which describes the usage of the "NetLab" software suite can be found in appendix D. A copy of this user manual will be kept with the plasma facility to assist users of the facility.

6.1.2 Inter-program communication

As described in appendix C, the data capture PC contains all the interface hardware and connects to all the data acquisition hardware. The user interface runs on the user computer, and is designed to allow the user computer to control the experiment from a remote location.

Since the "NetLab" program suite is actually executed on two separate computers simultaneously, there has to be some method of communication between them. For ease of use and maximum accessibility, it was decided to use the internet TCP/IP protocol to link the data capture and user computers. By using this protocol it becomes possible for the user computer to be located anywhere in the world, and

University of Cape Town

the user can still connect to the data capture computer and control the experiment. It is only necessary to know the IP address of the data capture computer and the port number at which the "NetLab" kernel is offering the connection. Since the "NetLab" kernel does not provide any access to the operating system or system disks, this program cannot be abused by internet hackers.

6.1.3 Design philosophy

The "NetLab" software suite has been written with a very modular design philosophy. This allows for relatively easy extensions since only that module which is being modified needs to be changed and secondly it is easy to add additional modules to extend the program functionality. The broad overview of the suite can be seen in figure 6.1.

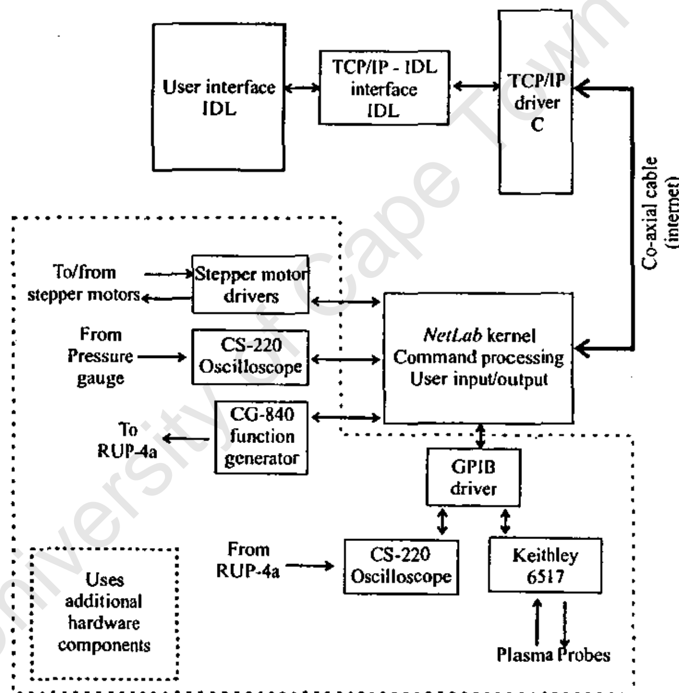

Figure 6.1: Block diagram showing the design of the "NetLab" software suite. The different levels of functionality are shown in separate blocks.

6.1.4 Software purpose

The "NetLab" software suite allows the user to initiate and monitor the experiment from a remote location (crucial when high implant voltages produce unsafe levels of x-ray radiation in the laboratory), using

- the implantation control window to regulate the implantation voltage and repeat frequency,
- the TDS-220 oscilloscope window to monitor the implantation current and hence determine the expected implantation time / dose.

The software also automatically shuts down the RUP-4a power supply when the desired implantation dose has been achieved. With suitable interface hardware the system can be extended to maintain constant pressure during implantation, change gasses, etc.

6.2 Software components

The "NetLab" software suite consists of multiple software components. At first glance, the software can be separated into two distinct components: the user interface and the "NetLab" kernel. The user interface is written in IDL and presents the user with a graphical user interface (GUI) to control most of the implantation parameters. The "NetLab" kernel is written in the "C" programming language and runs on the Linux[1] operating system of the data capture PC. The kernel accepts commands from the user interface and interfaces with the data capture hardware.

A TCP/IP software interface is used to connect the user interface with the kernel. The many different modules which process the commands and communicate with the connected data acquisition devices (oscilloscopes, electrometer, etc) use the TCP/IP protocol to pass the data between the kernel and the user interface.

Thus the package actually consists of three independent programs:

- The "NetLab" front-end, written in IDL, which offers a graphical front-end with which the operator can interact with the system.
- The "NetLab" TCP/IP interface, written in C, to allow the IDL front-end to communicate with the "NetLab" kernel.
- the "NetLab" kernel, written in C, and running under Linux. This kernel is written under an extremely flexible operating system, and communicates with various PC interface cards and other devices in the laboratory.

University of Cape Town

6.2.1 The TCP/IP library

The IDL module TCPIP.PRO provides the software interface between the user interface and the Windows NT compiled dynamic link library, TCPIP.DLL. Since IDL does not come provided with TCP/IP internet routines, it was necessary to write a TCP/IP interface library and call the routines using IDL's CALL_EXTERNAL procedure. Thus TCPIP.PRO provides the IDL function definitions needed by IDL modules to access the TCP/IP DLL routines.

6.2.2 The TDS-220 library

The IDL modules TDS220.PRO provides the command interface between the user interface and the TDS-220 oscilloscope data handling routines of the "NetLab" kernel. It communicates with the kernel using the TCP/IP interface routines mentioned above. The use of a module such as this allows easy modification of the suite to communicate with an alternate oscilloscope; only the routines in this module need be changed to communicate with the appropriate "NetLab" kernel routines for the new oscilloscope.

[1] A free Unix-like operating system, originally developed and written by Linus Torvaldes

6.2.3 The "NetLab" kernel

The "NetLab" kernel is written in the "C" programming language. It consists of numerous modules which are linked together to form the "NetLab" kernel executable program. These modules are called by the "NetLab" kernel command parser/processor and provide access to the different hardware components such as the GPIB interface, the stepper motor interface, the CG-840 and the CS-220 cards. Additional modules use the GPIB to communicate with the TDS-220 oscilloscope and the Keithley 617 series electrometer.

6.3 User interface

For the software to be used, the appropriate programs have to be executed on the data capture computer and the user interface computer. The "NetLab" kernel also has to be told to expect input from the network (by using the NetLab command "neti") before it will accept a connection from the user interface.

6.3.1 The Experiment Application window

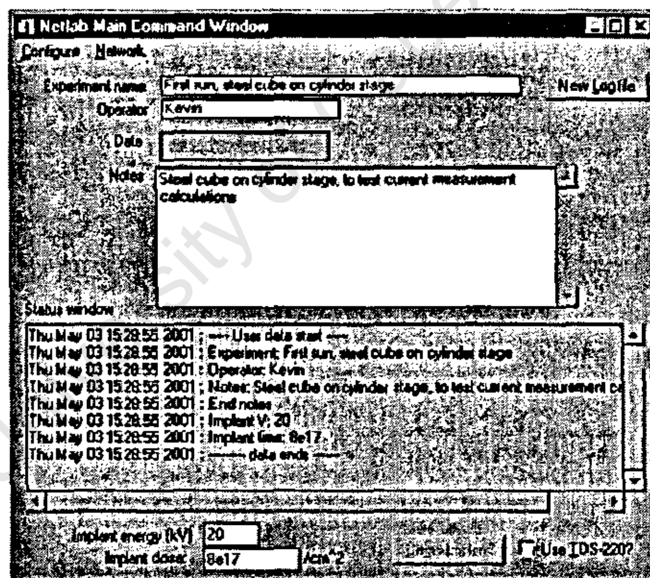

Figure 6.2: The "NetLab" experiment application window. The experiment details can be defined here.

This is the first window (figure 6.2) produced by the user interface application. It allows the user to configure the software, connect to the "NetLab" kernel and describe the details of the experiment. This window allows the user to select a log file, to which a log of all the notable events of the experiment will be written. It also allows the user to enter notes about the experiment, the desired implantation voltage and dose. All of this information is written to the log file. Once a connection has been established with the "NetLab" kernel, a button is used to invoke the implantation control window and optional TDS-220 oscilloscope window.

6.3.2 Implantation control window

This window (figure 6.3) provides the main interface to the implantation experiment, providing control of the implantation voltage and repeat rate, providing both a graphical record and printing the values of the chamber pressure and discharge current, and showing the calculated implanted dose based on the user definable values of target area, secondary electron emission coefficient (γ) and the mean current.

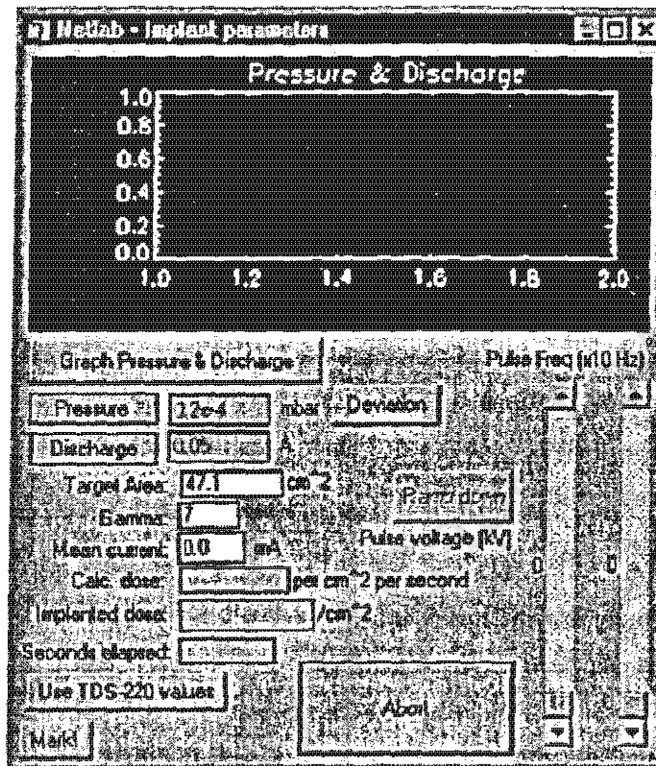

Figure 6.3: The "NetLab" implantation control window allows the operator to define the target and implantation parameters. If the TDS-220 oscilloscope is used, the mean current can be determined automatically.

If the TDS-220 is connected and being used, the mean current can be calculated by the software, else it must be manually entered. The implanted dose is calculated from the mean current according to

$$D(\text{ions per cm}^{-2}) = \frac{\text{Implanted charge}}{\text{Target area}} = \frac{I_{\text{mean}}/(1+\gamma)}{\text{Target area}}. \tag{6-1}$$

Thus the dose (in ions per cm^{-2}) is calculated based on the assumption that if 1 ion liberates γ electrons, then the ion current portion is $1/(1+\gamma)$ of the mean current.

This window also provides a large ABORT button to shut down the RUP-4a if necessary.

6.3.3 The TDS-220 Oscilloscope window

If the "Use TDS-220" checkbox was selected on the experiment application window, this window (figure 6.4) will be present with the implantation control window above. This window presents a graphical view of the two channels of the TDS-220 oscilloscope, used to measure the implantation current (channel

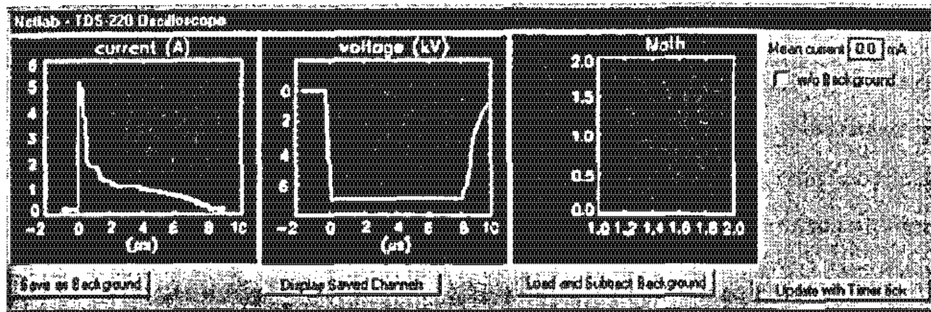

Figure 6.4: The "NetLab" TDS-220 Oscilloscope window. Traces of the implantation current and voltage are shown. This data can be used by the implantation control window to automatically calculate the mean implantation current.

1) and the voltage (channel 2) respectively. This window also allows one to define a "background current", usually measured in the absence of a plasma (or without the target attached to the target holder), and to subtract this current from the present implantation current.

This implantation current is used to calculate a mean current according to:

$$I_{\text{mean}} = \frac{Q_{\text{pulse}} \times \text{repeat rate}}{1(\text{second})} \tag{6-2}$$

where $Q_{\text{pulse}} = \int I dt$ and is determined by multiplying the integrated current from the oscilloscope by the time base:

$$\int I dt = \Sigma I \times \delta t = \delta t \times \Sigma I \tag{6-3}$$

where δt is the width of the oscilloscope time resolution and ΣI is calculated by adding the current values from the oscilloscope channel. If a background current has been selected it can be subtracted from the pulse current in this calculation.

6.4 Possible extensions

Additional modules can be written to extend the functionality of the "NetLab" software. Two such extensions could be to provide an interface to the Langmuir analysis routines to acquire the Langmuir characteristic I-V trace with the Keithley electrometer and then perform the analysis to extract the plasma parameters. This module would be mutually exclusive with the implantation control window since the long sampling time of the Keithley electrometer prevents any sensible result from being measured during an implantation experiment.

The second extension would be to add a user interface to control the stepper motor controller to allow one to move the probes to designated locations and capture probe measurements (either for plasma parameter measurements, or to measure saturation current traces for sheath evolution experiments). This module should allow for scan regions to be defined, to move the probe to each location in the scan region and perform the desired measurement at each location.

University of Cape Town

6.5 Summary

The "NetLab" software suite is a pair of computer programs that are run on two computers, one which presents the user interface, the other a data capture computer in the laboratory. The user interface has a full GUI which presents the implantation parameters and allows the user to control the implantation power supply characteristics. The data capture computer uses many different devices to read and control the various parameters, such as chamber pressure, implantation current and implantation voltage.

The user interface software has been written using TCP/IP networking protocols to allow remote access to the implantation facility.

University of Cape Town

University of Cape Town

Chapter 7

Analytical Techniques

Analysis of targets implanted by the facility should form a fundamental part of any research project. There are a wide range of analytical facilities available either at the National Accelerator Centre or the nearby universities (University of Cape Town, University of the Western Cape and the University of Stellenbosch). The facilities at the National Accelerator Centre, or at the Materials Research Group , in particular, primarily employ nuclear and x-ray technologies. The nuclear techniques of NRA, RBS and ERDA can be complemented by the x-ray diffraction facilities. PIXE can also be performed at the Materials Research Group, but since this technique is of limited interest to PSII applications, it will not be described any further.

In addition to the nuclear techniques above, there are other techniques of use to this facility, some of which are available at the Materials Research Group, others at nearby universities. These techniques include radiation effects, such as XRD, electron techniques, such as AES, and mechanical techniques, such as micro-hardness measurements.

University of Cape Town

7.1 Nuclear techniques

Nuclear analytical techniques were used to perform dose *versus* depth measurements on implanted samples. The implanted species being detected determined the technique used: for nitrogen in steel, Nuclear Reaction Analysis was most suitable, while for hydrogen in silicon, Elastic Recoil Detection Analysis was used. Rutherford Backscattering Spectrometry was used for charge correlation and (by using channelling techniques) to examine lattice damage in the implanted silicon samples.

7.1.1 General theory

The physical principles of nuclear analytical techniques are very similar: an incoming particle penetrates the target where it interacts with a target atom to produce a reaction particle in a binary collision. In ERDA, the reaction particle is a forward scattered (or recoil) target particle, in RBS it is a backscattered beam particle, while in NRA it is a nuclear reaction product.

If the interaction does not occur at the target surface, both the incoming and outgoing ions (figure 7.1)

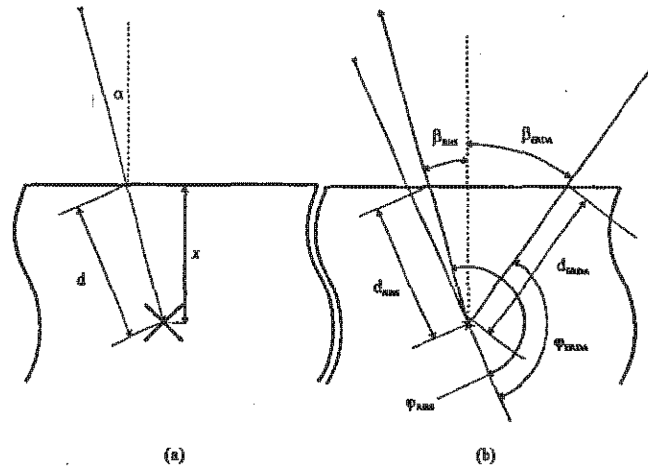

Figure 7.1: Depth scale. (a) The beam particle penetrates to a depth x, traversing a distance $d = x/\cos\alpha$. The depth x ranges from 0 (a surface collision) to a maximum depth determined by the minimum detectable energy of the detector. (b) The reaction particles also traverse a distance $d = x/\cos\beta$ as they leave the target material.

lose energy as they traverse the target material. These energy losses are as a result of collisions and other energy-loss interactions as a result of the *stopping power* (§7.1.1.1) of the target matrix.

The projectile/target interaction is determined by two main phenomena: the *cross-section* (§7.1.1.2) describes the probability of the interaction, and the *kinematic factor* (§7.1.1.3) determines the energy of the emerging particles.

Thus the stopping power of the target matrix and the kinematic factor of the interaction determine the energy of the particles while the cross-section determines the probability of a reaction. The cross-section also determines the quantitative *yield* (§7.1.1.5) and resolving power of the experiment since materials with greater cross-sections can be detected at lower concentrations.

7.1.1.1 Stopping power

As the projectile penetrates into the target matrix, it loses energy due mostly to glancing collisions with the electron shell (called electron stopping), but at lower energies nuclear collisions (called nuclear stopping) play a role. The energy loss per unit depth, or stopping power, determines the energy dE lost by the projectile traversing a segment of target thickness dx, typically calculated by

$$dE/dx(\,eV \text{per} 10^{15} \text{atoms/cm}^2) = S_e(\text{eV}) + S_n(\text{eV}) \tag{7-1}$$

where S_e and S_n are the electronic and nuclear stopping contributions respectively.

There are a few stopping models but the most common are the Andersen-Ziegler [And77a] and the Ziegler-Biersack [Zie85a] theories.

Stopping in compounds

Bragg's rule [Bra05a] can be used to calculate stopping in compounds. It assumes that the stopping of a compound is determined by the simple linear proportion of all the compound elements, such that for a

University of Cape Town

compound of i elements of concentration c_i (such that $\sum c_i = 1$) and stopping S_i, the stopping is given by

$$S = \sum_i c_i S_i \tag{7-2}$$

Bragg's rule assumes that the stopping of elements in compounds are not affected by the chemical state of the elements. Experimentally, however, deviations from Bragg's rule indicates that stopping does depend on the chemical and physical state of the constituent elements, by 10 – 20% for certain oxides, nitrides and hydrocarbons [Bou88a].

Stopping and depth calculations

The stopping power $\frac{dE}{dx} = S_e + S_n$ thus depends on the beam particle, its energy, and the composition of the target, and gives the energy lost by a particle traversing one atomic layer (in units of 10^{15} atoms per cm^2).

The stopping power is used to derive the energy of a particle at a depth x which is given by

$$E(x) = E_0 - \int_0^{x/\cos\theta} \frac{dE}{dx'} dx' \tag{7-3}$$

where E_0 is the particle energy at the surface, θ is the angle between the ion beam and surface normal (α in figure 7.1a) and $\frac{dE}{dx}$ is the energy dependent stopping power.

7.1.1.2 Cross-section

The cross-section or probability of scattering a projectile into a solid angle $d\Omega$ centred about a scattering angle θ (in RBS, or ϕ in ERDA) is expressed in two regimes, a Rutherford regime and a non-Rutherford regime.

Rutherford Cross-sections

When the energy of the particle is within a certain regime the Rutherford scattering cross-section can be easily determined. In particular, (a) the projectile energy must be high enough that it can approach the target nucleus without being deflected by the target electrons and (b) the energy should not be so high such that the smallest distance between them approaches the dimensions of the nuclei, to avoid any nuclear force interactions.

The Rutherford cross-section is given by Tesmer and Nastasi [Tes95a] as:

$$\frac{d\sigma_{RBS}}{d\Omega} = \left(\frac{Z_1 Z_2 q_e^2}{4E}\right) \frac{4\left(\sqrt{M_2^2 - M_1^2 \sin^2\theta} + M_2 \cos\theta\right)^2}{M_2 \sin^4\theta \sqrt{M_2^2 - M_1^2 \sin^2\theta}} \tag{7-4}$$

At low energies (E/amu *leq* 100 keV) electron screening can be taken into account with a correction factor, F, such that $\sigma = F \cdot \sigma_{RBS}$. Details can be found in L'Ecuyer [LEc79a], for $\theta < 90^\circ$, and Andersen [And80a], for $\theta > 90^\circ$.

The Rutherford cross-section for recoils is given by

$$\sigma_{\text{ERD}}[\text{mb/sr}] = 2.0731 \times 10^7 \frac{[Z_1 Z_2 (M_1 + M_2)]^2}{(2M_2 E[\text{ keV}])^2 \cos^3\phi} \tag{7-5}$$

University of Cape Town

where ϕ is the recoil angle in the laboratory system.

Non-Rutherford (NR) cross-sections

At high energies, $E > E_{NR}(Z)$, the cross-sections are affected by the nuclear force. Bozoian [Boz93a] has described a formula for $E_{NR}(Z)$ for which non-Rutherford cross-sections are expected to apply:

$$E_{\mathrm{NR}}[\mathrm{MeV}] = \begin{cases} \frac{M_1+M_2}{M_2}\frac{Z_2}{10} & \text{for } Z_1 = 1 \\ \frac{M_1+M_2}{M_2}\frac{Z_1 Z_2}{8} & \text{for } Z_1 > 1 \end{cases} \tag{7-6}$$

where E_{NR} is the energy at which the non-Rutherford cross-section deviates by more than 4%. For non-Rutherford energies, the cross-sections have to be experimentally determined.

7.1.1.3 Kinematic Factor

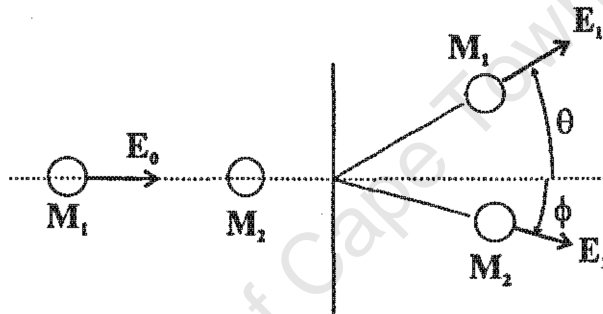

Figure 7.2: A schematic representation of a collision in the laboratory frame of reference. The incoming particle M_1 with energy E_0 strikes the stationary target nucleus M_2 and undergoes a Coulombic interaction. The energy E_1 of the scattered particle M_1 is measured at an angle θ. The energy E_2 of the recoiled particle M_2 is measured at an angle ϕ.

University of Cape Town

The kinematic factor determines the energies of the reaction particles after a reaction/collision. Considering a typical experiment in the laboratory frame of reference, as shown in figure 7.2, an incoming projectile with mass M_1 and energy E_0 strikes a target atom with mass M_2 at rest. In RBS the resultant scattered particle has an energy E_1 at an angle θ with respect to the incoming beam, while for ERDA the target atom recoils at an angle ϕ and energy E_2. In the elastic collisions of RBS and ERDA, the laws of conservation of energy and momentum precisely define the relation:

$$\begin{aligned} E_1 &= K_1 \cdot E_0 = \frac{M_1^2}{(M_1+M_2)^2}\left\{\cos\theta \pm \left[\left(\frac{M_2}{M_1}\right)^2 - \sin^2\theta\right]^{\frac{1}{2}}\right\}^2 \cdot E_0 \\ E_2 &= K_2 \cdot E_0 = \frac{4M_1M_2}{(M_1+M_2)^2}\cos^2\theta \cdot E_0 \end{aligned} \tag{7-7}$$

for the scattered and recoil particles respectively.

Nuclear reaction kinetics

For nuclear reactions, such as which occur in NRA, it is useful to define the nuclear reaction factors given below:

	Mass	Energy
Incident ion	M_1	E_1
Target nucleus	M_2	0
Light product	M_3	E_3
Heavy product	M_4	E_4
Energy released in reaction		Q
Total energy		$E_T = E_1 + Q + E_3 + E_4$

By defining the following quantities:

$$\begin{aligned} A_{13} &= \frac{M_1 M_2}{(M_1+M_2)(M_3+M_4)} \frac{E_1}{E_T} \\ A_{14} &= \frac{M_1 M_4}{(M_1+M_2)(M_3+M_4)} \frac{E_1}{E_T} \\ A_{23} &= \frac{M_2 M_3}{(M_1+M_2)(M_3+M_4)} \left(1 + \frac{M_1}{M_2} \cdot \frac{Q}{E_T}\right) \\ A_{24} &= \frac{M_2 M_4}{(M_1+M_2)(M_3+M_4)} \left(1 + \frac{M_1}{M_2} \cdot \frac{Q}{E_T}\right) \end{aligned} \tag{7-8}$$

the energy of the light particle created in the nuclear reaction is given by

$$E_3 = E_T A_{13} \left[\cos\theta \pm \left(\frac{A_{24}}{A_{13}} - \sin^2\theta\right)^{\frac{1}{2}}\right]^2 \tag{7-9}$$

where θ is the particle emission angle. The plus sign is only used when $A_{13} < A_{24}$, else the equation has two solutions and the maximum possible emission angle is given by

$$\theta_{\max} = \arcsin\left(\frac{A_{24}}{A_{13}}\right)^{\frac{1}{2}} \tag{7-10}$$

The energy of the heavy particle with emission angle ϕ is given by

$$E_4 = E_T A_{14} \left[\cos\phi \pm \left(\frac{A_{23}}{A_{14}} - \sin^2\phi\right)^{\frac{1}{2}}\right]^2 \tag{7-11}$$

Again, only the plus sign is used for $A_{14} < A_{23}$, while for $A_{14} > A_{23}$ both solutions exist. The maximum emission angle is given by

$$\phi_{\max} = \arcsin\left(\frac{A_{23}}{A_{14}}\right)^{\frac{1}{2}} \tag{7-12}$$

7.1.1.4 Straggling

As the energetic ion beam projectiles, or outgoing reaction particle, traverses matter, its stopping induced energy losses are also accompanied by an energy spread or straggling. This straggling is caused by statistical fluctuations in the energy transfer mechanisms of the different collision processes. Straggling losses have the following contributions:

- Statistical fluctuations in the energy transfer due to collisions with electrons.
- Statistical fluctuations in the energy transfer collisions between nucleii.
- Double and multiple scattering, which results in different path lengths, and hence energy and angular spread of the beam.

University of Cape Town

- Geometric straggling: A finite, non-zero detector solid-angle and beam-spot size result in different path lengths and scattering angles in any experimental arrangement.
- Topographic straggling: Surface and layer roughness, which results in different path lengths over the beam spot size and detector solid angle.

Further broadening of the measured energy occurs as a result of the non-zero energy resolution of the detector system. Straggling thus 'smears' the energy spectrum, causing loss of resolution of fine structure and broadening of spectrum peaks.

7.1.1.5 Yield

The yield is given by

$$Y_j = N_j Q \Omega \sigma_j \tag{7-13}$$

per element j. Where N_j is the concentration of the element, Q is the number of incident particles, Ω the detector solid angle and σ_j the reaction cross-section. In simulations, Q and Ω are often combined by the term 'particles-steradian' (P). Numerically, equation 7-13 becomes

$$Y_j = N_j[\text{atomic percentage}]\ 10^{-27}/10^{15} P \sigma_j[\text{mb/sr}] \tag{7-14}$$

where 10^{-27} is the area of a milli-barn in cm^2, 10^{15} are the number of atoms per layer per cm^2 and N_j is the relative portion (0 to 1) of that element (atomic concentration).

University of Cape Town

7.1.2 Analysing spectra

Analytical computer programs that simulate the reaction spectra typically use a user-defined target matrix, where the target is described in terms of layers each with a defined composition and thickness. Thus from a computer simulation point of view, the simulated spectrum can be constructed in the following way:

- The target layer thicknesses (if given in microns, for example) are converted to atomic layers of 10^{15} atoms per cm^2. (For example, silicon, which has an atomic density of 4.979×10^{22} atoms/cm^3 has an atomic layer thickness of $1 \times 10^{15}/4.979 \times 10^{22}$ cm, or 0.2008 nm. So 1 μm corresponds to 4980 atomic layers of Si).
- The stopping power equations are used to determine the energy losses of the beam particle as a function of target depth (penetration into the sample) as the particle traverses each atomic layer (equation 7-1 and 7-2).
- The scattering cross-sections determine the probability of an interaction. Often expressed in terms of differential cross section ($d\sigma/d\Omega$), or the probability ($d\sigma$) of scattering into the solid angle segment ($d\Omega$). Elements with high cross-sections return more counts per beam particle and per atom of the element present, and thus are more easily detected out of the background noise.
- At each layer the kinematic factors of each of the constituent elements are used to calculate the energy of the reaction particles headed for the detector (determined by the scattering angle, θ) for those collisions that occur there.

- The energy losses of the reaction particles as they leave the target are calculated according to the stopping powers above. If an absorber foil is fitted, stopping power energy losses in the foil are also calculated.
- Since the experimental system has an energy resolution determined by (a) the detector, and (b) the digitising hardware (the multi-channel analyser or MCA), final energy spectrum is discrete, with energy steps of typically a few keV per channel. Thus the particles reaching the "detector" in the simulation are also grouped into channels and counted (for each particle detected by a channel, that channel's particle count is incremented according to the yield calculation (§7.1.1.5)).
- The actual channel count per simulation particle is determined by (a) the deposited charge (or how many particles have entered the target so far), (b) the solid angle of the detector system (how much of the target can the detector 'see'), (c) the cross-section of the reaction (§7.1.1.2) and (d) the concentration of the element in the sample.

However, energy straggling, multiple scattering and detector resolution adversely affect the accuracy of the detected energy by causing energy broadening. These factors affect the resolution and quantitative interpretation of the reactions.

Software packages such as RUMP [Doo86a] and SIMNRA [May97a] allow the user to "construct" a target consisting of layers. The elemental composition and thickness of each layer and experimental set-up are used to calculate the expected spectrum, taking such effects as absorber foil thickness, detector response and beam energy into account. When a good match is achieved, the layered composition can be assumed to reasonably represent the target structure.

RUMP is used for the analysis of RBS and ERDA spectra while SIMNRA is used to analyse RBS, ERDA and NRA spectra. SENRAS [Viz90a] can also be used to analyse NRA spectra. There are also programs which are being developed to do this automatically [Pad01a, Tou99a].

University of Cape Town

7.1.3 Elastic Recoil Detection Analysis

The ERDA analytical technique allows one to determine concentration depth profiles of elements lighter than the beam projectile. The heaviest commonly used projectile for ERDA at the Materials Research Group is helium, allowing one to establish concentration depth profiles of hydrogen, deuterium and tritium.

ERDA was used in this thesis to examine the effect of substrate temperature on the hydrogen depth profile of hydrogen implanted silicon (§10.5).

In an ERDA measurement (figure 7.3) with an ion beam of energy E_0, a recoil particle is detected with energy E_r, given by

$$E_r(x) = K_2(E_0 - \Delta E_0) - \Delta E_r - \Delta E_{\text{foil}} \tag{7-15}$$

where K_2 is the kinematic factor (equation 7-7), ΔE_0 and ΔE_r are the energies lost by the beam and recoil particles entering and leaving the substrate, respectively, after an event at depth x. Δ_{foil} is the energy lost by the recoil particle traversing the filter foil used to absorb reflected beam particles.

Since ΔE_0 and ΔE_r increase with depth and $\Delta E_0 = \Delta E_r = 0$ at the surface, the depth from which the

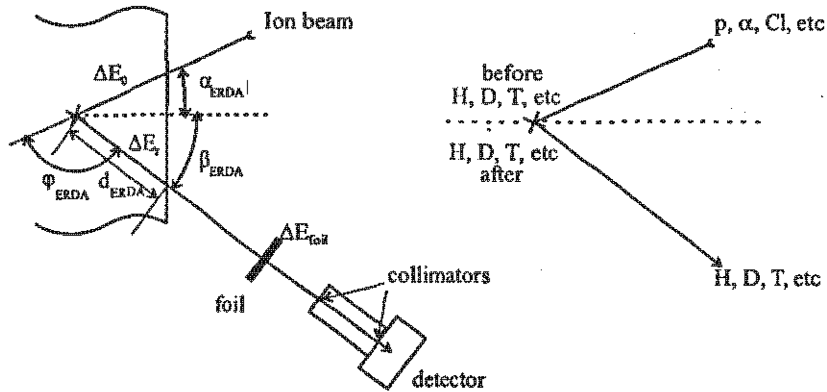

Figure 7.3: The ERDA experimental setup. On the left the reaction angles, particles and depths are defined. On the right various incident and detected recoil particles are indicated.

recoil particle originated can be established by iteratively solving $E_r = K_2 E_0 - K_2 \int \frac{dE_0}{dx} dx - \int \frac{dE_r}{dx} dx - \Delta E_{\text{foil}}$ to get the energy as a function of depth. The integrals determine the energy loss from the stopping function (equation 7-3).

The yield-energy distribution is determined by summing the yields as determined by equation 7-13 for the energy of the beam particle at the interaction energy (depth), and added to the energy bin as determined for the recoil particle when it is finally detected. In its simplest case, using ^{4}He, ERDA can only measure elements lighter than the beam particle, which is sufficient to measure implanted hydrogen profiles of Chapter 10. High energy ERDA can be used to measure elements heavier than the beam particle, though [Rij93a].

7.1.4 Rutherford Backscattering Spectrometry

The RBS analytical technique allows one to determine concentration depth profiles of elements heavier than the beam projectile. The most common projectile for RBS is helium, although protons are often used in the nuclear microprobe (figure 7.4).

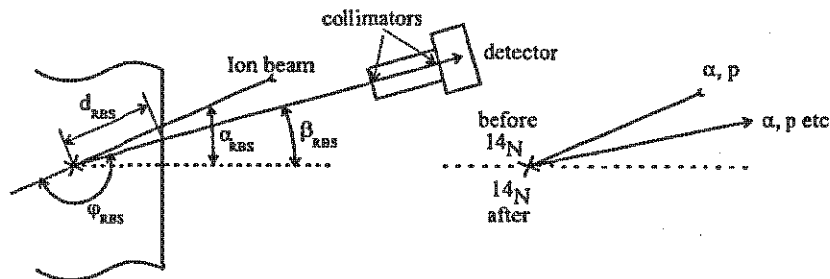

Figure 7.4: The RBS experimental setup. On the left the reaction angles, particles and depths are defined. On the right various incident and detected recoil particles are indicated.

RBS analysis was performed mainly to complement the other techniques to verify deposited charge,

University of Cape Town

etc, during analysis. This is because typically RBS has been of limited direct use to PSII investigations: for hydrogen implantation, RBS measurements do not detect hydrogen, while in the tribological measurements, the nitrogen peak is superimposed on top of the iron peak, which complicates analysis

Analysis of RBS spectra is performed in a similar method to the ERDA analysis described above. The energy of each detected particle is again determined in a similar manner as with ERDA above, but now the energy of the detected scattered RBS particle is given by

$$E_s = K_1(E_0 - \Delta E_0) - \Delta E_s \quad (7\text{-}16)$$

where ΔE_0 and ΔE_s are the energies lost by the projectile while penetrating into the sample and then leaving the sample after being scattered by a target particle, respectively.

The yield and depth information is calculated in the same manner for ERDA above, and must be performed for each element present in the target.

7.1.4.1 Channelling

When performing RBS on crystalline samples, e.g. silicon, it is possible to have a situation when the projectile enters the crystal along one of the major crystal axes within limits of the channelling critical angle. In this situation (figure 7.5), the bulk atoms in the substrate are masked by the surface atoms,

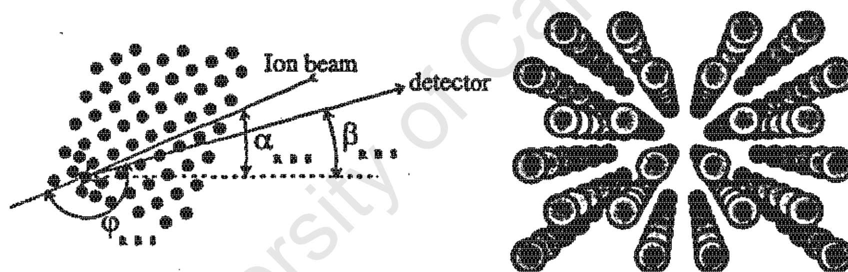

Figure 7.5: The RBS channelling measurement. When a crystalline target is oriented at certain angles to the incident beam, the surface atoms mask the bulk atoms of the crystal structure. Fewer collisions thus occur with bulk atoms resulting in reduced RBS yields. The beam particle's view is shown on the right.

University of Cape Town

which reduces the collision cross-section, and results in significantly lower RBS yields. The yield is therefore an indication of the 'perfectness' of the crystal allowing one to experimentally determine where damage occurs in crystalline materials. Thus, if the target consists of multiple layers and can be oriented in such a manner as to favour channelling in only one of the layers, or if a target layer has a damaged crystal structure, the change in yield as the layers are traversed can be experimentally measured. RBS channelling experiments can be performed to examine the damage (§10.5.5) caused by PSII implantation in silicon implanted for doping or cleaving (§10.1.2) experiments.

Example of RBS Application - Using channeling to examine lattice damage

The reduced RBS yield due to channelling in crystalline areas can be used to determine where non-crystalline areas exist within a crystalline lattice. Thus in areas where the lattice has been damaged or

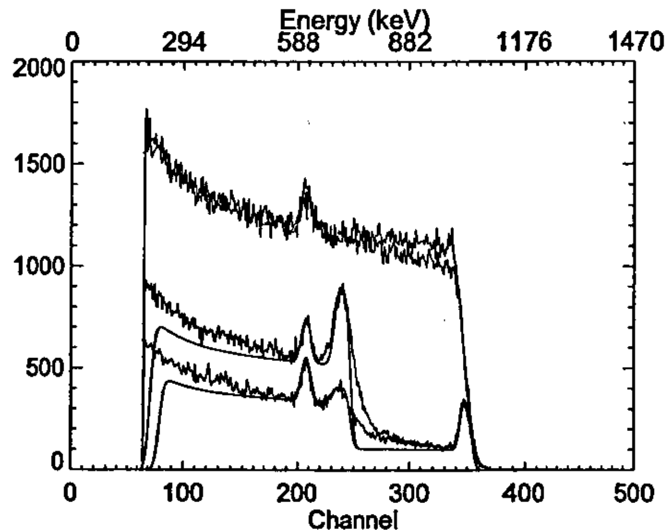

Figure 7.6: RBS spectra of two silicon samples implanted with a high and low hydrogen dose. All four spectra show the oxygen (channel 210) at the surface (where there is a thin SiO_2 layer). In the top two spectra, the samples are randomly aligned. The lower two spectra show RBS channelling of the same samples: low dose (bottom) and high dose (middle). In the channelling spectra, the damage peak is visible at about channel 240, while the surface amorphous SiO_2 can be seen at channels 350 (Si) and 210 (O). The greater yield behind the damage peak of the high dose sample (channels 60 through 250) is due to increased path-altering collisions.

University of Cape Town

otherwise disturbed (for example, in the region where the implanted hydrogen is deposited in hydrogen implanted silicon), the damaged region has a higher yield than the rest of the lattice in a channelling orientation.

Figure 7.6, shows four superimposed RBS spectra of two hydrogen implanted silicon samples, with a thin (400×10^{15} atomic layers, approximately 80 nm) layer of SiO_2 at the surface. The samples have been implanted with a high (8×10^{16} H.cm^{-2}) and low (1×10^{16} H.cm^{-2}) dose of hydrogen.

The top RBS spectra show the spectra measured when the samples are randomly aligned. The middle and bottom spectra respectively, show RBS channelling of the high implant dose and low dose samples. In the top spectra, the oxygen of the SiO_2 is visible as a small peak at about channel 210, but there is little other evidence of the existance of an amorphous surface layer. In both of the channelling spectra, the greater yield of the silicon and the oxygen of the surface amorphous SiO_2 becomes visible. Also, in both spectra the damaged lattice becomes visible at about channel 240. The damaged lattice has a higher yield since both the displaced silicon atoms and the implanted hydrogen deflect beam particles out of the lattice channels, raising the collision cross-section. Both spectra return similar yields in the region between the surface oxide and the damaged area, however, in the middle spectrum, the increased yield caused by the increased damage in the high dose implanted sample is easily distinguished from the low dose implanted sample. The remainder of the middle spectrum has a higher yield than the low dose sample since more ions were deflected in the high dose damaged region than the low dose damaged region. Once an ion has been deflected from the optimal channeling path, it is more likely to experience

a collision within the lattice than an ion still being channelled.

The damaged region occurs at a depth of about 3000×10^{15} atomic layers (approximately 0.6 μm) which is the approximate depth achieved by hydrogen implanted at 60 kV.

Thus it can be seen how not only does channelling make the surface oxygen more visible, but that additional information about perturbations to lattice structure can also be examined.

7.1.5 Nuclear Reaction Analysis

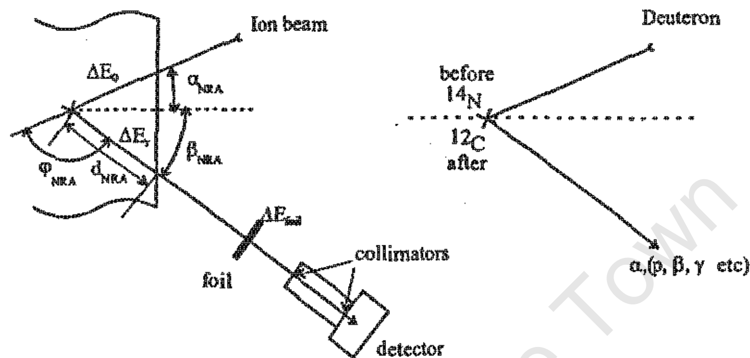

Figure 7.7: The NRA experimental setup. On the left the experiment angles and depths are defined. On the right an example incident and detected emission particle is indicated.

University of Cape Town

The NRA technique was used to establish nitrogen depth profiles since neither ERDA nor RBS could be used. By using a deuterium beam of about 1 MeV, various nuclear reactions can be induced in the target. By knowing the nuclear cross-section and the energy loss of the projectile and products in the target, concentration depth profiles of multiple elements can be determined simultaneously.

In NRA (figure 7.7), one measures the energies of emission particles and, like RBS, simultaneously records the spectra due to many different target elements. However, unlike RBS, not only are there multiple spectra due to different elements, but each element can have multiple reactions with the beam particle, for example, using a deuterium beam to analyse a sample containing nitrogen, yields 7 measureable reactions: two alpha particle emitting reactions, $^{14}N(D,\alpha_0)^{12}C$ and $^{14}N(D,\alpha_1)^{12}C$ and 5 proton emitting reactions, $^{14}N(D,p_0)^{15}N$, $^{14}N(D,p_{1,2})^{15}N$, $^{14}N(D,p_3)^{15}N$, $^{14}N(D,p_{4,5})^{15}N$ and $^{14}N(D,p_5)^{15}N$. Each reaction has it's own cross-section and energy with which the emission particle is emitted[1].

For any single reaction, though, the measured spectrum is a function of energy, and the concentration can be determined as a function of depth from

$$E_r = E_3 - \Delta E_3 - \Delta E_{\text{foil}} \tag{7-17}$$

where E_3, given by equation 7-9, is the energy of the light reaction product, and also depends on the energy of the incident projectile ion (and hence has a depth dependent energy). ΔE_3 and ΔE_{foil} are the energies lost by the emission particle as it leaves the substrate, and traverses the absorber foil, respectively.

[1]Notation: A(a,b)A′ where A is the target nucleus, a is the incident/beam particle, b is the emitted particle and A′ is the product nucleus.

NRA cross-sections typically have resonances, that is, energy regimes with much greater cross-sections than other energies. These resonances can be used to improve the detection resolution of target elements by sweeping the initial beam energy. The multiple spectra measured with incremental beam energies can be used to measure the depth profile of a specific element with greater sensitivity to low concentrations by using these resonances in a manner unachievable by RBS and ERDA techniques.

Example of NRA Application: Nitrogen dose and depth confirmation

As an example of NRA, samples implanted at the Forschungszentrum Rossendorf were analysed to determine their nitrogen dose and depth distribution. The recorded spectra (figures 7.8 and 7.9) show the NRA spectra used to examine the implanted nitrogen. A 900 keV deuterium beam was used to acquire these measurements. NRA spectra of an unimplanted (solid) and a high temperature (dashed) implanted

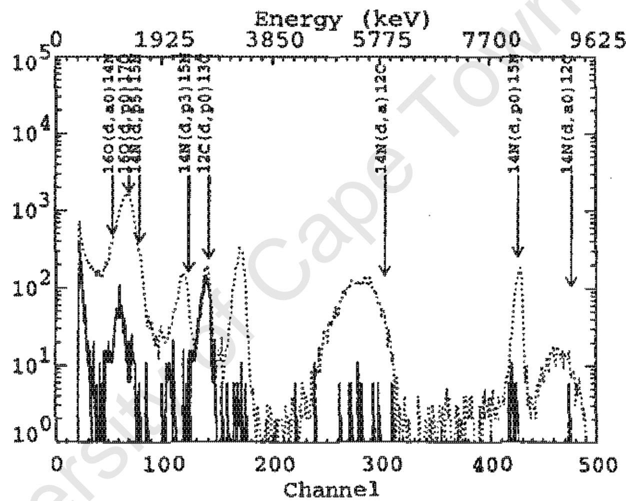

University of Cape Town

Figure 7.8: NRA spectra of an unimplanted sample (solid), and a sample implanted at high temperature (dashed). The various reactions used for fitting the simulation are indicated. The thickness of the high temperature implanted sample (dashed) could not be determined with this beam energy. Detector at 150°.

sample are shown in figure 7.8. A dose of 4×10^{17} ions cm^{-2} was predicted, based on calculations at implantation. Carbon and oxygen are visible in both spectra, while significant levels of nitrogen are only detected in the implanted sample. The sample temperature was not regulated and so a combination of thermal diffusion and ballistic processes resulted in nitrogen penetrating to great depths.

Both spectra of figure 7.9 show the recorded spectra for samples implanted with a calculated dose of 4×10^{17} ions cm^{-2}. The NRA spectrum from the high temperature implanted sample is shown again (dashed). For the solid line spectrum, the sample temperature was kept below 200°C (by reducing the implantation pulse frequency), and thus the implantation was dominated by ballistic processes. This is evident from the different widths of the nitrogen reaction peaks.

SIMNRA simulation results indicate that the 'shallow' nitrided layer of figure 7.9 has a thickness of about 5500×10^{15} At/cm^2 (layers). By approximating the alloy density by the density of iron (0.1179 nm

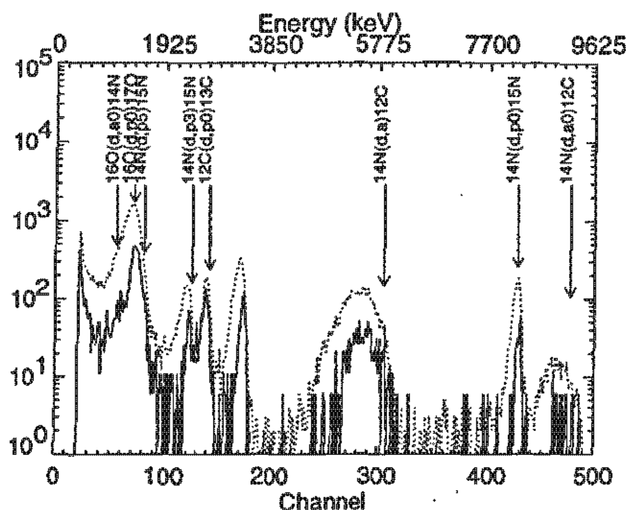

Figure 7.9: NRA spectra of samples implanted at low (solid) and high (dashed) temperatures. The various reactions used for fitting the simulation are indicated. A thicknes of 0.6 μm was determined for the low temperature implanted sample (solid) using the peak of the 14N(d,α)12C reaction. Detector at 150°.

per layer), a thickness of about 0.46 μm is calculated. The full thickness of the thicker layer (dashed) can not be established from this spectrum, since the layer is thick enough to prevent reaction particles from being detected (increasing the width of the simulated layer had no effect on the simulating spectrum: the layer was thicker than the analysable depth of the ion beam). A higher beam energy would be required to analyse deeper into the sample.

These samples were also depth profiled using AES at the Forschungszentrum Rossendorf (figures 7.20 and 7.21). The AES results show that for the low temperature implanted sample, the nitrogen reached a depth of about 0.15 μm, which is thinner than the 0.6 μm result determined by NRA.

Even taking peak broadening due to detector resolution, geometric and energy straggling into account, this difference can not be accounted for. A detailed set of calibration experiments would be required to eliminate the effects of dose variation within the sample (non-homogenous implantated dose due to sheath non-conformality) and surface roughness, two other major sources error in depth calculations.

7.2 Nuclear analytical apparatus

There are two commonly used nuclear analysis chambers at the Materials Research Group: the RBS chamber and the nuclear microprobe chamber. The analysing beams are provided by a 6 MV, single-ended vertical Van de Graaff accelerator.

7.2.1 The nuclear microprobe chamber at the Materials Research Group

The primary advantage of the nuclear microprobe over conventional analysis methods is the size of the analysing beam spot, which is of the order of tens of micron compared to that in the RBS chamber where the beam spot diameter is of the order of a millimetre. The small beam size allows one to analyse smaller

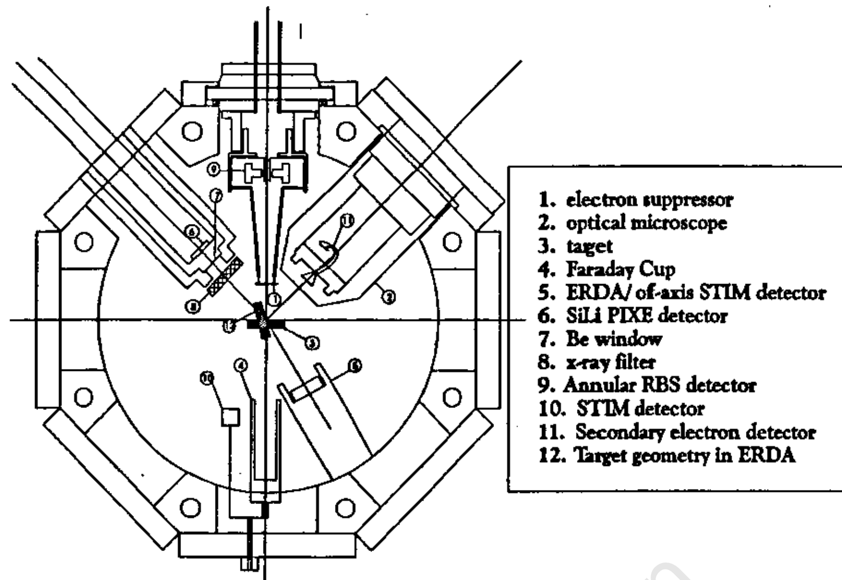

Figure 7.10: The layout of the microprobe chamber showing the positions of the various detectors and filters. Due to space restrictions the PIXE detector and filter have to be removed before ERDA measurements can be made.

University of Cape Town

areas as well as to obtain a better spatial resolution since the effects of beam smearing are smaller. The microbeam can also be scanned over an area of the sample, which allows for lateral elemental distributions to be determined.

The layout of the microprobe chamber is shown in figure 7.10. The detectors in the chamber allow it to be configured for PIXE, NRA, RBS, ERDA and STIM (scanning tunnelling ion microscopy). However, due to physical limitations, ERDA cannot be performed simultaneously with PIXE (the PIXE detector and filter have to be removed during ERDA measurements).

RBS and NRA measurements in the microprobe chamber use the annular surface barrier detector mounted at 176°, while the surface barrier detector mounted at 30° with respect to the incident beam is used for ERDA and off-axis STIM measurements.

7.2.2 The RBS chamber at the Materials Research Group

The layout of the RBS chamber is given in figure 7.11. In the RBS chamber, the RBS surface barrier detector is typically mounted at a scattering angle of 165°. In the ERDA configuration, the sample is rotated 75° (about the vertical axis) and the ERDA detector is mounted at a scattering angle of 30°.

A 13 μm aluminium foil is placed in front of the detector to absorb any forward scattered alpha particles. Unfortunately, the foil also causes an energy loss in the recoiled particles and a straggling broadening in the recoil energy spectrum. These parameters are all energy dependent, but can be read off the graph shown in figure 7.12. NRA measurements performed in the RBS chamber used two detectors fitted at scattering angles of 165° and 150°. Due to space constraints the detectors were fitted on either side of the beam line, and the sample was not rotated.

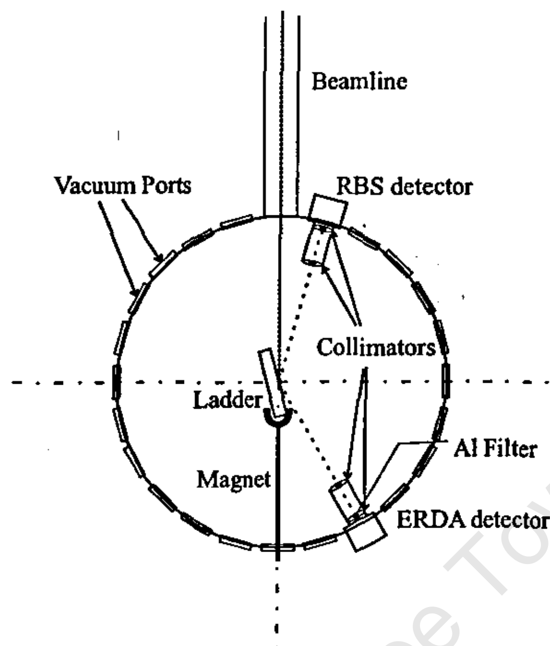

Figure 7.11: Layout of the RBS chamber with typical positions of the RBS and ERDA detectors shown. The detectors can be fitted in place of any of the indicated vacuum ports, which are fitted at 15° intervals.

University of Cape Town

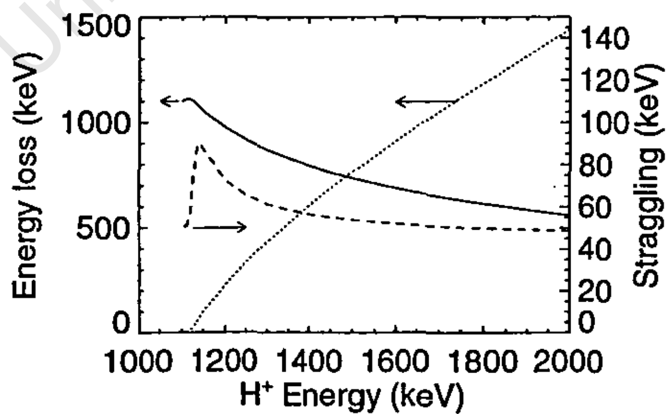

Figure 7.12: Energy loss (solid) and straggling (dashed) for a proton traversing a 13 μm Al foil as a function of incident energy. The transmitted ion energy is also shown (dotted).

7.3 X-ray diffraction

7.3.1 Introduction

X-ray scattering from an electron

X-rays are scattered from atoms in a material in a similar manner in which dust particles in air scatter light: an incident x-ray transfers its energy to an electron, causing it to oscillate at a frequency determined by the energy transferred. Since an oscillating electron is accelerating, and an accelerated charge particle emits radiation, shortly after absorbing the x-ray energy the electron re-radiates another x-ray. The emitted x-ray is called a scattered x-ray, and is emitted with a constant phase difference from the incident x-ray ($\frac{\lambda}{2}$). While it is coherent with the incident x-ray, it is emitted in a random direction.

J.J. Thompson, however, found that the intensity of the beam (which is related to the x-ray flux) is given by

$$I = I_0 \frac{K}{r^2} \sin^2 \alpha \tag{7-18}$$

where K is a constant, r the distance from the x-ray source to the detector, and α the angle between the scattering direction and the direction of the acceleration of the electron. The intensity of any x-ray beam scattered through a scattering angle 2θ can be expressed as the sum of two perpendicular E-field components

$$I_{Py} = I_{0y} \frac{K}{r^2}, I_{Pz} = I_{Oz} \frac{K}{r^2} \cos^2 2\theta \tag{7-19}$$

and since $I_{0y} = I_{0z} = \frac{1}{2} I_0$, the sum $I_{Py} + I_{Pz}$ gives the Thomson equation

$$I = I_0 \frac{K}{r^2} \left(\frac{1 + \cos^2 2\theta}{2} \right) \tag{7-20}$$

University of Cape Town

Compton scattering

X-rays can also have glancing collisions with electrons, in which case they are deflected from their original path in an elastic collision. The resultant x-ray has an energy lower than the incident x-ray, but with no fixed phase relation (incoherent scattering).

Scattering by an atom

Since all atoms have a number of electrons equal to the atomic number Z, atoms heavier than hydrogen have multiple electrons contributing to the final intensity. In the forward direction ($2\theta = 0$), the intensities of each electron can be added directly since all the waves are in phase. For other directions, the fact that the electrons are distributed in space around the nucleus (figure 7.13) means that the path difference between atomic electrons (CB-AD) causes phase shifts with partial interference. Thus a quantity f, called the scattering factor, scattering efficiency or form factor, defined by

$$f = \frac{\text{amplitude of wave scatterd by atom}}{\text{amplitude of wave scattered by one electron}} \tag{7-21}$$

must be experimentally determined. In the forward direction, $f = Z$, in other directions it is also a function of 2θ. Values of f have been tabulated by Peiser, Rooksby and Wilson [Pei55a].

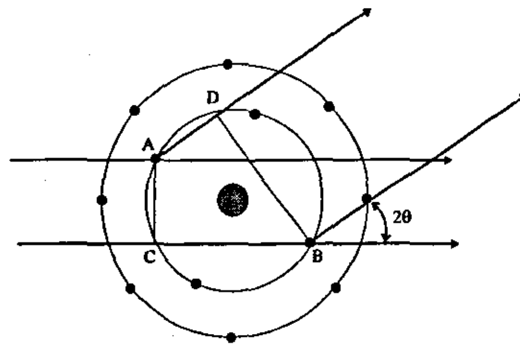

Figure 7.13: The x-ray intensity from all electrons of an atom is affected by phase differences due to the different path lengths (CB-AD).

7.3.2 Scattering from planes in a solid - X-ray diffraction

When x-rays are incident on a crystal, some are reflected from atoms at the surface while others penetrate into the crystal lattice. Reflections from within the lattice only occur under conditions of constructive interference, which occur at those angles at which the path difference between successive planes is an integral multiple of wavelengths. As can be seen in figure 7.14, this occurs at angles such that

$$2d\sin\theta = m\lambda \tag{7-22}$$

Equation 7-22 is called Bragg's Law and states the condition under which constructive interference

University of Cape Town

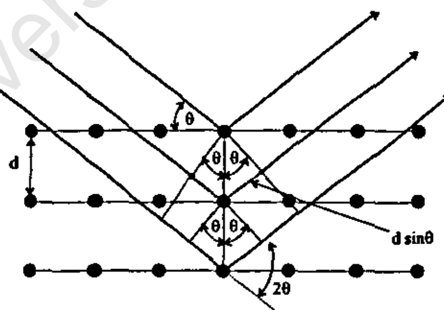

Figure 7.14: The Bragg Law. Diffraction as a result of scattering from multiple parallel planes, with plane spacing d. Constructive interference occurs only at angles θ such that the path difference ($2d\sin\theta$) is an integral multiple of wavelengths ($m\lambda$).

(diffraction) will occur. The factor m is called the 'order of reflection' and states that for a given wavelength (λ) and lattice spacing (d), diffraction peaks will occur at angles θ_1, θ_2,... etc, such that $\theta_m = \arcsin\left(\frac{m\lambda}{2d}\right)$ is valid. For a wavelength only slightly smaller than $2d$, only one such angle exists, and the scattering is almost glancing, while for a wavelength much smaller that the lattice spacing, many solutions exist. Thus the choice of wavelength affects the number of peaks measured, and is determined

by the scale of the lattice spacing investigated.

In addition, since there are many planes with different orientations within a crystal lattice (figure 7.15), many diffracting planes exist, each with a different spacing, and so again, many diffraction peaks are possible. The existance of databases of spacings of materials facilitate analysis.

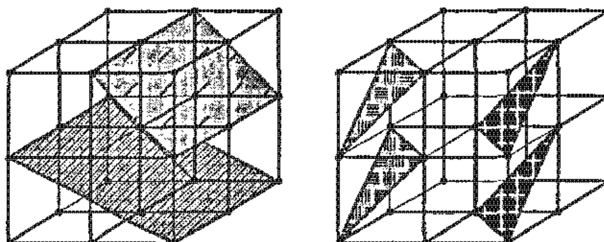

Figure 7.15: Within a crystal structure there are many crystal planes with different orientations which satisfy Bragg's Law.

University of Cape Town

7.3.3 Applications of XRD

There are many XRD techniques used to determine crystalline structures, such as:

- The Laue method, which uses a continuous spectrum (§8.3.1) x-ray beam projected through a crystal. Since θ_i is fixed, peaks occur due to the ranges of x-ray wavelengths which satisfy the Bragg Law.
- The rotating crystal method, which uses a monochromatic x-ray beam projected through a rotating crystal. The crystal is mounted with one axis in the plane of the beam, and rotated at a normal to the plane of the beam. In this method other planes will momentarily satisfy the Bragg Law for some angle of rotation, diffracting x-rays into the three-dimensional volume around the crystal.
- The powder method, which uses a monochromatic x-ray beam projected into the target material which has been pulverised into powder form. Since, amongst all the powdered crystals, the Bragg condition will be met for all crystal planes, all possible planes will be reflected in any given source-target-detector plane.

7.3.4 Metallurgical applications

The XRD techniques are of specific interest to metallurgical analysis since each metallurgical phase has it's own unique composition of crystal structures. Since each crystal contributes to a particular x-ray diffraction peak, the relative peak intensities can be used to determine the composition. Thus metallurgical phases can be determined.

In addition, since the crystal structure and phases of compounds are determined by the crystal composition, it becomes possible to detect the presence of compounds, *as they exist in the material*, in contrast to, for example, nuclear techniques which give the elemental concentrations, but with no information on how they are chemically bonded to form compounds (a sample containing nitrides will show the presence

of nitrogen, but with no indication of how much of it is bound in a nitride, and how much is in solution).

7.3.5 XRD Equipment at the Materials Research Group

The Materials Research Group XRD laboratory has two XRD devices, a Bruker D8 Advance multipurpose device and Bruker D8 Discover high resolution device, with Goebel mirrors, soller slits and 4-bounce monochromator. Both devices are presently fitted with copper x-ray source tubes. Both XRD machines analyse samples by measuring the x-rays reflected in the source-target-detector plane (figure 7.16). The source and detectors can be independently scanned through angles θ_i and θ_s with the

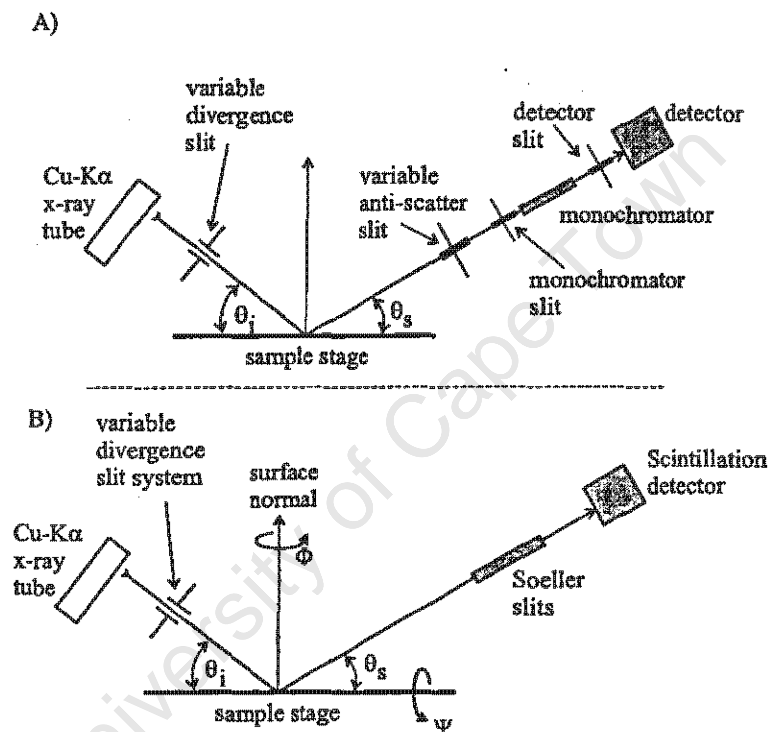

Figure 7.16: The experimental configuration of (A) the multipurpose Bruker D8 Advance, and (B) the Bruker D8 Discover XRD machines at the Materials Research Group.

University of Cape Town

target, respectively. In the conventional $\theta - 2\theta$ technique, the detector is set to the 2θ scattering angle for a particular source position. The multipurpose Bruker D8 advanced can rotate the sample during analysis and the high resolution Bruker D8 Discover also allows one to rotate the sample about the OX plane (figure 7.16). The XRD techniques can be used by users of this facility to verify the formation of desired metallurgical phases in the sample. These phases are created when new compounds are formed in the target during implantation and have a characteristic crystal structure. This structure produces peaks in the XRD $\theta - 2\theta$ graph according to Bragg's Law.

Figures 7.17 and 7.18 show the superposition of two XRD spectra obtained from the analysis of implanted (solid) and unimplanted (dashed) steel. Figure 7.17 shows the spectrum in the 2θ range of 35 to 55 degrees, and the <111> and <200> austenite peaks are visible at 43.7° and 50.7°, respectively. While the implantation of nitrogen does cause a change in the lattice parameters [Man00a], the broadening

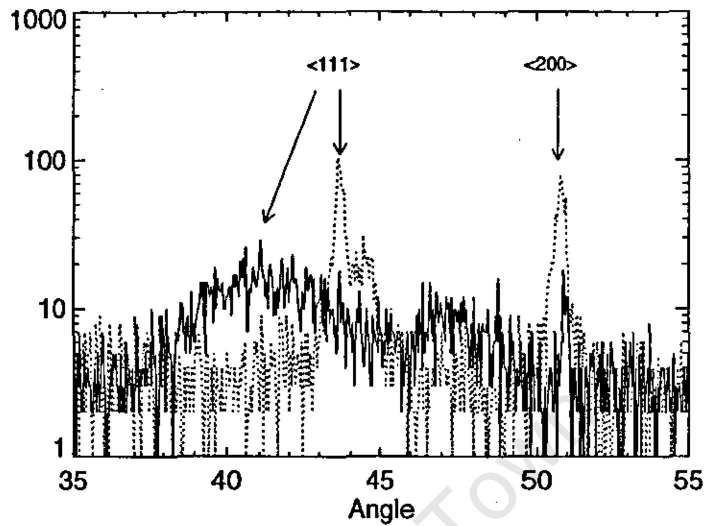

Figure 7.17: 35 to 55° $\theta - 2\theta$ XRD spectrum of implanted (solid) and unimplanted (dotted) stainless steel. Austenitic phase peaks are indicated. The broadening and shift of the <111> peak is probably caused by the implantation of nitrogen forming an amorphous layer, with different lattice parameters.

University of Cape Town

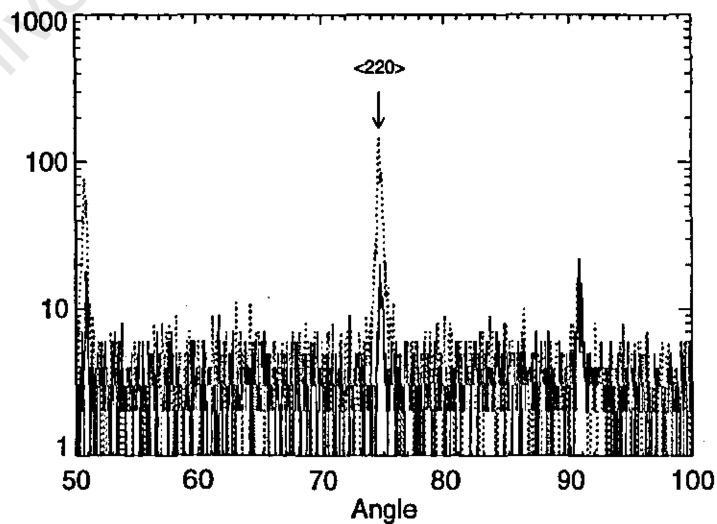

Figure 7.18: 50 to 100° $\theta - 2\theta$ XRD spectrum of implanted (solid) and unimplanted (dotted) stainless steel. Austenitic phase peaks are indicated.

of the <111> peak is probably due to a surface amorphous layer. Since the broadening is not visible in the other peaks (<220>, etc.), the amorphous layer seems to be very thin (less than 0.8 μm). Table 7.1

Reflection	A_{hkl}	Angle
111	0.333	43.7°
200	0.000	50.7°
220	0.250	74.7°
311	0.157	
222	0.333	
400	0.000	
331	0.274	
420	0.160	

Table 7.1: XRD reflection peak angles for DIN 1.4571 stainless steel with Cu x-ray tube. The 2θ angles for the dominant reflections have been given.

shows the reflection peak angles for the austenite phase of stainless steel DIN 1.4571 (or AISI 316Ti).

7.3.6 Microhardness measurements

Microhardness measurements are made by impressing an indentor against the surface of the material under investigation. By recording the indentation depth as a function of the applied force, it is possible to calculate certain material properties, such as the Young's modulus. By measuring the area of the indentation, the microhardness can be established.

Microindentors are different from macro-indentors, such as the Rockwell tests, which use large (millimeter sized) indentors, large loads (60 kg for Rockwell A, 100 kg for Rockwell B, and 150 kg for Rockwell C) and penetrate to depths of the order of millimeters into the sample.

Micro-indentors use small (10 μm) indentors, light loads (5 to 3600 grams) and typically only penetrates up to a few micron into the surface, and thus are suitable for use on thin films.

The Vickers indenter has become an important tool for the investigation of surface tribological properties. By measuring the size of the indentation made by an indentor of known shape under a known load, the Vickers hardness has been defined by the following equation:

$$H = \frac{F_{\max}}{A} \tag{7-23}$$

where $F_{\max}$ is the maximum force applied to the indentor, and A the indentation area, calculated by measuring the diagonal length of the indentation.

The geometry of the elasto-plastic penetration of a conical or Vickers indenter is shown in figure 7.19. Under the action of the loading force, F, the indenter penetrates a maximum depth h into the sample which can be subdivided into a contact depth (h_c) below the area of contact (A_c) between the indenter and the material, and the depth of the surface deformation (h_s) above the area of contact. When the load is removed, the surface deflection returns to the level of the material surface, and the inner surfaces of the indentation recover with a change in shape so that a final depth (h_f) is achieved. If the depth is

University of Cape Town

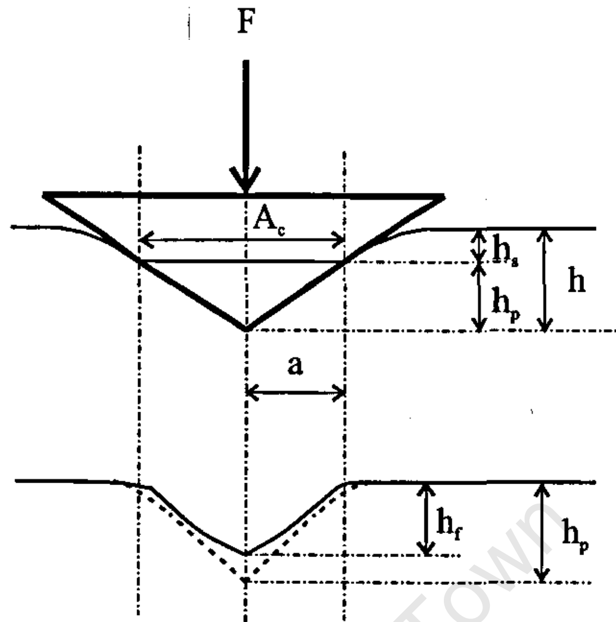

Figure 7.19: The geometry of the Vickers indenter under load (top) and after unloading (bottom). The area of contact A_c and applied force F are used to calculate hardness.

University of Cape Town

calculated using the geometry of the indenter, h_p is obtained, and defined to be the plastic depth. It is assumed that no elastic recovery occurs in the surface plane.

7.3.7 Dynamic depth hardness measurements

Instruments have been developed that can continuously measure the loading force and indentation depth at high resolution. A theory to calculate hardness values and Young's modulus from the unloading data of the load-depth measurements was developed by Loubert *et al* [Lou84a] and Doerner & Nix [Doe86a], and later improved upon by Oliver and Pharr [Oli92a].

It has been shown that the contact stiffness (S) is related to the contact area (A_c) by [Oli92a, Hen95a]

$$S = \beta \frac{2}{\sqrt{\pi}} E_r \sqrt{A_c} \tag{7-24}$$

where β is a shape correction factor to the indenter given by Hendrix [Hen95a], see table 7.2 and E_r is the reduced elastic modulus given by

$$\frac{1}{E_r} = \frac{1-\nu_i^2}{E_i} + \frac{1-\nu_s^2}{E_s} \tag{7-25}$$

where the subscripts i and s denote the indenter and substrate respectively, E is the Young's modulus and ν the Poisson ratio.

The contact depth (h_c) is determined from the experimental data by noting that

$$h_c = h_{\max} - h_s \tag{7-26}$$

Indenter	Shape	Correction, β
Axisymmetric	Circle	1.000
Vickers	Square	1.0055
Knoop	Rhombus	2.682
Berkovich	Equilateral triangle	1.0226

Table 7.2: Shape correction factors

and that h_s is given by

$$h_s = \varepsilon \frac{F_{\max}}{S} \tag{7-27}$$

where S is the stiffness, since Sneddon's force displacement relationship for a conical indenter gives

$$(h - h_f) = 2\frac{F}{S} \tag{7-28}$$

The geometric constant ε is 0.72 for a conical indenter and 0.75 for a paraboloid.

A corrected hardness comparable to the Vickers hardness has been given by Chudoba [Chu95a] as

$$H = \frac{F_{\max}}{K(h - \varepsilon\frac{F_{\max}}{S})^2} \tag{7-29}$$

where K is a constant factor determined by the shape of the indenter. $K = 1/\tan^2\alpha$ for a square pyramid, i.e. Vickers, with α as defined in figure 7.19. For best results, K should be determined experimentally as a function of depth.

7.3.8 Microhardness Equipment

Two indenters were used during the development of this facility, a nano-indenter at the Forschungszentrum Rossendorf capable of automatically measuring the depth as a function of the applied force and hence can be used to calculate the Young's modulus as well as the hardness and thickness of the hardened layer. The second, simpler micro-indenter is a Matsuzawa MXT-α7 microhardness tester with a Vickers indenter. This device simply makes a single indentation with a pre-selected force, ranging from 1 gram force to 200 gram force. The user must then measure the diagonal lengths of the indentation, which is entered into the device and used to calculate the surface hardness. A sample of known hardness is used to calibrate the measurements.

7.3.9 Auger electron spectroscopy - AES

AES is a technique which typically uses an electron beam to stimulate the emission of Auger electrons from the target. Since these electrons are emitted with an energy characteristic of the element and its chemical state from which they are emitted, AES is a powerful tool for determining composition. However, since the electrons are only emitted from outer shells with low energy, the AES technique can only analyse the target surface. In order to perform depth profiling, some method of removing surface layers has to be used. The typical method uses a tightly focussed argon ion beam to sputter erode layers

University of Cape Town

of the surface, with AES performed between successive sputterings to establish a depth profile. Due to the statistical nature of the sputtering process, it is difficult to predict the depth of the sputtered crater and hence the depth of the analysed region. Thus one must measure the depth profile of the sputter crater after analysis to establish the maximum depth analysed. By assuming a constant sputtering rate, one can then convert the time scale into a depth scale. One must also be aware of the potential problems associated with preferential sputtering of the different species of the target material. This is a destructive analytical technique.

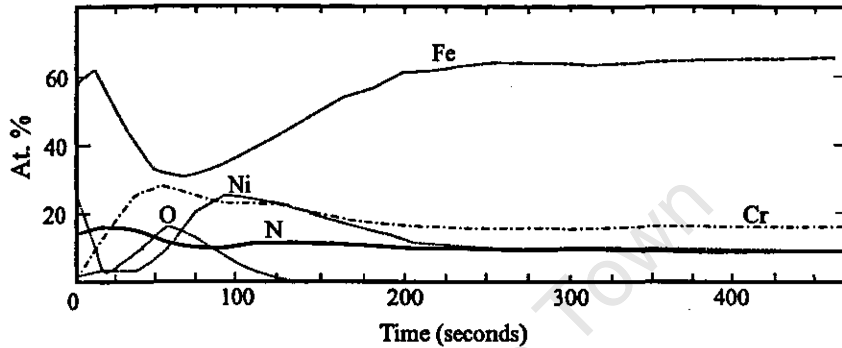

Figure 7.20: AES-derived composition of a high temperature (> 270°C) implanted sample, with relatively fewer sputter cycles to give only a shallow sputter depth. The dual peaks corresponding to implantation of N^{++} and N_2^+ are visible at 25 and 125 seconds, respectively.

University of Cape Town

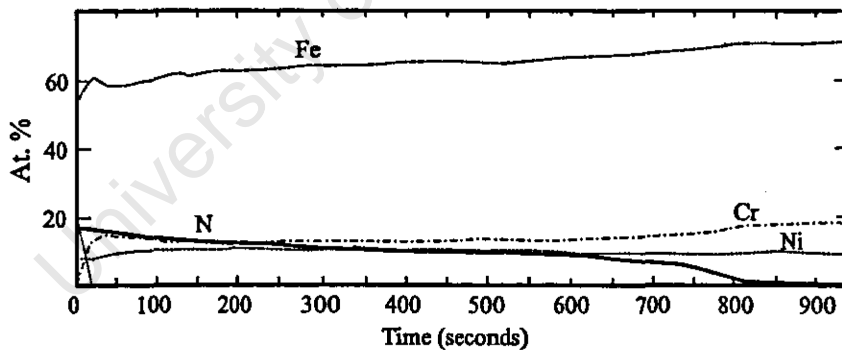

Figure 7.21: AES-derived composition of a low temperature (< 270°C) implanted sample, with more sputter cycles to analyse to a greater depth. The greater depth of the sputter crater reveals that nitrogen was implanted to a depth of about 0.15 μm.

Figures 7.20 and 7.21 show the AES depth profiles of high and low temperature implanted samples, respectively. Figure 7.20 shows the near-surface composition. The dual peaks visible in the nitrogen depth profile is caused by the implantation of the two nitrogen ion species (N^{++} and N_2^+) present in the plasma, which are implanted to different depths based on their masses. AES analysis of other samples implanted under similar conditions reveal the presence of nitrogen to depths of about 13 μm. Thermal diffusion processes assist the implanted nitrogen to reach these depths. In figure 7.21 the high concentration presence of nitrogen even after 750 seconds of analysis is determined with post-AES analysis of the sputter crater to correspond to depths of about 0.15 μm.

The AES-derived depth profiles of figures 7.20 and 7.21 also show the changes in chemical composition that occurred in the two samples. In figure 7.20, the high temperature implanted sample, the decrease in iron correlates with characteristically increased chrome and nickel concentrations. This sample also shows a well-defined oxygen peak. In figure 7.21, the low temperature implanted sample, there is much less variation in composition, indicating a lower perturbation to the alloy composition.

7.3.10 Other techniques

Depending on the requirements, there are other techniques such as glow discharge optical spectroscopy (GDOS), atomic force microscopy (AFM), scanning electron microscopy (SEM), etc, which may be of interest for determining target composition, topography, etc.

7.4 Summary

Several analytical techniques available to users of this facility have been introduced. These range from nuclear (techniques that interact with the nuclei of the analysed material), x-ray and mechanical. The nuclear techniques are generally used at the Materials Research Group to determine target elemental composition, the x-ray techniques are used to determine target state (metallurgic phase) and the mechanical techniques are used to determine tribological properties.

All except the last of these techniques are available at the Materials Research Group. For the microhardness techniques, the apparatus is available at local universities.

These techniques are used to analyse and quantify attributes of the implantation process.

RBS channelling was used to examine lattice damage and to reveal amorphous structures within a lattice. NRA and AES techniques were used to determine depth profiles of implanted nitrogen, and the greater power of AES was demonstrated. It was also demonstrated how XRD techniques can be used to identify changes in metallurgical phase (crystalline) structure.

University of Cape Town

University of Cape Town

Chapter 8

X-ray analysis

8.1 Introduction

During the PSII implantation pulse, electrons are accelerated away from the target by its high negative potential. When an energetic electron strikes any metal surface, like the chamber walls, the kinetic energy has to be dissipated. Phonon production processes convert some of the kinetic energy directly to heat, while collisions and deflections due to near misses with ions result in either the emission of x-rays by bremsstrahlung or the excitation of the target ion. These excitations further result in the emission of characteristic x-rays.

The dominant process depends on the energy of the electron. At high energies (>10 keV), bremsstrahlung processes dominate, while at lower energies, outer shell excitations result in the emission of visible light.

Since the number of electrons emitted is related to the condition of the surface (§8.2.2), this also affects the x-ray flux.

Additionally, since the electrons are accelerated by the high voltage implantation pulse, the x-rays are also generated in short duration pulses. The pulsed nature of the x-ray flux greatly impairs the ability of standard radiation meters to accurately determine the equivalent dose and this poses a potential health hazard to users of the facility.

The experiments and measurements described in this chapter were performed to determine the nature of the x-ray flux.

Since the x-ray emissions are pulsed, it was decided to measure the time as well as the energy distribution of the x-ray spectra. These measurements can be used for a variety of applications, ranging from determining the x-ray shielding needed to protect users and operators of the PSII facility, to monitoring the target surface condition. The initial results of these studies were presented at PBII'98 [Pro99a], the 4th International Workshop on Plasma Based Ion Implantation at Dearborn, Michigan, USA held in June 1998 [PBII98].

University of Cape Town

8.2 Electron sources

There are two dominant processes which contribute to the electron flux away from the implantation target: those plasma electrons displaced from the sheath region (§A.1) by the target potential (§8.2.1), and those secondary emission electrons emitted from the target by implanted ions (§8.2.2).

The total electron flux, Γ_e, is given by the sum of the components:

$$\Gamma_e = \Gamma_{\text{disp}} + \Gamma_{\text{SEE}} + \Gamma_{\text{Auger}} + \ldots \tag{8-1}$$

where Γ_{disp} are the electrons displaced by the plasma sheath, Γ_{SEE} are secondary emitted electrons, and $\Gamma_{\text{Auger}} + \ldots$, electrons emitted by other, multiple interaction processes, such as Auger electrons.

The energy distribution of the emitted electrons is determined by which of the processes that produced it.

Additionally, since the electron current is also carried through the implantation power-supply, it severely restricts the ion current available for implantation and affects calculations of dose based on the measured implantation current.

The measured current can be described by

$$I_{\text{total}} = I_{\text{ion}} + I_{\text{electron}} \approx I_{\text{ion}} + \gamma I_{\text{ion}} \tag{8-2}$$

where γ is the secondary electron emission coefficient, and I_{ion} and I_{electron} are the implanted ion and secondary emitted electron currents, respectively. Assuming that γ remains constant during the pulse (since it depends most strongly on ion energy (equation 8-3) which is in turn proportional to the applied voltage pulse which is constant during the pulse), then the secondary electron current I_{electron} is $\left(\frac{\gamma}{1+\gamma}\right) I_{\text{total}}$.

8.2.1 Displaced plasma electrons

Due to the quasineutrality of the plasma, the ion and electron densities are effectively equal. Thus there are an equal number of ions as electrons within the sheath region, and the plasma electron flux away from the target will be equal to the ion flux toward the target. As can be seen in figure 8.1, electrons originating within the sheath region (§A.3), gain an energy dependent on the potential difference between their position within the sheath and the sheath edge.

8.2.2 Ion induced electron emission

Each implanted ion typically causes between one to over 20 electrons to be ejected from the target surface. Called secondary emitted electrons, to distinguish them from secondary plasma electrons, these electrons are accelerated away from the target and toward the chamber walls by the high target potential. The exact number of electrons emitted per ion (γ, the secondary electron emission co-efficient) can not be precisely determined due to the statisical nature of the process, but it does depend on the ion energy, the quality and the chemical composition of the surface.

Like ion induced sputtering (§2.5.3), ion induced electron emission is a statistical phenomenon affected

University of Cape Town

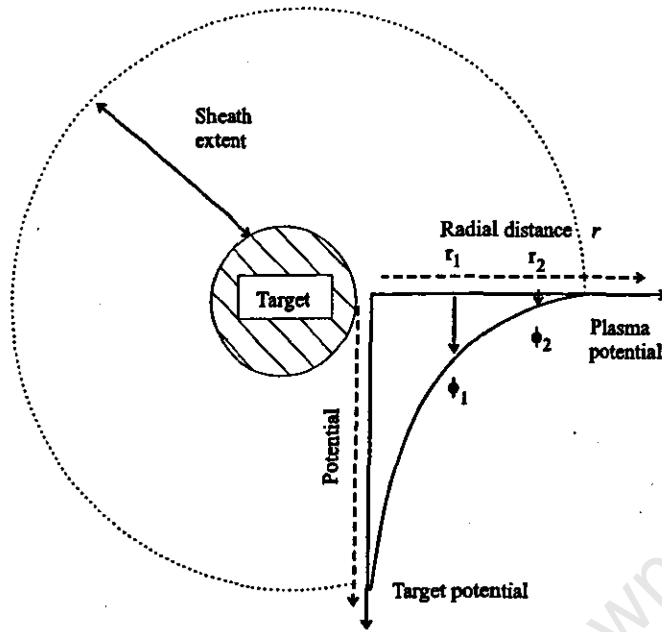

Figure 8.1: The energy given to an electron depends on it's initial position in the ion matrix sheath. The potential difference between the sheath edge and r_1 (ϕ_1) is greater than at r_2 (ϕ_2), thus electrons from closer to the target gain more energy than electrons closer to the sheath edge.

University of Cape Town

by many different processes. A detailed theoretical treatment of ion induced electron emission is given by Rául Baragiola [Bar93a], the salient points of which are:

- Since the process of electron emission depends on the projectile ion undergoing a collision with the electron shell of the target atom, the probability of an electron being emitted from an atom depends strongly on the electron stopping power (§7.1.1.1) of the interaction.
- Once electrons have been knocked off from target atoms, they have to be transported to the surface. Since electrons lose most of their energy in inelastic collisions, this process is dominated by the mean free path of inelastic collisions (which helps define an attenuation length from which electrons may reach the surface). Analysis has shown that electrons are typically emitted only by collisions within 5 to 15Å of the surface.
- Electrons reaching the surface only overcome the surface energy barrier if they have enough energy. This further limits the number of emitted electrons.

However complex the general theory of electron emission, Baragiola *et al* [Bar79a] have experimentally determined a fairly universal relationship between the electron yield (γ) and the electron stopping $\frac{dE}{dx}$ of

$$\gamma \approx B \left(\frac{dE}{dx}\right)_e / \cos(\alpha) \tag{8-3}$$

where $B = 0.10 \pm 0.03$ Å/ eV for clean metal targets implanted with 5 to 50 keV H^+. B is about 20% lower for heavier ions (helium through neon). α is the incident angle of ion impact with respect to the surface normal.

Equation 8-3 predicts electron yields of about 4 for 30 keV nitrogen implanted in iron, and 2 for

30 keV hydrogen implanted into silicon. These values need to be verified experimentally.

However, since the actual value of γ is also affected by target surface condition (presence of oxide surface layer, chemical composition, etc), it is always best determined experimentally on a per-target basis.

The ion-induced emitted electron flux Γ_{SEE} is related to the ion flux by

$$\Gamma_{SEE} = \gamma \cdot \Gamma_{ion} \tag{8-4}$$

In the time frame of the implantation pulse ($t > 1\ \mu s$) the secondary electron emission process dominates the electron flux, and hence needs to be understood.

The electrons ejected by ion bombardment typically have a very low energy compared to the target potential, but gain the full target potential as they are accelerated away from the target.

Thus during the first μs, electrons are repelled from the target with a wide energy distribution as the ion-matrix sheath forms, but later they are ejected with a narrow energy distribution (of the order of a few eV) and accelerated by the target potential, which (for a collisionless plasma) remains constant for the period it takes the electron to traverse the plasma sheath.

These monoenergetic electrons thus form the dominant component of the total electron energy distribution incident on the chamber walls (or any other structure in the plasma chamber) during an implantation pulse. Thus, in a first approximation, one can assume that the x-ray spectrum will be that of a monoenergetic electron beam incident on the metal of the chamber wall.

University of Cape Town

8.2.3 Measuring the secondary electron flux

The secondary electron flux is required in order to be able to establish the implantation ion current. Additionally, if the x-ray energy spectrum can not be measured directly, a quantitative determination of the secondary electron flux will assist in determining the expected x-ray emission flux, a factor affecting the safety of the users of the facility.

8.2.3.1 Retarding field energy analyser

A retarding field energy analyser allows one to measure the energy spectrum of a charged particle beam by recording the measured current as a function of the retarding electric field. Conventional retarding field energy analysers use grids biased against the particle being analysed, for example, as used by Xia and Chan [Xia93a]. Consisting of 4 grids insulated from the housing and each other, a typical example is shown in figure 8.2.

Grid 1 is left floating. Grid 2 is biased with a relatively low potential to repel particles of the opposite charge to that being analysed. Grid 3 is the retarding grid, biased with a variable potential, to sweep the analysed particle energy distribution. The analysed current is recorded at a collector plate. Grid 4 is negatively biased to suppress secondary electron emission from the collector plate.

If a time sensitive measuring apparatus is used (such as an oscilloscope), it will be possible to use a retarding field energy analyser to measure a time dependent energy spectrum. Unfortunately, retarding

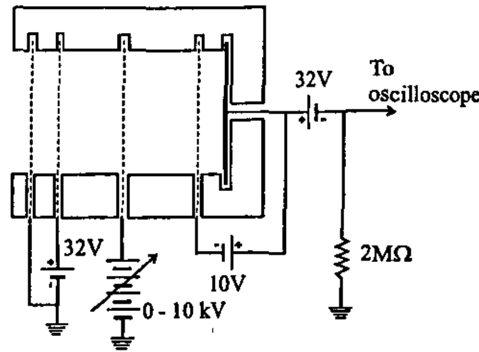

Figure 8.2: Retarding field energy analyser. The variable bias is used to discriminate against particles with lower energies than the bias. A plot of analyser current *versus* bias will give the energy distribution.

field energy analysers are like Langmuir probes, and require potentials greater than the maximum energy of the incoming particle flux to completely determine the flux energy distribution. Thus, assuming space charge limited processes do not interfere due to the high potential, a 30 kV retarding field is required to analyse an electron flux emitted from a target biased at 30 kV.

A retarding field energy analyser was used by Xia and Chan [Xia93a] to measure directly the electron flux during PSII for potentials up to 9 kV.

University of Cape Town

8.2.3.2 Scintillator

By using a CaF_2 scintillator coupled to a monochrometer and photon counter, Nakamura *et al* [Nak97a, Nak97b] were able to establish a quantitative measurement of the electron flux during a typical plasma implantation experiment with an argon plasma and a steel target. A 1 μm aluminium film on the front surface of the scintillator coupled with the fact that electron energies of the order of several keV are required to induce luminescence within the crystal meant that their experiments were only sensitive to the high energy electrons present during the experiment. However, while this technique does not return any information about the electron energy distribution, they were able to correlate the electron flux with the implantation current.

8.2.3.3 By comparison with models of the implanted ion flux

Xia and Chan [Xia93a] also used the measured implantation current compared with a computed ion current based on their model of the PSII experiment. En and Cheung [En96a] calculate γ as a function of ion energy in a similar manner.

Shamim *et al* [Sha91b] calculate γ by subtracting the current without a plasma to eliminate displacement current effects and then proceed as above to calculate the ion current from the measured implantation current.

8.3 X-ray production

The two processes responsible for x-ray production during PSII are bremsstrahlung and the excitation of atoms.

8.3.1 Bremsstrahlung background continuum

The dominant energy loss process in high energy collisions, electron induced bremsstrahlung, is used to produce x-rays in the x-ray tubes used in XRD, XRF and other x-ray analytical tools. Since these tools are commonly used for quantitative analytical work, the electron induced bremsstrahlung process has been well researched and theory developed to quantify the emission spectra of x-ray tubes is appropriate to quantify the x-ray radiation from PSII devices.

Pella, Feng and Small [Pel85a, Pel91a] and Finkelshtein and Pavlova [Fin99a] describe similar methods of calculating the x-ray tube spectral emissions. Extensive experimental data from electron microprobe measurements have been used in their papers to present theories that can be used to calculate quantifiable emission spectra that compare well with experimental measurements.

The bremsstrahlung background spectrum can be described by [Pel85a, Pel91a, Fin99a]

$$N(\lambda) = 3.42 \times 10^{-5} Z(\lambda/\lambda_0 - 1)/\lambda^2 \tag{8-5}$$

where N is the number of photons expected for a given wavelength, in units of photons/Å$\cdot$ e$^-$. Z is the target atomic number, λ the wavelength of the x-ray and λ_0 the short wavelength limit (determined by the energy E_0 of the electron beam $\lambda_0 = hc/E_0$, where h is Planck's constant and c is the speed of light).

The measured intensity $I(\lambda)$ can be calculated from

$$I(\lambda) = 2.72 \times 10^{-6} Z(\lambda/\lambda_0 - 1)/\lambda^2 f W_{ab} \tag{8-6}$$

where f is the Philibert target absorption correction term and W_{ab} the detector window absorption correction term. Experimental results show that f ranges from 1 to 2.5. For a Be window, $W_{ab} = \exp(-\mu_{Be}\rho_{Be}d_{Be})$ where $\mu_{Be} = 0.35\lambda^{2.86}$ is the mass attenuation coefficient for Be, and ρ_{Be} and d_{Be} are the density and thickness, respectively, of the window.

8.3.2 Characteristic x-rays

When atoms are bombarded by high-energy particles, inner-shell electrons are either knocked out or elevated to unfilled upper states, thereby creating a vacancy in the inner shell. An electron from an upper level then drops to fill the vacancy and the excess energy is emitted either as an x-ray or an Auger electron. The process continues until the atom has returned to the ground state.

X-rays are classified according to the level which had the original vacancy, e.g. x-rays arising from transitions from the L, M, N, ... levels to the K level are K_α, K_β, K_γ, ... x-rays, respectively. L x-rays arise when there is a vacancy in the L level, M x-rays when there is a vacancy in the M level, and so on.

These x-rays are emitted with specific energies characteristic of these energy levels for each element, and are called characteristic x-rays. They have specific energies uniquely associated with the target atom and are used by such techniques as PIXE to determine elemental composition.

University of Cape Town

X-ray line	a	b	d
K_α	3.22×10^6	9.76×10^4	-0.39
$K_{\beta 1}$	5.13×10^5	2.05×10^5	-0.014
$L_{\alpha 1,2}$	2.02×10^7	2.65×10^6	0.21
$L_{\beta 1}$	1.76×10^7	6.05×10^6	-0.09
M_α	1.76×10^8	1.02×10^6	0

Table 8.1: Values of the x-ray characteristic constants in equation 8-7

The characteristic line emission intensity is described by Pella *et al* [Pel85a, Pel91a] to be given by

$$\frac{N_{\rm chr}}{N_{\rm con}} = \exp\left[0.5\left(\frac{U_0 - 1}{1.17U_0 + 3.2}\right)^2\right] \times \left[\frac{a}{b + Z^4} + d\right] [U_0 \ln U_0/(U_0 - 1) - 1] \qquad (8\text{-}7)$$

where $N_{\rm chr}$ and $N_{\rm con}$ are the intensities of the characteristic line and continuum directly beneath the line, respectively, for a overvoltage $U_0 = \frac{E_0}{E_q} \approx \frac{E_0}{E_l} = \frac{\lambda_l}{\lambda_0}$, where E_0 is the initial electron energy, E_q the critical excitation energy of a given shell and λ_l the wavelength of the line of interest. The constants a, b and d are determined experimentally for the different lines and given in table 8.1.

8.3.3 Attenuation

When x-rays pass through matter, the x-ray flux is attenuated according to the energy of incident x-ray and the composition of the material being traversed. This attenuation is given by

$$I = I_0 e^{-\frac{\mu}{\rho}x} \qquad (8\text{-}8)$$

where μ/ρ is the mass attenuation coefficient, which is obtained experimentally and presented either in published sources [Cul89a] or electonically on the world wide web[1], and $x = \rho t$, where ρ is the material density and t the material thickness. The mass attenuation coefficient is a function of x-ray energy.

Figure 8.3 shows the attenuation length of x-rays as a function of x-ray energy for aluminium and iron. The attenuation length is the length required for the x-ray flux to drop to $1/e$ of the initial flux[2]. Calculations of transmission show that 20 mm aluminium still transmits 0.44% of a 30 kV x-ray flux, while 2 mm of iron only transmits 0.004%.

The x-ray flux can also be used to monitor the secondary electron emission co-efficient (γ) and hence the surface condition of the target.

8.3.4 Simulation

Fitting of theoretical curves to experimental data using the continuum (Kramer's law, equation 8-5) and attenuation due to the perspex (PMMA) window (equation 8-8) is shown in figure 8.9.

[1] http://physics.nist.gov/PhysRefData/XrayMassCoef/cover.html
[2] Data from Lawrence Berkeley National Laboratory (LBNL), http://www-cxro.lbl.gov/optical_constants/

University of Cape Town

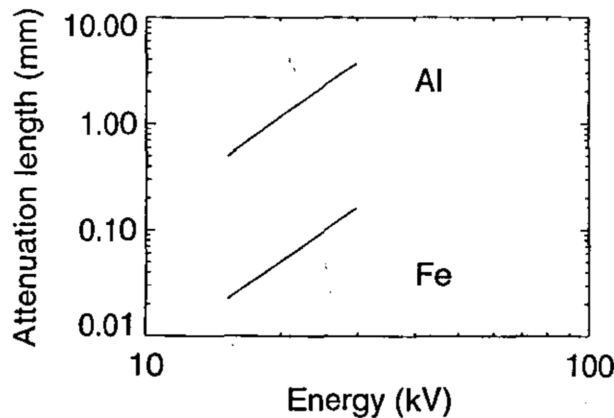

Figure 8.3: Attenuation length *versus* energy for iron and aluminium.

University of Cape Town

8.4 Experiment and measurements

As the maximum energy of the electrons is 30 keV, the use of a standard lithium drifted Si detector (SiLi) is appropriate. With the detector connected to a Multi-channel Analyser (MCA), and timing with respect to the pulse trigger provided by gate & delay hardware (figure 8.5), energy resolved x-ray spectra were measured over short time windows in a typical implantation experiment. The x-ray detector was fitted with a collimator to reduce the x-ray count rate and to provide the ability to aim the detector at specific surfaces within the PSII chamber. A 3 mm thin perpex window separated the detector from the plasma, which is thin enough to allow 6 kV x-rays to pass with attenuation.

8.4.1 Hardware

Electronics & timing

As is shown in figure 8.4, by using a combination of, firstly, a delay after receipt of a pulse trigger (τ_d) and, secondly, a short acquisition interval (τ_a), a 20 μs (τ_p) implantation pulse, for example, can be separated into 10, 2 μs windows. Since a complete energy resolved spectrum can be acquired during each of these windows, the evolution of the x-ray spectrum over time can be determined. Figure 8.5 shows the timing circuit used to perform these measurements. The timing of the x-ray measurement is made with respect to the pulse trigger provided by the CG-840 (§C.4.1). This signal is also used to trigger the RUP-4a pulse generator, and thus ensures measurement reproducibility. A Time to Amplitude converter and Gate & Delay generator were used to gate the MCA such that only those x-rays detected within a pre-defined timing window were recorded.

Experimental arrangement

The experimental layout is shown in figure 8.6. The target to be implanted is placed at the geometric centre of the chamber. The Si(Li) detector is placed outside the chamber, pointing through the thin perspex at the x-ray source. Metal shielding placed around the port prevents secondary electrons repelled

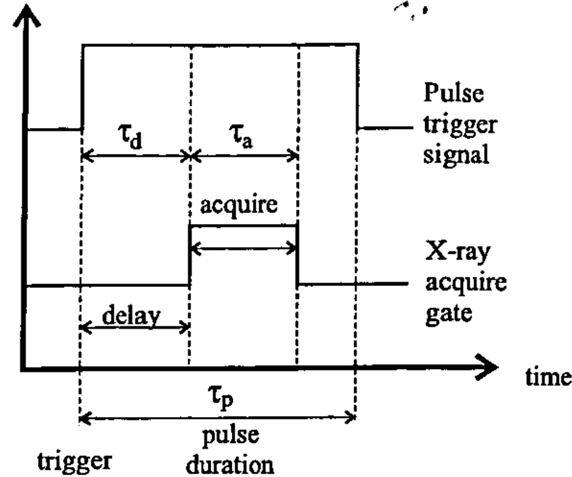

Figure 8.4: Timing of the x-ray measurements. The time resolved x-ray measurements were made by using gate and delay timing circuits to record the x-rays detected during a timing window (τ_a).

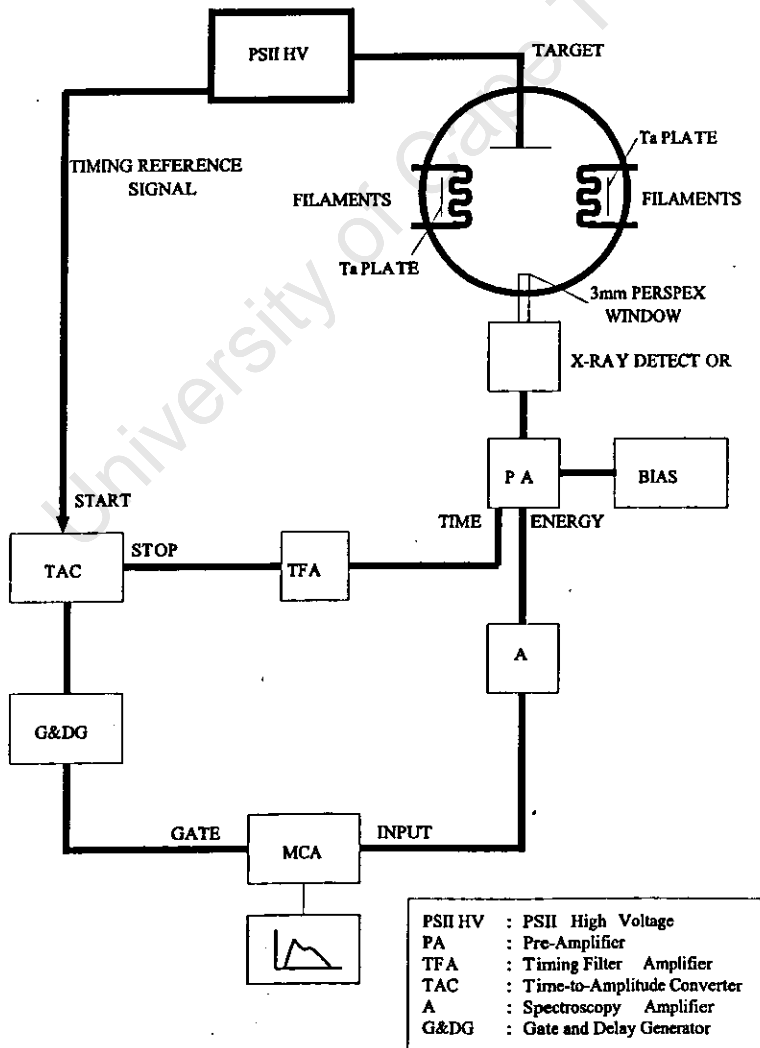

Figure 8.5: Schematic diagram showing the time-resolved x-ray experimental setup.

University of Cape Town

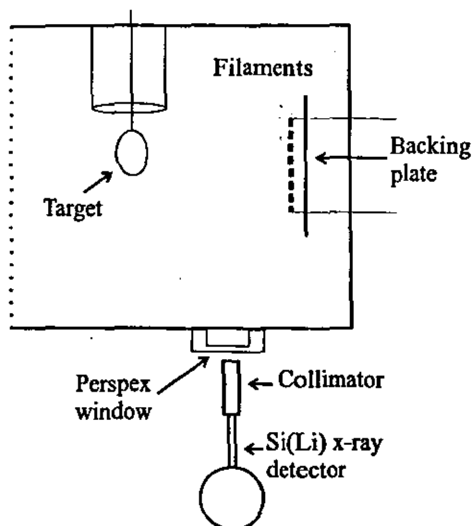

Figure 8.6: Experimental layout of the x-ray measurement hardware

University of Cape Town

from the target from striking the port directly and producing x-rays at the window. A moveable metal shield within the chamber is used to dynamically provide additional screening as neccessary.

8.4.2 Time resolved measurements

To make these measurements, a 20 kV pulse of width 23 μs was used. The x-ray detector was aimed into the chamber, where it would detect the x-rays emitted from an inner chamber wall. The timing hardware was gated to record the x-ray spectra with a moving 2 μs window. Thus the first 20 μs of the pulse could be recorded in ten 2 μs intervals. The results of these experiments are shown in figure 8.7. The 10 spectra obtained by moving a 2 μs window are shown in figure 8.7B. These spectra are best understood by considering the surface they describe (as a shaded surface in figure 8.7A). By plotting the contours of the surface, as in figure 8.7C, one can see how the energy spectrum evolves over time.

Different information can be extracted from the different figures. In particular, the superposition of the x-ray spectra in figure 8.7B shows how high-energy x-rays are detected for the duration of the voltage pulse (as expected), but that the energy profile of the x-ray flux decreases over time. This phenomenon is demonstrated in the contour plot (figure 8.7C) which shows the decreasing high-energy flux as a contour which starts at 20 keV at 0 μs, but decreases to less than 15 keV after 20 μs.

One can also see the apparently long duration for which relatively high x-ray fluxes are measured at the energies corresponding to the characteristic lines. This is seen from the many similar spectra in figure 8.7B and by the long "islands" reaching down, as at 9.48 keV (1.30678Å for the Ta $L_{\beta 3}$ line) lasting for nearly 16 μs, in the contour plot (figure 8.7C).

In addition to the flux of particular energies being maintained for longer, one can also see that the highest x-ray flux is measured during the first 2 μs window. This high flux correlates with the initial high current spike measured during the first microsecond of the applied pulse and confirms that the high current spike is not due purely to capacitive effects within the target/power-supply circuit. This

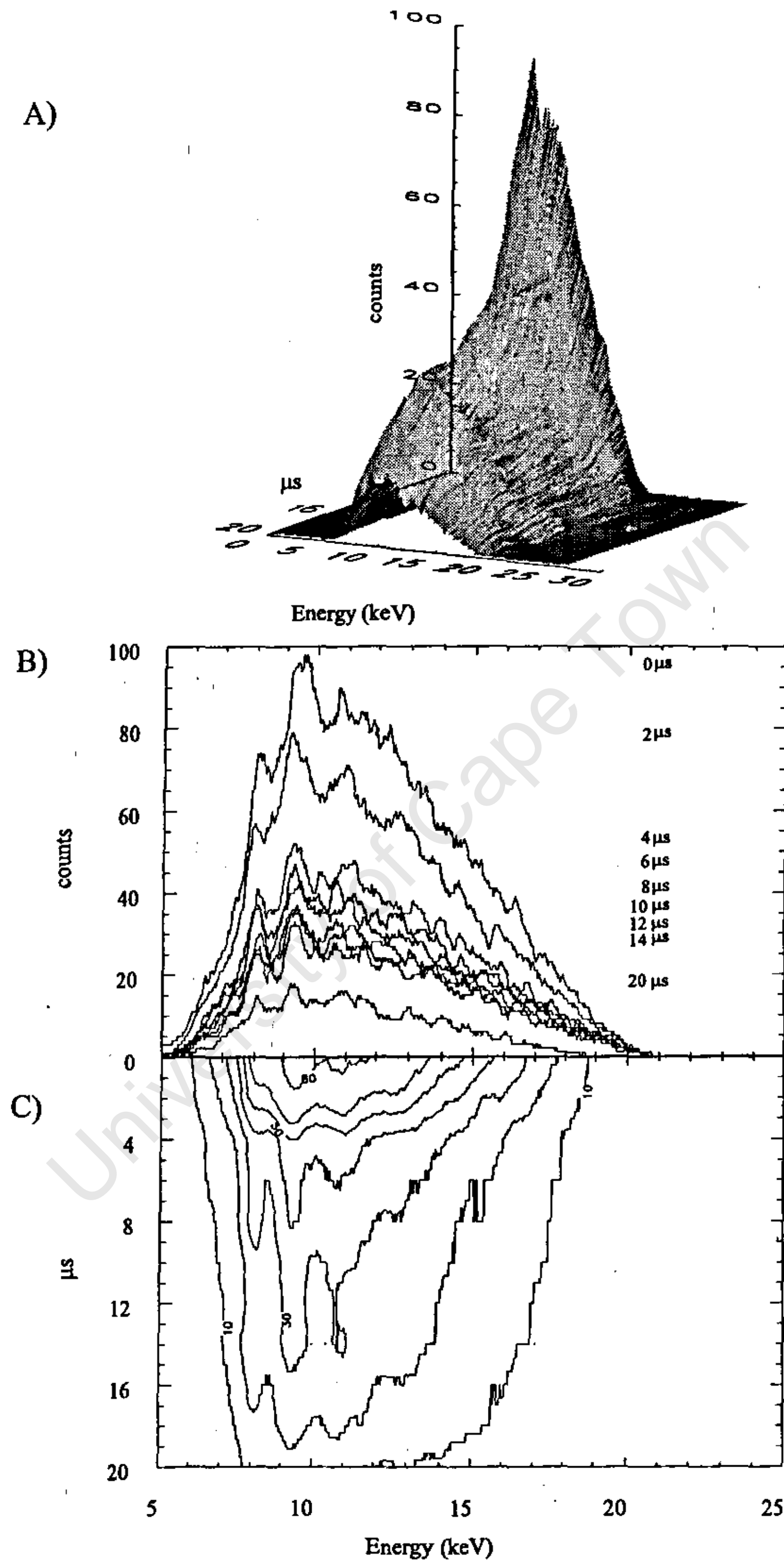

University of Cape Town

Figure 8.7: Different methods of demonstrating the evolution of x-ray spectra over time. The spectra were measured using a 23 μs 20 kV pulse. Panel (A) shows the surface described by the raw data. Panel (B) shows the raw measured x-ray spectra. Panel (C) shows the contours of constant x-ray count of the surface, and the long life-time of certain x-ray energies.

relationship between the implantation current and the x-ray flux can also be seen in figure 8.8.

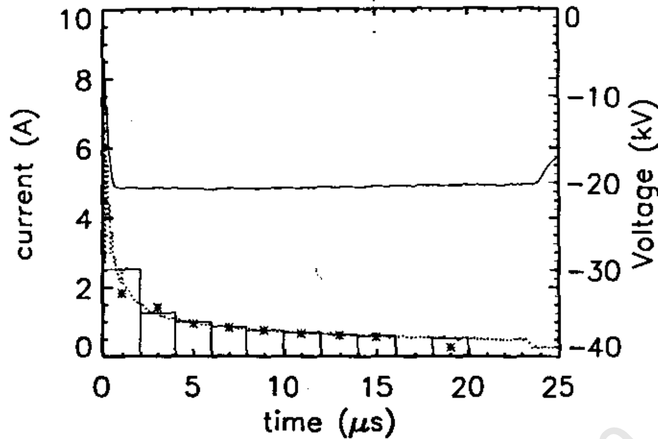

Figure 8.8: The integrated x-ray counts and current measured using a 23 μs 20 kV pulse. The implantation current (dotted), voltage (solid), normalised integrated current (bars) and the normalised integrated x-ray counts (asterisks) are shown. The normalised integrated x-ray counts shows a correlation with the integrated current.

University of Cape Town

Figure 8.8 shows the implantation current (dotted) and voltage (solid) and, for each sampling window, the integrated and normalised current (bars) and the integrated and normalised x-ray counts (asterisks). Comparing the integrated current and x-ray counts, one can see that the total x-ray counts are lower than the total current for the 0 – 2 μs period, but between 4 μs and 14 μs there is a very good agreement, indicating that one can directly relate the x-ray flux to the total current. The initial discrepency is possibly due to displacement current effects or indicative of the presence of attenuated low energy x-rays (if a large low-energy spectrum component existed but was attenuated by the perspex window such that it was not detected, the total integrated x-ray spectrum count would be lower than expected).

Since the total current is related to the ion current by equation 8-2, $I_{\text{total}} \approx (1+\gamma)I_{\text{ion}}$, any change in γ would change both the measured total current and the measured x-ray counts. Early models [Sch90a, Xia93a] of the PSII process indicate that the ion current is expected to decrease as the sheath expands.

The question of whether γ changes during the implantation pulse can be further investigated by using target materials with a very different expected γ and melting temperatures. With targets of the same size and shape but of different composition, the only parameters that would be different would be γ and the target surface condition, and the total current (and total integrated x-ray flux) graphs could be compared.

8.4.3 Comparison with predicted x-ray emission

Figure 8.9 shows the arbitrarily scaled spectrum measured during the first 2 μs. This figure shows the structure discussed earlier: a background x-ray spectrum, with characteristic lines. The presence of tantalum is due to material having evaporated from the filaments. The nickel has possibly been deposited

from material sputtered from the steel target, conductor wire or filament holders. An empirically normalised background x-ray spectrum, as predicted by Kramer's Law (equation 8-5), has also been added.

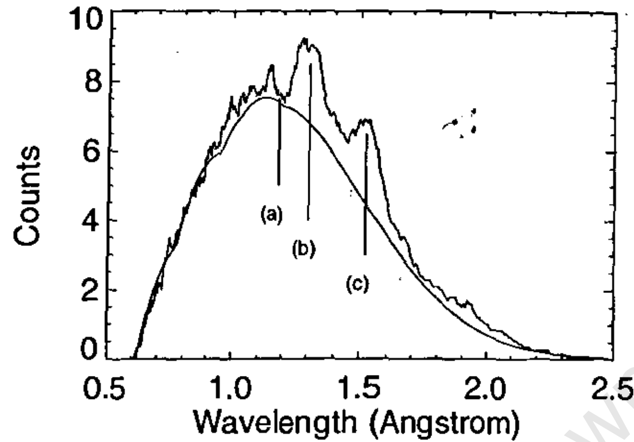

Figure 8.9: The x-ray spectrum measured during the first 2 μs of a 23 μs 20 kV pulse, with an empirically derived theoretical curve added. Features marked are (a) the Ta K edge, (b) Ta $L_{\beta 3}$ line and (c) Ni K_β line.

University of Cape Town

Figure 8.10 shows the spectrum measured during the 6 to 8 μs window. The theoretical curves consist of a 20 kV continuum and the addition of continuum spectra of other energies. The other components were also each multiplied by a 'weighting' factor to improve the fit. The weighting factor was used to account for relatively increased flux (when required) of electrons of that energy.

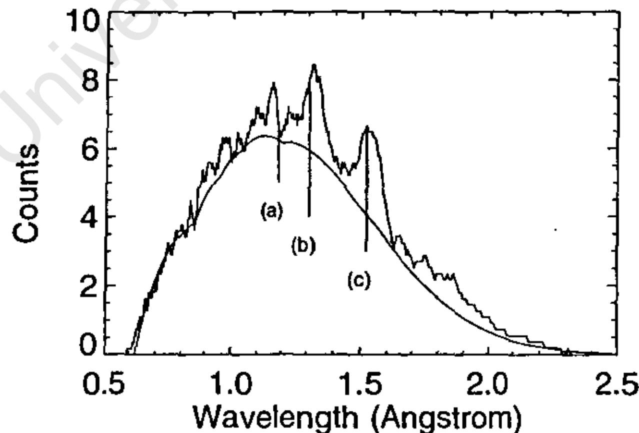

Figure 8.10: The x-ray spectrum measured during the 6 to 8 μs window of a 23 μs 20 kV pulse, with an empirically derived theoretical curve added. Features marked are (a) the Ta K edge, (b) Ta $L_{\beta 3}$ line and (c) Ni K_β line.

For figure 8.9, four other contributions (16, 13, 12 and 10 kV) were added, corresponding approximately with the energies of the lines in the spectrum. The weighting factors used were (1.2, 2.5, 1, and

3), respectively. These weights would imply a larger flux of lower energy electrons than the high energy implantation voltage.

Figure 8.10, which shows the spectrum measured 4 μs later, has four contributions of energies of (14.5, 13, 12 and 10 kV) and weighting factors of (1.5, 1, 1, and 3).

The change in weighting factors for these figures show how the energy distribution of the electron flux changes over time, with a greater 13 kV component initially. At later times the contribution of the 14.5 kV energy component appears to increase, at the expense of the lower energies.

This is compatible with the expected energy evolution of electrons liberated within the evolving plasma sheath, but could also be due to the presence of energy loss mechanisms (collisions). With a mean free path of about 340 metres, collisions are not expected to be a major contribution.

8.5 Safety

Most of the high energy electrons repelled from the target during implantation strike the aluminium alloy chamber walls, producing x-rays. This x-ray emission affects the safety of users of this facility, since the aluminium alloy chamber walls are fairly transparent to the x-rays.

A standard radiation monitor was used to determine that at higher energies (>25 keV) there was a very large x-ray flux. Two ionisation chamber radiation monitors have been assigned to the laboratory to allow users to determine both general radiation levels, and to find localised regions of increased x-ray flux due to reduced attenuation of, for example, vacuum seals or chamber windows.

The experiments described in this chapter were performed to determine the energy spectrum of the x-rays, and hence attempt to establish the health hazards and safety implications for operating personnel. While the energy spectra indicate that the highest energies do not dominate, the energies of the bulk of the emitted x-rays still have enough energy to cause damage in skin tissue.

Since it was not feasible to completely shield the existing chamber, it was decided to adopt the procedure of controlling higher energy implantation experiments from outside the laboratory. This was facilitated by the remote access software (chapter 6).

Safety conditions can be improved by the installation of a steel vacuum chamber. However, with the existing chamber, it would be advised to couple the RUP-4a interlock to an x-ray detector and the laboratory door which would disable the implantation voltage if the door is opened while a high energy x-ray flux is detected. This interlock would have to be enabled only after the door has been locked from the outside. These improvements could not be implemented during the term of this project due to financial constraints.

8.6 Summary

Despite the fact that there are many physical processes between the impact of an ion and the detection of an x-ray, these measurements indicate that there is a direct correlation between the ion current and the measured x-ray flux. The apparent correlation between implantation current and measured x-ray flux over

University of Cape Town

time is presented. The high initial x-ray flux which is measured at the beginning of the pulse is interpreted as demonstrating that the measured high initial current is not dominantly caused by displacement current effects.

The energy distribution measurements also show that most of the x-ray flux has significantly lower energies than the implantation potential. This impacts how net x-ray readings should be interpreted for health purposes: an x-ray flux counter which does not detect the peak flux energies (which in these measurements occurs at about 9 keV) will under-read the total x-ray flux, and while wide-energy band detectors will measure the high flux, it must be remembered that most of this measured flux does not have the implantation potential energy.

8.6.1 Further work

A more detailed analysis of the x-ray spectrum, including fitting of characteristic lines, absorption edges, etc., to improve the fit of the theoretical x-ray spectrum should reveal more information of the electron energy distributions. Use of a detector mounted inside the plasma chamber would reduce attenuation of lower energy x-rays and improve the analysis. Comparative measurements of samples with different temperature profiles and secondary electron emission co-efficients may reveal more information on the evolution of γ during the pulse.

University of Cape Town

University of Cape Town

Chapter 9

Metal applications

9.1 Background of PSII

The ease of producing a nitrogen plasma and the already well understood application of nitrogen induced hardening made the invention of PSII an almost inevitable event. Since the early days of the technique, this process has been used for the nitrogen implantation of metals to achieve surface hardening of metallic applications ranging from stainless steel femoral knee components [Che91a], to titanium alloy surgical implants [Alc97a]. PSII was a new and cost-effective process suitable for hardening everything from drill-bits to motor vehicle crankshafts, and, globally, numerous groups began research with this technique. New applications of the PSII technique to the silicon industry further improved the reputation of the technique, expanding the industrial applications being developed, ranging from the huge implantation chambers of Los Alamos [Woo93a] (4.6 by 1.5 metre) and Hughes Research Laboratory [Mat96a] (2.4 by 1.2 metre), to the silicon wafer cleaving technique pioneered by Bruel [Bru96b] in Grenoble, France.

As time passed, the technique expanded to include the implantation of metals into metals, oxygen into silicon for buried oxide formation, boron into silicon for doping and combination PSII with plasma nitriding, PSII of carbon for deposition of DLC layers, and other coating techniques.

University of Cape Town

9.1.1 PSII research at the National Accelerator Centre

The original intention was for the PSII facility at the National Accelerator Centre to be developed in order to investigate new applications of the PSII process of surface hardening of metals, with specific applications relevant to South African industry. Three potential applications were identified: A stainless steel sliding seal used in the mixing of liquid ingredients for the food industry, diesel fuel injection components (in collaboration with the Centre for Automotive Engineering, Materials Engineering, University of Stellenbosch) and a sand sampling probe used by Namakwa Sands (Part of the De Beers group) to sample a sand transport line.

9.1.2 Preparation of metallic samples

The steel samples analysed had to be polished to a mirror finish to remove surface impurities and irregularities that could otherwise adversely affect analysis. In nuclear analytical techniques surface roughness adversely affects energy resolution and calculations dependant on angle of incidence, while for the microhardness measurements, the surface roughness adversely affects the measurement of the indentation size.

Thus the standard method of preparing samples for implantation and subsequent analysis involved mounting the sample in resin when necessary, grinding under flowing water with sand paper of decreasing roughness (from 200 down to 600 roughness) to remove coarse irregularities, being careful to always work across the grain of the previous grinding and to remove all scratches coarser than the current grinding. After a final grinding with 1000 water paper, the sample was thoroughly cleaned in an ultrasound alcohol bath to remove any coarse contaminants left behind by the sand-paper. The first polishing phase was achieved by using 3 μm diamond paste on a polishing disk followed by further cleaning in alcohol and a final polish with 0.25 μm diamond paste. During the final diamond paste polishing stages the target was examined under an optical microscope to ensure that no scratches remained in the area of interest.

University of Cape Town

Industrial samples

Industrial samples are those manufactured components which are implanted for later field use. If the samples are small enough to be analysed, the surface to be analysed must be as polished as possible, although if the dimensions are critical, it may be possible to progress directly to the final 1000 waterpaper and diamond paste polishing steps. If the sample is too bulky for conventional polishing, an appropriate area can be polished for analysis and buffed to minimise surface roughness. To maximise the retained dose and minimise sputtering damage caused by implantation at non-normal angles of incidence on the microscale, all samples to be implanted should have as fine a finish as possible.

9.2 Steel sliding seal

In this particular application, the sliding seal is the interface between a rotating mixing barrel and the product inlet/outlet ports. Oil and water based emulsions such as margarine and mayonnaise are mixed in the rotating barrel.

9.2.1 Methods of hardening

Various alternate hardening techniques had already been used with varying degrees of success:

- a very successful but expensive ceramic coating available from Germany. These coatings are reliable until excessive wear results in cracks in the coating, at which point the coating can fail catastrophically, with ceramic debris forming a "grinding paste" if regular maintenance checks are not performed to detect such wear. The expense of these coatings was the only factor which prompted investigations into locally available alternatives.

- Locally manufactured hard-chrome and ceramic coatings were found to be too coarse and unreliable. It was decided to perform PSII to investigate the hardenability of the seal material.

9.2.2 Implantation procedure

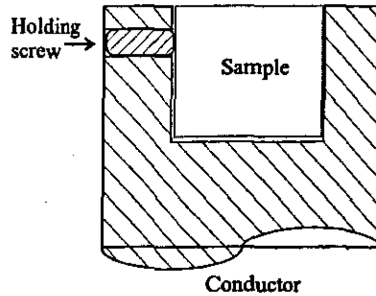

Figure 9.1: Cut-way side view of the sample holder used to implant the 9 mm cubic samples

A sample of the material used (Steel type: DIN 1.2083, or AISI 420 or X42Cr13) was cut into smaller 9 mm per side cubes for implantation and subsequent testing. One face of the these samples was polished to a mirror finish according the procedure of §9.1.2. A special target holder (figure 9.1) was manufactured to allow the polished sample face to be implanted. Five samples were implanted, four at 20 kV and one at 30 kV. The implantation parameters can be found in table 9.1.

Sample	Energy kV	Freq. Hz	Current mA	duration mins	dose 10^{16} cm^{-2}	Hardness HV
A1	20	600	≈10	90	5	270
A2	20	850	≈12	140	8	1090
A3	20	400	≈8	105	6	360
A4	20	400	≈4	355	21	440
A5	30	200	≈4	240[a]	14	300

[a]During the implantation of sample A5 the plasma was lost due to excessive filament degradation. Unfortunately the exact time at which this occurred is unknown.

Table 9.1: Table of implantation parameters for sliding seal, pulse width was 5 μs for all samples. Vickers hardness values are given.

Plasma parameters

The plasma parameters during these experiments were typically:

Pressure	Filament bias	Discharge current
8×10^{-4} mbar	60 V	2.0 A

9.2.3 Testing

Hardness testing was performed at the Department of Materials Engineering, University of Cape Town, with their Matsuzawa MXT-α7 microhardness tester. The samples were mounted on the tester stage

University of Cape Town

and an indentation was made under a known load (20 g to 200 g). The two perpendicular widths of the indentation were measured with the built-in microscope. These values were then used by the instrument to calculate Vickers hardness values according to equation 7-23. The hardness values were measured twice and compared with an unimplanted reference. The values were adjusted according to a provided calibration standard and presented in table 9.2.

Sample ID	indentation size (μm)	Hardness measurements (HV)	Average hardness (HV)	Corrected hardness (HV)	improvement factor
Calib. 710 HV			620	710 factor = 1.15	correction
Ref.	13.0 13.2 12.5 13.3	270 278	274	315	(reference)
A1	12.7 13.1 12.8 13.2	278 276	277	319	1
A2	5.8 6.4 6.6 7.4	1245 946	1095	1259	4
A3	11.0 11.5 11.6 10.9	366 366	366	421	1.3
A4	10.3 10.3 10.2 10.4	437 437	437	503	1.6
A5[a]	12.8 13.5 11.5 12.3	268 327	298	343	1.1

[a]During the implantation of sample A5 the plasma was lost due to excessive filament degradation. Unfortunately the exact time at which this occurred is unknown.

Table 9.2: Table of hardness measurements of sliding seal samples at 25 g loading

University of Cape Town

9.2.4 Results

A clear improvement in microhardness can be seen for samples A2 through A4. Sample A1 was not implanted for a sufficient duration to achieve any definite effect, and the unknown implantation time of sample 5 makes that an unreliable result. While it was evident during measuring the hardness of sample A2 that it was harder than any of the other samples, the exceptionally high hardness of this sample may have been caused by inaccuracies in measurement of the indentation size due to the implantation induced surface roughness.

9.2.5 Conclusions

A degree of surface hardening was definitely measured, although the surface condition and inherent unreliability of the microhardness testing method mean that extended conclusions about the success of the process can only be determined in an in-situ test.

9.3 Diesel fuel pump components

Diesel fuel pump elements were obtained from Dr A.B. Taylor of the Centre for Automotive Engineering (CAE[1]), Department of Mechanical Engineering, University of Stellenbosch. These elements make up the high pressure diesel pump mechanism used to compress the diesel before injection into the ignition (combustion) chamber. An opportunity arose to perform this investigation at the Forschungszentrum Rossendorf during a two week visit to the Forschungszentrum Rossendorf in June of 1998.

9.3.1 Composition

Due to the competitive nature of the automotive industry, it is very difficult to get exact information which may be considered industrially sensitive. While no official report was forthcoming from Bosch, unconfirmed reports suggest that the needle valve is manufactured out of S600 high speed tool steel (DIN 17350), and that the pump element was a chrome, manganese, carbon steel alloy. Post implantation compositional analysis with GDOS, figure 9.5, indicates a composition of 1.22% Cr, 1% C and 0.26% Mn. Optical analysis indicated that the material was a tempered martensite.

9.3.2 Sample preparation

A pump piston and needle valve component were cut radially into smaller cylindrical samples, as shown in figure 9.2.

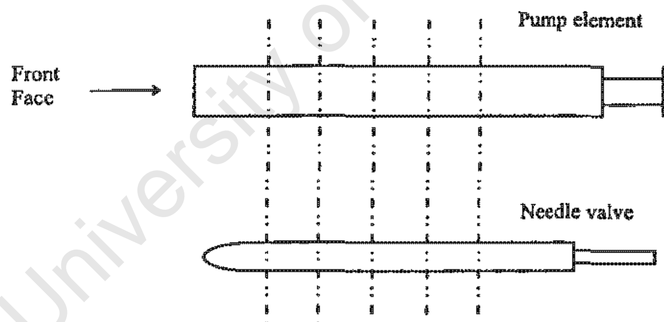

Figure 9.2: Side-view diagram of diesel pump components. The dashed vertical lines indicate where they were cut.

9.3.3 Implantation procedure

Except for the front face of the pump element (marked with an arrow in figure 9.2), these pieces were polished to a mirror finish and implanted at 40 kV. The pump element head was only lightly polished to remove large surface structures, and initially left unimplanted to allow comparison between the PSII implanted pieces and the factory treated surface. The Forschungszentrum Rossendorf plasma vessel is a 40 cm diameter steel vessel with an ECR plasma source. The implantation temperature was maintained at 380°C by a feedback circuit which uses the sample temperature, as measured by an optical pyrometer, to control the implantation frequency. A higher implantation frequency increases the power input to the

[1] http://www.cae.co.za/

University of Cape Town

sample and produces greater sample heating. Cooling is provided via a water cooled base and through radiative heat losses. Three samples of each material were implanted, at calculated doses of 2, 4 and 8×10^{18} ions cm^{-2}. Hardness *versus* depth measurements were made on each of the implanted samples and compared with measurements made on unimplanted regions of the sample material and the pump face. After measuring the hardness of the pump front face, it was implanted at 4×10^{18} ions cm^{-2}.

9.3.4 Results

Hardness measurements

These samples were analysed at the Forschungszentrum Rossendorf with a nano-indenter probe capable of performing hardness *versus* depth measurements. The surface hardness values are determined with a Knoop indenter (Knoop hardness values differ slightly from Vickers hardness values, due to the difference in indenter shape).

The surface microhardness measurements of the samples is given in table 9.3.

sample	hardness (kgf/mm^2)			
pump bulk	811	850	910	970
pump face	1000		815	
needle valve bulk	944	1460	1549	1412
dose (10^{18} cm^{-2})	As received	2	4	8

Table 9.3: Table of hardness measurements of the implanted diesel pump components.

The hardness *versus* depth measurements of the implanted pump element is shown in figure 9.3 and of the implanted needle valve in figure 9.4.

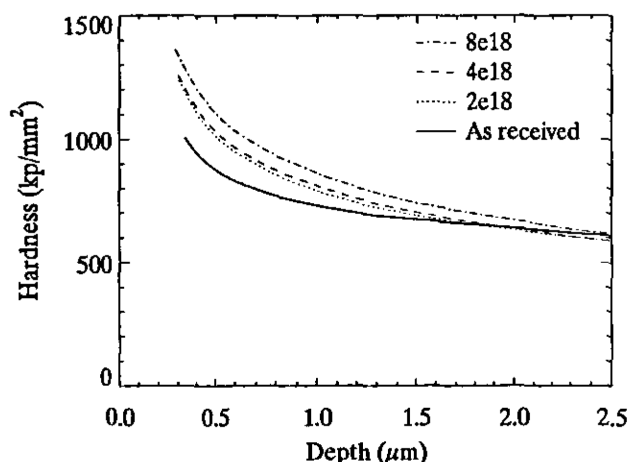

Figure 9.3: Hardness *versus* depth measurements for the different implant doses of the implanted pump element.

University of Cape Town

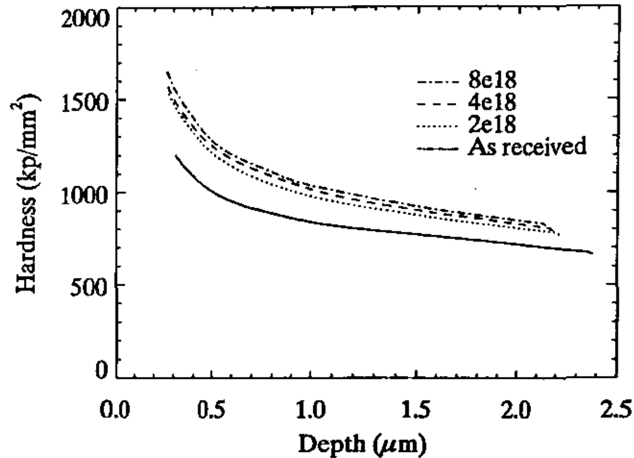

Figure 9.4: Hardness *versus* depth measurements for the needle valve. The different implantation doses are given.

University of Cape Town

Compositional analysis

Post implantation GDOS analysis was performed to determine the implanted nitrogen depth profile. A typical profile is shown in figure 9.5, which shows an implanted nitrogen peak at about 0.4 μm of 22.5 [wt %] ($0.9 \times 25\% = 22.5\%$) which decreases to about 1% at 6.7 μm.

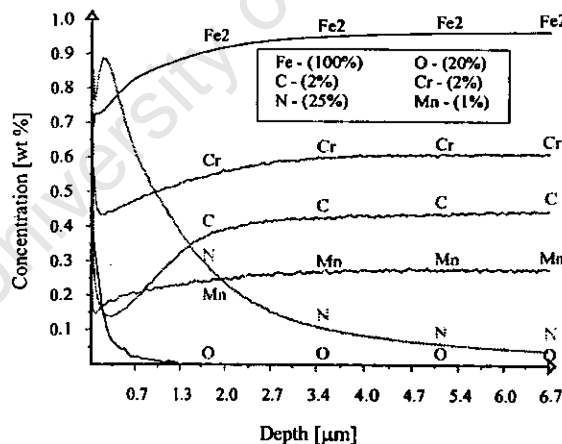

Figure 9.5: GDOS depth profiling compositional analysis. The actual composition is determined by multiplying the y-axis value by the factor specified in the key.

9.3.5 Discussion

As can be seen from the hardness measurements (table 9.3), the pump element bulk material had an initial hardness of 811, and that the hardness improved with each increased implanted dose, such that a hardness of 970 was achieved at a dose of 8×10^{18} ions cm^{-2}.

It can also be seen that the pump element had already been factory surface hardened. Due to the

confidential nature of the industry, it was difficult to establish what procedure was used, although it was noticed that the hardness of the front face was reduced after implantation with nitrogen.

With the needle valve material, the hardness improved from the unimplanted 944 up to a peak of 1549 at 4×10^{18} ions cm^{-2}, but it decreased to 1412 at 8×10^{18} ions cm^{-2}. This decrease in hardness may be as a result of overheating during the implantation process, leading to precipitation of CrN.

9.3.6 Conclusions

A comparison of the original face hardness and the nitrogen implanted samples showed that these pieces were factory hardened and that there was no reason to implant the original Bosch components. PSII treatment would then only be of interest to users of unhardened parts bought from other manufacturers. Private discussions with an engine component remanufacturer indicated that the original Bosch parts can be machined at least once to eliminate scour marks and other wear-induced scratches, and still have a "reasonable" life-expectancy.

Analysis of the needle valve material demonstrated that it could be hardened by plasma implantation of nitrogen using the PSII technique, but no information was available about the factory hardened surface, since the microhardness instrument required a flat area for analysis.

University of Cape Town

9.4 Sand sampling probe

The Namakwa Sands plant mines sand and extracts a variety of products from it, ranging from glazes to titanium dioxide. In particular, the plant collects sand from a quarry and during several stages of the process, transports it within pipes using compressed air. When the material in a pipe needs to be sampled (for quality control, etc.), a steel probe is inserted into the sand stream which intercepts the stream and extracts a sand sample. The process is extremely abrasive as the sand is travelling at a high velocity and the wear is equivalent to the conventional sand blasting process. Since the probes last only a few weeks before they are too badly eroded to continue functioning, it was decided to try a hardening procedure in an attempt to prolong the probe life expectancy.

9.4.1 Probe description

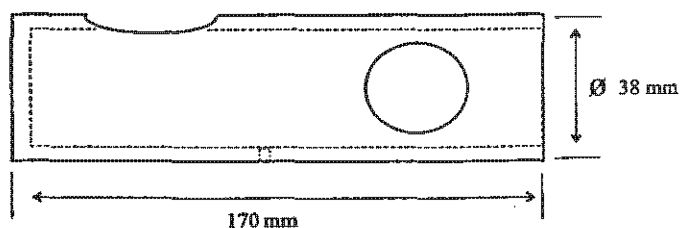

Figure 9.6: Side view of the sand sampling probe used to sample the high velocity sand stream.

As can be seen from figure 9.6, the probe is essentially a hollow tube with entry and exit ports. Periodically, the probe is inserted into the sand stream for a short interval, during which a calculable

amount of sand is extracted. This sand can be tested for quality control purposes.

9.4.2 Hardening procedures

Beta-40

In addition to PSII hardening by nitrogen implantation, another hardening procedure called Beta-40[2]. Thus two sets of probes of two different materials were processed, the original probes, as received from Namakwa Sands, manufactured out of steel type En24 and two additional probes manufactured at the National Accelerator Centre out of En19. The second material was used on recommendation of the metallurgist at P.H. Heat Treatment, since its composition is apparently better suited for the Beta-40 hardening process. En24 has a higher nickel content, and since Ni is an austenite stabiliser, this decreases the effectiveness of the hardening process via the martensitic phase. The Beta-40 process is a heat treatment in a nitrogen rich environment, possibly a nitrogen rich salt bath, which is tested to assure a "40 thou" (or about 1 mm) case depth, on both the inside and outside walls of the processed sample.

PSII

The En24 probe was implanted in 3 sequential experiments, with hardness measurements being made after each implantation. To minimise oxide formation, the probes were left to cool for at least 12 hours under vacuum in the plasma vessel before venting. The regions analysed were lightly buffed to provide a smooth finish for the indentation measurements. The probes were implanted at 30 kV, 700 Hz with a 2 μs pulse. A mean implantation current of 9 mA, a calculated probe surface area of about 200 cm^2 and a secondary electron emission coefficient of 5 results in an approximate implantation rate of 4×10^{13} ions cm^{-2}s^{-1}. To thus achieve a 4×10^{17} ions cm^{-2} dose, an implantation time of 166 minutes would be required.

The En19 probe was implanted in two 300 minute implantation sessions. The implantation conditions were the same as before: 30 kV, 700 Hz with a 2 μs pulse width and mean current of 9 mA. This duration was determined from a desired implantation dose of greater than 4×10^{18} ions cm^{-2}.

9.4.3 Results

The implantation procedure and results for the En24 and En19 samples are summarised in table 9.4 and table 9.5.

En24

The En24 probe hardness measurements showed improvements in surface hardness with each implantation experiment. It is obvious from the comparison with the Beta-40 process that the PSII experiments take much longer than the Beta-40 process (Beta-40 processing of all probes was completed within a single working day), and with a lower eventual surface hardness result. Since the expected implantation duration was based on calculations using measured current and calculated area, and an approximate value for the

[2]run under license in South Africa by P.H. Heat Treatment, 17 Activia Rd, Activia Park, Germiston, South Africa.

University of Cape Town

Duration (min)	Total (min)	Hardness measurements								Avg. (HV)
		(μm)	(HV)	(μm)	(HV)	(μm)	(HV)	(μm)	(HV)	
Ref			306		354		336		348	336 ± 21
200	200	20.0 20.0	464	19.6 19.7	483	20.0 20.0	454			467 ±15
420	620	20.0 20.0	464	19.5 19.5	488	19.4 19.4	493	20 20.4	464	477 ±15
360	980	17.5 18.2	583	17.9 19.0	546	16.8 17.8	620	18.7 19.1	519	567 ±44
Beta-40		16.3 16.3	698	16.3 16.3	698					698

Table 9.4: Implantation procedure and measured hardness values for sample En24. 100 gf load. The measured size of the indentation and the converted hardness values are given.

secondary electron emission co-efficient, γ, differences between the calculated dose and measured dose are expected. The actual implanted dose rate is probably much lower than the calculated dose due to such factors as 1) the retained dose being lower than the implanted dose, 2) errors in calculating the implanted area, 3) errors in estimating γ and 4) errors in reading the mean implanted dose current. The "NetLab" software had not been completed at this point and hence a computationally established current was not available (the current was read from a 0 to 30 mA analogue meter on the RUP-4a power supply).

The Beta-40 hardening process was able to achieve a greater measured hardness than the PSII implanted probes after more than 16 hours of implantation. Further tests with longer pulse widths (and hence lower pulse frequencies, to maintain the power safety limits) may yield different results due to the altered implantation conditions. Longer pulse widths result in greater surface heating during the pulse and hence possibly improve the diffusion of nitrogen to greater depths, provided the temperature does not exceed a critical phase temperature (usually 500°C) when the nitrides start to precipitate out of solution. Thus while the reduced pulse frequency results in an equivalent power input to the sample, the target surface can reach much higher temperatures during the pulse period, which affects diffusion rates, retained dose and sputtering yield. The exact effects would have to be determined empirically in additional experiments.

The hardness measurements of these samples were adversely affected by the curved surface of the probe, although it was possible to locate the top-most probe surface, which was considered flat on the scale of the indentation.

En19

This sample was implanted for a total time of 10 hours in two 5 hour steps on two consecutive days. The resultant hardness measurement showed an increased surface hardness, comparable to the equivalent implantation period (620 minutes) of the En24 probe.

The Beta-40 measurements offer mixed results. Two En19 probes were processed, with one later cut in half as a test piece by P.H. Heat Treatment to check the resultant case depth. The accompanying

University of Cape Town

Exp.	Duration (min)	Hardness measurements						Avg. (HV)
		(μm)	(HV)	(μm)	(HV)	(μm)	(HV)	
Ref		26.2 23.6	299	24.2 26.3	291	24.9 30.6	241	277 ± 31
PSII	600	21.4 20.1	431	19.9 20.0	466	19.7 19.9	473	457 ±23
Beta-40		20.0 20.0	466	21.2 21.4	407			437±42
Beta-40 (test)		16.2 16.9	677	16.6 16.6	673	16.6 16.6	673	674±2

Table 9.5: Implantation procedure and measured hardness values for sample En19. 100 gf load. The measured size of the indentation and the converted hardness values are given.

laboratory report from P.H. Heat Treatment and the measurements performed at the University of Cape Town both confirm a surface hardness of greater than 770 HV for this test piece. The laboratory report established a case depth of 0.75mm, with values ranging from 724 HV at the surface, to 439 HV at a depth of 0.5 mm. The unhardened core was measured to have a hardness of 257 HV.

However, microhardness measurements at the University of Cape Town of the second probe produced surface hardness values of only 500 HV, which, while harder than the as-received value, is considerably softer than the test piece, and lower than the PSII treated sample.

9.4.4 Conclusions

The microhardness measurements performed demonstrate that it is possible to improve the surface hardness of these materials with PSII. However, since the already available Beta-40 commercial process is also able to also improve the surface hardness on a much shorter time scale (1 working day), that process is probably preferred for commercial applications needing rapid process times.

University of Cape Town

9.5 Summary

With the primary emphasis of this thesis being on the construction of the facility, these attempts at finding applications for the facility in industry were initiated as initial applications. While the initial results indicate that materials used in typical industrial applications can be hardened at this facility, a much more detailed investigation is required to evaluate the contribution this facility may be able to make.

It is apparent that, at least at the moment, the long process times and slow turn around (time to process a second sample) restrict the valuable contributions of this facility to research work in as-yet untested sample materials and processes.

University of Cape Town

Chapter 10

Silicon applications

10.1 Introduction and background

Applications of the PSII process in semiconductor applications were researched even before the first PBII workshop in 1993 [Qin91a]. These early applications typically used low energy (-5 kV) PSII for silicon doping, e.g. a BF_2 or B_2H_6 plasma for doping with boron [Qin94a]. In the second PBII workshop, N.W. Cheung presented a paper on the applications of PSII to buried oxide formation using a technique he called SPIMOX (Separation by Plasma IMplantation of OXygen), implantation of oxygen by PSII into a silicon wafer with a 50 kV implantation voltage to form a buried oxide layer under 30 nm of silicon with just 3 minutes of implantation [Che96a] (as opposed to hours with traditional ion beam implantation techniques) and 2 hours of annealing. Similar developments were presented at the third PBII workshop in Dresden, 1996. In 1996, M. Bruel [Bru96b] presented his work on the Si cleaving process, SmartCut^{TM}.

10.1.1 Wafer doping and related techniques

While there is some doubt about the appropriateness of the PSII techniques for surface hardening, plasma implantation has become a major technique used in certain manufacturing processes in the silicon-based integrated circuit industry. In particular, PSII is used for large area implantation of silicon for the manufacture of devices ranging from diodes and transistors [Qin94a] to large area displays [LeC97a]. The ability of PSII to uniformly implant large areas simultaneously can not be reproduced by ion beam techniques. In addition to doping applications, PSII is also used for silicon wafer surface engineering in the Smart-Cut^{TM} and related techniques for the alternative manufacture of silicon on insulator (SOI) devices.

10.1.2 Silicon cleaving applications

These techniques use an implant gas, such as hydrogen or helium, to weaken the bond between a surface layer and the bulk of a silicon wafer at a specific depth. The weakened layer is typically bonded to an insulating substrate and separated from the silicon bulk. Circuitry can then be added to the silicon layer, with protection from stray charge and cosmic radiation provided by the insulating substrate.

University of Cape Town

A graphic representation of the wafer cleaving concept is given in figure 10.1. Referring to figure 10.1,

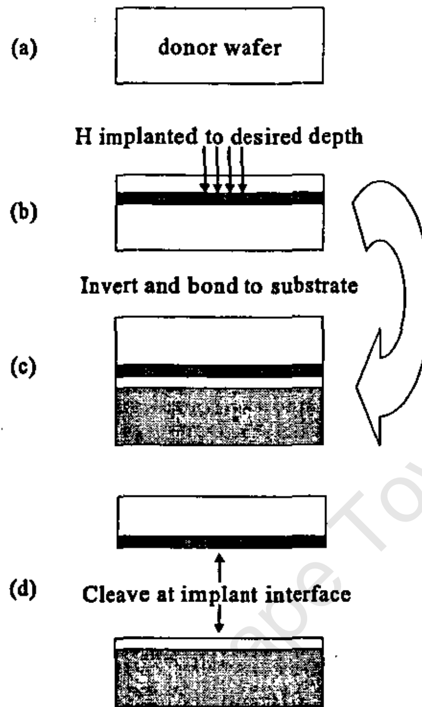

Figure 10.1: A graphical representation of the basic theory of wafer cleaving by implantation of an inert gas.

University of Cape Town

the process can be described as follows

b) The Smart-Cut™ process uses PSII to implant high doses of hydrogen into a silicon donor wafer, with the implantation energy determining the depth (λ_{ion}) to which this hydrogen is implanted.

c) The implanted donor wafer is inverted and bonded to a daughter substrate. Using an appropriate technology, the donor wafer is weakened by the implanted hydrogen

d) the surface of the donor wafer is separated from the donor wafer bulk, to form a new surface on the daughter wafer.

The implantation of hydrogen into the silicon bulk produces a concentration of hydrogen at the implanted depth, λ_{ion}. If the wafer is annealed, the implanted hydrogen accumulates at this depth over the entire implanted area and forms micro-bubbles [Lu97a]. These micro-bubbles can grow large enough to link up, but if no strengthening daughter wafer has been used, the stresses at the bubble edge invariably result in fracture to the surface resulting micro-blisters, preventing complete wafer separation. However, if a strengthening substrate has been used, the bubbles are prevented from blistering and can eventually cover the entire surface area of the donor wafer to form a fracture line at the implantation depth. With suitable annealing or mechanical force, the surface can be separated from the bulk along this fracture line.

Smart-Cut^{TM}

The Smart-Cut^{TM} process developed by M.Bruel [Bru96b] uses thermal annealing steps to form the hydrogen induced fracture line. Results indicate that annealing at 500°C is sufficient to induce wafer separation.

Genesis Process

The Genesis Process, developed by N.W. Cheung and co-workers [En98a] in [IEEESOI98], differs from the Smart-Cut^{TM} process in that it uses a high velocity nitrogen gas stream to separate the wafer after a much lower temperature (300°C) annealing step.

Applications

These processes are then able to, for example, create a buried oxide layer by the four-stage process of

1) creating a surface oxide layer using standard techniques on a donor wafer.
2) By then implanting hydrogen through the oxide layer and into the wafer bulk to a suitable depth, and
3) bonding the implanted wafer to a daughter wafer and applying either of the above mentioned wafer separation techniques, the donor wafer surface can be separated from it's bulk, leaving a buried oxide layer in the new compound wafer.
4) A final annealing and polishing step removes any defects that may have been introduced by this process.

It is further projected that by bonding the donor wafer to a suitable insulator substrate, it will be possible to manufacture mono-crystalline silicon-on-insulator wafers.

Recently, research has also been performed into the first steps of manufacturing three-dimensional circuits. These circuits would be assembled layer-by-layer using a technique of implanting hydrogen into gaps left behind during the normal device building procedure. By manufacturing devices on the surface of a silicon wafer as per normal, but leaving a mask pattern untouched, the device-laden surface can be separated from the bulk even though the implanted hydrogen has been implanted only into the un-used areas [Yun99a] in [IEEESOI99]. After separation, the original layer of devices will be buried, with a fresh surface available on which it is possible to build further devices. In principle, this procedure could be repeated to create true three dimensional circuits in semiconductor volumes.

10.2 Research at this facility

This chapter describes two research projects in the area of PSII of silicon performed at this facility, the implantation of hydrogen into silicon, and the in-situ ERDA analysis of hydrogen implanted silicon.

10.2.1 Implantation of hydrogen into silicon

An initial study into the ability of this facility to implant hydrogen into silicon was performed. While the contaminants present (tantalum, etc) would void the ability to manufacture silicon devices, there is

University of Cape Town

still scope to investigate wafer cleaving topics.

10.2.2 In-situ analysis of hydrogen implanted silicon

The thermal dependence of hydrogen in hydrogen implanted silicon was examined using an in-situ ERDA analytical technique. By measuring the hydrogen depth profile with ERDA and the hydrogen gas concentrations in the analysing vacuum vessel in-situ while the silicon substrate is heated, the temperature at which hydrogen became mobile could be determined. Of particular interest was the complex depletion rates of the implanted hydrogen profile.

10.3 Silicon sample preparation

While the metallic samples for tribological applications had to be cleaned and polished to a mirror finish, the silicon samples only had to be cleaned of organic impurities.

The silicon samples were already highly polished as part of their manufacture process. Thus it was only necessary to remove surface contaminants by washing the samples in a series of ultrasound solvent baths. The oxide layer could be removed in an ultrasound bath of a weak hydrofluoric acid solution.

The sample was placed in an appropriate beaker with enough solvent to cover it by about 1 cm. It was then placed in the ultrasound cleaner and left for about 10 minutes. In the final rinsing step, the sample was rinsed with pure filtered and de-ionised water and dried with compressed nitrogen gas.

Table 10.1 shows all the solvents used in order to maximise the cleaning process

Step	Solvent
1.	Methanol
2.	Acetone
3.	Trichloroethylene
4.	Acetone
5.	Methanol
6.	De-ionized H_2O
7.	20% HF

Table 10.1: The cleaning order and solvents used to clean silicon samples.

10.4 Hydrogen PSII of silicon

Silicon ⟨111⟩ samples were implanted with this facility to evaluate its ability to perform research into this new field of silicon wafer cleaving and similar processes. The samples were cleaned according to the cleaning regiment described in §10.3, and mounted on a flat steel stage. Silver paste was used to improve the electrical conductivity and mechanical adherence. The samples were implanted at 25 kV, with 1 μs pulses at a repeat frequency of 700 Hz for 6 hours in two different batches.

University of Cape Town

10.4.1 ERDA analysis and Results

ERDA was performed on the implanted samples to determine the depth profile of the implanted hydrogen. These measurements were performed using a 4.3 MeV alpha beam. A porous silicon sample, which was annealed in a deuterium-rich environment, was used for energy calibration (figure 10.2). This figure shows hydrogen and deuterium at the surface, as well as some hydrogen in the bulk. All samples analysed show a surface hydrogen peak, probably due to hydrogen bonded to the surface silicon (Si-H), surface organics (such as oils from the vacuum system) and water. Figure 10.3 shows the superimposed ERDA results

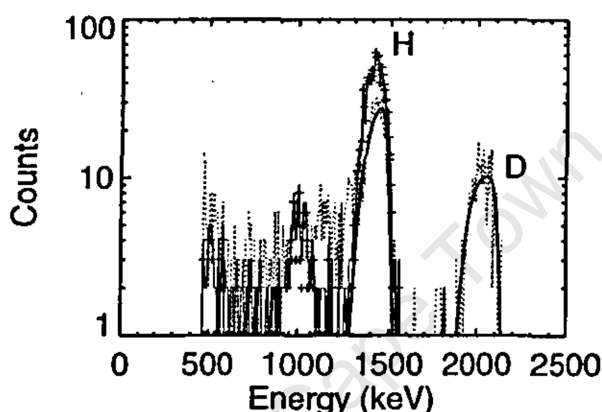

Figure 10.2: ERDA spectrum of a deuterium- and hydrogen-impregnated silicon (dotted) sample and the simulated spectrum (solid) used to determine the energy calibration. The spectrum of a hydrogen implanted crystalline silicon sample ('+'s) shows only hydrogen near the surface. The peak at 1000 keV is an experimental artefact which was independent of target material and hydrogen concentration. It was not present at beam energies less than 4 MeV.

University of Cape Town

of implanted (dotted) and unimplanted (diamonds) silicon. SIMNRA was used to simulate the spectrum and establish the implantation profile. The implanted sample shows a shoulder on the low-energy side of the surface hydrogen peak, indicating that the hydrogen was only implanted a short distance into the target.

Figure 10.3 shows the presence of a small percentage (2%) of hydrogen implanted in the bulk over a depth of between 200 and 500 nm. While this depth is not sufficient to separate the implanted hydrogen from the surface peak, it is visible as a shoulder on the surface peak. These depths are also insufficient for wafer cleaving experiments.

The second peak occurring to the left of the surface peak is an artefact of the analytical conditions under which the measurements took place. Experiments performed at different energies with different samples (including glass) show that it does not appear to be related to the hydrogen content of the target, but does depend strongly on beam energy, the lower the beam energy, the lower the energy of this peak. Later experiments performed verify that at an analysing beam energy of 3.6 MeV, this peak has disappeared completely from the ERDA spectrum.

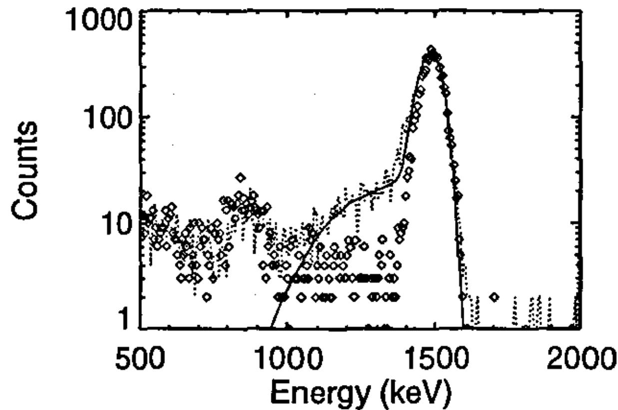

Figure 10.3: Superposition of ERDA spectra of unimplanted silicon (diamonds) and hydrogen implanted silicon (dotted). The fitted SIMNRA simulation result (solid) shows the surface hydrogen (1500 keV) and a narrow region of implanted hydrogen just below the surface.

10.4.2 Conclusions

These experiments have demonstrated that this PSII facility can implant hydrogen into silicon, but that the maximum implantation energy of the power supply is too low to be able to implant the hydrogen deep enough to support research into wafer cleaving. The power supply can be upgraded if this line of research is to be continued.

University of Cape Town

10.5 In-situ ERDA during annealing

The preliminary results from the previous investigation, which were presented at the 14th International Ion Beam Analysis conference (Dresden, 1999), included ERDA analysis of implanted samples which were heated in discrete steps to investigate the temperature dependence of the hydrogen. Those samples were mounted on a heating stage and a complete ERDA spectrum was recorded before the heating stage temperature was increased. By increasing the temperature by 100°C in each measurement, the temperature dependence of the hydrogen was measured in seven temperatures ranging from room temperature (22°C) to 600°C.

The ERDA spectra in figure 10.4 show that hydrogen is lost in two temperature regimes: as soon as the stage is heated (100°C), and between 300 and 400°C.

Since these results do not provide much temperature resolution, it was decided to follow the method described by C.C. Theron *et al* [The98a], and to dynamically record the ERDA spectra of samples while slowly increasing the substrate temperature to better examine the mobility of implanted hydrogen. Additionally, since this facility was not able to implant hydrogen with sufficient energy to obtain hydrogen at a depth useful for the industrial ion cleaving techniques, some high energy (60 kV) beamline implanted samples were obtained from N.W. Cheung[1] to collaboratively develop this technique.

[1] Prof. Nathan Cheung, Dept of EECS: UC-Berkeley, 513 Cory Hall #1770, Berkeley, CA, 94720-1770

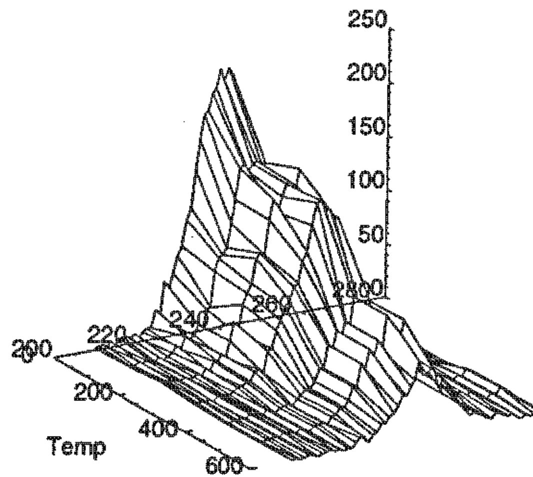

Figure 10.4: A wireframe surface showing the ERDA spectra of a hydrogen implanted sample at 7 heating stage temperatures (room, 100, 200, 300, 400, 500, 600°C)

University of Cape Town

10.5.1 Apparatus

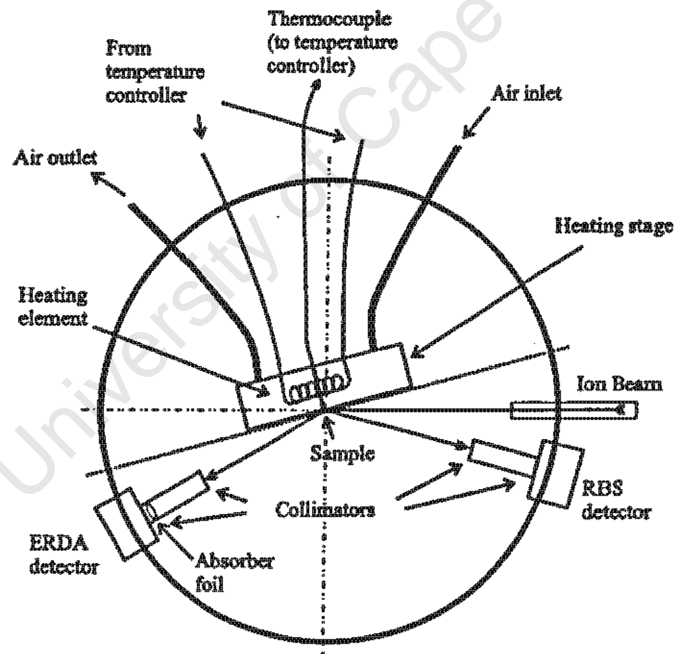

Figure 10.5: Experimental layout for the in-situ ERDA measurements.

This analysis was performed in the RBS chamber of the Materials Research Group. The experimental configuration is shown in figure 10.5. As can be seen from the figure, this chamber can be configured to use a heating stage.

RBS detector

The RBS detector was mounted at a scattering angle of 165°, and collimators were used to reduce the solid angle to 1.14 mSr. A ruggedised detector was used, which is less susceptible to the effects of being

heated by the radiative heat from the heating stage.

ERDA detector

The ERDA detector was mounted at a scattering angle of 30°. Collimators were used to reduce geometric straggling, and a solid angle of 0.46 mSr was derived experimentally. A 17 μm aluminium foil was used to absorb scattered alpha particles. The foil width was determined experimentally by solving for the measured energy loss of alpha particles emitted by Am^{241}. Since the alpha particles are emitted with a known energy, 5.4857 MeV, the energy loss in the foil can be established and used to determine the foil thickness.

The heating stage

The heating stage temperature is raised by a thermocoax heating coil, and controlled by an external temperature controller which monitors the heating stage temperature with a thermocouple. The thermocouple is inserted into a hole bored into the rear of the heating stage assembly to bring it to within 1 mm of the heating stage surface. Cooling is provided by compressed air forced through an attached cooling circuit. The sample to be analysed is mounted on the front face of the heating stage, which is rotated 75° in an ERDA configuration.

Other apparatus

A liquid nitrogen cold trap was fitted to the RBS chamber (figure 10.6) to improve base pressure and outgassing rates and a Balzers residual gas analyser (RGA) was fitted to the vacuum extraction port for analysis of the hydrogen gas levels in the RBS chamber exhaust gases. The RGA ionises the sampled gas stream and uses an ion mass selector (magnetic and electric fields) to measure the ion current (and hence concentration) of the gasses present.

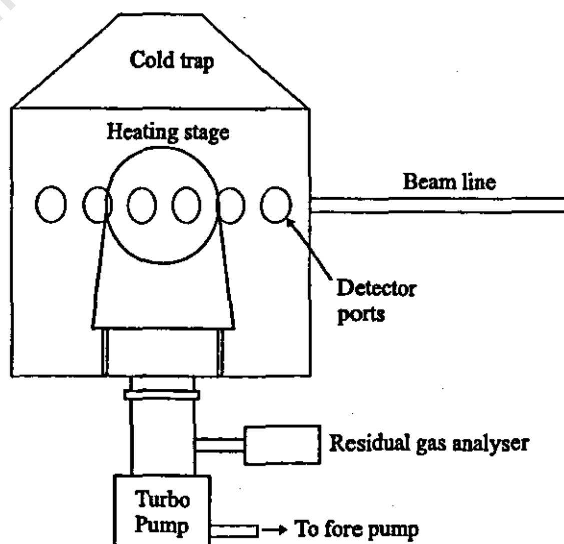

Figure 10.6: Side view of the RBS chamber in the ERDA configuration for in-situ ERDA analysis

University of Cape Town

Samples

Five implanted CZ-grown p-type Si (100) sample quarter-wafers were provided for these experiments. The implanted doses were confirmed experimentally (figure 10.13), with ion doses of approximately 1, 2, 3 and 8×10^{16} H.cm^{-2}. All samples were implanted with an ion-beam facility to assure a narrow implanted hydrogen profile. The original quarter-wafer samples were cut into 9 mm by 9 mm samples.

10.5.2 XSYS data processing

Data capture and processing at the Materials Research Group accelerator uses a CAMAC-based hardware acquisition system. The system uses XSYS software to handle and process data events from the connected hardware, such as x-ray and particle detectors, and to store the appropriate information according to the programmer/users needs.

In this application, ERDA and RBS particle energy information (energy spectra) were stored in temporary spectrum arrays. Chamber pressure, deposited charge and heating stage temperature were recorded at intervals called timer ticks. In the dynamic ERDA configuration, two different timing modes were used, depending on whether a short-time (80 minutes) or a long-time (500 minutes) analysis was performed.

University of Cape Town

Program operation

In the first attempt to acquire an ERDA *versus* temperature dataset, an iterative procedure was used;

1) The heating stage was heated to a pre-determined temperature,
2) The temperature was allowed to stabilise for two minutes,
3) An ERDA spectrum was acquired over a 10-minute interval.

This technique was too cumbersome with insufficient temperature resolution for good analysis of temperature dependent results. The in-situ ERDA analytical technique based on C.C. Theron's earlier in-situ RBS work was developed in order to address these issues.

This technique operates by acquiring spectra over short time intervals while slowly ramping the temperature of the heating stage. By later adding together groups of spectrum "slices", spectrum "windows" (with sufficient counts to be statistically meaningful) can be assembled for hydrogen depth profiling investigations. For example, an experimental data set would be acquired as follows:

- The measurement is started, with the acquired ERDA and RBS spectra being stored in temporary spectrum arrays.
- A defined clock 'tick' is programmed to occur every 3 seconds.
- With every tick, the chamber pressure, target temperature and deposited charge is recorded.
- After 10 ticks, the temporary RBS and ERDA spectra are stored in one of the 1000 spectrum-deep RBS and ERDA spectrum data structures, and the slot counter is incremented. These spectra are called 'slices'.
- The temporary spectra are cleared and the process repeats until all 1000 slices have been acquired.

Thus, in this example, the chamber pressure, target temperature and beam current are measured every 3 seconds, while the ERDA and RBS spectra are acquired every 30 seconds. Since the channel with the highest number of events has only about 5 to 10 counts in the these 30 second spectrum 'slices', it is usually necessary to add many slices together to improve the counting statistics. For example, by adding 20 slices together, 50 spectrum 'windows' (of both ERDA and RBS) can be obtained. In a typical experiment, the heating stage temperature is rapidly brought to 200°C, and then slowly ramped to 600°C over the 1000 slice measurement, or at a rate of 1.25°C per minute. Thus the temperature only increases by 12.5°C per 20-slice (10 minute) window. Better temperature resolution can be achieved at the expense of counting statistics by reducing the number of spectra added together in each window.

These spectra can be normalised either with respect to the integrated beam current or the integrated RBS yield over the sampling interval to enable quantitative comparisons between spectrum windows.

University of Cape Town

10.5.3 Measurements

RGA data

The residual gas analyser recorded the measured ion current of selected ion masses at regular time intervals. According to the RGA ion-mass catalogue, the molecular ion mass-number (M/e) of 2 corresponds only to H_2^+ and He^{++} ions. These gas fragments are, in turn, only produced by H_2 and He_2, respectively, and thus the M/e mass number of 2 was associated with hydrogen gas concentrations in the RBS chamber. While, the M/e mass number of 1 is only associated with H^+, this ion is a by-product of many molecular gasses, including H_2, H_2O and the C_xH_y-family. It is not deemed a reliable indicator of the presence of H_2 in the chamber.

Nuclear technique data

In the dynamic in-situ RBS measurements performed by C.C. Theron, the RBS spectrum height of a manually selected region of the RBS spectrum is used to quantify the charge×solid angle product used to normalise the data. This can be done since the RBS counts of a region well into the silicon bulk (for example) will not vary by any other process than as a result of variations in the beam current and random statistical variations in the RBS counts due to the statistical nature of the RBS measurement. Since the variations in the counts vary as $\sqrt{N}$, where N is the number of counts in the channel, once more than about 4,000 counts have been acquired, the uncertainty due to statistical counts is of the order of 1 to 2%, and variations in counts are dominated by current fluctuations. The normalisation matrices established by current normalisation and RBS bulk normalisation should be equivalent.

Single slice results

Typical, unnormalised ERDA and RBS spectra for the beginning of a low hydrogen dose ($\approx 1 \times 10^{16}$ ions cm^{-2}) and high dose ($\approx 8 \times 10^{16}$ ions cm^{-2}) measurements are shown in figure 10.7.

These spectra are normalised by RBS yield, thus to compare them, one would first have to determine the RBS normalisation factor. Roughly, examining figure 10.7A shows that the RBS yield around channel

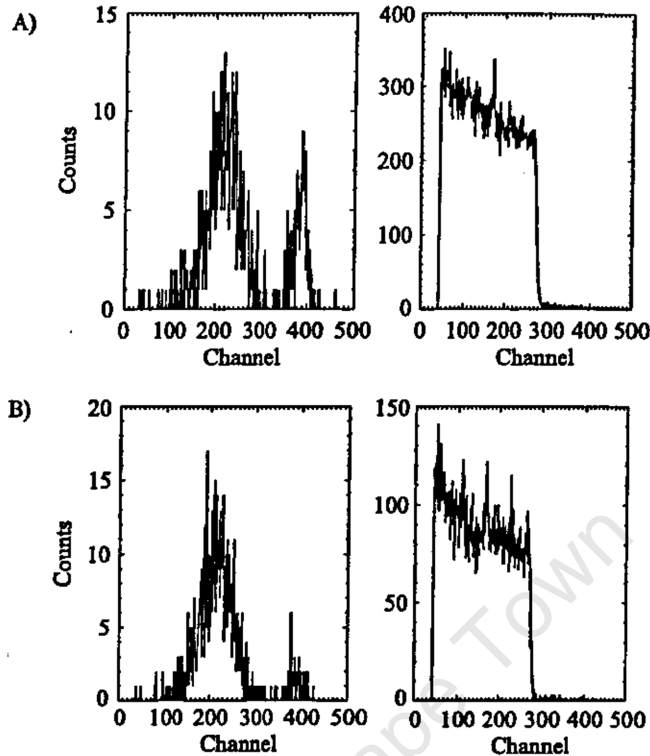

Figure 10.7: Typical unnormalised single slices (slice 100) of the ERDA (left) and RBS (right) spectra from (A) a low dose sample and (B) a high dose sample. The counts between the doses cannot be compared as the spectra have not been normalised.

University of Cape Town

100 is about 300, while for figure 10.7B, it is about 100. Thus the RBS normalisation factor is about 3. Multiplying the ERDA spectrum of figure 10.7B by 3 brings the implanted hydrogen ERDA peak (channel 220) to about 36, and the surface hydrogen ERDA peak (about channel 400) to about 6. One can now compare the surface hydrogen ERDA peaks of both figures and determine that they are both about the same, whereas the implanted hydrogen ERDA peak is about 3 times greater for the high dose implanted sample.

This rough calculation is not satisfactory for data processing and research purposes, and so proper RBS normalisation involves integrating a portion of the RBS spectrum, and programmatically calculating floating-point (real) normalisation factors.

20-slice windows

By adding 20 slices together, the spectra become smoother due to the improved count statistics. The typical ERDA slice windows from near the beginning and end of the experiment of a low (3×10^{16}ions cm^{-2}) and high (8×10^{16}ions cm^{-2}) dose experiment are shown superimposed in figures 10.8 and 10.9, respectively. The decreased bulk hydrogen is visible in these figures.

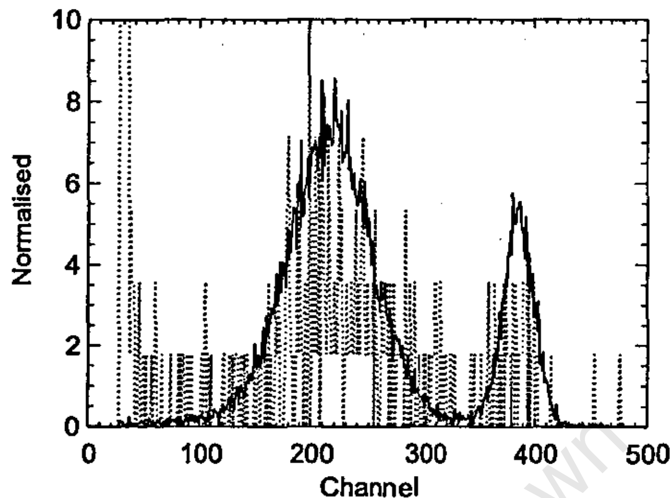

Figure 10.8: Superposition of RBS normalised 20-slice windows of the 4th and 42nd (out of 50) windows of a low dose (3×10^{16}ions cm^{-2}) sample. The greater ERDA yield of the 4th window (solid) than the 42nd window (dotted) is due to hydrogen leaving the sample as it was heated. The discrete steps visible in the (dotted) spectrum is an artefact of multiplying a low count spectrum by a large normalisation factor.

University of Cape Town

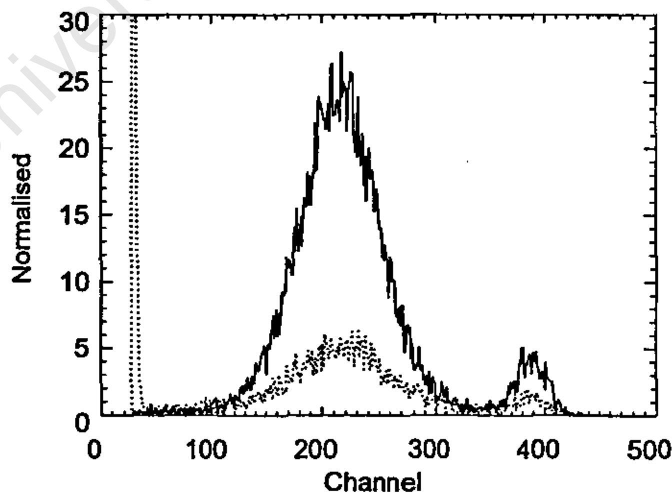

Figure 10.9: Superposition of RBS normalised 20-slice windows of the 4th and 42nd (out of 50) windows of a high dose (8×10^{16}ions cm^{-2}) sample. The greater ERDA yield of the 4th window (solid) than the 42nd window (dotted) is due to hydrogen leaving the sample as it was heated. The loss of hydrogen from the bulk is visible.

ERDA count contours

By adding a third dimension, time (or temperature) to the spectra, one can then plot all the spectrum windows described in the previous section in one figure. The surface described by such a figure could be plotted as a wireframe (or shaded solid) surface (like figure 10.17). However, since it is difficult to extract much qualitative information from such a figure, especially since often certain surface features obscure other features "behind" them, it is generally more productive to plot such data with contour lines of constant count. In figure 10.10, the contours of constant ERDA count are shown for a sample implanted with a high ion dose. Contour plots such as this are able to simultaneously show the drop in bulk hydrogen concentration, and give an indication as to the processes involved. If the hydrogen were to diffuse out into the neighbouring bulk region, this would be evident as peak broadening of the ERDA bulk, and be visible in the contour plot.

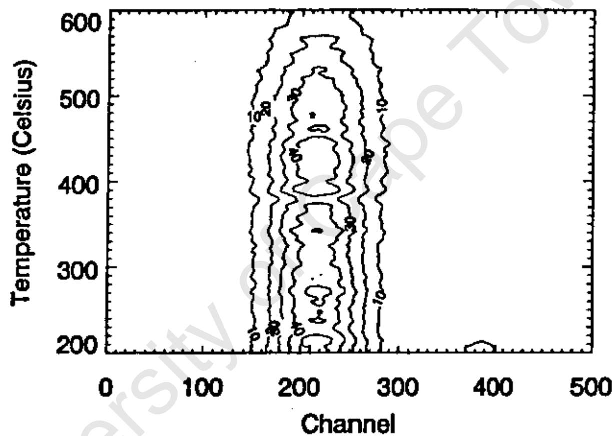

Figure 10.10: Contour plot of constant ERDA count as a function of heating stage temperature. The rapid loss of surface hydrogen is visible around channel 400. The bulk hydrogen is seen to be rapidly depleted above 500°C. Sample implanted with 8×10^{16}ions cm^{-2}.

University of Cape Town

Integrated bulk hydrogen

In figures 10.8 and 10.9, the bulk hydrogen (the hydrogen implanted into the bulk of the Si substrate) is seen to be contained between channels 80 and 350. Thus, for each window, the integrated bulk hydrogen can be calculated by integrating the ERDA spectrum between the appropriate channels. A plot of integrated bulk *versus* temperature is given in figure 10.11. Figures of this form show the temperature dependence of the bulk hydrogen and can be used to extract the temperature dependent phenomena. By adding RGA gas analysis data to these figures, any correlation between hydrogen concentrations in the vacuum vessel and structures in the integrated bulk hydrogen *versus* temperature graphs will be apparent.

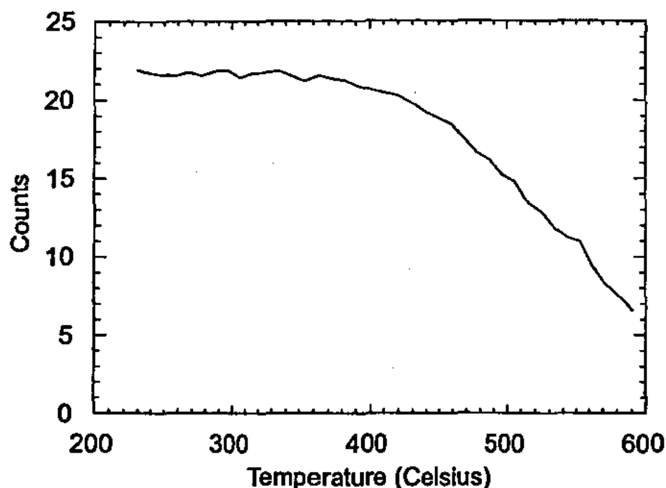

Figure 10.11: Plot of integrated bulk hydrogen. By integrating the ERDA counts between channels 60 and 330, the total bulk hydrogen contribution can be determined. This figure shows the relative decrease in hydrogen concentration within the silicon bulk as a function of sample temperature. Sample implanted with 8×10^{16}ions cm^{-2}

University of Cape Town

RBS integrated bulk

Since the composition of the silicon bulk does not change during the experiment, a suitably chosen portion of the RBS bulk spectrum can be used for spectrum normalisation. For each experiment analysed, a portion of the RBS bulk was identified and integrated in the same manner as the ERDA bulk integration described above. The RBS and ERDA spectra were then normalised with respect to these values.

10.5.4 Results

During analysis of the data, it quickly became apparent that the surface hydrogen was rapidly depleted as the heating stage temperature reached 200°C. This is expected since the dominant source of surface hydrogen, once the wafers had been cleaned, is due to atmospheric water vapour. Since the analysis starts with the substrate temperature being ramped to 200°C, any water vapour is quickly boiled off and only near surface hydrogen remains.

The integrated bulk *versus* temperature spectra can be used to examine the temperature dependence of the bulk hydrogen density on substrate temperature.

Temperature dependence - high dose

Figure 10.12 show the RBS normalised superposition of three different in-situ measurements of samples implanted with 8×10^{16} H^+ cm^{-2}. The figure shows the identical profile for each of the three samples (E01, E07 and E09). All three measurements exhibit almost the same temperature profile.

Examining figure 10.12, one can see that the retained bulk hydrogen dose rate is relatively constant between 200 and 350°C. The bulk hydrogen concentration decreases steadily above 350°C.

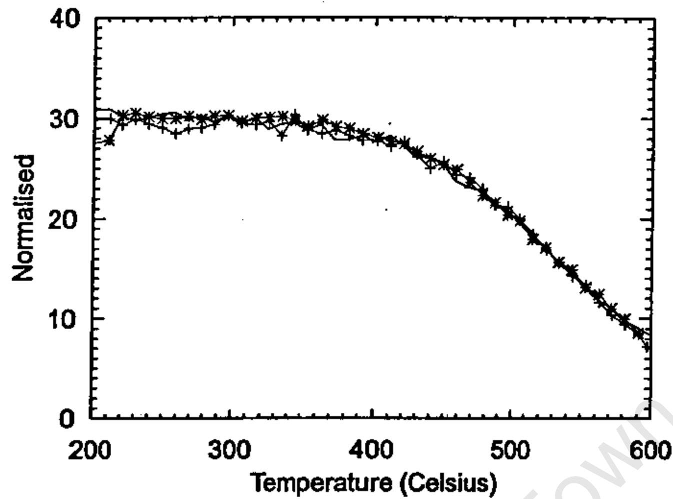

Figure 10.12: Superposition of three different integrated bulk ERDA measurements *versus* temperature for samples implanted with 8×10^{16} H^+ cm^{-2}. There is little variation in the temperature profile for the different samples.

University of Cape Town

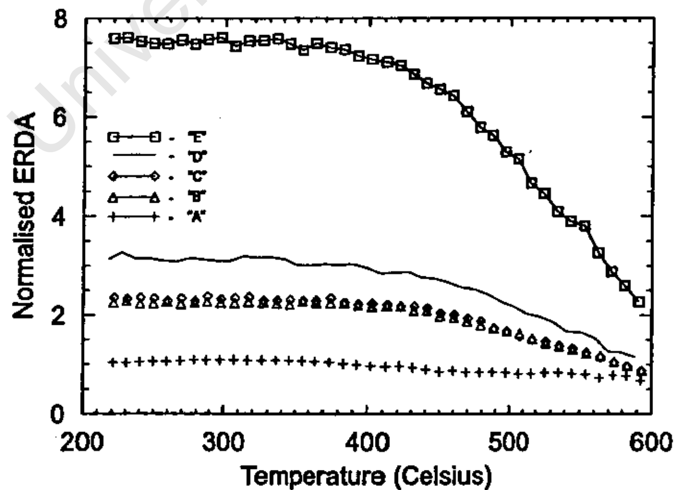

Figure 10.13: Superposition of integrated bulk ERDA measurements for each of the different sample doses. ERDA analysis was used to determine the following doses: A - 1×10^{16} H^+ cm^{-2}, B,C - 2×10^{16} H^+ cm^{-2}, D - 3×10^{16} H^+ cm^{-2}, E - 8×10^{16} H^+ cm^{-2}.

Temperature dependence *versus* dose

Figure 10.13 shows the integrated bulk ERDA measurements for samples of different implanted doses. ERDA analysis was used to determine the implant dose, to determine that samples A,D,E were implanted with doses of 1, 3 and 8×10^{16} H^+ cm^{-2}, respectively. Samples B and C were both implanted with a dose of about 2×10^{16} H^+ cm^{-2}. To examine if the temperature dependence of the implanted hydrogen varies with implantation dose, one would compare the temperature/dose dependence data of all implanted doses. By normalising the data of these samples such that they are all equal at a (reasonably arbitrary) temperature, and superimposing the results, any variation should be visible. Figure 10.14 shows the five samples normalised according to the measured integrated bulk ERDA count at 300°C, where it is clear that, except for the lowest dose sample, all the samples show the same temperature dependence. The deviation in the lowest dose sample is possibly caused only by poor counting statistics and errors introduced by multiplying by a large normalisation factor.

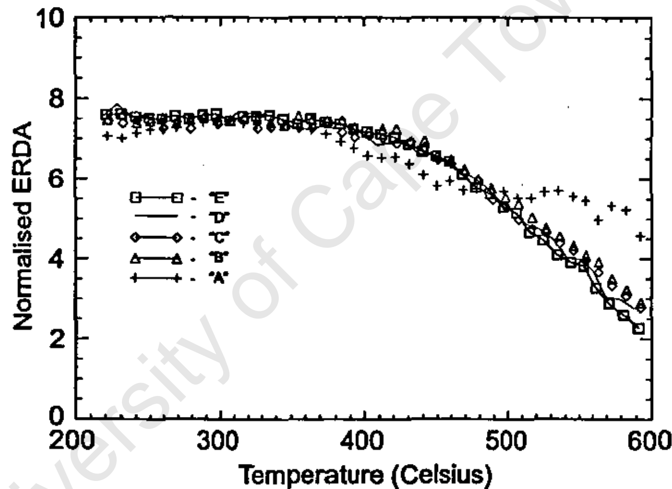

University of Cape Town

Figure 10.14: Superposition of normalised integrated bulk ERDA measurements *versus* temperature for all five implanted doses. Spectra normalised to be equal at 300°C. The deviations in the low dose sample (A) are probably due to rounding errors in the normalisation process.

Thus it can be seen from figures 10.12 and 10.14 that the dose-temperature profile of retained hydrogen in the sample bulk is independent of dose.

RGA results

Figure 10.15 shows the superposition of the ERDA measurements (diamonds) of an $8 \times 10^{16} H^+$ cm^{-2} implanted sample, and the RGA measurements (solid) of the concentration of ion fragments with mass number $M/e = 2$, as a function of heating stage temperature. The RGA analyser measured the relative concentrations of ionised molecular fragments from a pick-up mounted in the vacuum pump port of the RBS chamber (figure 10.6). As can be seen in figure 10.15, the peak current for this molecular fragment (mass $M/e = 2$) occurs at about 410–420°C. There is a perturbation in the integrated ERDA data at about this temperature. The correlation between this perturbation and the increased RGA data can be

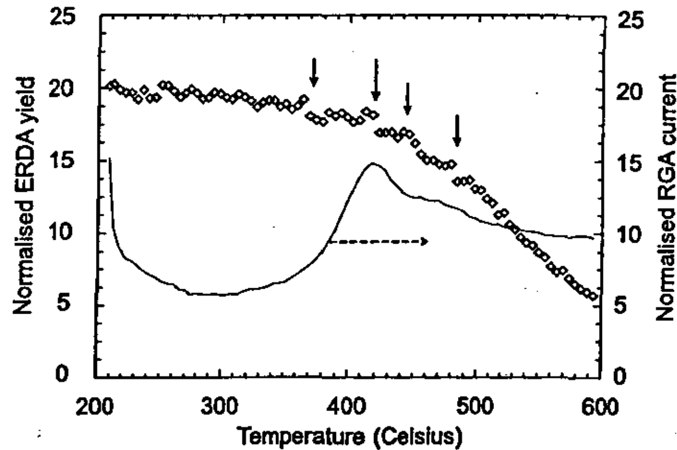

Figure 10.15: Superposition of integrated bulk ERDA measurements (diamonds) and RGA measurements (solid) of mass number, M/e = 2, *versus* temperature for a sample implanted with $8 \times 10^{16}H^{+}$ cm^{-2}. There are small drops (arrows) in the ERDA spectrum in the temperature region of the peak in the RGA measurements (around 370 – 490 °C).

University of Cape Town

interpreted to suggest the action of a real physical process, and not just random statistical variations.

10.5.5 Other features - RBS spectra of sample E09

Occasionally, one of the samples demonstrate some interesting features. In particular, the RBS spectra of sample E09 (figure 10.16) showed an interesting change in silicon yield in the near-surface region *versus* temperature. This reduced yield is probably due to channelling of the analysing ion beam in the near surface regions (the channelling stops at the depth of the implanted hydrogen (§7.1.4.1, figure 7.6).

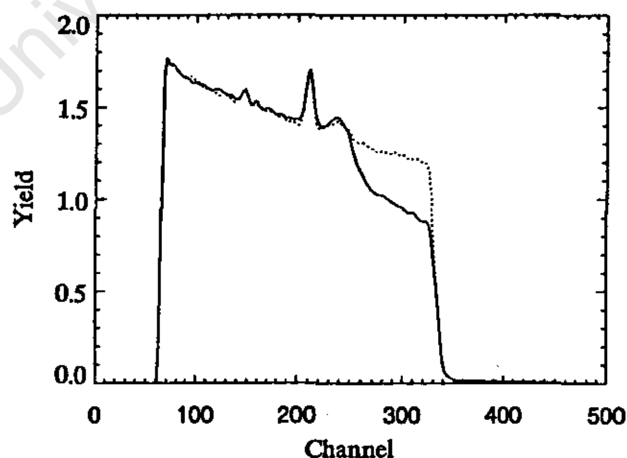

Figure 10.16: Superposition of two RBS windows showing spectra measured near the beginning (dark) and later (light) in the in-situ experiment. The reduced yield (probably due to channelling) near the surface is visible.

As can be seen in figure 10.16, which shows the time-integrated windows of slices 80 through 100 and slices 840 through 860 (heating stage temperatures of about 240°C and 600°C, respectively) the surface

edge of the RBS spectrum showed a clear change in yield.

The full evolution of this feature can be seen in figure 10.17 which presents a 3-D wireframe of the RBS spectra *versus* temperature. In this figure it can be seen how the yield starts to return to 'normal' at about 300°C, reaching the more conventional RBS yield around 370°C.

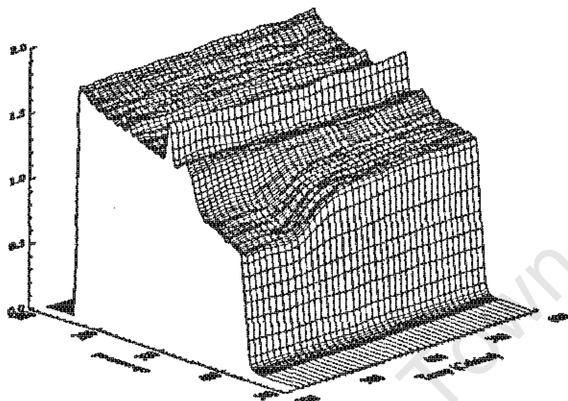

Figure 10.17: Wireframe figure of all the RBS spectra showing the evolution of a shallow-depth Si structure as a function of heating stage temperature.

The key features of these spectra are a reduced RBS yield similar to the channelling phenomenon between the surface edge (channel 330 for about 70 channels, a hump at channel 240 (the yield of which decreases as the sample is heated), an oxygen peak at about channel 210 and a small carbon peak at about channel 150. Since the hump at channel 240 occurs at about the same location as the lattice damage peak of §7.1.4.1.

SIMNRA was used to determine that the hump at channel 240 corresponds to a feature 580 nm into the silicon bulk, which corresponds to the expected implantation depth of 60 keV hydrogen.

For <100> silicon, the angle between the [100] plane and the [103] plane is 71.6°, and between the [100] plane and the [104] plane is 76.0°. Since the target has been rotated by 75°, there may be channelling down a [104] axis.

The temperature dependence of the channelling phenomenon may be due to lattice expansion; the lattice 'channel' would be very narrow and hence easily disturbed by a slight increase in lattice expansion. Of course, it is also possible that the silver paste used to bond the sample to the heating stage settled slightly, causing a slight shift in sample orientation.

10.5.6 Conclusions

The features discussed in the previous sections show a correlation between the observations of Lu*et al* [Lu98a]. The blister formation at 450°C correlates with the observed hydrogen loss at this temperature, while further losses can be attributed to the increased blistering which occurs with additional heating.

A surprising result is the almost perfect correlation between the normalised profiles of all the implant

University of Cape Town

doses analysed. Irrespective of implanted dose, most samples show an almost identical dose-temperature profile, indicating that either microblisters (or cracks) are still forming even at the low implantation dose of $1 \times 10^{16}\text{H}^{+}\ \text{cm}^{-2}$, or that the hydrogen losses are due purely to thermal diffusion. This result was not anticipated since one would expect a different temperature profile if hydrogen loss occurred due to blister formation *versus* thermal diffusion. It is also possible that the hydrogen dynamics that occur when blisters form can not be tracked with ERDA techniques, since ordinary diffusion of the hydrogen into the wafer bulk would be visible in figure 10.10 as contour broadening, and while some slight broadening is visible between 200 and 320 minutes (400 to 500°C), it is not convincing evidence.

Future work

All the analytical possibilities of this technique have not yet been exhausted, as it is still possible to perform additional experiments with lower temperature gradients and with greater time and energy resolution. Additionally, the ERDA techniques only indicate the approximate depth and concentration of hydrogen within the wafer, but not where, structurally, the hydrogen is in the lattice (interstitial, in a lattice site, or, if the lattice is sufficiently damaged, as bubbles within voids in the lattice).

In order to determine where the hydrogen exists within the silicon lattice, other techniques, such as neutron scattering or a comparison of channelling ERDA experiments from the different channelling angles, could possibly yield useful results.

10.6 Summary

While the preliminary research into implanting samples with hydrogen at this facility show that the low energies available (maximum 30 kV) are not sufficient to implant the hydrogen deep enough to experiment with wafer cleaving techniques, the analytical tools available in the Ion Beam Analysis division have a lot to contribute to research in the solid state chemistry of the wafer cleaving process.

Until this facility is upgraded to increase the available implantation voltage to something appropriate (60 kV), research will have to be performed in collaboration. Collaborations with other facilities which do have the ability to implant hydrogen will combine the abilities of both institutions to push back the boundaries of knowledge in this field of research.

In this manner it was possible to use samples from Berkeley to experimentally determine that the hydrogen solubility of the silicon bulk is independent of wafer temperature.

University of Cape Town

University of Cape Town

Chapter 11

Conclusions

This thesis describes the construction and operation of a 30 kV plasma source ion implantation facility as well as the analytical techniques available for sample examination and characterisation at the Materials Research Group of the National Accelerator Centre, Faure, South Africa.

In addition to some basic research into the characteristics of the bremsstrahlung induced x-ray emission and the development of an in-situ ERDA technique for examining the temperature dependent behaviour of hydrogen in silicon, results of some experiments using this facility for surface hardening of materials used in the local South African industry is also presented.

University of Cape Town

11.1 The implantation facility

This facility has been built using a modular design philosophy. The key components, namely the plasma chamber, the RUP-4a pulsed power supply, and control apparatus can all be used independently for other applications, and can be independently modified or upgraded. Even the RUP-4a pulsed power supply is modular in design and can be upgraded to independently increase both the peak current switching ability (by the addition of another tetrode switch) and the maximum implantation voltage (up to 45 kV, by changing the capacitor charging power-supply unit).

The plasma chamber presently uses a DC-discharge system with hot filaments and an applied ionising potential for plasma formation, however an RF power feedthrough has been fitted to the chamber to allow for RF plasma generation. A 13.65 MHz RF system has been donated to the facility.

The control system has been designed to allow the facility to be operated remotely. By using two computers, one for data capture and processing, and the other to run the user front end, the control system operates by using the TCP/IP network protocol to pass commands and data between the two computers. In principle, collaborators at external institutions can implant samples without coming to the National Accelerator Centre, requiring only the services of someone to actually change and mount samples for them.

11.2 X-ray emission research

Time and energy resolved x-ray measurements were performed during a typical implantation experiment. These measurements, which were the first of their kind presented to the PSII community, used the x-ray detector hardware of the nuclear microprobe. The measurements were presented at the 4th PBII workshop in Dearborn, Michigan, USA in June 1998.

These results indicate the presence of a large component of low energy (10 kV) electrons during a 20 kV implantation. The origin of these lower energy electrons has not been reliably established.

The results also suggest that there is a correlation between the measured x-ray flux and the mean current. There was a suspicion that the high initial implantation current that is measured during the first μs of the implantation pulse may have been caused by capacitive or displacement current effects, and did not necessarily indicate a high ion current to the target. The high x-ray flux measured during this initial period is taken to support the existence of a large ion current, causing a high flux of secondary emitted electrons, which, in turn, produce x-rays when the hit the chamber walls.

11.3 Metal applications

Several experiments were performed to investigate the ability of this facility to improve the surface microhardness of some metals used in typical industrial applications. These preliminary experiments were successful in demonstrating the ability of this facility to implant nitrogen and measurable improvements in surface microhardness were achieved. One set of experiments were performed as a commercial service.

11.4 Silicon applications

While the available implantation energies are presently too low to attempt silicon wafer cleaving experiments, an experimental technique was developed to allow analysis of the temperature dependent behaviour of the implanted hydrogen within the silicon matrix. Preliminary results using the ERDA technique indicate that the temperature regulated hydrogen mobility is independent of implantation dose.

11.5 Future projects

Future research that can be performed with this facility include:

- Further research into the x-ray measurements to establish what relationship can be found between surface condition and x-ray flux. It is suspected that secondary electron emission yield increases as the surface is roughened by sputtering. This change in yield should be measurable as an increased x-ray flux and would be visible in differences in x-ray yield at the beginning *versus* after a sufficient dose has been implanted.
- Implantation of polymer materials. Especially with the RF plasma source to reduce local heating caused by the filaments, further research into the low temperature implantation of polymers and other exotic materials to alter their surface structure can be performed.

University of Cape Town

- Low voltage (less than 15 kV) implantation research, in particular, applications to solid state research. By using this facility to implant dopants, it should be possible to construct complex mixtures of otherwise insoluble materials. With the RF plasma source it becomes possible to implant oxygen to slowly alter the elemental composition of, for example, low temperature superconductors, to maximise the superconductive properties of the material.
- Construction of an electron energy analyser to examine the energy spectrum of ejected electrons directly. X-ray measurements can only indirectly measure the energy of the secondary electron and much information is lost in the process. It would be much more informative to measure the electron energy distribution directly.

University of Cape Town

University of Cape Town

Appendix A

PSII sheath theory

During the plasma implantation process high negative voltages are applied to the PSII target. These high voltages extract the positive ions from the plasma and implant them into the target surface. However, a full understanding of this process requires an understanding of the potential sheaths which exist around bodies in plasmas, and the sheath dynamics during the implantation process.

Langmuir [Lan29a] was the first to describe the plasma sheath near the plasma chamber walls. Plasma sheaths surround all objects immersed in a plasma and evolve to counteract the electrical disturbance caused by the object. A simple explanation of sheath formation is based on the different velocities of the ions and electrons. Since the plasmas typical of this facility have the electron temperature, T_e much greater than the ion temperature T_i, the electron velocity ν_e is much greater than the ion velocity ν_i. Thus the rate of electron loss to any object in a plasma is greater than the rate of ion loss, leaving the object with a net negative potential. The electric field of this potential does not penetrate far into the plasma since Debye shielding restricts it to a size of the order of a few Debye lengths λ_D. This region is called a sheath. Thus sheaths act to confine the more mobile of the plasma charged species within the plasma to maintain charge neutrality.

Since previous results of plasma sheath measurements [Mey96a] under similar conditions to those described in this thesis have demonstrated that the sheath rapidly acquires a spherical shape independent of target shape, the theory of sheath formation and evolution can be limited to this case. However, since planar sheath theory is very simple it will also be covered. Assuming that the target is small compared to the plasma chamber, spherical sheath theory can be applied in general since, even in the case of PSII where a high voltage is applied to the target, the expanding sheath rapidly acquires a spherical shape. In the absence of the high voltage, the sheath thickness is of the order of the Debye length (λ_D), and hence effectively conforms to the target shape.

A.1 Time scales

There are three timescales of interest in PSII sheath theory:

- The electrons are much more mobile than the ions and react on a timescale of the order of the

University of Cape Town

electron plasma period $\tau_{\mathrm{pe}} = \sqrt{\frac{\epsilon_0 m_e}{n_e q_e^2}}$. When the pulse is first applied the electrons respond very rapidly and are repelled from the target, leaving behind the so-called ion matrix sheath.

- On a much longer timescale, of the order of the ion plasma period $\tau_{\mathrm{pi}} = \sqrt{\frac{\epsilon_0 m_i}{n_i q_e^2}}$ the ions start to move toward the target. On this timescale the ions are attracted to the target and the plasma sheath grows to uncover more ions to maintain the implantation current. The electrons continue moving away from the target so as to keep enough ions between them and the target to shield the target potential, and the sheath edge propagates outwards.
- The final timescale is determined by the pulse width τ_{pulse}. Normally, the sheath would expand outward until it reaches that distance described by the steady state Child Law [Chi11a], however in the PSII process the voltage pulse width is typically sufficiently short that the voltage is returned to zero before the steady state sheath forms. If the pulse length is very long, however, care has to be taken to ensure that the expanding sheath does not reach the chamber walls.

Since plasma sheaths are defined by electron and ion densities, sheath theories always use a timescale defined by the ion plasma period.

A.2 Dimensionless co-ordinates

It is useful to define dimensionless quantities for all the co-ordinates used in the subsequesnt theory:

$$\begin{aligned} \tilde{r} &= \frac{r}{\lambda_D} && \text{distance} \\ \tilde{\phi} &= \frac{e\phi}{kT_e} && \text{potential energy} \\ \tilde{n}_e &= \frac{n_e}{n_0} && \text{electron density} \\ \tilde{n}_i &= \frac{n_i}{n_0} && \text{ion density} \end{aligned} \tag{A-1}$$

A.3 The initial plasma sheath

For potentials close to the plasma potential, the sheaths around conductors are of the order of the Debye length λ_D. During a PSII pulse, however, the target potential is much greater than the plasma potential ($\phi_p \approx 10$eV *versus* $\phi_{\mathrm{target}} \approx -10$ keV to -100 keV). Under these conditions the initial plasma sheath, or ion matrix sheath, forms as the electrons are expelled from the sheath region by the high target potential. Conrad [Con87a] describes how to establish the thickness of this initial sheath and outlines a simplified theory describing its subsequent evolution:

The potential profile is obtained from Poission's equation

$$\frac{d^2\phi}{dr^2} + \frac{\alpha}{r}\frac{d\phi}{dr} = -\frac{1}{\epsilon_0}e(n_i - n_e) \tag{A-2}$$

where ϕ is the applied pulse potential, n_i and n_e the ion and electron densities, and α=0, 1 and 2 for planar, cylindrical and spherical geometries respectively. Restricting the analysis to the formation of the initial plasma sheath, that is when the potential is first applied to the electrode, it is assumed that the plasma is of uniform density and $n_0 = n_i = n_e$. For the case of planar geometry the spatial variable r is measured from the surface of the electrode, while for cylindrical and spherical geometries, r is the radial distance from the centre of the electrode.

University of Cape Town

Substituting for the dimensionless co-ordinates defined by equations A-1 into equation A-2, yields the dimensionless Poisson's equation

$$\frac{d^2\tilde{\phi}}{d\tilde{r}^2} + \frac{\alpha}{r}\frac{d\tilde{\phi}}{d\tilde{r}} = -(\tilde{n}_i - \tilde{n}_e) \tag{A-3}$$

During this initial sheath phase, the electron density in the region of interest is zero, and the ion density is equal to the background density, so equation A-3 reduces to

$$\frac{d^2\tilde{\phi}}{d\tilde{r}^2} + \frac{\alpha}{r}\frac{d\tilde{\phi}}{d\tilde{r}} = -1 \tag{A-4}$$

Evaluating equation A-4 subject to the following boundary conditions:

- The potential at the electrode position, r_0, must be equal to the applied potential ϕ_0,
- and the electric field must vanish at the sheath position, r_s,

that is

$$\tilde{\phi} = \tilde{\phi}_0 \equiv \frac{q_e\phi_0}{kT_e} \quad \text{at} \quad \tilde{r} = \tilde{r}_0 \equiv \frac{r_0}{\lambda_D} \tag{A-5}$$

$$\frac{d\tilde{\phi}}{d\tilde{r}} = 0 \quad \text{at} \quad \tilde{r} = \tilde{r}_s \equiv \frac{r_s}{\lambda_D} \tag{A-6}$$

Solutions are found using standard ordinary differential equation techniques, and are:

Planar geometry:

$$\tilde{\phi}(\tilde{r}) = -\tilde{\phi}_0 + \tilde{r}_s(\tilde{r} - \tilde{r}_0) + (\tilde{r}_0^2 - \tilde{r}^2)/2 \tag{A-7}$$

Cylindrical geometry:

$$\tilde{\phi}(\tilde{r}) = -\tilde{\phi}_0 + (\tilde{r}_s^2/2)\ln(\tilde{r}/\tilde{r}_0) + (\tilde{r}_0^2 - \tilde{r}^2)/4 \tag{A-8}$$

Spherical geometry:

$$\tilde{\phi}(\tilde{r}) = -\tilde{\phi}_0 + (\tilde{r}_s^3/3)(1/\tilde{r}_0 - 1/\tilde{r}) + (\tilde{r}_0^2 - \tilde{r}^2)/6 \tag{A-9}$$

Expressions for the sheath position are found by setting the potential to zero in equations A-7–A-9. By defining f to be the ratio of sheath radius to electrode radius, $f \equiv \tilde{r}_s/\tilde{r}_0 = r_s/r_0$, the results are:

Planar geometry:

$$(f-1)^2 = 2\tilde{\phi}_0/\tilde{r}_0^2, \tag{A-10}$$

Cylindrical geometry:

$$f^2\ln f^2 - f^2 + 1 = 4\tilde{\phi}_0/\tilde{r}_0^2, \tag{A-11}$$

Spherical geometry:

$$2f^3 - 3f^2 + 1 = 6\tilde{\phi}_0\tilde{r}_0^2. \tag{A-12}$$

Rewriting in dimensional units, equations A-10 and A-12 can be expressed as

Planar:

$$r_s = (2\epsilon_0\phi_0/n_0q_e)^{\frac{1}{2}} \text{ or } r_s(\text{cm}) = 1050[\phi_0(\text{volts})/n_0(\text{cm}^{-3})]^{\frac{1}{2}} \tag{A-13}$$

Spherical:

$$r_s \simeq (3\epsilon_0\phi_0 r_0/n_0q_e)^{\frac{1}{3}} \text{ or } r_s(\text{cm}) \simeq 118\left(\frac{\phi_0(\text{volts})r_0(\text{cm})}{n_0(\text{cm}^{-3})}\right)^{\frac{1}{3}} \tag{A-14}$$

Plotting equations A-13 and A-14 in figure A.1, the dependance of ion-matrix sheath width on target potential and plasma density can be seen.

University of Cape Town

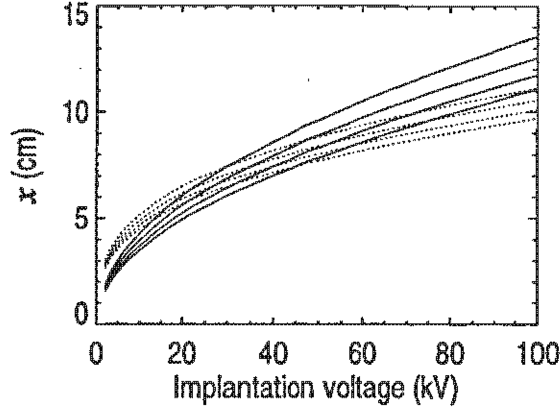

Figure A.1: Planar (dashed) and spherical (solid) ion-matrix sheath width as a function of target potential for different densities. Spherical calculations use a 10 cm diameter target. Densities are (top to botton) 6, 7, 8 and 9 $\times 10^8$ cm^{-3}

University of Cape Town

A.4 Sheath Evolution

Once the ion matrix sheath has formed, numerous theories have been proposed to describe subsequent sheath evolution, in particular Lieberman [Lie89a] proposes a one dimensional planar model describing sheath evolution due to the application of a voltage step [V=0, for $t < 0$, $t > t_p$, and $V = -V_0$, $0 \leq t \leq t_p$]. This model is based on the following assumptions:

- The ion flow is collisionless,
- Compared to the ions, electron motion is inertialess,
- The applied voltage V_0 is much greater than T_e, so $\lambda_D \ll S_0$ and the sheath edge at S is abrupt,
- During implantation a quasi-static Child-law sheath forms,
- The electric field is assumed to remain constant for ion motion through the sheath.

Scheuer [Sch90a] *et al* further simplify the Lieberman model which solves the Child-Langmuir law [Lan23a] for space-charge limited emission quasi-statically,

$$j = \frac{4\epsilon_0}{9}\sqrt{\frac{2q_e}{M}}\frac{V^{\frac{3}{2}}}{S^2} \quad \text{(A-15)}$$

where j is the current density crossing the sheath edge, M is the mass of the ion, V is the magnitude of the applied potential, and S is the distance of the sheath edge from the target. Based on the assumption that

$$j = nq_e(\frac{ds}{dt} + \nu_d) \quad \text{(A-16)}$$

where ν_d is the ion drift velocity which is equal to the ion acoustic speed, C_s. By assuming that $\nu_d = 0$, the ions are stationary until the sheath reaches them, and equations A-15 and A-16 are solved to give Planar:

$$\frac{ds}{dt} = \frac{4\epsilon_0}{9n}\sqrt{\frac{2}{q_e M}}\frac{V^{\frac{3}{2}}}{S^2} \quad \text{(A-17)}$$

which is intergrated analytically to yield

$$S = S_0 \left[\frac{2}{3}\omega_{\mathrm{pi}}t + 1\right]^{\frac{1}{3}} \tag{A-18}$$

If the more realistic case of non-stationary plasma ions is considered, equation A-17 becomes

$$\frac{ds}{dt} = \frac{4\epsilon_0}{9n}\sqrt{\frac{2}{q_e M}}\frac{V^{\frac{3}{2}}}{S^2} - \nu_d \tag{A-19}$$

which is integrated numerically.

In spherical geometries, the Child-Langmuir relation is written as

$$j = \frac{4\epsilon_0}{9}\sqrt{\frac{2q_e}{M}}\frac{V^{\frac{3}{2}}}{r^2\alpha^2} \tag{A-20}$$

where α is given by Xia and Chan [Xia93a] as $\alpha^2 = \gamma^2 - 0.6\gamma^3 + 0.24\gamma^4 - 0.074\gamma^5$, where $\gamma = \ln(r/r_0)$, producing the following differential equation for sheath evolution in spherical geometries:

$$\frac{dr}{dt} = \frac{4\epsilon_0}{9n}\sqrt{\frac{2}{q_e M}}\frac{V^{\frac{3}{2}}}{r^2\alpha^2} \tag{A-21}$$

They present a solution for the ion matrix sheath as

$$R_0 \simeq (3A)^{\frac{1}{3}} + (1/2), \tag{A-22}$$

where $A = \frac{q_e V \lambda_D^2}{kT_e r_t^2}$. Figure A.2 shows a comparison between the theoretical planar and spherical sheath

University of Cape Town

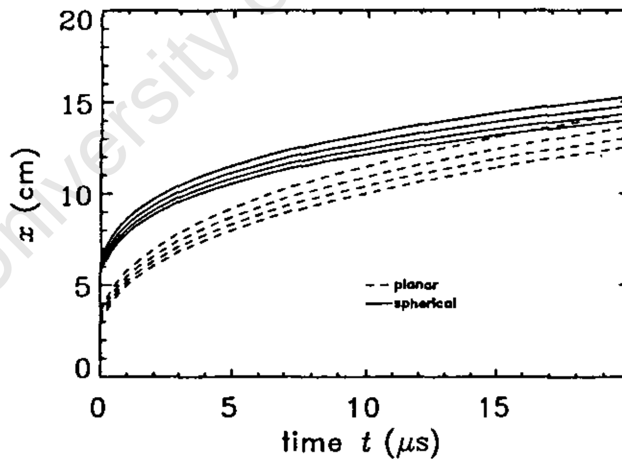

Figure A.2: A comparison of planar and spherical sheath evolution. Plots are for densities (bottom to top) of 6, 7, 8 and 9 $\times 10^8$ cm^{-3}. Target potential is 20 kV, spherical target diameter of 10 cm.

evolutions for various densities. It is produced by numerically integrating equations A-17 and A-21.

A.5 Extensions to the basic theory

So far, only planar and spherical targets have been considered. For targets which two-dimensional structure, such as edges, concave and concave wedges and other two-dimensional structures, sheath formation and evolution is no longer so simple.

A.5.1 Sheath conformality to target shape

Donnelly and Watterson [Don88a] and Watterson [Wat88a] developed theory and a simulation which showed that the sheath thickness reduced in thickness near a convex edge, with a corresponding increased dose nearer the wedge apex. However, the ion dose incident on the edge apex decreased, dropping to zero for a knife edge. Lim *et al* [Lim91a] presented experimental results of phase measurements of ion acoustic waves launched from concave and convex structures which supported these results.

A.5.2 Additional considerations: pulse rise-time, displacement current, collisions, etc.

Stewart and Lieberman [Ste91a] extended the theory of sheath evolution by considering pulses of finite rise time, deriving a time dependent expression for equation A-18. Wood [Woo93a] considered the effects of displacement current across the sheath and ion depletion caused by multiple pulse effects (repeat frequency high enough such that the plasma does not recover). Collisional plasmas were considered by Wang *et al* [Wan93a] (one dimensional), Sheridan and Goeckner [She94a] (collisional ion fluid model) and Qin *et al* [Qin94a] (multispecies plasma). Mändl *et al* [Man98a] considered the effects of the pre-sheath, which accelerates ions into the plasma sheath.

A.5.3 One dimensional special cases

Sheridan has considered many different one-dimensional special cases, such as into a cylindrical bore and trench [She93b, She95C].

A.5.4 Two-dimensional simulations

Numerical simulations around two-dimensional corners have been presented by Hong and Emmert [Hon94a] and Sheridan [She95b, She96b].

A.5.5 Plasma filling-in

Plasma filling in after the pulse has been turned off has been treated by Mändl *et al* [Man98a], Wood [Woo93a] and En *et al* [En94a].

University of Cape Town

Appendix B

Ion - surface physics

B.1 Ion induced sputtering

In ion implantation, ions are introduced into a target by energetic collision. However, high velocity ion projectiles penetrating into a target can also cause target ions to be removed through a process called sputtering. The following sections summarise the ion induced sputtering theory presented by Nastasi, Mayer and Hirvonen [Nas96a].

For low doses the depth concentration profiles are well understood and predicted to have a Gaussian distribution centred about an average projected range, R_p. For high doses ($\geq 10^{17}$ cm^{-2}), the concentrations of implanted ions approaches tens of atomic percent, and other factors, such as sputtering and induced migration can significantly affect concentration profiles.

In particular, sputtering is the process whereby an incident projectile ion erodes the target by removing target atoms via collisions as it penetrates the target. The generally accepted theory by Sigmund [Sig81a] explains that sputtering is based on a collision cascade and that the incident ion induces collisions in a volume (the collision cascade) surrounding the ion track. The energy of the incident ion is dissipated amongst the atoms in the collision volume, but only collisions near the target surface are effective at knocking atoms out of the target. Most of the sputtered atoms originate from the first few atomic layers and hence the greater the number of collisions within the near-surface region, the greater the sputtering yield, Y. Thus the sputtering yield is proportional to the nuclear stopping power of the incident projectile in the near surface region.

The sputtering yield ranges from 0.5 to 20, depending on projectile ion species, projectile energy, geometry, and target material, and sets a limit on the maximum concentration of implanted ions. For direct ion implantation of projectiles into a target, the maximum implanted concentration is inversely proportional to the sputtering yield. Thus for projectile/target combinations with high sputter yields, the maximum implantable concentration may only be of the order of a few atomic percent.

University of Cape Town

B.2 Sputtering of single element targets

The sputtering yield Y is the number of target atoms knocked out per incident projectile, and can be written as:

$$Y = \frac{\text{mean number of emitted ions}}{\text{incident particle}} \tag{B-1}$$

and depends on the composition of the target, the implantation geometry and the parameters (energy and composition) of the projectile. Controlled sputtering yield experiments under laboratory conditions have measured sputter yields of between 1 and 10 for most medium mass projectiles, up to energies of several keV.

An extensive list of sputtering yields have been compiled by Matsunami *et al* [Mat84a].

Since the sputtering process involves a complex set of collisions, involving a series of deflections and energy transfers, the most important parameter is the energy deposited near the surface and the sputtering yield should be proportional to the number of displaced or recoil atoms. In the linear cascade regime applicable to medium mass ions, the number of recoils is proportional to the energy deposited by nuclear energy loss per unit depth. The sputtering yield, Y, can then be expressed as [Sig81a]

$$Y = \Lambda F_D(E_0) \tag{B-2}$$

where Λ is called the "materials factor" (equation B-5) and contains all the material properties, such as binding energy. $F_D(E_0)$ is the energy deposited by nuclear processes per unit length at the surface, and is defined by Winterbon, Sigmund and Sonders [Win70a] according to

$$dE = NS_n(E(x))dx = F_D(x)dx \tag{B-3}$$

where $S_n(E(x))$ is the energy dependent nuclear stopping, which ignores electronic energy losses from recoiling target atoms.

Thus the energy deposited at the surface by nuclear processes is

$$F_D(E_0) = \alpha N S_n(E_0) \tag{B-4}$$

where N is the atomic density of the target at the surface, $S_n(E_0)$ the nuclear stopping cross-section at energy E_0. $NS_n(E_0) = \frac{dE}{dx}|_n$, is the nuclear energy loss rate. α is a correction factor which includes M_1/M_2. Values for α can be read off figure B.1.

The evaluation of $S_n(E)$ depends on the collision cross-section for energy transfer to a substrate atom and in the keV sputtering regime, electron screening of the nuclear charge must be taken into account.

Thus in order to calculate the sputtering yield, one must first determine the nuclear stopping cross-section deposited via nuclear processes, and hence the sputtering yield.

B.2.1 Deposited energy

The deposited energy $F_d(E_0) = \alpha N S_n$, where α is a function of the mass ratio M_1/M_2 and the angle of incidence, β, measured from the surface normal.

University of Cape Town

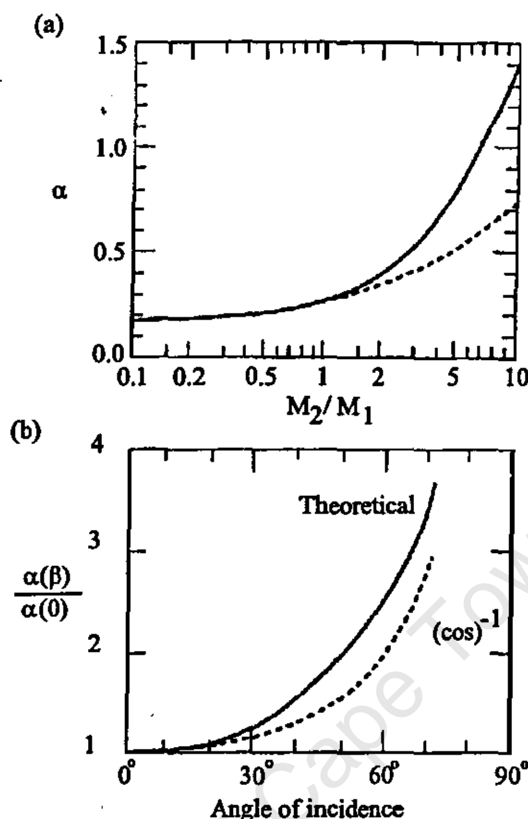

Figure B.1: Determination of α for different masses and angle of incidence. Reproduced from [Nas96a].

University of Cape Town

B.2.2 Sputtering yield

The materials function, Λ, defined by Sigmund [Sig81a] accounts for the material parameters of the interaction and describes the number of recoil atoms that can escape from the target:

$$\Lambda \cong 4.22/NU_0 \text{ nm} \cdot \text{eV}^{-1} \tag{B-5}$$

where N is the atomic density (in nm^{-3}) and U_0 is the surface binding energy in eV. U_0 can be estimated, using cohesion energy, and is given by Kittel [Kit76a].

Thus the sputtering yield can be written as

$$Y \cong 4.2\alpha S_n(E_0)/U_0 = 4.2\alpha(dE/dx)_n(NU_0)^{-1} \tag{B-6}$$

where N is in nm^{-3}, $NS_n = dE/dx$ in eV nm^{-1} and U_0 in eV.

B.3 Semi-empirical formula for sputtering of single element targets

A semi-empirical formula for sputtering due to both heavy and light projectile ions has been developed by Matsunami*et al* [Mat84a] and Yamamura & Itoh [Yam89a]. By using a combination of Lindhard's

theory of nuclear and electronic stopping with numeric values from sputtering data, they have derived an equation Y_E (empirical yield) for ions at normal incidence:

$$Y_E(E) = 0.42\frac{\alpha_s Q_s S_n(E)}{U_0[1 + 0.35U_0 S_e(\varepsilon)]}[1 - (E_{\text{th}}/E)^{\frac{1}{2}}]^{2.8} \tag{B-7}$$

where α_s and Q_s are empirical materials parameters determined from experiments, E_{th} is the sputtering threshold energy, $S_e(\varepsilon)$ is the reduced Lindhard electronic stopping cross-section, $S_n(E)$ the nuclear stopping cross-section in units of 10^{-15} eV$\cdot$ cm^2.

The reduced energy, ε, in eV is [Zie85a]

$$\epsilon = \frac{0.03253 M_2 E}{Z_1 Z_2 (M_1 + M_2)(Z_1^{0.23} + Z_2^{0.23})}. \tag{B-8}$$

The Lindhard's reduced nuclear stopping cross-section can be approximated by:

$$S_n(E) = K_n S_n(\varepsilon) \tag{B-9}$$

where

$$K_n = \frac{8.478 Z_1 Z_2}{(Z_1^{2/3} + Z_2^{2/3})^{\frac{1}{2}}}\frac{M_1}{M_1 + M_2}\ (10^{15}\ \text{eV}\cdot\text{cm}^2/\text{atom}) \tag{B-10}$$

and

$$S_n(\varepsilon) = \frac{3.441\varepsilon^{\frac{1}{2}}\ln(\varepsilon + 2.718)}{1 + 6.355\varepsilon^{1/2} + \varepsilon(6.882\varepsilon^{1/2} - 1.708}. \tag{B-11}$$

While the Lindhard's reduced electronic stopping cross-section can be approximated by:

$$S_e(\varepsilon) = K_e \varepsilon^{\frac{1}{2}} \tag{B-12}$$

where

$$K_e = \frac{Z_1^{\frac{2}{3}} Z_2^{\frac{1}{2}}\left(1 + \frac{M_2}{M_1}\right)^{3/2}}{12.6(Z_1^{2/3} + Z_2^{2/3})^{3/4} M_2^{1/2}}. \tag{B-13}$$

U_0 is the surface binding energy, which can be estimated from the cohesive energy.

The sputtering threshold energy, E_{th}, is calculated according to:

$$E_{\text{th}} = \begin{cases} \left(\frac{4}{3}\right)^6 \frac{U_0}{\gamma} & M_1 \geq M_2 \\ \left(\frac{2M_1 + 2M_2}{M_1 + 2M_2}\right)^6 \frac{U_0}{\gamma} & M_1 < M_2 \end{cases} \tag{B-14}$$

where γ is the energy transfer factor for elastic collisions

$$\gamma = 4\frac{M_1 M_2}{(M_1 + M_2)^2}. \tag{B-15}$$

Best fit values for the empirical variables α_s and Q_s where obtained by fitting equation B-7 to experimental data. α_s was found to be dependent on each ion/target combination and the following empirical expression was obtained

$$\alpha_s(M_2/M_1) = 0.10 + 0.155(M_2/M_1)^{0.73} + 0.001(M_2/M_1)^{1.5} \tag{B-16}$$

Q_s was found to only depend on the target material and has been tabulated in table B.1. (pg 226 of [Nas96a].)

University of Cape Town

Target	Z	U_0(eV)[a]	Q_s[b]
Be	4	3.32	1.97
B	5	5.77	4.1
C	6	7.37	2.69
Al	13	3.39	1.11
Si	14	4.63	0.95
Ti	22	4.85	0.58
V	23	5.31	0.76
Cr	24	4.10	1.03
Mn	25	2.92	1.09
Fe	26	4.28	0.9
Co	27	4.39	0.98
Ni	28	4.44	0.94
Cu	29	3.49	1.27
W	74	8.90	0.77

[a] Values of U_0 from Kittel [Kit76a] (p. 74),
[b] Values of Q_s from Yamamura and Itoh [Yam89a].

Table B.1: Table of Cohesive energies U_0 and Q_s from [Nas96a]

University of Cape Town

B.3.1 Calculations

Using the semi-empirical formula, the sputtering yields of two typical implantation experiments performed at this facility can be calculated. The results of implanting hydrogen into silicon and nitrogen into iron at 30 kV, table B.2, show that only 1 silicon atom is expected to be sputtered for 50 implanted hydrogen ions, while 5 iron atoms are expected to be sputtered for every 4 nitrogen ions implanted.

Value	30 kV H into Si	30 kV N into Fe
E(eV)	30,000	30,000
M_1/M_2	1/28	14/56
Z_1/Z_2	1/14	7/26
Q_s (table B.1)	1.11	0.9
U_0 (eV) (table B.1)	4.63	4.28
E_{th} (eV) (equation B-14)	38.59	12.58
γ (equation B-15)	0.133	0.640
α_s (equation B-16)	2.01	0.53
ε (equation B-8)	0.92	0.30
K_n (10^{-15} eV cm^2) (equation B-10)	1.57	87.51
$S_n(E)$ (equation B-11)	0.37	0.41
$S_e(\varepsilon)$ (equation B-12)	2.00	0.18
Y_E (equation B-7)	0.02	1.25

Table B.2: Calculations of sputtering yields of typcial PSII experiments

B.3.2 Sputtering at glancing angles

When the projectile ion is incident at non-normal angles of incidence, $\beta \neq 0$ with respect to the surface normal, it is observed that in general the sputtering due to a projectile ion at an incident angle of β is related to Y by

$$Y(\beta) = (\cos\beta)^{-f_s} \cdot Y(0) \tag{B-17}$$

where f_s is a function of M_2/M_1. Since plasma based ion implantation assumes $\beta = 0$ for most applications, with only such applications as implantation into a trench or hole have glancing angle implantation into sidewalls, the results of glancing angle sputtering will only be briefly mentioned: [Yam89a] For light ions ($M_2/M_1 > 10$)

$$f_s = 1 + (\Delta R_{p_x}/\Delta_{p_y})^2 \tag{B-18}$$

where ΔR_{p_x} and ΔR_{p_y} are the ion-range straggling in the ion direction and perpendicular to the ion direction, respectively. For large mass ratios, $(\Delta R_{p_x}/\Delta R_{p_y}) \cong 1$ and $f_s \rightarrow 2$.

For heavy ion sputtering, $(M_2/M_1 < 10)$ f_s is approximated by

$$f_s = 1 + \left(\frac{\langle Y^2\rangle_D}{\langle \Delta X^2\rangle_D} \frac{\langle X\rangle_D^2}{\langle \Delta X^2\rangle_D}\right) \tag{B-19}$$

where $\langle X\rangle_D$ is the average depth of damage, $\langle Y^2\rangle_D^{1/2}$ and $\langle \Delta X^2\rangle_D^{1/2}$ are the damage straggling in the direction of the ion and perpendicular to the ion trajectory, respectively. For values of $M_2/M_1 < 1$, $f_s \cong 1.9$.

B.3.3 Ion implantation and the steady state condition

While ions are added by the implantation procedure, the surface is being eroded by sputtering. Eventually an equilibrium, or steady state, is reached whereby just as many ions are removed by sputtering as are being added by implantation. The depth distribution under this condition typically has a peak at the surface, but drops off with depth according to the ion range (figures B.2 and B.3).

The steady state surface condition is calculated by considering the implantation of ion species A into a target material B. If N_A and N_B are the surface concentrations per unit volume of the projectiles and target respectively, the surface composition is given by N_A/N_B. If J_A and J_B are the flux of the sputtered projectiles and target respectively, then

$$J_B/J_A = r(N_B/N_A) \tag{B-20}$$

where r is the ratio of the probability for a B atom to be sputtered to that of an A atom being sputtered. If the implantation flux is J_i, then the total sputtering yield will be

$$YJ_i = (J_A + J_B) \tag{B-21}$$

At steady state $J_A = J_i$ so that equation B-21 becomes

$$J_B = (Y - 1)J_i \tag{B-22}$$

University of Cape Town

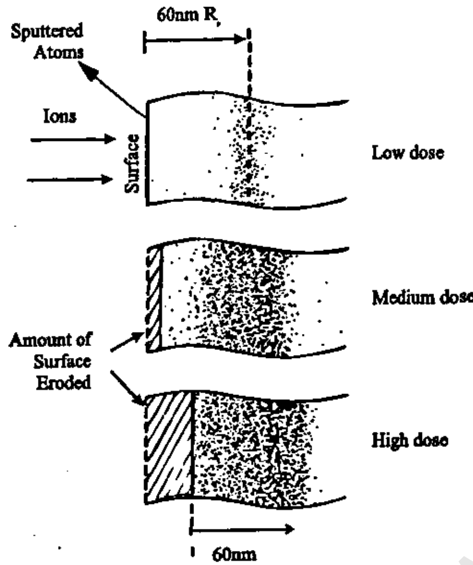

Figure B.2: Schematic view of the development of the concentration profile of ions implanted from low to high doses [Nas96a].

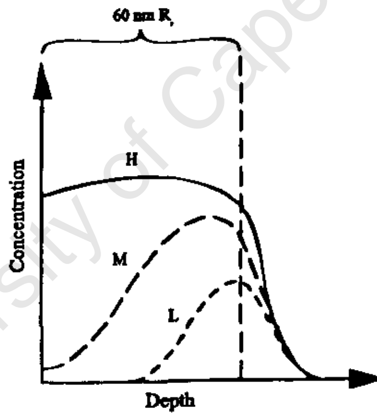

Figure B.3: The implantation depth profiles for low (L) to high (H) doses [Nas96a].

University of Cape Town

Substituting back into equation B-20,

$$N_A/N_B = r(Y-1)^{-1} \tag{B-23}$$

Thus the steady state surface concentration is roughly inversely proportional to the yield Y, but is multiplied by the preferred sputtering factor, r (§B.4.1).

B.4 Sputtering of alloys and compounds

The theory of sputtering from alloys and compunds is similar to that of Sigmund [Sig81a] for single elements, but for some additional considerations. Firstly, the different target species may be sputtered at different rates, as a result of preferential sputtering, and secondly the mixing of implanted ions and preferential sputtering can result in composition changes which affect the build-up and saturation of implanted ions.

B.4.1 Preferential sputtering

By limiting the theory to binary, or two-element, targets, sputtering of alloys can be understood. In particular the influence of preferential sputtering of one of the target species and the subsequent surface segregation can be described in the following manner: In a homogeneous target of two compunds, A and B, with surface concentrations, N^s equal to the bulk concentrations, N^b, then the pre-sputtered composition has

$$N_A^s/N_B^s = N_A^b/N_B^b \tag{B-24}$$

in preferential sputtering, the partial yield of species A is Y_A and for B is Y_B, thus the total yield Y is equal to

$$Y_{A,B} = \frac{\text{number of ejected atoms of A, B}}{\text{incident projectile}} \tag{B-25}$$

The ratio of partial yields is

$$\frac{Y_A}{Y_B} = r\frac{N_A^s}{N_B^s} \tag{B-26}$$

where r is the sputtering factor and accounts for differences in surface binding energies, sputter escape depths and energy transfers within the cascade, $r > 1$ implies that A is preferentially sputtered over B. Measured values for r range from 0.5 to 2.

For $r \neq 1$, the surface yields and concentrations will change from the initial conditions of $N_{A,B}^s(0)$, $Y_{A,B}^s(0)$ to the steady state values of $Y_{A,B}^s(\infty)$, $Y_{A,B}^s(\infty)$. Thus at $t = 0$,

$$\frac{Y_A(0)}{Y_B(0)} = r\frac{N_A^s(0)}{N_B^s(0)} = r\frac{N_A^b}{N_B^b} \tag{B-27}$$

Any preferential sputtering of one species (e.g. A) causes a relative depletion of that species and a corresponding increased concentrastion of the other ($N_A^s < N_B^s$). This in turn results in an increased yield of the other (Y_B). But under steady state conditions, the processes are balanced as the surface erodes into the bulk and the surface concentration differs from the bulk according to

$$\frac{N_A^s(\infty)}{N_B^s(\infty)} = r\frac{N_A^b}{N_B^b} \tag{B-28}$$

B.4.2 Composition changes

As can be seen from considering such processes as steady-state sputtering and preferential sputtering, the surface composition can be greatly affected. This is epsecially true in surface modification applications where high dose implants are used to form modified surface alloys and should be taken into account in calculating implant doses. Surface composition changes in multi-component targets has been documented by Betz and Wehner [Bet83a].

B.4.3 Composition depth profiles

Since ion implantation applications relevent to materials science deliberately alter the composition of the surface, one expects composition profiles to vary and for changes in composition to extend to the range of the implanted ion. However sputtering experiments have shown that a steady state composition depth

University of Cape Town

profile is reached after an amount of material approximately equivalent to the thickness of the altered layer has been eroded. Measurements of Ar sputtered PtSi reveal that the surface PtSi compisiton under steady state is independent of sputtering ion energy [Lia80a]. Thus the ability of plasma implantation techniques to implant required doses can be severely limited if the steady state composition occurs before the desired implantation composition is reached. Fortunately thermal diffusion and radiation enhanced diffusion can promote diffusion of the implanted projectile to greater dpeths and hence affecting the steady state composition. A detailed discussion of sputtering composition depth profiles is given by Betz and Wehner [Bet83a].

B.5 High dose ion implantation

The composition depth profile in high dose ion implantation, such as N into Fe for tribological benefits is affected by atomic mixing, sputtering and chemcial effects. In general, the maximum implantable concentration is limited by the reciprocal of the sputtering yield (§B.1). This occurs because of a combination of the surface receding due to sputtering and the sputter removal of implanted ions. The maximum concentration is therefore established after a thickness comparable to the ion range has been removed (§B.3.3). One should be especially aware of sputter processes if there is preferential sputtering of the implanted ion.

Based on the assumption that atomic mixing is very good, such after an initial dose of about 10^{16} atoms/cm^2 the implanted species spreads uniformaly over the effective depth R_p, and assuming also that the depth profile shape remains constant, with only the amplitude increasing with further implantation, the steady state erosion thickness can be established as follows:

Conservation of atoms requires

$$R_p \frac{dN_A}{dt} = J_i - J_A \tag{B-29}$$

where N_A is the concentration of the implanted species, J_i the projectile flux, J_A the flux sputtered A atoms. J_A, J_B and J_i are related according to equations B-20 and B-21. By defining $x \equiv N_A/N_B$ and assuming that Y remains constant, then equations B-20 and B-21 give

$$J_A = \frac{x}{r+x} Y J_i \tag{B-30}$$

$$J_B = \frac{r}{r+x} Y J_i \tag{B-31}$$

Substituting equations. B-30 and B-31 into equation B-29 obtains

$$R_p \frac{d}{dt}\left(\frac{x}{1+x}\right) N_0 = J_i - \frac{x+r+x}{Y} J_i \tag{B-32}$$

where $N_0 \equiv N_A + N_B$. With some rearrangement, equation B-32 can be rewritten as

$$\frac{r+x}{(1+x)^2[r+(1-Y)x]} dx = \frac{1}{N_0 R_p} d\phi_A \tag{B-33}$$

where $d\phi_A \equiv J_i dt$ is the incremental ion dose. Equation B-33 is a differential equation for $x(\phi_A)$ which is solved by taking partial fractions for the left hand side and integrating to get

$$Y\left[\frac{Ax}{1+x} + B\ln\left(\frac{1+x}{1-x/x(\infty)}\right)\right] = \frac{Y\phi_A}{N_0 R_p} \tag{B-34}$$

University of Cape Town

where $A \equiv (r-1)/[r-(1-Y)]$, $B \equiv Yr/[(1-Y)-r]^2]$ and $x(\infty) = r/(Y-1)$. The expression $Y\phi_A/N_0R_p$ can be interpreted as the amount of material sputtere as measured bythe thickness of the implanted layer.

The steady state compositions are still given by equation B-23. The amount of material to be eroded before steady state conditions are reached can be found as follows: Define

$$\phi_0 = \frac{x(\infty)}{(dx/d\phi_A)|_{\phi_A=0}} \tag{B-35}$$

which is the dose required to achieve steady state. Equation B-33 gives

$$\frac{dx}{d\phi_A}|_{\phi_A=0} = \frac{1}{N_0R_p} \tag{B-36}$$

Since $s(\infty) = r(Y-1)^{-1}$, equations B-35 and B-36 give

$$(Y-1)\phi_0 = r(N_0R_p) \tag{B-37}$$

which for $Y \gg 1$ gives

$$\frac{Y\phi_0}{N_0R_p} \cong r \tag{B-38}$$

B.6 Factors that influence concentration in high-dose ion implantation

Since most of the sputtered atoms originate from the first few atomic layers near the surface, sputtering is very sensitive to surface conditions. A thin oxide layer or other surface contaminant can reduce the sputtering yield and therefore protect the surface. However because of ion mixing, which causes the surface contaminant to be mixed into the modified layer, these surface contaminants may be a source of significant detrimental side-effects.

The surface layer is affected by such things as the residual gases in the processing chamber, target preparation and other contaminants, such as pump oils. Oxide layers and carbon films are the most common contaminants, though in plasma vessels, filaments or plasma forming antennae can also become contaminant sources.

Surface topography also affects sputtering yields. Thus target preparation, initially, and later, sputtering can both affect surface roughness. Preferential sputtering around target impurities and, in crystalline targets, crystallographic orientation can resuly in increased surface roughness. While extremely rough surfaces can reduce the sputtering yield, they also adversely affect implantation.

Inert gas implantation measurements have revealed low retained doses near surface regions even without sputtering. This implies that inert-gas ions can escape from the target material, reducing surface concentrations.

In all of these cases, the simple model can no longer be applied.

B.7 Sputtering from spikes

The Sigmund model discussed thus far assumed that the collision cascade produced by the projectile was linear and could be approximated by binary collisions. However, if the projectile energy results in

University of Cape Town

a mean free path between displaced target atoms approaching the atomic lattice spacing, the binary collision approximation breaks down. Under these conditions the energy is disipated over a very short distance, producing surface temperatures that can exceed the melting and vapourization temperatures of the material. These conditions are called the spike regime, and anomalous high sputtering yields may result.

In the spike regime the sputtering yield can be estimated by assuming that the atoms in the spike behave as an ideal gas, This assumes that the surface atoms have a Maxwellian velocity distribution, from which a mean velocity can be calculated, and which in turn can be used to estimate an evaporation rate from the spike surface area.

Thus from the kinetic theory of gases, the one-dimensional velocity distribution of atoms of mass M_2 at a temperature T is given by

$$f(v_x) = \left(\frac{M_2}{2\pi k_B T}\right)^{\frac{1}{2}} e^{-\frac{1}{2}\frac{M_2 v_x^2}{k_B T}} \tag{B-39}$$

where k_B is Boltzmann's constant. The average velocity is then given by

$$\begin{aligned} \langle v_x \rangle &= \int_0^\infty v_x f(v_x) dv_x \\ &= \left(\frac{M_2}{2\pi k_B T}\right)^{\frac{1}{2}} \int_0^\infty v_x e^{-\frac{1}{2}\frac{M_2 v_x^2}{k_B T}} dv_x \\ &= \left(\frac{k_B T}{2\pi M_2}\right)^{\frac{1}{2}} \end{aligned} \tag{B-40}$$

Thus by assuming that the activation energy for evaporation in the surface binding energy U_0, the evaporation J_e per unit time and unit area at the surface temperature, T_{surf}, is given by Sigmund [Sig81a] as

$$\begin{aligned} J_e &\cong N\langle v_x \rangle e^{-U_0/k_B T_{\mathrm{surf}}} \\ &\cong N(k_B T_{\mathrm{surf}}/2\pi M_2)^{\frac{1}{2}} e^{-U_0/k_B T_{\mathrm{surf}}} \end{aligned} \tag{B-41}$$

where N is the target atomic density.

This spike surface temperature, T_{surf}, can be related to the average deposited damage energy at the surface, $\bar{\theta}_{\mathrm{surf}}$, by the expression

$$\bar{\theta}_{\mathrm{surf}} = \frac{3}{2} k_B T_{\mathrm{surf}} \tag{B-42}$$

The mean deposited damage energy at the surface, $\bar{\theta}_{\mathrm{surf}}$, can be calculated from the expression

$$\bar{\theta}_{\mathrm{surf}} = \frac{(0.68)^2 S_n(E)}{A_{\mathrm{cas}}^{\mathrm{surf}}} \tag{B-43}$$

where $S_n(E)$ is the nuclear stopping cross-section and $A_{\mathrm{cas}}^{\mathrm{surf}}$ is the cascade surface area emitting J_e atoms/cm^2. This expression assumes that the spike damage energy is equal to the nuclear stopping. By assuming that the spike can be approximated by a cylinder at the surface, the cascade area is given by

$$A_{\mathrm{cas}}^{\mathrm{surf}} = \delta_{\mathrm{corr}}^2 A_T = \delta_{\mathrm{corr}}^2 (\pi \langle Y^2 \rangle_D) \tag{B-44}$$

where A_T is the transport cascade area and calculated either using transport theory or the average of many Monte-Carlo histories. The transport cascade radius is taken as the perpendicular distance from

University of Cape Town

the ion trajectory of the ion damage straggling, $\langle Y^2\rangle_D^{1/2}$. $\delta_{\rm corr}$ is the cascade volume correction factor, relating the transport cascade area to the individual cascade area. The factor $(0.68)^2$ accounts for the fraction of the damage energy lying within a standard deviation of the damage distribution (section 7.11.4 of [Nas96a])

For a spike of lifetime τ, the sputtering yield is given by

$$Y_{\rm spike} = \tau A_{\rm cas}^{\rm surf} J_e. \tag{B-45}$$

University of Cape Town

Appendix C

Computers and electronic hardware

Two computers and several dedicated electronic devices were used in the construction of this laboratory. This chapter outlines the use of these devices, and briefly describes how they are linked and used in the operation of the laboratory.

C.1 Facility Configuration

The facility configuration is shown in figures C.1 and C.2. As can be seen in these figures, the operation of the facility can be separated into two categories: digital and analogue. The digital apparatus are all connected to the data capture PC via one of the interfaces discussed above. The analogue components are connected directly via the appropriate cable to their destination.

University of Cape Town

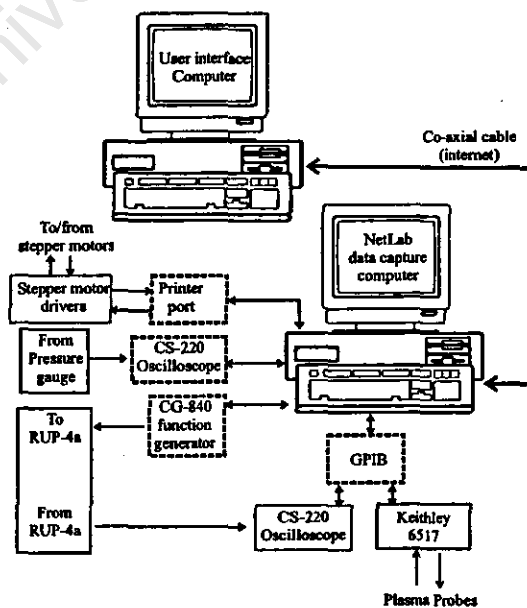

Figure C.1: Broad overview of the facility apparatus and the connections linking them.

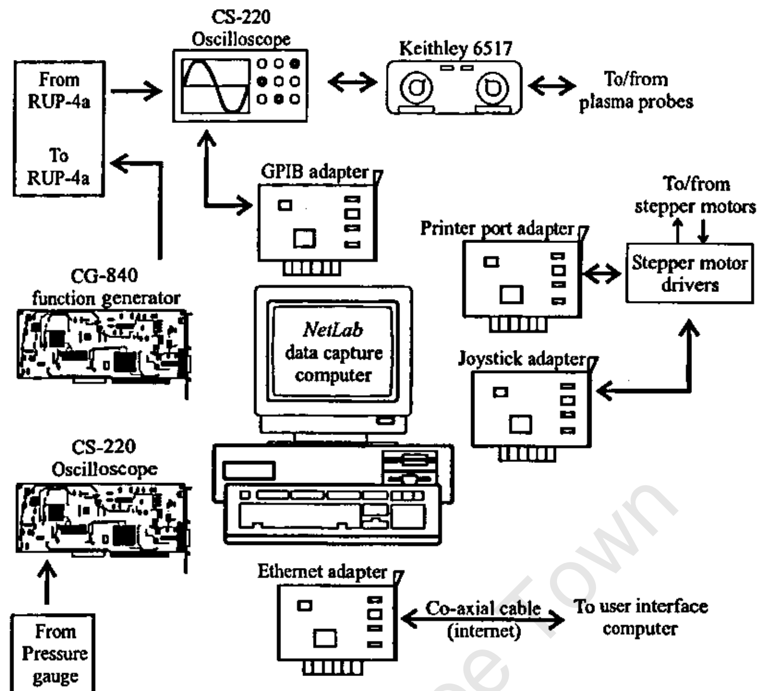

Figure C.2: The interfaces and connections between the data capture PC and the facility apparatus. Additional hardware devices are indicated.

University of Cape Town

C.2 Interfaces

Every electronic device accessed by the laboratory facility needs an interface between the device and the computer processor. In the case of the Gage Applied Sciences[1] devices (the CS-220 oscilloscope and the CG-840 arbitrary waveform generator cards) they are installed directly into the data capture P.C. ISA bus slots. These devices can then be accessed directly through I/O port calls and their memory can be accessed via memory read/write calls. Other devices are accessed through interface cards, such as the GPIB interface bus, the parallel port interface and the joystick interface.

C.2.1 The GPIB interface

The GPIB or General Purpose Interface Bus is an interface system through which connected electronic devices can communicate. Originally developed by Hewlett-Packard (hence the alternate name Hewlett-Packard Interface Bus - HPIB) to connect and control instruments manufactured by them, it was rapidly accepted by industry and was designated IEEE-488. Companies like National Instruments, which specialised in high-speed interface hardware, expanded the use of GPIB into products of manufacturers other than Hewlett-Packard.

The GPIB interface uses separate handshaking lines for flow control, data lines for carrying command and data message packets, and a set of lines for communicating with the interface. This configuration

[1]Gage Applied Sciences Inc., 5465 Vanden Abeele, Montreal PQ, Canada H4S 1S1, http://www.gageapplied.com/

supports data through-puts up to 1 megabyte per second (1978). The GPIB protocol supports the definition of an interface controller with up to 15 connected devices, any of which can act as Talkers, Listeners or Controllers.

Types of messages

The GPIB supports communication between devices by method of messages. These messages can be device dependent or interface messages. Device dependent messages, or data messages, contain device specific information such as programming instructions, measurement results, machine status and data. Interface messages manage the interface bus itself. Also called commands or command messages, they perform such tasks as initialising the bus, addressing and unaddressing devices and setting device modes for local (or front panel) or remote programming.

Talkers, Listeners and Controllers

A GPIB network consists of Talkers, Listeners and at least one Controller. A Talker is a device that sends data to Listeners, while the Controller manages the flow of information on the GPIB by sending commands to all devices. Devices can be Listeners, Talkers and/or Controllers, depending on the device ability. The role of the GPIB network can be compared to a telephone system: The exchange (Controller) monitors the network (GPIB). When the exchange (Controller) notices that someone (device) wants to make a call (send a data message), it connects the caller (Talker) to the receiver (Listener). The controller usually addresses a Talker and Listener before the Talker can send it's message to the Listener. After the message has been sent, the Controller can unaddress both devices.

Certain configurations do not require a controller, such as when there is only one Talker and one or more Listeners, and they never change their roles. A Controller is only needed when the active configuration needs to be changed. The GPIB-PC interface card allows the PC to fulfil all three roles.

Although there can be multiple Controllers, there can only be one active controller at a time (the Controller in Charge - CIC). Active control can be passed from an active Controller to an idle Controller, but only one device, the System Controller, can take control and make itself the CIC. In a PC environment, the GPIB-PC is usually the System Controller.

C.2.2 The PC parallel printer port

The parallel printer port, or parallel port for short, is also used as an interface between the data capture PC and the laboratory. This interface is very simple since it occupies only three I/O ports and has no on-board RAM. The original parallel port definition operates as follows:

- The BASE port is used to output 8-bit digital data to the printer,
- BASE+1 is a 5-bit input port used to read printer status,
- BASE+2 is a 4-bit output port used to control the printer interface and the printer device.

More recently, the parallel printer interface has been extended to allow the BASE port to be bi-directional (the PS/2 printer interface), to allow buffers and automatic writing of buffered data (EPP and ECP).

University of Cape Town

This facility uses a single parallel port to control the stepper motors (table C.1) and sense the state of the end-stop switches. In addition to the parallel port, the stepper motor driver software also uses a single joystick bit for timing purposes.

Port	Bit	Hex value	Identification	Usage	D-25 pin
BASE	0	1	D0 (out)	EN Y	2
BASE	1	2	D1 (out)	CLK Y	3
BASE	2	4	D2 (out)	DIR Y	4
BASE	3	8	D3 (out)	EN X	5
BASE	4	10	D4 (out)	CLK X	6
BASE	5	20	D5 (out)	DIR X	7
BASE + 1	4	10	SLCT (in)	Xin END	13
BASE + 1	5	20	PE (in)	Xout END	12
BASE + 1	6	40	ACK (in)	Yin END	10
BASE + 1	7	80	-BUSY (in)	Yout END	11

Table C.1: Printer port programming. 17 of the 24 available bits correspond to pins on the 25-D pin connector with 12 output pins and 5 input pins. Unlisted bits are either unused or reserved.

C.2.3 Joystick port

Occupying a single port in the PC I/O port space, the joystick port is actually a combination digital and linear-integrator based analogue-to-digital converter (ADC) input device. In addition to sensing the digital states of two pairs of two buttons, it can also be used to determine the value of two pairs of two-resistor analogue joysticks.

Bit	Hex value	Identification
0	1	Joystick A resistor X (JAX)
1	2	Joystick A resistor Y (JAY)
2	4	Joystick B resistor X (JBX)
3	8	Joystick B resistor Y (JBY)
4	10	Joystick A button 1 (BA1)
5	20	Joystick A button 1 (BA2)
6	40	Joystick B button 1 (BB1)
7	80	Joystick B button 2 (BB2)

Table C.2: Joystick port programming. Each bit of the joystick port corresponds to either a button value (open or closed), or the state of a joystick resistor comparator.

Mode of operation

The joystick interface operates as follows: an I/O "write" to the joystick port charges up four capacitors and clears their comparator state buffer. Each capacitor is discharged through a joystick resistor and the charge state is sensed by comparators in the interface. Thus, after a time proportional to the joystick

University of Cape Town

resistance, the capacitor sense-logic changes state. Thus the time taken for the capacitor to change state can be used to determine the appropriate resistor value.

Hardware determined timing

The stepper motor controller software functions by sending a stream of pulses out the parallel port to step the selected motor. However, due to the mechanical nature of the motor hardware these pulses are best sent out with a regular period, the exact timing of which depends on the exact motor configuration, taking into account such parameters as motor drive voltage, motor load and step method. Thus it was decided to use an externally mounted variable resistor connected to the joystick port to regulate the timing of the stepper motor pulses. This circuit, which includes a feedback check which the stepper motor driver software uses to ensure that the timing circuit is connected and functioning, allows easy on-the-fly control of the stepper motor drive frequency. The circuit diagram is shown in figure C.3.

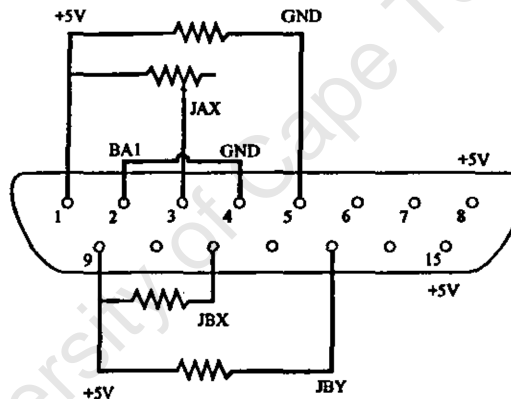

University of Cape Town

Figure C.3: Wiring diagram to use the joystick port for hardware timing. The resistor across JAX is used by the software to set the stepper motor timing. See table C.2 for port definition.

C.3 Data acquisition

C.3.1 Data acquisition hardware

The electronic phenomena of interest during the implantation process can be classified into two categories: short time (or high frequency, or greater than 10 kHz) DC and long time (low frequency, or less than 1 Hz) DC. A Tektronix TDS-220 digital oscilloscope connected to the data capture computer via GPIB was used to record the short-time events (such as the implantation current and voltage traces) while a Gage Applied Sciences CS-220 analogue-to-digital converter (ADC) card was used to monitor the DC levels (such as temperature, pressure and discharge current). Since the ADC card has only two channels, an analogue multiplexer was built to allow access to three more analogue inputs. All software was written as part of the establishment of this facility, and details can be found in chapter 6. The graphical analysis

and presentation was performed with IDL (Interactive Data Language) by RSI[2]. An IDL application was written to use a customised internet access run-time library to connect to the data capture computer and provide a real-time graphical indication of the implant status. This IDL application shows the current state of the implantation voltage and pressure traces, the pulse time settings, the relative stepper motor position and a history of the pressure, temperature and discharge current. It also enables control of the high voltage power supply by use of sliders which control the voltage and the pulse frequency. The pulse width is fixed by a pulse generator, for safety reasons.

C.3.2 Data and voltage sources

From the point of view of the user, a data source converts analogue voltages from the laboratory into data for processing. The data sources are the analogue voltages present in the laboratory that are of interest. These voltages are produced by such devices as

- the discharge current power supply,
- the pressure gauge, to monitor chamber pressure,
- the plasma probes, to acquire Langmuir characteristic I-V plots,
- the high voltage pulsed power supply, in particular the implantation voltage and current

These data sources all need to be attached to some form of ADC, in order to convert them to a computer-readable form.

Maintaining the above point of view, voltage sources convert data into voltages for use in the laboratory. These voltages may be of variable potentials, like the zero to ten-volt signal used to program the high-voltage pulsed power supply output voltage (0 to 30 kV) or the -20 to +30 V voltages sweep used to record the I-V Langmuir characteristic trace used to establish the plasma parameters. They may also be of fixed voltages, like the 5 V TTL values used to trigger the high voltage pulse, or move the stepper motors.

University of Cape Town

C.4 Voltage sources

C.4.1 The CompuGen CG-840 arbitrary waveform generator card

Manufactured by Gage Applied Sciences the CompuGen 840, or CG-840, is a dual arbitrary waveform generator and digital pattern generator. It can simultaneously output user-defined analogue waveforms as well as output a user defined pattern of digital signals.

Architecture

The CG-840 consists of a PC interface, 16KB static CMOS memory, memory control hardware, digital-to-analogue converter (DAC), amplifier and gain hardware, clock control circuit, trigger circuit and appropriate terminators and connectors.

[2]Research Systems Incorporated, 4990 Pearl East Circle, Boulder, Colorado 80301-9959, USA. URL: http//www.rsinc.com/

Modes of operation

The bit pattern describing the analogue and/or digital waveforms is loaded into the RAM and the clock rate is programmed via registers accessed through the PC I/O bus. Depending on the mode selected, the data in the RAM is converted into an analogue waveform through the DAC and the amplified signal is output through the rear BNC connector. For digital waveforms, the bit pattern is read directly from memory and sent to the digital output connector via buffers.

The 16K bytes of memory is utilised differently in the different modes:

- in analogue only mode, it can be configured to use up to the full memory address space for either 16384 (16×1024) bytes of 8-bit resolution arbitrary waveform, or 8192 (8×1024) words of 16-bit resolution arbitrary waveform.
- in dual mode (analogue and digital) the device can output up to 8192 (8KB) of 8-bit resolution arbitrary waveform and up to 4096 16-bit words (8KB) of digital pattern.
- in digital only mode, up to 8192 words of 16-bit digital bit pattern may be output.

Clock rates

The clock rate can be programmed to different rates by multiplying the base of 1, 2 or 5 by a multiplier over 7 decades (from Hz to MHz) up to a maximum of 40 MHz. The clock can either be operated in single-shot or continuous mode. In continuous mode, the CG-840 continuously repeats the programmed waveforms until stopped by software.

Application

The CompuGen function generator card has one analogue output and 16 digital output bits (two bytes). This card was used to allow computer control of the high voltage pulsed power supply. The analogue output was used to determine the high voltage pulse voltage via the voltage level input of the high voltage charger (§5). One of the digital output lines was used to trigger the HV pulse. The CG-840 has 8 KB of RAM and re-triggerable address counters. This means that once a time-base has been chosen, say 1 kHz, up to 8 seconds of analogue and digital data can be pre-loaded into the card. The card can be programmed to execute this data once, or continually re-execute it.

In this manner, a high implant voltage can be reached and switched off by simply programming a relatively slow ramp, both up and down, respectively, and executing the program once. Once a steady state voltage has been reached, the card can be re-programmed to continually repeat the trigger pattern, while holding the pulse voltage constant. Thus long-time runs of hundreds of thousands of pulses can be executed and monitored by simply counting the number of seconds since initiation.

C.5 Data sources

C.5.1 The GageScope CS-220 oscilloscope card

The GageScope CS-220 oscilloscope card is an ISA-bus interface card which plugs into an 8-bit XT ISA bus slot in the data capture PC. This card is a 20 MHz bandwidth, two-channel 8-bit oscilloscope

University of Cape Town

card. If operated in single channel mode, it can digitise an analogue signal at a maximum of 40 MSPS (Mega-samples per second).

CS-220 architecture

The CS-220 consists of a PC interface, memory control hardware, 2 ADCs, amplifier and gain hardware, clock control circuit, trigger circuit and appropriate terminators and connectors. It can be configured to operate with different amounts of on-board memory, ranging from 32KB to 8MB. The on-boards amplifiers support gains which allow digitisation of signals ranging from +-100 mV to +-5 V (that is, from 200 mV, peak to peak, to 10 V, peak to peak).

Modes of operation

The CS-220 can be configured to operate in either a single-channel or dual channel mode. In single channel mode, all of the on-board memory is available for storing digitised signals, at up to a maximum sampling rate of 40 MSPS. In dual channel mode, half the on-board memory is available to each channel, and the device can operate at up to 20MSPS. Each channel has a maximum bandwidth of 20 MHz and can operate with either AC or DC coupling.

Clock rates

The clock rate can be programmed to different rates by multiplying the base of 1, 2 or 5 by a multiplier over 7 decades (from Hz to MHz) up to a maximum of 40 MHz. The clock can either be operated in single-shot or continuous mode. In continuous mode, the CS-220 continuously acquires and digitises the incoming waveforms until stopped by software.

University of Cape Town

C.5.2 The Tektronix TDS-220 digital oscilloscope

The Tektronix TDS-220 is a 100 MHz bandwidth real-time digital oscilloscope. It has two channels that can sample at up to 1 GSPS and a 2500-byte 8-bit memory per channel.

Computer interface

The TDS-220 can be fitted with optional extension modules to provide, for example, real-time Fast-Fourier Transform (FFT) analysis and RS-232C and GPIB interface functionality. The GPIB was used to transfer digitised data from the oscilloscope to the data capture PC.

Specification summary and application

A brief overview of the TDS-220 measurement ranges and capabilities is given in table C.3. This oscilloscope was used primarily to digitise the implantation current and voltage.

Specification	Range	Comments
Voltage sensitivity	from 2 mV/div to 200 mV/div	for V < +−2 V
	>200 mV/div to 5 V/div	for V up to +−50 V
Digitiser	Dual 8-bit DACs	
Volts/div range	2 mV/div to 5 V/div	
Bandwidth	100 MHz bandwidth above 50 mV/div	
	20 MHz bandwidth below 50 mV/div	
Sample rate	50 SPS to 1 GSPS	
Memory	2500 samples per channel	
Seconds/div	5 ns/div to 5 s/div	in a 1, 2.5, 5 sequence

Table C.3: Specification summary for the TDS-220 digital oscilloscope

C.6 Bi-directional devices - The Keithley 6517 and 617 electrometers

University of Cape Town

A bi-directional device is one which can act as either a data source or a voltage source. All the devices discussed thus far have been only one or the other. The Keithley 617 electrometer is on loan from the Plasma Physics Research Institute while the 6517 is shared with the Electrical Characterisation Laboratory of the Materials Research Group.

The Keithley electrometers are powerful electronic tools which provide the ability to both produce a voltage or current, and measure the resultant current or voltage, respectively. These devices were interchangeably used to measure the Langmuir characteristic current/voltage curves used to determine the plasma parameters. They were connected to the data-capture PC via the GPIB.

These highly sensitive instruments are designed to measure voltage, current, charge and resistance. They can measure resistance in either a constant current mode or a constant voltage method that uses the built-in voltage source. The voltage source can also be used to generate positive and negative voltages in the range of -100 to +100 V, in steps of 50 mV.

Computer Interface

These devices are fitted with a GPIB, which allows full programmable operation of the device by the data capture PC.

Specification summary

A brief overview of the Keithley measurement ranges and capabilities is given in table C.4.

Current *versus* voltage measurements

In order to measure the current *versus* voltage Langmuir characteristic trace, the electrometer has to configured in the V/I resistance mode, as described on pages 2-17 through 2-19 of the device manual. In this mode, the "LO" input lines of the voltage source and current input connectors are linked together, and the current is recorded between the "HI" lines of the voltage source and current input connectors,

Measurement	Measurement range
Voltage	between 10 μV and 200 V
Current	0.1fA and 20 mA
Resistance	0.1Ω and 200GΩ
Charge	10fC and 20nC
Memory	100 readings
Front panel display	$4\frac{1}{2}$ digit

Table C.4: Specification summary of the Keithley 617 electrometer

as shown in figure C.4.

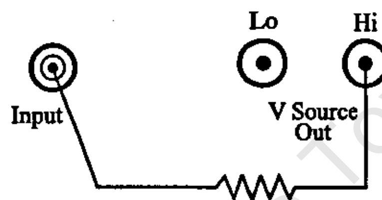

Note: V-SOURCE LO connected to ammeter input LO via METER-CONNECT option of CONFIGURE V-SOURCE menu.

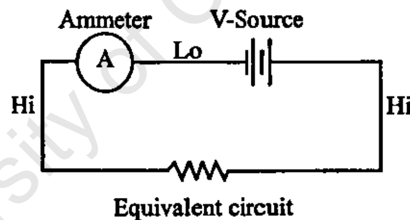

Equivalent circuit

Figure C.4: Wiring diagram to connect the Keithley 617 in V/I mode

University of Cape Town

Appendix D

"NetLab" User Manual

University of Cape Town

University of Cape Town

NetLab Software
&
Plasma Laboratory

Users Manual

Version 1.0

May 2001

All software for version 1.0 written by Kevin Meyer

University of Cape Town

Table of contents

Table of contents 2
Introduction to the facility 3
The NetLab software 4
The Plasma Laboratory 8
1. Opening the chamber 8
2. Closing the plasma chamber 9
3. Achieving chamber vacuum 9
4. Turning on the plasma 10
5. Turning on the RUP-4a HV power supply 10
6. Starting / Running an implantation experiment 11
7. Switching off the RUP-4a power supply 11
Safety 12

University of Cape Town

Introduction to the facility

This facility was constructed between April 1996 and November 1999. It was constructed at the Materials Research Group to broaden the scope of research of the group. In this sense, the PSII facility can be considered as a stand-alone construction, existing independently of the rest of the group.

However materials research is best performed in a tight sample manufacturing and analysis environment, whereby the processed materials are thoroughly analysed immediately after manufacture. In this manner, it is easier to gain a deeper understanding of the physical processes involved. Thus it is apparent that the PSII facility must be used and understood in the context of the larger analytical capabilities of the Materials Research Group.

The PSII chamber can be used to implant positive plasma ion species into (semi-) conducting targets. By creating a plasma within the chamber, the positive plasma ions can be accelerated into the target by the high negative voltage generated by the RUP-4a pulsed power supply. Thus PSII should be of interest to any researcher wanting to manufacture a material which has components that exist in gaseous form (or which one can use to produce a plasma). The implanted ions can either be of use by themselves (e.g. implanted oxygen to created oxides, or nitrogen for nitrides, etc), or the process (or consequence) of implantation may be of interest (e.g. hydrogen into silicon for wafer cleaving).

The Plasma chamber

The PSII facility uses an ~1m^3 aluminium alloy plasma chamber (on loan from the Plasma Physics Research Institute of the School of Pure and Applied Physics, University of Natal, Durban). Tantalum filaments are used to provide the primary ionising electrons used for plasma formation. Features of the chamber include multiple, independently controlled Langmuir probes (for plasma analysis and diagnostics), multiple viewports and flanges (including one flange that has been modified to accept an RF antenna for future RF plasma generation capabilities) and a large plasma volume.

The RUP-4a high voltage pulsed power supply

This pulsed power supply was designed by Dr. J. Brutscher to use a tetrode thermionic valve for switching the high voltage and was constructed at the Forschungszentrum Rossendorf (FZR or Rossendorf Research Centre) within the scope of this project. The Rossendorfer Universal Pulsgenerator, model 4a (RUP-4a, the economy version), is a self-contained variable voltage (up to -30kV) pulsed (width from < 1μs up to 1ms, repeat rate up to 3kHz) power supply (maximum power of 600W). The maximum implantation current of 8A and duty-cycle (< 4%) complete the operational parameters. The output voltage and pulse timing can be remotely programmed using a 0--10V analogue voltage to select the output voltage and a TTL logic input to operate the tetrode switch.

Data acquisition and processing

Two computers using interface cards are used to record parameters of interest during the plasma implantation process. One computer is kept in the PSII laboratory, and is used as a data capture and control computer. It uses a digital oscilloscope and several interface cards to (1) measure the chamber pressure, implantation current and implantation voltage, (2) control the implantation voltage and timing parameters and (3) control the stepper motors. The second computer implements the user interface and communicates with the data capture computer via the internet using the TCP/IP network protocol. This was done to allow remote control and monitoring of the implantation experiments. A necessary requirement since implantation at voltages higher than -25kV produce high levels of x-ray radiation in the plasma processing laboratory.

University of Cape Town

The NetLab software

The NetLab software has two parts, the GUI (Graphical User Interface) and the data-capture kernel/engine. Almost all of the user interaction with the software will take place via the GUI.

However, for the GUI to operate, the NetLab kernel has to be started. This kernel resides on the Linux data capture PC (plasmoid). The recommended way to access the kernel is via the X-terminal shortcut on the start menu (NetLab Terminal).

Selecting the 'NetLab Terminal' will cause a dialog box to appear: use the username and password of **netlab** to login. When the command prompt appears in the terminal window, enter *netlab* to start the program:

```
plasmoid:~$ netlab
NetLab
Copyright Mef 1998
Joystick timer hardware detected and initialised!
Warning! Motor hardware not correctly identified! Is it switched on?
     (Ignore this error if not using stepper motors)
Gage_init_mem installed successfully!
Card installed OK!
Card initialised OK!
Names: [200], Status: [f00]
.........................................CG840 card base: D0000
cg_generate_mode : 0
Base: 300
Channels: 0
Mode: 1
Rate: 500
Multiplier: 2
Oneshot: 1
Busy? : 0
Triggered? : 0
Do main
doing main: 0
0 >
```

The messages shown are diagnostic messages indicating that the various hardware components were identified and initialised.

To let the GUI talk to the kernel, the kernel must be told to expect commands from the network: enter *neti*

When finished, the GUI will send a *netx*, which will return control of the kernel to the user input (keyboard). Enter quit to end the kernel.

```
1 > neti
Network communications module
Listening on port: 5555

Redirecting input to network
```

```
received: [netx]
Fetched: [netx,netx]
Resetting input to local
9 >
10 > quit
Quit received!
terminating
CG_TERM termination code..
CS-220 termination code
plasmoid:~$
```

University of Cape Town

The GUI software is accessed by running "C:\Usr\NetLab\IDL\NetLab.pro".
This IDL program is compiled (Ctrl-F5) and executed (F5) within the IDL IDE. The IDE (Integrated Development Environment) is started by double-clicking on the *NetLab.pro* file.

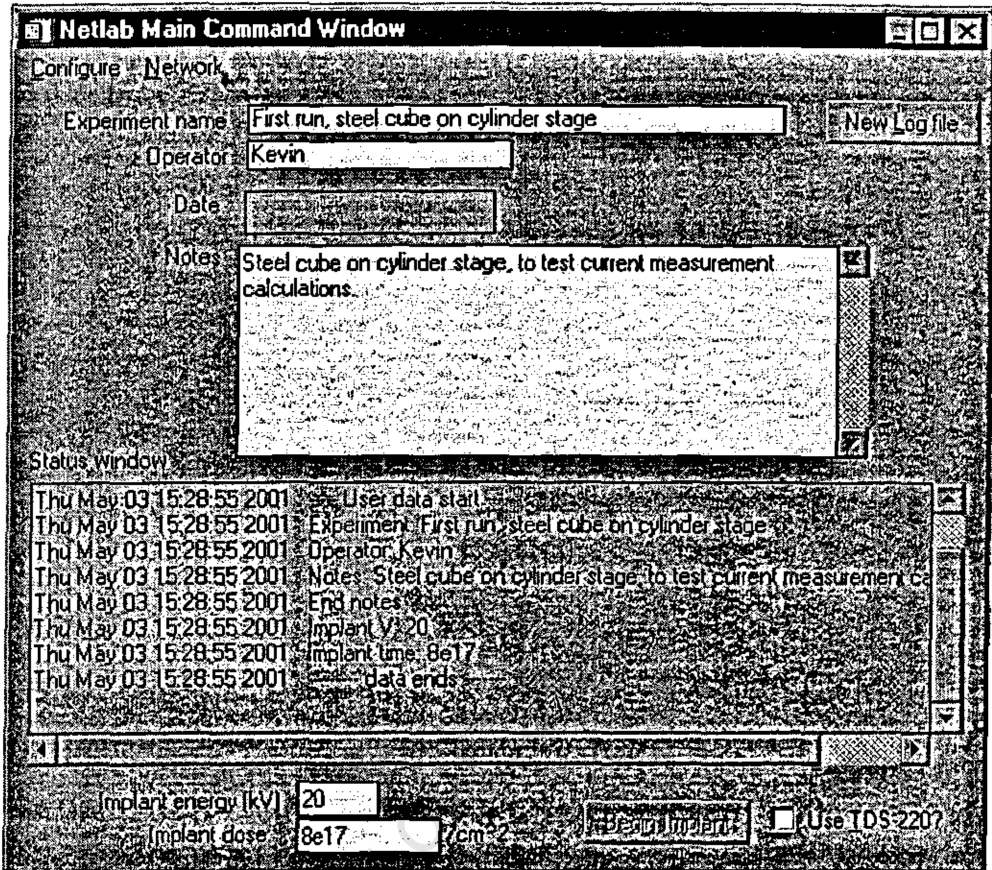

The main NetLab command window (above). Allows the user to configure the connection (where to find the data capture computer running NetLab), choose a log file (keeps a record of all system messages), and set experiment information, such as operator name, notes, implant energy and desired dose. If the TDS-220 oscilloscope is attached to the data-capture computer, the user has to opportunity here to use it.

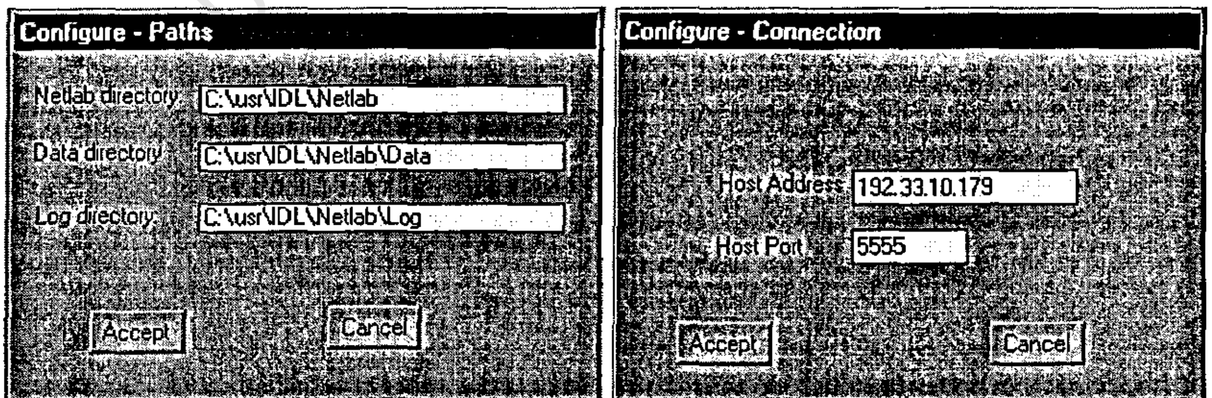

The Path and Connection configuration menus. Used to change the defaults. The data directory is where saved channels, etc, are stored. The Log directory is for the experiment log.

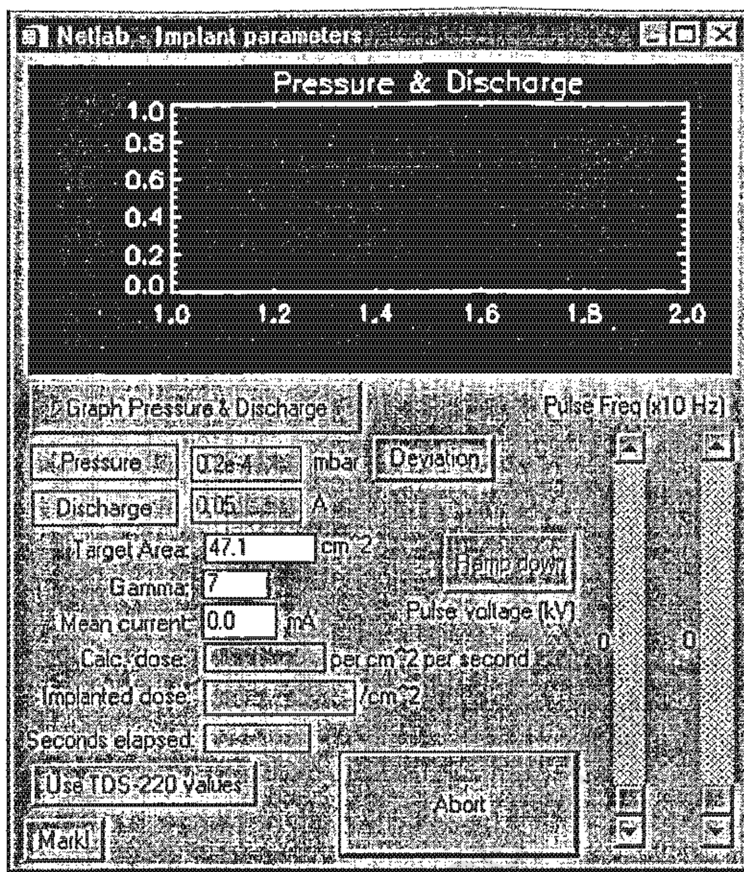

The main NetLab experiment window. This windows uses routines to calculate the implanted dose based on the values entered by the user. The graph allows the user to monitor the discharge current and the chamber pressure.

User input fields:

Target area (in cm^2): The approximate surface area of the target that is exposed to the plasma. This area must also include the area of the conductor.
Gamma: The secondary electron emission co-efficient. Used to separate the ion current from the total current.
Mean current: If the "Use TDS-220 Values" button has not been pressed (or the oscilloscope is not available), this field is used to input the mean implantation current of the RUP-4a high voltage power supply. If the oscilloscope is being used, the mean current is calculated based on the oscilloscope timer parameters (see the "TDS-220 Oscilloscope window").

Deviations/tolerance fields: These input fields are used to specify the maximum deviation that the last-retrieved pressure/discharge may deviate from the first retrieved values before an alarm is triggered. The alarm serves to alert the operator that the pressure or discharge has deviated out of bounds.

Buttons:

"Graph Pressure & Discharge": Used to retrieve and graph the chamber pressure and discharge current values from the CS-220 oscilloscope card.
"Deviation": Used to register new tolerance for pressure and discharge.
"Mark!": Used to reset the timer and implanted dose counters.
"Pulse Freq" slider: Set the pulse frequency (in tens of Hz)
"Pulse Voltage" slider: Set the implantation voltage (in kV)
"Abort": Used to abort the experiment: voltage and frequency set to 0.

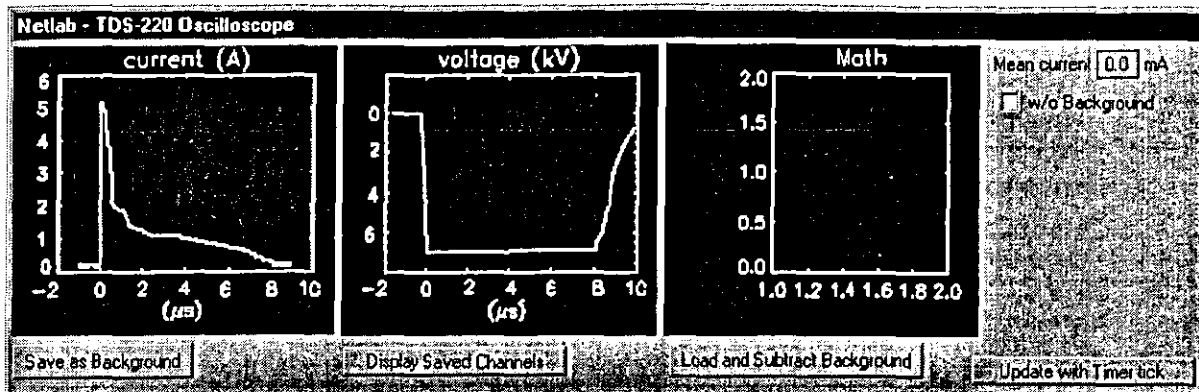

The TDS-220 oscilloscope window, showing a possible current / voltage combination. The buttons are used as follows:
"Save as Background" : Allows the user to save the current for use as a 'background' current for later subtraction (see "w/o Background")
"Display Saved Channels": Allows the user to retrieve the data stored in the oscilloscopes saved channels (To possibly retrieve a previously stored waveform).
"Load and Subtract Background": Allows the users to select a previously saved background (see "Save as Background" above), which is then subtracted from the acquired current measurement. The new current is shown in the "Math" window.
"Update with Timer Tick": Is used to enable/disable the channel updates. If enabled, the current and voltage traces are retrieved with every timer tick (about every 5 seconds). All additional processing is then performed (e.g. to calculate implantation current).

"w/o Background": Is used to select which current is used to calculate the mean current. If this checkbox is ticked, then the stored background current is subtracted from the active current. Otherwise, only the active current is used.

University of Cape Town

The Plasma Laboratory

The plasma laboratory consists of the plasma chamber, the vacuum pumps (and supporting apparatus), the RUP-4a high voltage power supply, the plasma formation power supplies, the water cooling circuit (and supporting apparatus) and the controlling computers (and supporting hardware).

Operation of the facility will be described in order of use:

1. Opening the chamber
2. Closing the plasma chamber
3. Achieving chamber vacuum
4. Turning on the plasma
5. Turning on the RUP-4a HV power supply
6. Starting / Running an implantation experiment
7. Switching off the RUP-4a power supply
8. Turning off the plasma

1. Opening the chamber

Before opening the chamber, be sure to turn off all the vacuum pumps and close the butterfly valve between the main pump and the chamber (under the chamber). The main pump is switched powered from the right-hand mains switch (mounted behind the door), the fore-pump uses the 3-phase switch next to the pump (in the annex outside the laboratory).

All typically accessed components within the plasma chamber can be reached by only opening the front flange. This flange is secured by four (size 19) bolts, located at the (approximately) 30, 120, 210, 300 degree positions.

Before opening the chamber, the chamber needs be brought up to atmospheric pressure. This can be done by loosening one of the many unused feedthrough plugs and drawing out the 6mm diameter sealing rod.

Before removing the water cooling pipes, ensure that the recirculated water has been turned off (the taps are mounted on the east wall) and that the water pressure has been released (open the little plastic tap under the coarse filter).

With the four restraining bolts removed, taking care not to rotate the flange trolley (to prevent the probes mounted on the inner side from touching the chamber inner walls) the flange can be pulled away from the chamber.

The filaments, probes and target holder can now all be accessed.

Precautions:

1. The longer the chamber is left at atmospheric pressure, the longer it will take to pump down again (while the chamber is open, the walls are absorbing water, etc, from the atmosphere.. these take time to out-gas again).

2. **Be sure to touch the target using the provided grounding rod to discharge the charging capacitor**. This is to prevent accidental shocks.

University of Cape Town

Replacing the filaments

The figure shows where the filaments can be wound. Each filament can be wound 2 or 3 times around the electrode pins (which are welded to the conductors).

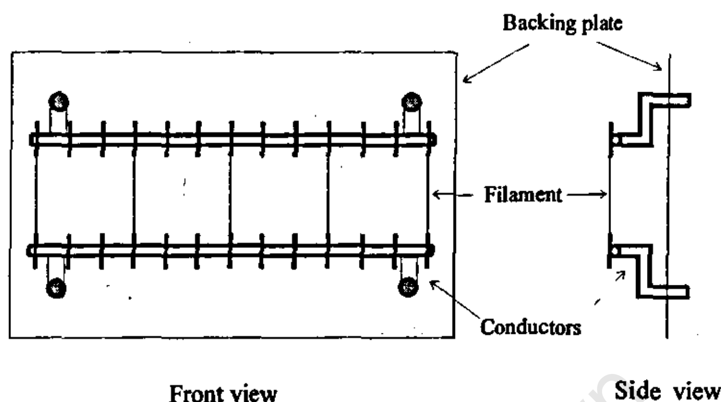

2. Closing the plasma chamber

The chamber is closed using the reverse process described above:

1. Check that the O-ring seal is clear of hairs or other dirt that may destroy vacuum integrity. If the seal is dry, a thin, fresh layer of vacuum grease may be applied.
2. Push the flange trolley back into place, taking care not to let the probe apparatus hit the chamber walls, and align the bolt holes.
3. Insert the four restraining bolts into the flange and lightly tighten them. Since the chamber is made of an aluminium alloy, it is quite soft and the threads are easily damaged. The bolts only need be sufficiently tight to bring the rubber o-ring into contact with the chamber.
4. Re-attach the water cooling pipes.

3. Achieving chamber vacuum

Once the flange has been closed:

1. Close the opening made to bring the chamber to atmospheric pressure (re-insert the sealing rod and gently tighten the feedthrough plug).
2. Turn the roughing / backing valve (under the chamber) to the roughing position.
3. Turn on the fore-pump (rotary pump). This pump uses the 3-phase switch next to the pump (in the annex outside the laboratory).
4. When the chamber pressure has dropped to at least 1e-1 mbar:
   - i) Turn on the recirculated cooling water,
   - ii) turn the roughing / backing valve (under the chamber) to the roughing position, and
   - iii) turn on the main pump (switch on the south wall, to the left of the door).
5. Once the chamber pressure has reached 8e-5 mbar, the plasma can be turned on.

University of Cape Town

4. Turning on the plasma

Most power supplies in the laboratory can not be operated if the cooling water water-flow rate switch is not operating. This requires sufficient flow (2 litres per minute) to turn on the contactor. The recirculated water taps are on the south wall.

The plasma is turned on by:

1. Ensure that the filament current control resistor (mounted on the control box) is turned completely anti-clockwise (lowest current).
2. Turn on the filament power supplies (switches under the control box and on the north wall).
3. Turn on the discharge power supply (on the trolley behind the rear flange). Set the discharge voltage to 60V.
4. Gently open the gas taps: one on the regulator (mounted on the gas cylinder), the other below the needle valve on the chamber.
5. Use the needle valve to regulate the chamber pressure (typical pressure: 8e-4 mbar).
6. Use the filament control resistor to gently increase the discharge current (the current should start increasing with a filament current about 20A). Take care to ensure that the filament current does not exceed 40A (the rated maximum of the fixed-voltage filament power supply).
7. The current regulating control resistor (bottom of the control box) can be used to maintain a constant discharge current. The green light indicates when the circuit is in operation.

Plasma gases:
Any non-reactive gas can be used with relative safety. Typical gasses used are nitrogen (N), argon (Ar), hydrogen (H), methane (for C), etc. Care must be taken when using reactive gases, such as oxygen, as they would rapidly degrade the filaments. The RF plasma source would be preferred in such a case.

University of Cape Town

5. Turning on the RUP-4a HV power supply

According to the RUP-4a user manual for full instructions. In short:

1) The main power switches on the tetrode-cooling fan.
2) The "filament power" switch turns on the tetrode filaments
3) The "grid and high-voltage power" turns on the 30kV DC charging supply and the ~1000V tetrode grid switching power supplies.

Pulse width and frequency can be set using the front panel (top left) variable resistors. The implantation voltage can be set using the front panel (top right) variable resistor.

6. Starting / Running an implantation experiment

Once a plasma has been achieved, and the RUP-4a PS has been turned on, an implantation experiment is ready.

The parameters described below can either be set using the NetLab software, or the RUP-4a front panel controls. If the front panel controls of the RUP-4a PS are used, care must be taken to not exceed a 25kV-implantation voltage (x-ray radiation hazard).

1. Set the implantation pulse timing parameters (pulse width and frequency) taking care not to exceed the critical duty cycle for the pulse power switched.
2. Set the implantation voltage, taking care to watch for arcing. If arcing occurs and does not stop after a short time (seconds), the target needs to be cleaned, with all sharp points removed. Arcing will be clearly visible in the implantation current trace on the oscilloscope.
3. For the duration of the implantation,
    - i) The implantation current must be monitored against arcing.
    - ii) The discharge current must be monitored to ensure filament integrity.
    - iii) The chamber pressure must be monitored to ensure plasma integrity.

7. Switching off the RUP-4a power supply

At the end of the experiment, the implantation voltage must be reduced to zero.

Once the implantation has been completed, the RUP-4a PS must be switched off. If another experiment is planned to start within four hours, the tetrode filament need not be switched off (to prevent thermal shock / damage). The grid and high voltage power must be turned off before opening the chamber (preferably as soon as the experiment has ended).

University of Cape Town

Safety

RUP-4a

The greatest healt risk in the plasma processing laboratory is the high voltage RUP-4a pulsed power supply. This device is capable of generating up to 30,000 V, which is stored in the unit charging capacitor. While every precaution has been taken to ensure that the high voltage electrode is completely insulated outside the plasma chamber, it is accessible from within the chamber.

Care must be taken to prevent accidental shock / electrocution.

Ensure that the RUP-4a is disconnected from the main power is the unit is ever opened for servicing. The high voltage stored in the grid power supply capacitors can be dangerous.

Electricity

The remaining electrical circuits are: The DC filament and discharge current circuits, and the AC mains supply circuits.

i) **DC filament**: Typically 2 to12V, 40A maximum. Take precautions to prevent short-circuits. There is minimal shock hazard at these low voltages.

ii) **Discharge circuit**: 60V, 2.5A max. Take precautions to prevent short-circuits. There is minimal shock hazard at these voltages, but a noticeable discomfort (don't touch the filament conductors while the plasma is switched on: not only do they carry 60+12 V, but they also get hot).

iii) **AC Mains circuits**. Take precautions to prevent short-circuits. Avoid contact with AC circuits as both the single phase (220V, 15A max) and the three-phase (380V, 15A) can kill. Ensure that all apparatus is switched off before servicing.

Gasses

Appropriate care must be taken when handling the plasma gasses:

1) High nitrogen gas concentrations can result in asphyxiation by reducing the available oxygen.

2) Hydrogen gas is highly flammable.

In general, check the safety sheet for the gas being used and take the appropriate precautions.

X-rays

Measurements show that x-rays are generated with a maximum energy the same as the implantation voltage. The greatest x-ray flux has energies lower than the implantation energy. The x-ray flux is pulsed. Due to the problems associated with determining x-ray dose, it is best if exposure to x-rays is completely eliminated (operate the control computer from the next office: use the hole in the wall for co-axial monitoring cables, etc).

Revision history: Kevin Meyer, May 2001

University of Cape Town

Appendix E

Datasheets

University of Cape Town

University of Cape Town

THE L297 STEPPER MOTOR CONTROLLER

The L297 integrates all the control circuitry required to control bipolar and unipolar stepper motors. Used with a dual bridge driver such as the L298N forms a complete microprocessor-to-bipolar stepper motor interface. Unipolar stepper motor can be driven with an L297 plus a quad darlington array. This note describes the operation of the circuit and shows how it is used.

The L297 Stepper Motor Controller is primarily intended for use with an L298N or L293E bridge driver in stepper motor driving applications.

It receives control signals from the system's controller, usually a microcomputer chip, and provides all the necessary drive signals for the power stage. Additionally, it includes two PWM chopper circuits to regulate the current in the motor windings.

With a suitable power actuator the L297 drives two phase bipolar permanent magnet motors, four phase unipolar permanent magnet motors and four phase variable reluctance motors. Moreover, it handles normal, wave drive and half step drive modes. (This is all explained in the section "Stepper Motor Basics").

Two versions of the device are available : the regular L297 and a special version called L297A. The L297A incorporates a step pulse doubler and is designed specifically for floppy-disk head positioning applications.

ADVANTAGES

The L297 + driver combination has many advantages : very few components are required (so assembly costs are low, reliability high and little space required), software development is simplified and the burden on the micro is reduced. Further, the choice of a two-chip approach gives a high degree of flexibility-the L298N can be used on its own for DC motors and the L297 can be used with any power stage, including discrete power devices (it provides 20mA drive for this purpose).

University of Cape Town

Figure 1 : In this typical configuration an L297 stepper motor controller and L298 dual bridge driver combine to form a complete microprocessor to bipolar stepper motor interface.

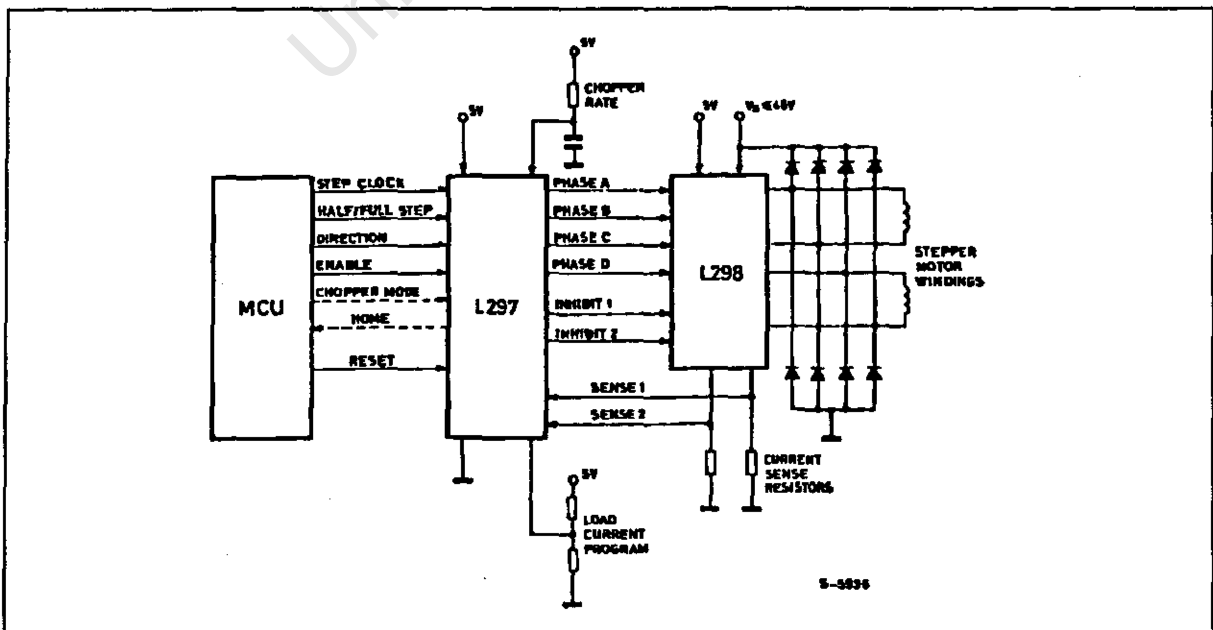

For bipolar motors with winding currents up to 2A the L297 should be used with the L298N ; for winding currents up to 1A the L293E is recommended (the L293 will also be useful if the chopper isn't needed). Higher currents are obtained with power transistors or darlingtons and for unipolar motors a darlington array such as the ULN2075B is suggested. The block diagram, figure 1, shows a typical system.

Applications of the L297 can be found almost everywhere... printers (carriage position, daisy position, paper feed, ribbon feed), typewriters, plotters, numerically controlled machines, robots, floppy disk drives, electronic sewing machines, cash registers, photocopiers, telex machines, electronic carburetos, telecopiers, photographic equipment, paper tape readers, optical character recognisers, electric valves and so on.

The L297 is made with SGS' analog/digital compatible I^2L technology (like Zodiac) and is assembled in a 20-pin plastic DIP. A 5V supply is used and all signal lines are TTL/CMOS compatible or open collector transistors. High density is one of the key features of the technology so the L297 die is very compact.

THE L298N AND L293E

Since the L297 is normally used with an L298N or L293E bridge driver a brief review of these devices will make the rest of this note easier to follow.

The L298N and L293E contain two bridge driver stages, each controlled by two TTL-level logic inputs and a TTL-level enable input. In addition, the emitter connections of the lower transistors are brought out to external terminals to allow the connection of current sensing resistors (figure 2).

For the L298N SGS' innovative ion-implanted high voltage/high current technology is used, allowing it to handle effective powers up to 160W (46V supply, 2A per bridge). A separate 5V logic supply input is provided to reduce dissipation and to allow direct connection to the L297 or other control logic.

In this note the pins of the L298N are labelled with the pin names of the corresponding L297 terminals to avoid unnecessary confusion.

The L298N is supplied in a 15-lead Multiwatt plastic power package. It's smaller brother, the functionally identical L293E, is packaged in a Powerdip – a copper frame DIP that uses the four center pins to conduct heat to the circuit board copper.

Figure 2 : The L298N contains two bridge drivers (four push pull stages) each controlled by two logic inputs and an enable input. External emitter connections are provided for current sense resistors. The L293E has external connections for all four emitters.

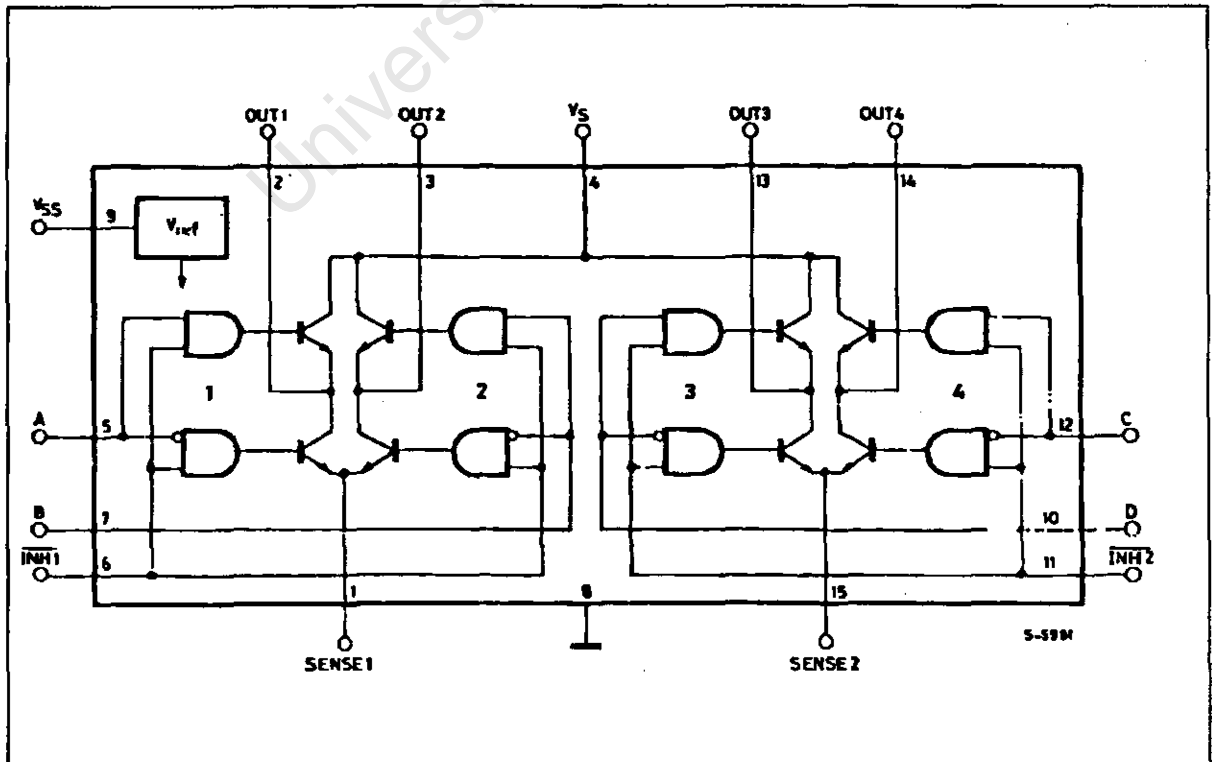

STEPPER MOTOR BASICS

There are two basic types of stepper motor in common use : permanent magnet and variable reluctance. Permanent magnet motors are divided into bipolar and unipolar types.

BIPOLAR MOTORS

Simplified to the bare essentials, a bipolar permanent magnet motor consists of a rotating permanent magnet surrounded by stator poles carrying the windings (figure 3). Bidirectional drive current is used and the motor is stepped by switching the windings in sequence.

For a motor of this type there are three possible drive sequences.

Figure 3 : Greatly simplified, a bipolar permanent magnet stepper motor consist of a rotaring magnet surrounded by stator poles as shown.

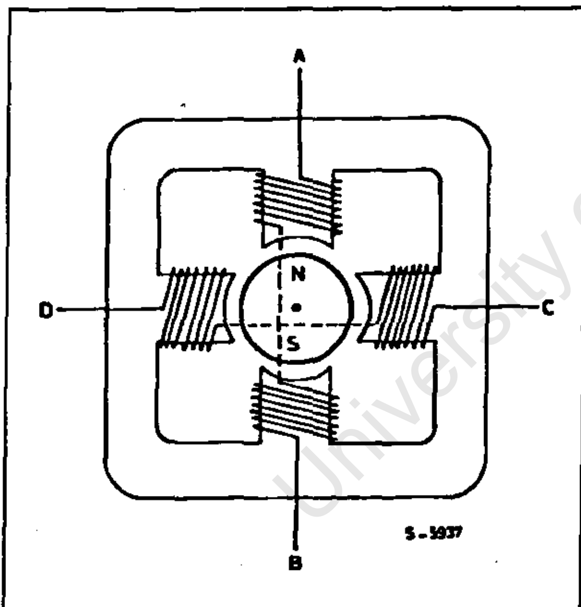

The first is to energize the windings in the sequence AB/CD/BA/DC (BA means that the winding AB is energized but in the opposite sense). This sequence is known as "one phase on" full step or wave drive mode. Only one phase is energized at any given moment (figure 4a).

The second possibility is to energize both phases together, so that the rotor always aligns itself between two pole positions. Called "two-phase-on" full step, this mode is the normal drive sequence for a bipolar motor and gives the highest torque (figure 4b).

The third option is to energize one phase, then two, then one, etc., so that the motor moves in half step increments. This sequence, known as half step mode, halves the effective step angle of the motor but gives a less regular torque (figure 4c).

For rotation in the opposite direction (counter-clockwise) the same three sequences are used, except of course that the order is reserved.

As shown in these diagrams the motor would have a step angle of 90°. Real motors have multiple poles to reduce the step angle to a few degrees but the number of windings and the drive sequences are unchanged. A typical bipolar stepper motor is shown in figure 5.

UNIPOLAR MOTORS

A unipolar permanent magnet motor is identical to the bipolar machine described above except that bifilar windings are used to reverse the stator flux, rather than bidirectional drive (figure 6).

This motor is driven in exactly the same way as a bipolar motor except that the bridge drivers are replaced by simple unipolar stages - four darlingtons or a quad darlington array. Clearly, unipolar motors are more expensive because thay have twice as many windings. Moreover, unipolar motors give less torque for a given motor size because the windings are made with thinner wire. In the past unipolar motors were attractive to designers because they simplify the driver stage. Now that monolithic push pull drivers like the L298N are available bipolar motors are becoming more popular.

All permanent magnet motors suffer from the counter EMF generated by the rotor, which limits the rotation speed. When very high slewing speeds are necessary a variable reluctance motor is used.

University of Cape Town

Figure 4 : The three drive sequences for a two phase bipolar stepper motor. Clockwise rotation is shown.

Figure 4a : Wave drive (one phase on).

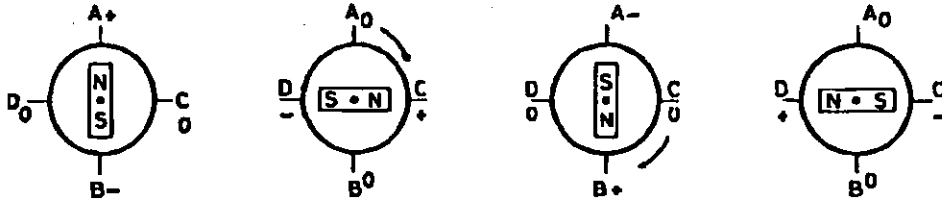

Figure 4b : Two phase on drive.

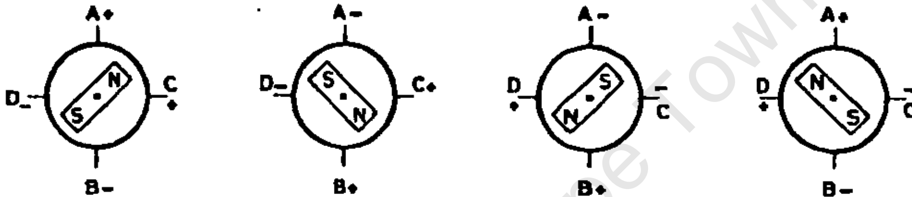

Figure 4c : Half step drive.

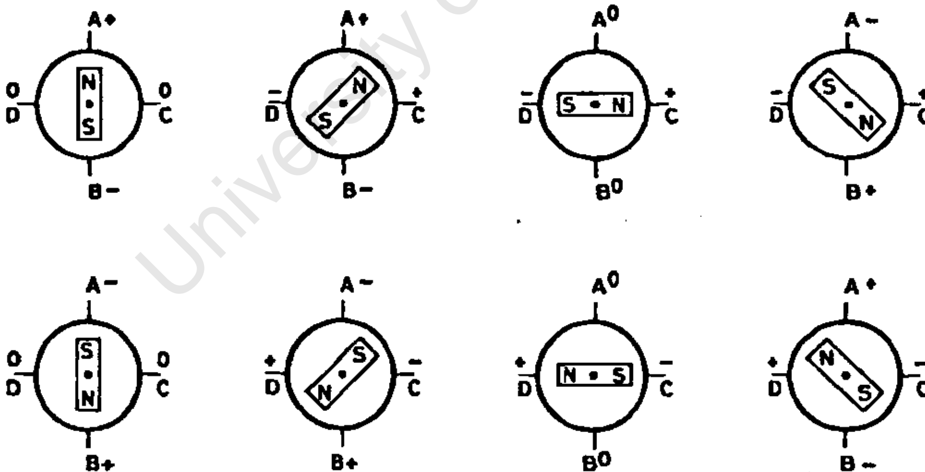

University of Cape Town

SGS-THOMSON MICROELECTRONICS

Figure 5 : A real motor. Multiple poles are normally employed to reduce the step angle to a practical value. The principle of operation and drive sequences remain the same.

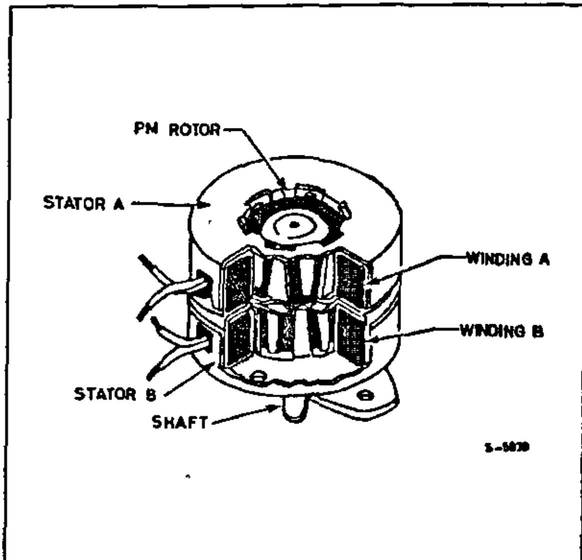

Figure 6 : A unipolar PM motor uses bifilar windings to reverse the flux in each phase.

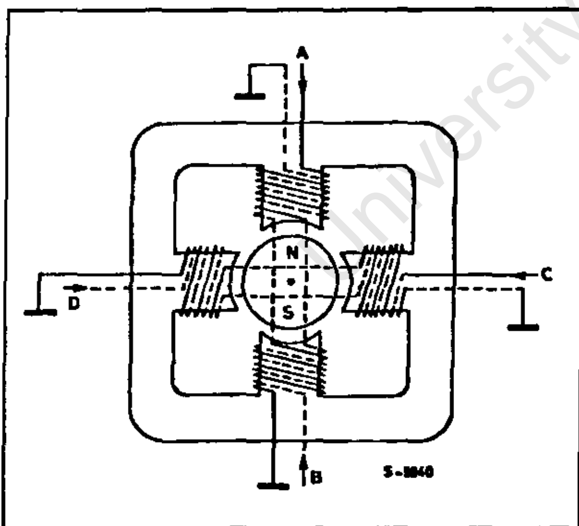

VARIABLE RELUCTANCE MOTORS

A variable reluctance motor has a non-magnetized soft iron rotor with fewer poles than the stator (figure 7). Unipolar drive is used and the motor is stepped by energizing stator pole pairs to align the rotor with the pole pieces of the energized winding.

Once again three different phase sequences can be used. The wave drive sequence is A/C/B/D ; two-phase-on is AC/CB/BD/DA and the half step sequence is A/AC/C/BC/B/BD/D/DA. Note that the step angle for the motor shown above is 15 °, not 45 °.

As before, pratical motors normally employ multiple poles to give a much smaller step angle. This does not, however, affect the principle of operation of the drive sequences.

Figure 7 : A variable reluctance motor has a soft iron rotor with fewer poles than the stator. The step angle is 15 ° for this motor.

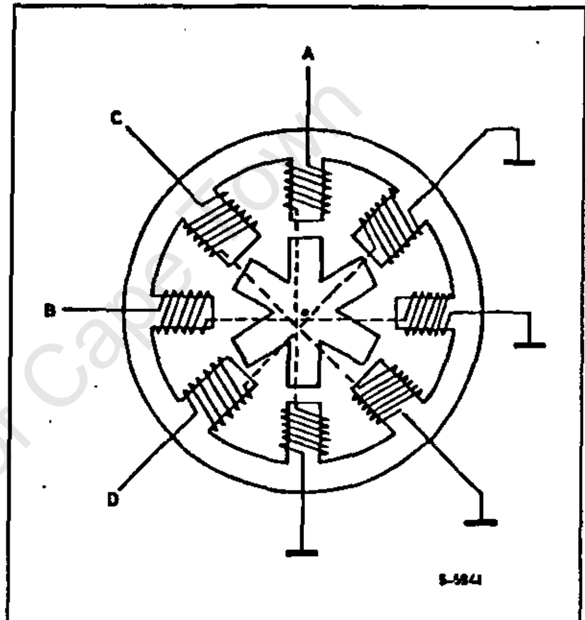

GENERATING THE PHASE SEQUENCES

The heart of the L297 block diagram, figure 8, is a block called the translator which generates suitable phase sequences for half step, one-phase-on full step and two-phase-on full step operation. This block is controlled by two mode inputs – direction (CW/ $\overline{\text{CCW}}$) and HALF/ $\overline{\text{FULL}}$ – and a step clock which advances the translator from one step to the next.

Four outputs are provided by the translator for subsequent processing by the output logic block which implements the inhibit and chopper functions.

Internally the translator consists of a 3-bit counter plus some combinational logic which generates a basic eight-step gray code sequence as shown in figure 9. All three drive sequences can be generated easily from this master sequence. This state sequence corresponds directly to half step mode, selected by a high level on the HALF/ $\overline{\text{FULL}}$ input.

University of Cape Town

The output waveforms for this sequence are shown in figure 10.

Note that two other signals, $\overline{INH1}$ and $\overline{INH2}$ are generated in this sequence. The purpose of these signals is explained a little further on.

The full step modes are both obtained by skipping alternate states in the eight-step sequence. What happens is that the step clock bypasses the first stage of the 3-bit counter in the translator. The least significant bit ot this counter is not affected therefore the sequence generated depends on the state of the translator when full step mode is selected (the HALF/ $\overline{FULL}$ input brought low).

If full step mode is selected when the translator is at any odd-numbered state we get the two-phase-on full step sequence shown in figure 11.

By contrast, one-phase-on full step mode is obtained by selecting full step mode when the translator is at an even-numbered state (figure 12).

Figure 8 : The L297 contains translator (phase sequence generator), a dual PWM chopper and output control logic.

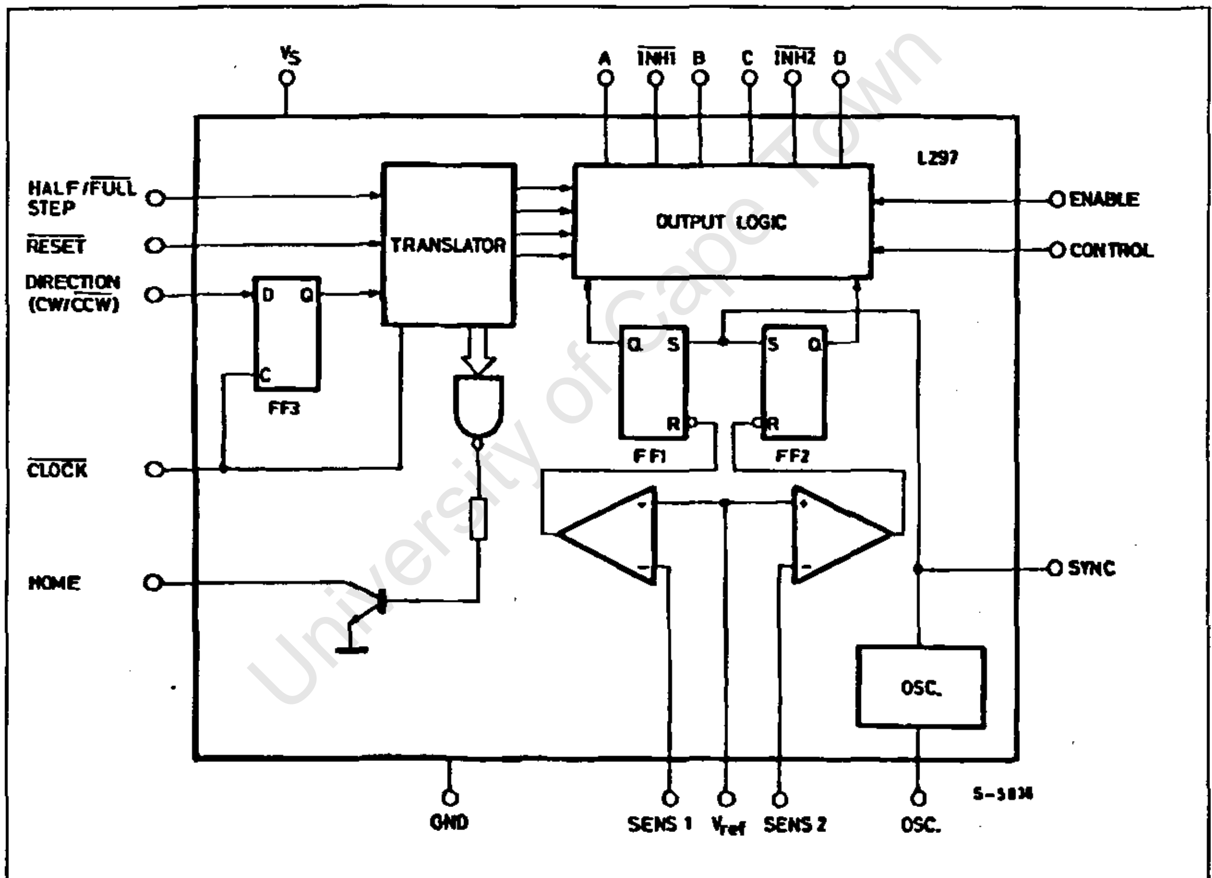

University of Cape Town

Figure 9 : The eight step master sequence of the translator. This corresponds to half step mode. Clockwise rotation is indicated.

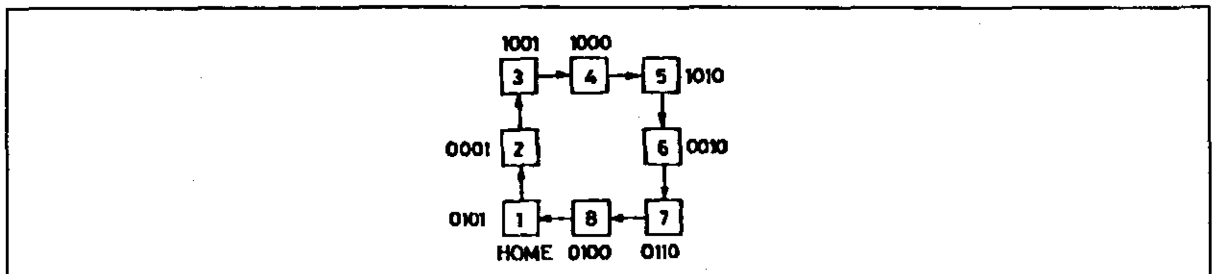

Figure 10 : The output waveforms corresponding to the half step sequence. The chopper action in not shown.

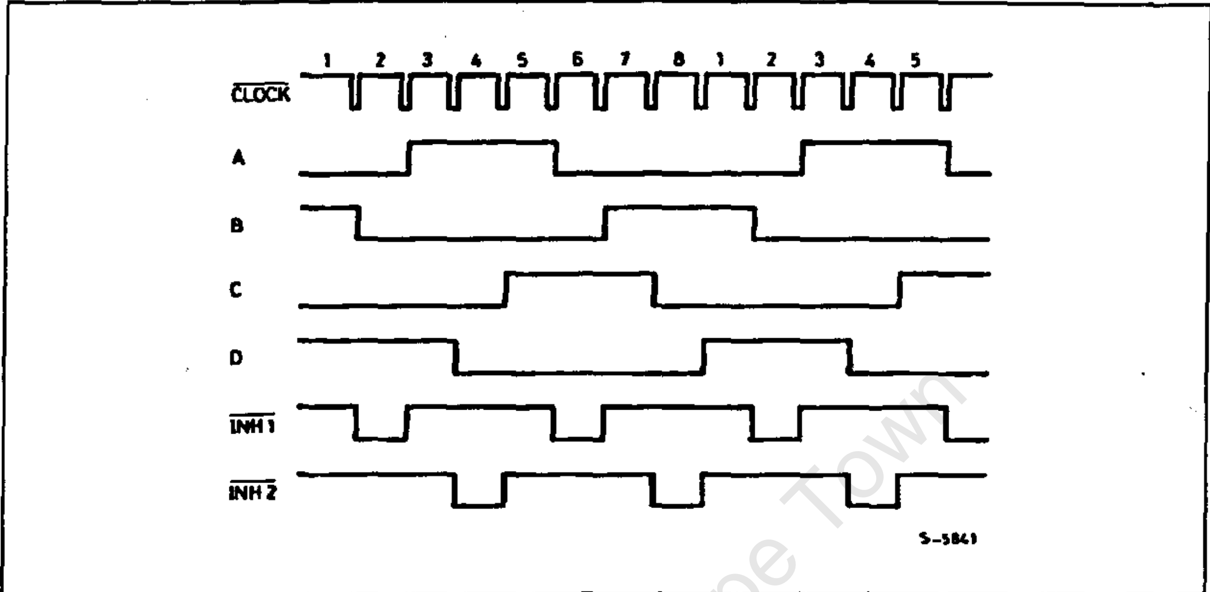

Figure 11 : State sequence and output waveforms for the two phase on sequence. $\overline{INH1}$ and $\overline{INH2}$ remain high throughout.

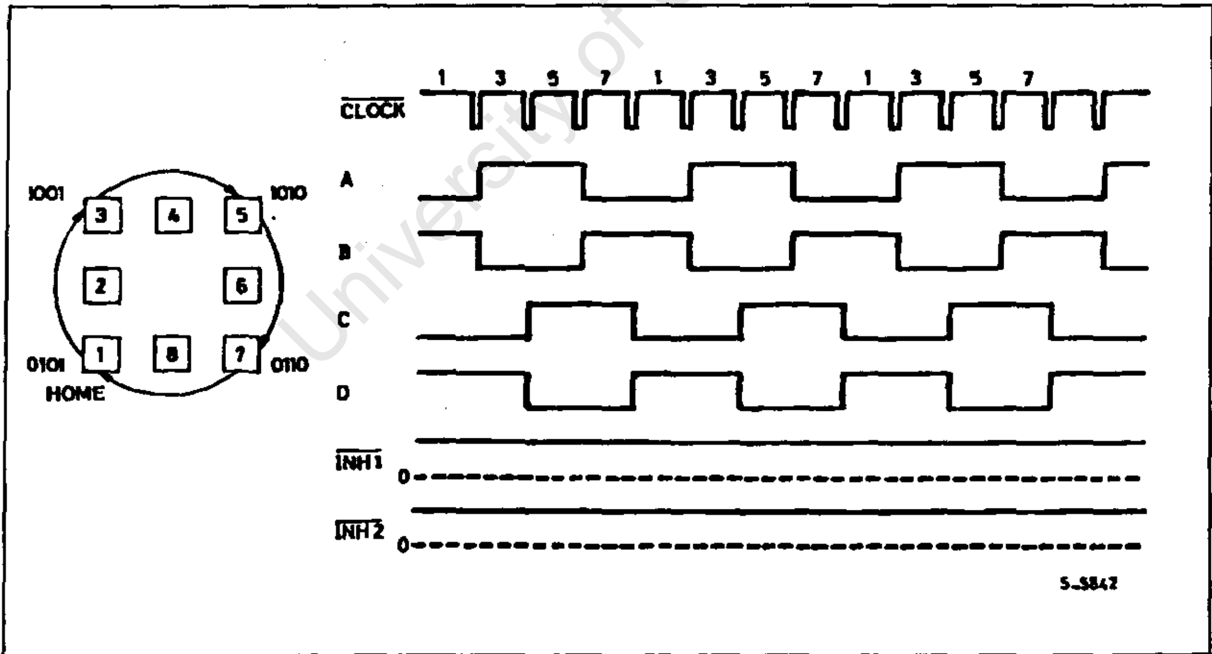

University of Cape Town

Figure 12 : State Sequence and Output Waveforms for Wave Drive (one phase on).

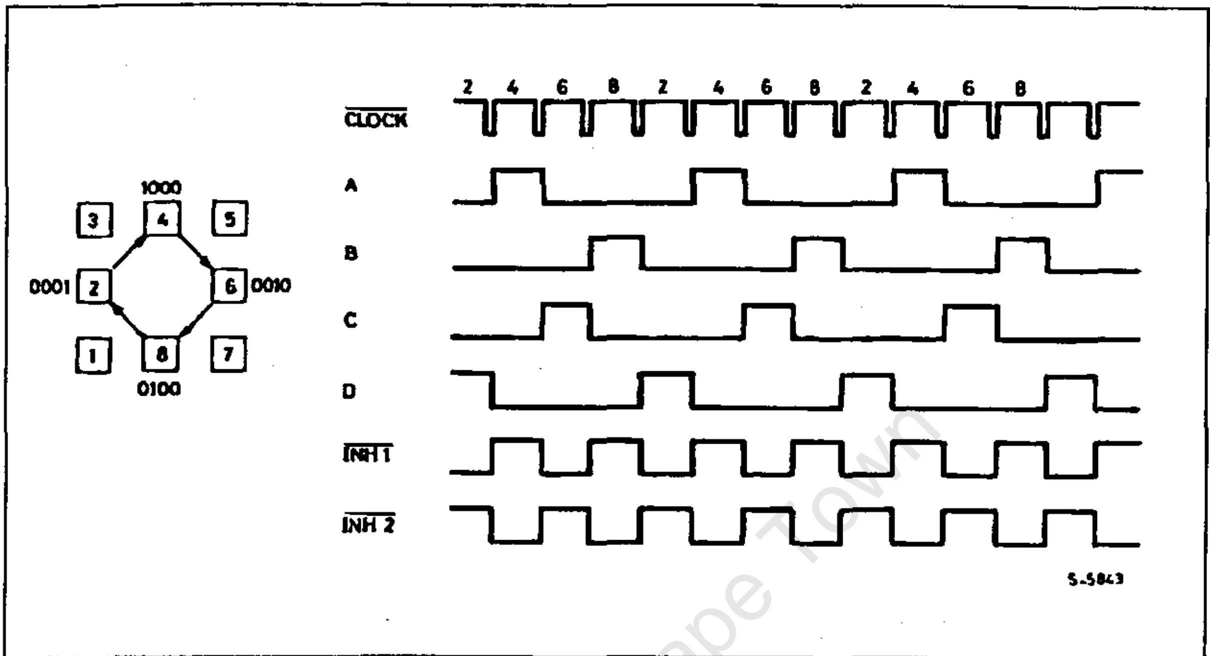

$\overline{INH1}$ AND $\overline{INH2}$

In half step and one-phase-on full step modes two other signals are generated: $\overline{INH1}$ and $\overline{INH2}$. These are inhibit signals which are coupled to the L298N's enable inputs and serve to speed the current decay when a winding is switched off.

Since both windings are energized continuously in two-phase-on full step mode no winding is ever switched off and these signals are not generated.

To see what these signals do let's look at one half of the L298N connected to the first phase of a two-phase bipolar motor (figure 13). Remember that the L298N's A and B inputs determine which transistor in each push pull pair will be on. $\overline{INH1}$, on the other hand, turns off all four transistors.

Assume that A is high, B low and current flowing through Q1, Q4 and the motor winding. If A is now brought low the current would recirculate through D2, Q4 and R_s, giving a slow decay and increased dissipation in R_s. If, on a other hand, A is brought low and $\overline{INH1}$ is activated, all four transistors are turned off. The current recirculates in this case from ground to V_s via D2 and D3, giving a faster decay thus allowing faster operation of the motor. Also, since the recirculation current does not flow through R_s, a less expensive resistor can be used.

Exactly the same thing happens with the second winding, the other half of the L298 and the signals C, D and $\overline{INH2}$.

The $\overline{INH1}$ and $\overline{INH2}$ signals are generated by OR functions:

$$A + B = \overline{INH1} \qquad C + D = \overline{INH2}$$

However, the output logic is more complex because inhibit lines are also used by the chopper, as we will see further on.

OTHER SIGNALS

Two other signals are connected to the translator block: the RESET input and the HOME output

RESET is an asynchronous reset input which restores the translator block to the home position (state 1, ABCD = 0101). The HOME output (open collector) signals this condition and is intended to the ANDed with the output of a mechanical home position sensor.

Finally, there is an ENABLE input connected to the output logic. A low level on this input brings $\overline{INH1}$, $\overline{INH2}$, A, B, C and D low. This input is useful to disable the motor driver when the system is initialized.

LOAD CURRENT REGULATION

Some form of load current control is essential to obtain good speed and torque characteristics. There are several ways in which this can be done – switching the supply between two voltages, pulse rate modulation chopping or pulse width modulation chopping.

University of Cape Town

Figure 13 : When a winding is switched off the inhibit input is activated to speed current decay. If this were not done the current would recirculate through D2 and Q4 in this example. Dissipation in R_S is also reduced.

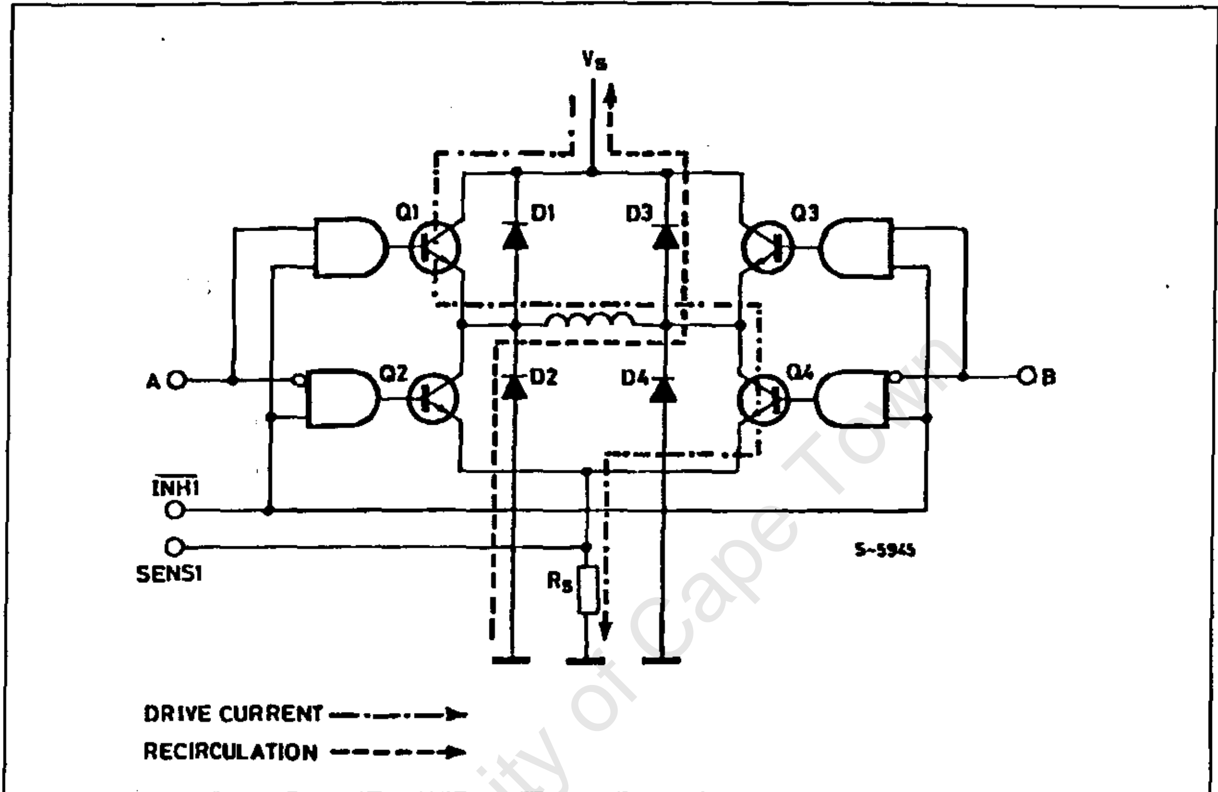

University of Cape Town

The L297 provides load current control in the form of two PWM choppers, one for each phase of a bipolar motor or one for each pair of windings for a unipolar motor. (In a unipolar motor the A and B windings are never energized together so thay can share a chopper ; the same applies to C and D).

Each chopper consists of a comparator, a flip flop and an external sensing resistor. A common on chip oscillator supplies pulses at the chopper rate to both choppers.

In each chopper (figure 14) the flip flop is set by each pulse from the oscillator, enabling the output and allowing the load current to increase. As it increases the voltage across the sensing resistor increases, and when this voltage reaches V_{ref} the flip flop is reset, disabling the output until the next oscillator pulse arrives. The output of this circuit (the flip flop's Q output) is therefore a constant rate PWM signal. Note that V_{ref} determines the peak load current.

Figure 14 : Each chopper circuit consists of a comparator, flip flop and external sense resistor. A common oscillator clocks both circuits.

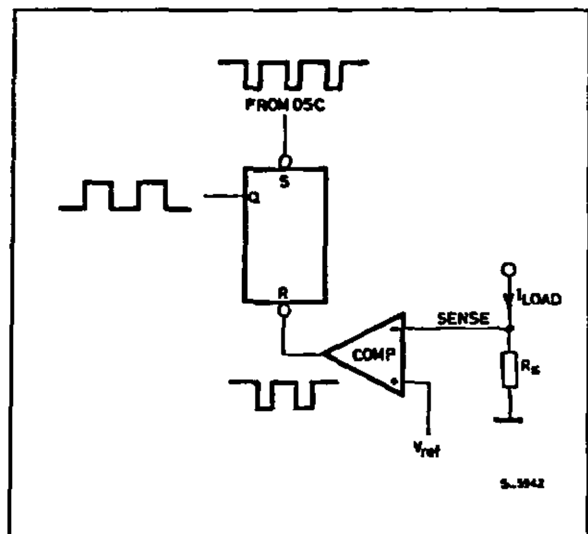

PHASE CHOPPING AND INHIBIT CHOPPING

The chopper can act on either the phase lines (ABCD) or on the inhibit lines $\overline{INH1}$ and $\overline{INH2}$. An input named CONTROL decides which. Inhibit chopping is used for unipolar motors but you can choose between phase chopping and inhibit chopping for bipolar motors. The reasons for this choice are best explained with another example.

First let's examine the situation when the phase lines are chopped.

As before, we are driving a two phase bipolar motor and A is high, B low (figure 15). Current therefore flows through Q1, winding, Q4 and R_s. When the voltage across R_s reaches V_{ref} the chopper brings B high to switch off the winding.

The energy stored in the winding is dissipated by current recirculating through Q1 and D3. Current decay through this path is rather slow because the voltage on the winding is low ($V_{CEsat\ Q1} + V_{D3}$) (figure 16).

Why is B pulled high, why push A low ? The reason is to avoid the current decaying through R_s. Since the current recirculates in the upper half of the bridge, current only flows in the sensing resistor when the winding is driven. Less power is therefore dissipated in R_s and we can get away with a cheaper resistor.

This explain why phase chopping is not suitable for unipolar motors : when the A winding is driven the chopper acts on the B winding. Clearly, this is no use at all for a variable reluctance motor and would be slow and inefficient for a bifilar wound permanent magnet motor.

The alternative is to tie the CONTROL input to ground so that the chopper acts on $\overline{INH1}$ and $\overline{INH2}$. Looking at the same example, A is high and B low. Q1 and Q4 are therefore conducting and current flows through Q1, the winding, Q4 and R_s, (figure 17).

Figure 15 : Phase Chopping. In this example the current X is interrupted by activating B, giving the recirculation path Y. The alternative, de-activating A, would give the recirculation path Z, increasing dissipation in R_s.

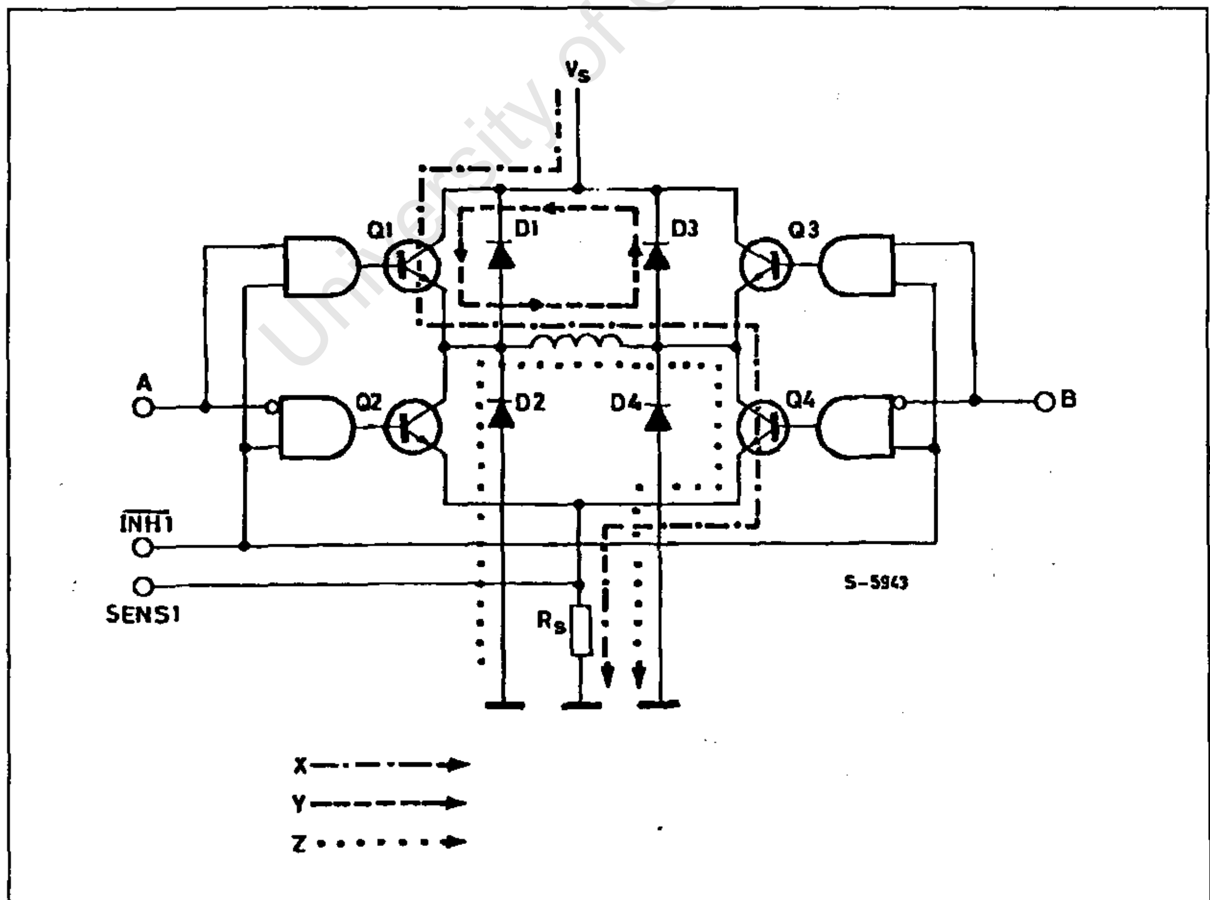

University of Cape Town

Figure 16 : Phase Chopping Waveforms. The example shows AB winding energized with A positive with respect to B. Control is high.

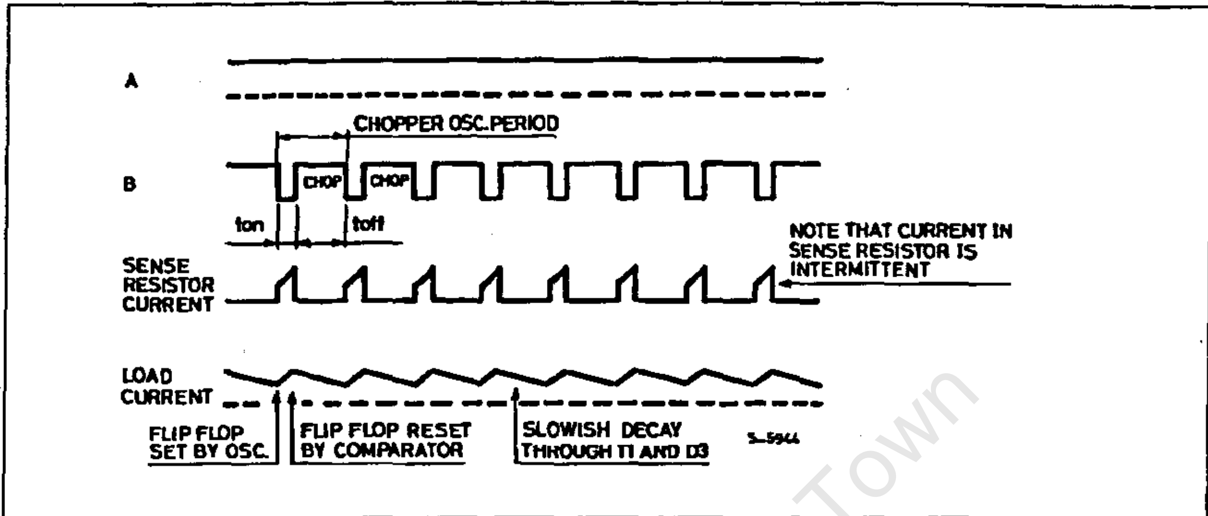

Figure 17 : Inhibit Chopping. The drive current (Q1, winding, Q4) in this case is interrupted by activating $\overline{INH1}$. The decay path through D2 and D3 is faster than the path Y of Figure 15.

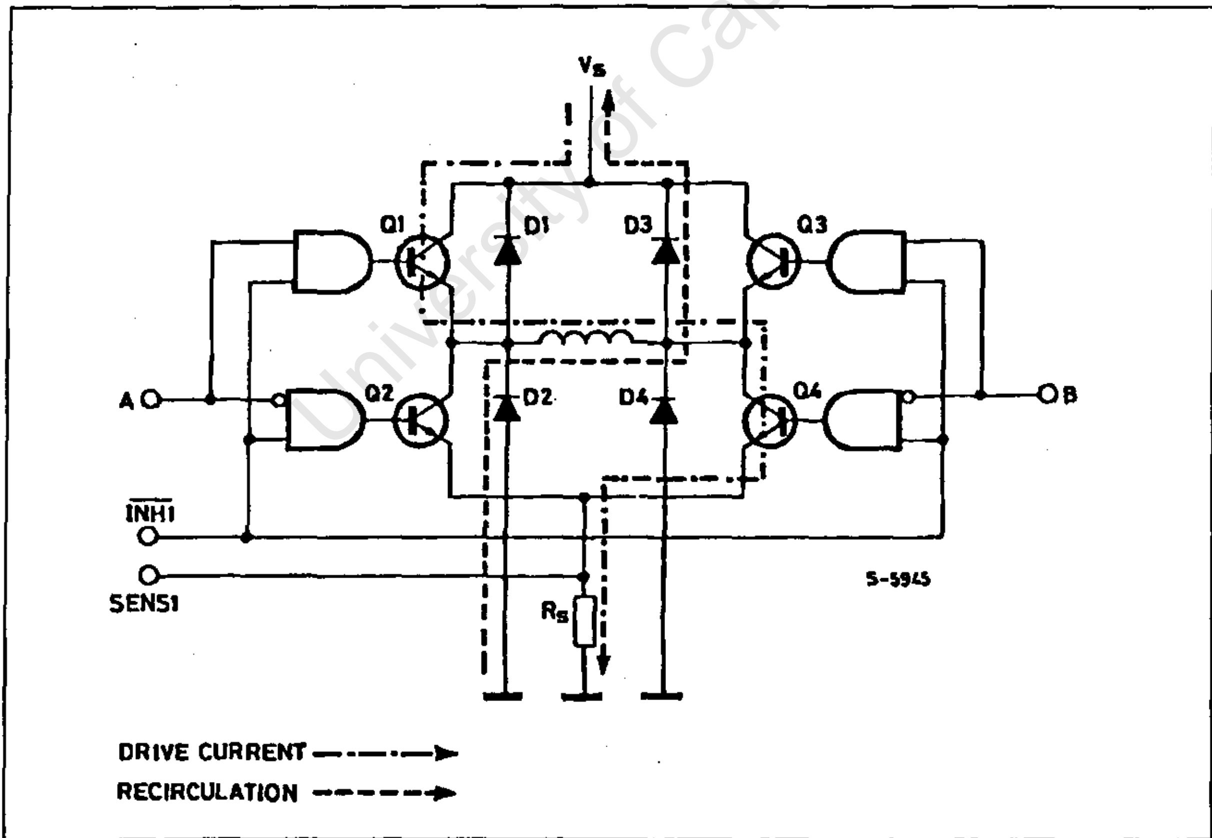

University of Cape Town

In this case when the voltage accross R_S reaches V_{REF} the chopper flip flop is reset and INH1 activated (brought low). INH1, remember, turns off all four transistors therefore the current recirculates from ground, through D2, the winding and D3 to V_S. Discharged across the supply, which can be up to 46V, the current decays very rapidly (figure 18).

The usefulness of this second faster decay option is fairly obvious ; it allows fast operation with bipolar motors and it is the only choice for unipolar motors. But why do we offer the slower alternative, phase chopping ?

The answer is that we might be obliged to use a low chopper rate with a motor that does not store much energy in the windings. If the decay is very fast the average motor current may be too low to give an useful torque. Low chopper rates may, for example, be imposed if there is a larger motor in the same system. To avoid switching noise on the ground plane all drivers should be synchronized and the chopper rate is therefore determined by the largest motor in the system.

Multiple L297s are synchronized easily using the SYNC pin. This pin is the squarewave output of the on-chip oscillator and the clock input for the choppers. The first L297 is fitted with the oscillator components and outputs a sqarewave signal on this pin (figure 19). Subsequent L297s do not need the oscillator components and use SYNC as a clock input. An external clock may also be injected at this terminal if an L297 must be synchronized to other system components.

Figure 18 : Inhibit Chopper Waveforms. Winding AB is energized and CONTROL is low.

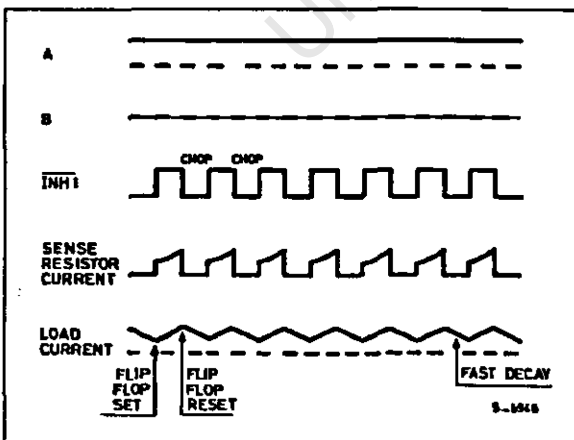

Figure 19 : The Chopper oscillator of multiple L297s are synchronized by connecting the SYNC Inputs together.

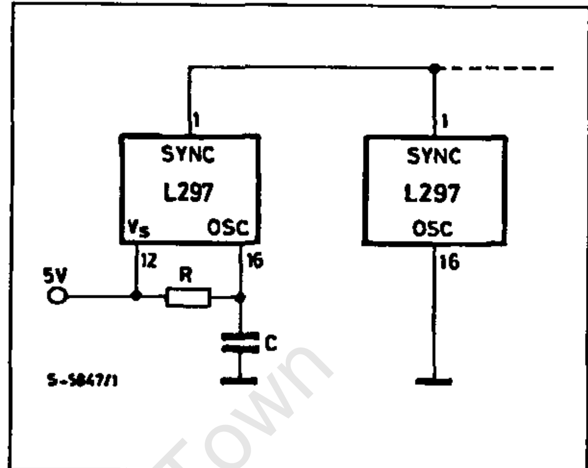

THE L297A

The L297A is a special version of the L297 developed originally for head positioning in floppy disk drives. It can, however, be used in other applications.

Compared to the standard L297 the difference are the addition of a pulse doubler on the step clock input and the availability of the output of the direction flip flop (block diagram, figure 20). To add these functions while keeping the low-cost 20-pin package the CONTROL and SYNC pins are not available on this version (they are note needed anyway). The chopper acts on the ABCD phase lines.

The pulse doubler generates a ghost pulse internally for each input clock pulse. Consequently the translator moves two steps for each input pulse. An external RC network sets the delay time between the input pulse and ghost pulse and should be chosen so that the ghost pulses fall roughly halfway between input pulses, allowing time for the motor to step.

This feature is used to improve positioning accuracy. Since the angular position error of a stepper motor is noncumulative (it cancels out to zero every four steps in a four step sequence motor) accuracy is improved by stepping two of four steps at a time.

University of Cape Town

Figure 20 : The L297A, includes a clock pulse doubler and provides an output from the direction flip flop (DIR – MEM).

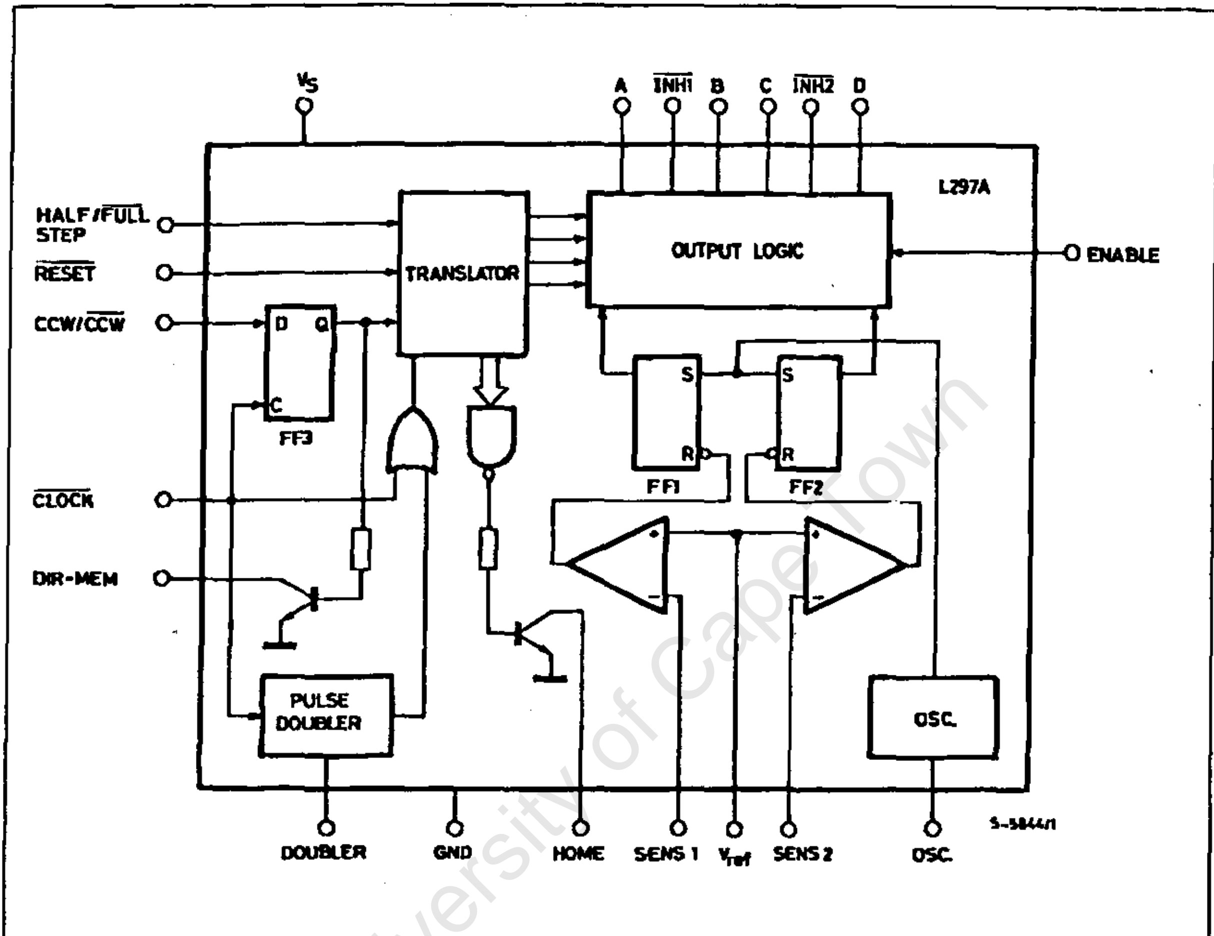

University of Cape Town

APPLICATION HINTS

Bipolar motors can be driven with an L297, an L298N or L293E bridge driver and very few external components (figure 21). Together these two chips form a complete microprocessor-to-stepper motor interface. With an L298N this configuration drives motors with winding currents up to 2A ; for motors up to 1A per winding and L293E is used. If the PWM choppers are not required an L293 could also be used (it doesn't have the external emitter connections for sensing resistors) but the L297 is underutilized. If very high powers are required the bridge driver is replaced by an equivalent circuit made with discrete transistors. For currents to 3.5A two L298N's with paralleled outputs may be used.

For unipolar motors the best choice is a quad darlington array. The L702B can be used if the choppers are not required but an ULN2075B is preferred. This quad darlington has external emitter connections which are connected to sensing resistors (figure 22). Since the chopper acts on the inhibit lines, four AND gates must be added in this application.

Also shown in the schematic are the protection diodes.

In all applications where the choppers are not used it is important to remember that the sense inputs must be grounded and V_{REF} connected either to V_S or any potential between V_S and ground.

The chopper oscillator frequency is determined by the RC network on pin 16. The frequency is roughly 1/0.7 RC and R must be more than 10 KΩ. When the L297A's pulse doubler is used, the delay time is determined by the network R_d C_d and is approximately 0.75 R_d C_d . R_d should be in the range 3 kΩ to 100 kΩ (figure 23).

Figure 21 : This typical application shows an L297 and L298N driving a Bipolar Stepper Motor with phase currents up to 2A.

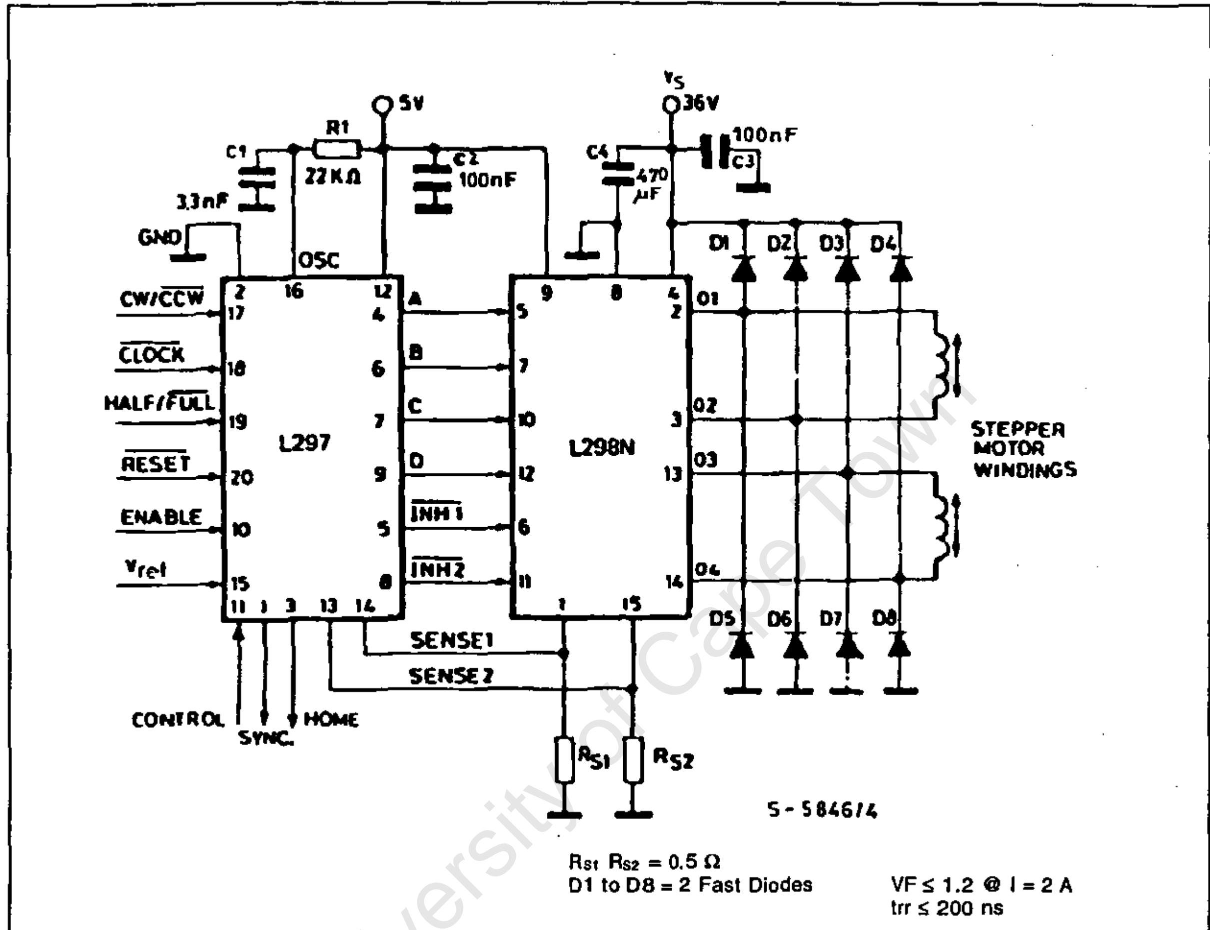

University of Cape Town

Figure 22 : For Unipolar Motors a Quad Darlington Array is coupled to the L297. Inhibit chopping is used so the four AND gates must be added.

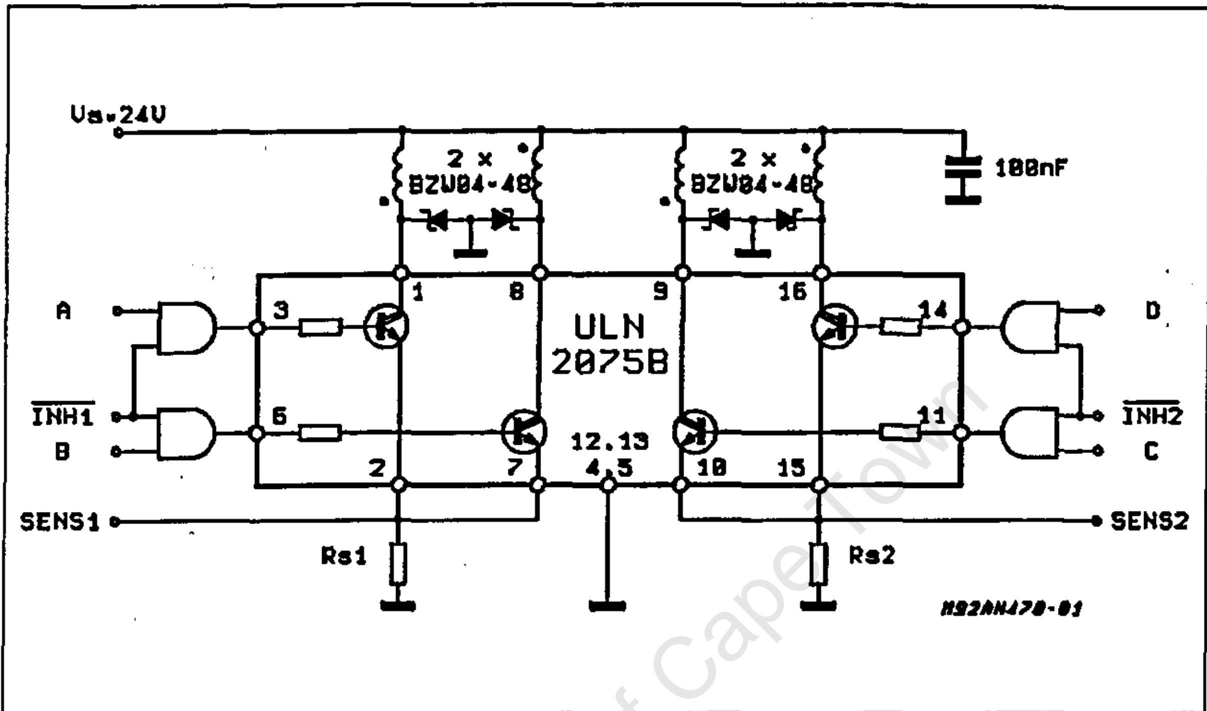

Figure 23 : The Clock pulse doubler inserts a ghost pulse τ_o seconds after the Input clock pulse. $R_d C_d$ is closen to give a delay of approximately half the Input clock period.

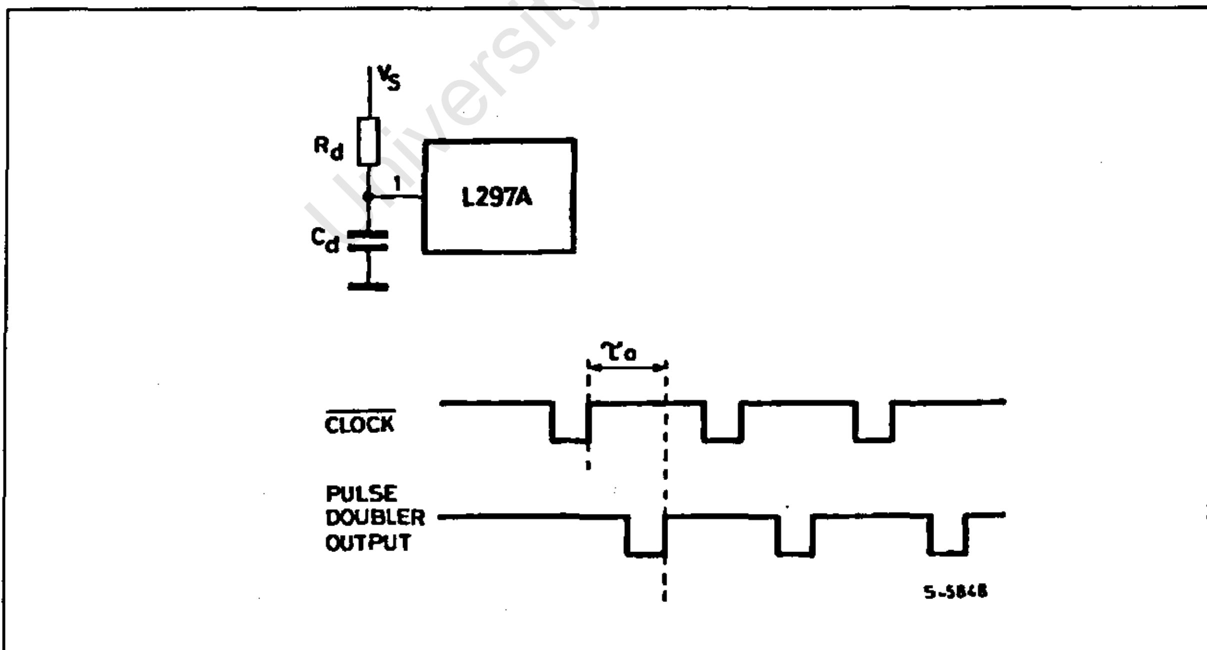

University of Cape Town

PIN FUNCTIONS - L297

N°	NAME	FUNCTION
1	SYNC	Output of the on-chip chopper oscillator. The SYNC connections The SYNC connections of all L297s to be synchronized are connected together and the oscillator components are omitted on all but one. If an external clock source is used it is injected at this terminal.
2	GND	Ground connection.
3	HOME	Open collector output that indicates when the L297 is in its initial state (ABCD = 0101). The transistor is open when this signal is active.
4	A	Motor phase A drive signal for power stage.
5	$\overline{INH1}$	Active low inhibit control for driver stage of A and B phases. When a bipolar bridge is used this signal can be used to ensure fast decay of load current when a winding is de-energized. Also used by chopper to regulate load current if CONTROL input is low.
6	B	Motor phase B drive signal for power stage.
7	C	Motor phase C drive signal for power stage.
8	$\overline{INH2}$	Active low inhibit control for drive stages of C and D phases. Same functions as INH1.
9	D	Motor phase D drive signal for power stage.
10	ENABLE	Chip enable input. When low (inactive) INH1, INH2, A, B, C and D are brought low.
11	CONTROL	Control input that defines action of chopper. When low chopper acts on INH1 and INH2; when high chopper acts on phase lines ABCD.
12	V_s	5V supply input.
13	$SENS_2$	Input for load current sense voltage from power stages of phases C and D.
14	$SENS_1$	Input for load current sense voltage from power stages of phases A and B.
15	V_{ref}	Reference voltage for chopper circuit. A voltage applied to this pin determines the peak load current.
16	OSC	An RC network (R to V_{CC}, C to ground) connected to this terminal determines the chopper rate. This terminal is connected to ground on all but one device in synchronized multi - L297 configurations. $f \cong 1/0.69\ RC$
17	CW/$\overline{CCW}$	Clockwise/counterclockwise direction control input. Physical direction of motor rotation also depends on connection of windings. Synchronized internally therefore direction can be changed at any time.
18	$\overline{CLOCK}$	Step clock. An active low pulse on this input advances the motor one increment. The step occurs on the rising edge of this signal.
19	HALF/$\overline{FULL}$	Half/full step select input. When high selects half step operation, when low selects full step operation. One-phase-on full step mode is obtained by selecting FULL when the L297's translator is at an even-numbered state. Two-phase-on full step mode is set by selecting FULL when the translator is at an odd numbered position. (The home position is designate state 1).
20	$\overline{RESET}$	Reset input. An active low pulse on this input restores the translator to the home position (state 1, ABCD = 0101).
PIN FUNCTIONS - L297A		(Pin function of the L297A are identical to those of the,L297 except for pins 1 and 11)
1	DOUBLER	An RC network connected to this pin determines the delay between an input clock pulse and the corresponding ghost pulse.
11	DIR-MEM	Direction Memory. Inverted output of the direction flip flop. Open collector output.

University of Cape Town

Figure 24 : Pin connections.

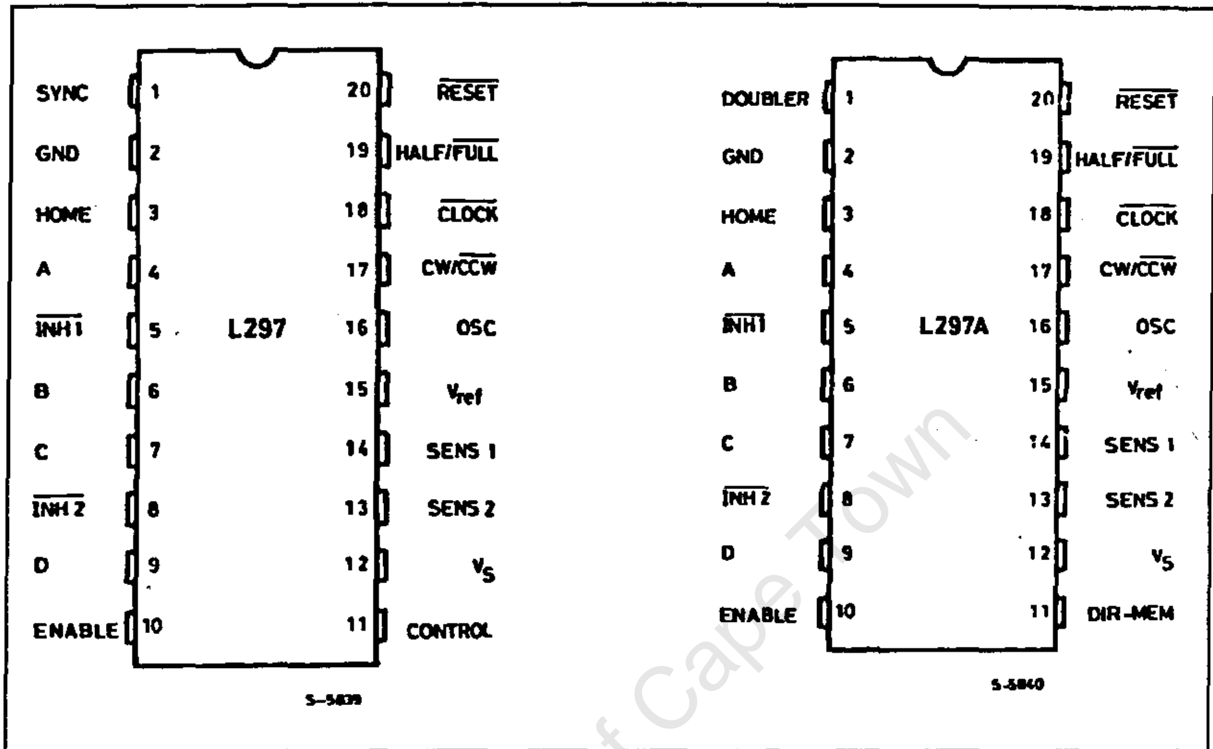

University of Cape Town

University of Cape Town

Information furnished is believed to be accurate and reliable. However, SGS-THOMSON Microelectronics assumes no responsibility for the consequences of use of such information nor for any infringement of patents or other rights of third parties which may result from its use. No license is granted by implication or otherwise under any patent or patent rights of SGS-THOMSON Microelectronics. Specifications mentioned in this publication are subject to change without notice. This publication supersedes and replaces all information previously supplied. SGS-THOMSON Microelectronics products are not authorized for use as critical components in life support devices or systems without express written approval of SGS-THOMSON Microelectronics.

© 1995 SGS-THOMSON Microelectronics - All Rights Reserved

SGS-THOMSON Microelectronics GROUP OF COMPANIES

Australia - Brazil - France - Germany - Hong Kong - Italy - Japan - Korea - Malaysia - Malta - Morocco - The Netherlands - Singapore - Spain - Sweden - Switzerland - Taiwan - Thailand - United Kingdom - U.S.A.

Bibliography

[Alo97a] F. Alonso, M. Rinner, A. Loinaz, J.I. Onate, W. Ensinger, and B. Rauschenbach, *Characterisation of Ti-6Al-V modified by nitrogen plasma immersion ion implantation*, In PBII96 [PBII96], 305–308.

[And77a] H.H. Andersen and J.F. Ziegler, *Hydrogen - stopping powers and ranges in all elements, volume 1*, Pergamon Press, New York, 1977.

[And80a] H.H. Andersen, F. Besenbacher, P. Loftager, and W. Moller, *Large-angle scattering of light ions in the weakly screened Rutherford region*, Phys. Rev. **A21** (1980), 1891–1901.

[Ask88a] D.R. Askeland, *The Science and Engineering of Materials*, s.i. ed., Von Nostrand Reinhold, London, 1988.

[Bar79a] R.A. Baragiola, E.V. Alonso, and A. Oliva-Florio, *Electron emission from clean metal surfaces induced by low-energy light ions*, Phys. Rev. B **19** (1979), 121–129.

[Bar93a] R.A. Baragiola, *Principles and mechanisms of ion induced electron emission*, Nucl. Instr. and Meth. B **78** (1993), 223–238.

[Bet83a] G. Betz and G.K. Wehner, *Sputtering of Multicomponent Materials*, Sputtering by Particle Bombardment I: Physical Sputtering of Single Element Solids (R. Behrisch, ed.), Topics in Applied Physics, Vol. 47, Springer-Verlag, Berlin, 1983, pp. 11–90.

[Bou88a] D. Boutard, W. Moller, and B.M.U. Scherzer, *Influence of H-C bonds on the stopping power of hard and soft carbonized layers*, Phys. Rev. B **38** (1988), 2988–2994.

[Boz93a] M. Bozoian, *A useful formula for departures from Rutherford Backscattering*, Nucl. Instr. and Meth. B **82** (1993), 602–603.

[Bra05a] W.H. Bragg and R. Kleeman, *On the alpha particles of radium, and their loss of range in passing through various atoms and molecules*, Philos. Mag. **10** (1905), 318–340.

[Bro76a] S.C. Brown, *Basic Data of Plasma Physics*, revised second ed., M.I.T. Press, Cambridge, Massachusetts, 1976.

University of Cape Town

[Bru96a] J. Brutscher, *A 100kV 10A High-Voltage Pulse-Generator for Plasma Immersion Ion-Implantation*, Rev. Sci. Instr. **67** (1996), no. 7, 2621–2625.

[Bru96b] M. Bruel, *Application of Hydrogen-Ion Beams to Silicon-on-Insulator Material Technology*, Nucl. Instr. and Meth. B **108** (1996), no. 3, 313–319.

[Che84a] Francis F. Chen, *Introduction to Plasma Physics and Controlled Fusion*, second ed., Plenum Press, New York, 1984.

[Che91a] A. Chen, J.T. Scheuer, C. Ritter, R.B. Alexander, and J.R. Conrad., *Comparison between conventional and plasma source ion-implanted femoral knee components*, J. Appl. Phys. **70** (1991), no. 11, 6757–6760.

[Che96a] N.W. Cheung, *Plasma Immersion Ion-Implantation for Semiconductor Processing*, Mater. Chem. Phys. **46** (1996), no. 2-3, 132–139.

[Chi11a] C.D. Child, *Discharge from hot CaO*, Phys. Rev. **32** (1911), 492–511.

[Chu75a] P.M. Chu, L. Talbot, and K.J. Touryan, *Electric probes in stationary and flowing plasmas*, Springer-Verlag, New York, 1975.

[Chu95a] T. Chudoba, *Interpretation of Depth Sensing Hardness Measurements*, Annual Report: Forschungszentrum Rossendorf (1995), 49–53.

[Con87a] J.R. Conrad, J.L. Radtke, R.A. Dodd, F.J. Worzala, and N.C. Tran., *Plasma source ion-implantation technique for surface modification of materials.*, J. Appl. Phys. **62** (1987), 4591–4596.

[Con88b] J.R. Conrad, *Plasma Source Ion Implantation: A new approach to ion beam modification of materials.*, Mater. Sci. Eng. **116** (1989), 197–203.

[Con88c] J.R. Conrad, S. Baumann, R. Fleming, and G.P. Meeker, *Plasma source ion implantation dose uniformity of a 2x2 array of spherical targets*, J. Appl. Phys. **65** (1989), no. 4, 1707–1712.

[Con89a] J.R. Conrad, R.A. Dodd, and F.J. Worzala, *Plasma Source Ion Implantation: A New Manufacturing Process for Surface Modification of Materials*, Society of Manufacturing Engineers: 15th NSF Grantees conference on Production Research and Technology, 1989.

[Cul89a] D.E. Cullen, M.H. Chen, J.H. Hubbell, S.T. Perkins, E.F. Plechaty, J.A. Rathkopf, and J.H. Scofield, *Tables and Graphs of Photon-Interaction Cross Sections from 10 eV to 100 GeV Derived from the LLNL Evaluated Photon Data Library (EPDL), Part A: Z = 1 to 50; Part B: Z = 51 to 100*, Lawrence Livermore National Laboratory Report UCRL-50400 6, Rev. 4 (1989).

University of Cape Town

[Doe86a] M.F. Doerner and W.D. Nix, *A method for interpreting the data from depth-sensing indentation measurements*, J. Mater. Res. **1** (1986), no. 4, 601–609.

[Don88a] I.J. Donnelly and P.A. Watterson, *Ion-matrix sheath structure around cathodes of complex shape*, J. Phys. D **22** (1989), 90–93.

[Doo86a] R.L. Doolittle, *A semi-automatic algorithm for Rutherford Backscattering Analysis*, Nucl. Instr. and Meth. B **15** (1986), 227–231.

[En94a] W. En and N.W. Cheung, *Analytical Modeling of Plasma Immersion Ion-Implantation Target Current Using the Spice Circuit Simulator*, J. Vac. Sci. Technol. B **12** (1994), no. 2, 833–837.

[En96a] W. En and N.W. Cheung, *A New Method for Determining the Secondary-Electron Yield Dependence on Ion Energy for Plasma Exposed Surfaces*, IEEE Trans. Plasma Sci. **24** (1996), no. 3, 1184–1187.

[En98a] W.G. En, I.J. Malik, M.A. Bryan, S. Farrens, F.J. Henley, N.W. Cheung, and C. Chan, *The Genesis Process[TM]: A New SOI wafer fabrication method*, In *1998 IEEE International SOI Conference Proceedings* [IEEESOI98], pp. 163–164.

[Fer82a] J. Feron, E.V. Alonso, R.A. Baragiola, and A. Oliva-Florio, Surf. Sci. **120** (1982), 427.

[Fin99a] A.L. Finkelshtein and T.O. Pavlova, *Calculation of X-Ray Tube Spectral Distributions*, X-Ray Spectrom. **28** (1999), 27–32.

[Hen95a] R.C. Hendrix, *The use of shape correction factors for elastic indentation measurements*, J. Mater. Res. **10** (1995), no. 2, 255–257.

[Her79a] N. Hershkowitz, J.R. DeKock, P. Coakley, and S.L. Cartier, *Surface trapping of primary electrons by multidipole magnetic fields*, Rev. Sci. Instr. **51** (1980), 210–218.

[Hon94a] MunPyo Hong and G.A. Emmert, *Two-dimensional fluid modeling of time-dependant plasma sheath*, J. Vac. Sci. Technol. B **12** (1994), no. 2, 889–896.

[IEEESOI98] *1998 IEEE International SOI Conference Proceedings*, Florida, Indian River Plantation, 1998.

[IEEESOI99] *1999 IEEE International SOI Conference Proceedings*, California, Rohrnet Park, 1999.

[Kit76a] C. Kittel, *Introduction to Solid State Physics*, 5th edn ed., Wiley, New York, 1976.

[Lan23a] I. Langmuir, *The effects of Space Charge and Initial Velocities on the Potential Distribution and Thermionic Current between Parallel Plane Electrodes*, Phys. Rev. **21** (1923), 4.

[Lan29a] I. Langmuir, *The Interaction of Electron and Positive Ion Space Charges in Cathode Sheaths*, Phys. Rev. **33** (1929), 954–989.

University of Cape Town

[LEc79a] J. L'Ecuyer, J.A. Davies, and N. Matsunami, *How accurate are absolute Rutherford Backscattering yields*, Nucl. Instr. and Meth. **160** (1979), 337–346.

[LeC97a] F. Le Coeur, Y. Arnal, R.R. Burke, O. Lesaint, and J. Pelletier, *Ion implantation based on the uniform distributed plasma*, Surf. Coat. Technol. **93** (1994), 265–268.

[Lia80a] Z.L. Liau and J.W. Mayer, *Ion Bombardment Effects on Material Composition*, Treatise on Materials Science and Technology (J.K. Hirvonen, ed.), Academic Press, New York, 1980.

[Lie89a] M.A. Lieberman, *Model of plasma immersion ion implantation*, J. Appl. Phys. **66** (1989), no. 7, 2929–2929.

[Lim91a] Wee Beng Lim, J. Cooney, M.S. Ghaemi, M. Gavin, D.R. Anderson, and K.E. Lonngren, *On Plasma Sheaths Surrounding complex shapes as measured using ion acoustic waves*, J. Phys. D **24** (1991), 1081–1085.

[Lou84a] J.L. Loubert, J.M. Georges, O. Marchesini, and G. Meille, J. Tribology **106** (1984), 43.

[Lu97a] X. Lu, N.W. Cheung, M.D. Strathman, P.K. Chu, and B. Doyle, *Hydrogen induced silicon surface layer cleavage*, Appl. Phys. Lett. **71** (1997), no. 13, 1804 – 1806.

[Lu98a] X. Lu, S.S.K. Iyer, J. Lee, B. Doyle, Z.N. Fan, P.K. Chu, C.M. Hu, and N.W. Cheung, *Plasma Immersion Ion-Implantation for SOI Synthesis - Simox and Ion-Cut*, J. Electron. Mater. **27** (1998), no. 9, 1059–1066.

[Man00a] S. Mandl and B. Rauschenbach, *Anisotropic strain in nitrided austenitic stainless steel*, J. Appl. Phys. **88** (2000), no. 6, 3323–3329.

[Man97c] S. Mandl, J. Brutscher, R. Guenzel, and W. Moeller, *Ion energy distribution in plasma immersion ion implantation*, Surf. Coat. Technol **93** (1997), 234–237.

[Man98a] S. Mandl, R. Gunzel, and W. Moller, *Sheath and presheath dynamics in plasma immersion ion implantation*, J. Phys. D: Appl. Phys. **31** (1998), 1109–1117.

[Mat84a] N. Matsunami, Y. Yamamura, Y. Itikawa, N. Itoh, Y. Kazumata, S. Miyagawa, K. Morita, R. Shimizu, and H. Tawara, *Energy dependence of the ion-induced sputtering yields of monatomic solids*, Atomic data and nuclear data tables, vol. 31, Academic Press, New York, 1984.

[Mat94a] J.N. Matossian, *Plasma Ion Implantation technology at Hughes Research Laboratories*, J. Vac. Sci. Technol. B **12** (1994), no. 2, 850–853.

[Mat96a] J.N. Matossian and R. Wei, *Operating characteristics of a 100kV, 100kW plasma ion implantation facility*, Surf. Coat. Technol **85** (1996), 92–97.

University of Cape Town

[May97a] M. Mayer, *SIMNRA User's Guide*, Technical Report IPP 9/113, Max-Planck-Institute Fur Plasmaphysik, Garching, Germany, 1997.

[Mey96a] K.A. Meyer, *Two-dimensional plasma sheath observations in Plasma Source Ion Implantation*, Master's thesis, University of Natal, Durban, 1996.

[Nak97a] K. Nakamura, S. Mandl, J. Brutscher, R. Guenzel, and W. Moeller, *Direct Measurements of High-energy Secondary Electrons During Plasma Immersion Ion Implantation*, Proceedings of the 3rd International Conference on Reactive Plasmas and 14th Symposium on Plasma Processing (Nara, Japan), 1997, pp. 307–308.

[Nak97b] K. Nakamura, S. Mandl, J. Brutscher, R. Guenzel, and W. Moeller, *Incident ion monitoring during Plasma Immersion Ion Implantation by Direct Measurements of High-energy Secondary Electrons.*, In PBII96 [PBII96], pp. 242–246.

[Nas96a] M. Nastasi, J.W. Mayer, and J.K. Hirvonen, *Ion-Solid Interactions: Fundamentals and applications*, Cambridge Solid State Science Series, Cambridge University Press, Cambridge, 1995.

[Oli92a] W.C. Oliver and G.M. Pharr, *An improved technique for determining hardness and elastic modulus using load and displacement sensing indentation experiments*, J. Mater. Res **7** (1992), no. 6, 1564–1583.

[Pad01a] J. Padayachee, K.A. Meyer, and V.M. Prozesky, *The automatic fitting of Rutherford Backscattering Spectrometry specta*, Nucl. Instr. and Meth. B (2001), (in press).

[PBII96] *Proceedings of 3rd International Workshop on Plasma-based Ion Implantation, Dresden, 15–18 September 1996*, vol. 93, Surf. Coat. Technol., no. 2–3, 1997.

[PBII98] *Proceedings of 4th International Workshop on Plasma-based Ion Implantation, Dearborn, 2–4 June 1998*, vol. 17, J. Vac. Sci. Technol., no. 2, 1999.

[Pei55a] H.S. Peiser, H.P. Rooksby, and A.J.C. Wilson (eds.), *X-ray diffraction of Polycrystalline Materials*, Institute of Physics, London, 1955.

[Pel85a] P.A. Pella, L. Feng, and J.A. Small, *An Analytical Algorithm For Calculation Of Spectral Distributions of X-Ray Tubes for Quantitative X-Ray Flourescence Analysis*, X-Ray Spectrom. **14** (1985), no. 3, 125–135.

[Pel91a] P.A. Pella, L. Feng, and J.A. Small, *Addition of M- and L-series Lines to NIST Algorithm for Calculations of X-Ray Tube Output Spectral Distributions*, X-Ray Spectrom. **20** (1990), 109–110.

[Pro99a] V.M. Prozesky, K. Meyer, M. Alport, and C. Comrie, *Plasma-based Ion Implantation Facility and Research at the National Accelerator Centre, Faure*, In PBII98 [PBII98], pp. 808–812.

University of Cape Town

[Qin91a] Shu Qin, Chung Chan, N.E. McGruer, J. Browning, and K. Warner, *The response of a microwave multipolar bucket plasma to a high voltage pulse*, IEEE Trans. Plasma Sci. **19** (1991), no. 6, 1272–1278.

[Qin94a] S. Qin and C. Chan, *Plasma Immersion Ion-Implantation Doping Experiments for Microelectronics*, J. Vac. Sci. Technol. B **12** (1994), no. 2, 962–968.

[Rea94a] W.A. Reass, *Survey of high-voltage pulse technology suitable for large scale plasma source ion implantation processes*, J. Vac. Sci. Technol. B **12** (1994), no. 2, 854–860.

[Rij93a] H.A. Rijken, S.S. Klein, L.J. van IJzendoorn, and M.J.A. de Voigt, *Elastic recoil detection analysis with high energy alpha beams*, Nucl. Instr. and Meth. B **79** (1993), 532–535.

[Sch90a] J.T. Scheuer, M. Shamim, and J.R. Conrad, *Model of plasma source ion implantation in planar, cylindrical and spherical geometries*, J. Appl. Phys. **63** (1990), no. 3, 1241–1245.

[Sha91b] M.M. Shamim, J.T. Scheuer, R.P. Fetherson, and J.R. Conrad, *Measurement of electron emission due to energetic ion bombardment in plasma source ion implantation*, J. Appl. Phys. **70** (1991), no. 9, 4756–4759.

[She93b] T.E. Sheridan, *Ion-Matrix Sheath in a Cylindrical Bore*, J. Appl. Phys. **74** (1993), no. 8, 4903–4906.

[She94a] T.E. Sheridan and M.J. Alport, *Ion-matrix sheath around a square bar*, J. Vac. Sci. Technol. B **12** (1994), no. 2, 897–900.

[She95b] T.E. Sheridan and M.J. Goeckner, *Collisional Sheath Dynamics*, J. Appl. Phys. **77** (1995), no. 10, 4967–4972.

[She95C] T.E. Sheridan, *Pulsed-Sheath Ion Dynamics in a Trench*, J. Phys. D **28** (1995), no. 6, 1094–1098.

[She96b] T.E. Sheridan, *Ion Focusing by an Expanding, 2-Dimensional Plasma Sheath*, Appl. Phys. Lett. **68** (1996), no. 14, 1918–1920.

[Sig81a] P. Sigmund, *Sputtering by Ion Bombardment: Theoretical concepts*, Sputtering by Particle Bombardment I: Physical sputtering of single element solids (R. Behrisch, ed.), Topics in Applied Physics, vol. 47, Springer-Verlag, Berlin, 1981, pp. 9 – 71.

[Ste91a] R.A. Stewart and M.A. Lieberman, *Model of plasma immersion ion implantation for voltage pulses with finite rise and fall times*, J. Appl. Phys. **70** (1991), no. 7, 3481–3487.

[Tes95a] J.R. Tesmer and M. Nastasi, *Handbook of Modern Ion Beam Materials Analysis*, MRS, Pitsburgh, 1995.

University of Cape Town

[The98a] C.C. Theron, J.A. Mars, C.L. Churms, J. Farmer, and R. Pretorius, *In-Situ, Real-Time RBS Measurement of Solid-State Reaction in Thin-Films*, Nucl. Instr. and Meth. B **139** (1998), no. 1-4, 213–218.

[Tou99a] U. von Toussaint, R. Fischer, K. Krieger, and V. Dose, *Depth profile determination with confidence intervals from Rutherford backscattering data*, New J. Phys. **1** (1999), 11.1–11.13.

[Viz90a] G. Vizkelethy, *Simulation and Evaluation of Nuclear Reaction Spectra*, Nucl. Instr and Meth. B **45** (1990), 1–5.

[Wan93a] Dezhen Wang, Tengcai Ma, and Xinlu Deng, *Model of collisional sheath evolution in plasma source ion implantation*, J. Appl. Phys. **74** (1993), no. 4, 2986–2988.

[Wat88a] P.A. Watterson, *Child-Langmuir sheath structure around wedge-shaped cathodes*, J. Phys. D **22** (1989), 1300–1307.

[Win70a] K.B. Winterbon, P. Sigmund, and J.B. Sanders, *Spatial Distributions of Energy Deposited by Atomic Particles in Elastic Collisions*, Mat. Fys. Medd. Dan Vid. Selsk. **37** (1970), no. 14, 1–73.

[Woo93a] B.P. Wood, *Displacement current and multiple-pulse effects in plasma source ion implantation*, J. Appl. Phys. **73** (1993), no. 10, 4770–4778.

[Xia93a] Zhongyi Xia and Chung Chan, *Modelling and experiment on plasma source ion implantation*, J. Appl. Phys. **73** (1993), no. 8, 3651–3656.

[Yam89a] Y. Yamamura and N. Itoh, *Sputtering Yield*, Ion Beam Assisted Film Growth (T. Itoh, ed.), Elsevier, Amsterdam, 1989.

[Yun99a] C. H. Yun, A. B. Wengrow, N. W. Cheung Y. Zheng, R. J. Welty, Z. F. Guan, K. V. Smith, P. M. Asbeck, E. T. Yu, and S. S. Lau, *Fractional implantation area effects on patterned ion-cut silicon layer transfer*, In *1999 IEEE International SOI Conference Proceedings* [IEEESOI99], pp. 129–130.

[Zie85a] J.F. Ziegler, J.P. Biersack, and U. Littmark, *The stopping and range of ions in solids*, The stopping and Ranges of Ions in Matter, no. 1, Pergamon Press, New York, 1985.

University of Cape Town